CONTENTS

Acta Technica *62* No. 3A/2017, 1–12

On ZigBee location technology in football training

Lu Huang[1,3], Rong Huang[2]

Abstract. ZigBee location technology was applied to football training system to achieve a practical wireless sensor training system with low cost. The studied football training system was mainly made up of mobile node, reference node, coordinate and monitoring software of upper computer, and their installation methods and functions were elaborated. Node hardware, based on CC2430 and CC2431 chips which integrated radio frequency (RF) and 8051 controller, was an interacting platform for RF module, debugging module, functional module and indication circuit. Specific algorithm was developed based on ZStack protocol stack and specific methods to achieve functions of various nodes were provided. Finally, test was made accordingly and data relevant to football training were recorded, such as total running distance, start reaction and movements of all football players and their intentions to execute coach's strategies. Besides, the studied system met requirements of low cost and high performance.

Key words. ZigBee technology, wireless location system, football training, movements, node
.

1. Introduction

With the rising competitiveness level, requirement of coach for players were more strict than used to be, which means that physical states and capabilities of all athletes should be measured [1]. In recent years, wireless communication technology and sensor technology were developed, which can be used to measure physical states and capabilities of all athletes. Generally, wireless sensor network (WSN) was made up of small sensor nodes with functions of data calculating and communication. Those nodes are communicating and collaborating with radio wave formed an interconnected network system which was used to upload data to PC terminal server. Thus, it is easier to process and fed back data of surroundings and tested object. ZigBee network technique was used to build hardware platform for new WSN which

[1]Department of Physical Education, Science and Technology College GanNan Normal University, Ganzhou, 341000, Jiangxi, China
[2]Six Bridge Township Central primary school of Chongren Country, Jiangxi, 344200, China
[3]Corresponding author; E-mail: luhuangwork@yeah.net

was used to collect and transmit information within the monitored range in football field continuously and stably.

2. Literature review

ZigBee WSN, which is a wireless data transmission network, is designed based on IEEE802.15.4 technical standard and ZigBee network protocol [2, 3]. Zigbee technology, featuring low cost, high efficiency, low power consumption and position function, is more and more widely used in fields such as smart home, industrial control and medical care because more and more people need the relative position of specific object in some specific situations. In other word, more and more people are eager to have access to ZigBee WSN with real time position technology and tracking technique [4]. Thus, monitoring system for football running position is researched and developed based on Zigbee technique.

Compared with other wireless communication technology, terminal of Zigbee wireless sensor network technology can be represented by an ad hoc network that is launched by coordinator and with which special requirements of WiFi to fields is avoided. Because transmission distance of traditional Bluetooth technology is within 10 m and football players run on field randomly and their distance cannot be limited by 10 m, Zigbee wireless sensor network technology with transmission distance of 100 m is more suitable. Thus, location technique of Zigbee wireless sensor network is applied to monitoring system of football positioning and its location performance is studied.

3. Research method

3.1. Overall design

Football players should not only have a good physical fitness but also have a well understand of tactic running position. ZigBee locating technology applied in football training was to be studied and running positions of players were selected as main objects of study. Each parts of system will be analyzed briefly. Figure 1 represents the principal simulation for whole system.

It is obvious from Fig. 1 that the system is mainly made up of controlling host PC, reference node, mobile node and coordinator. Controlling host PC is also called upper computer. Relevant control and monitoring software were built in the upper computer for coach to observe players' running position and evaluate players' understanding of tactics. CC2430 was used as coordinator to build ZigBee network, which was used to transmit coordinate of location node (mobile node) and parameters of external environment to controlling host PC during communication. Besides, CC2430 was also used as reference node in order to serve as a router [5] and provide coordinate of mobile node and RSSI average value because each player needs to be located. Moreover, coordinate of reference node was fixed by users. CC2431 was used as mobile coordinate because CC2431 was internal integrated location engine

while CC2430 was not. CC2431 can be used to provide reference coordinate and average value of RSSI of reference node. Thus, relative position coordinates of a mobile node compared with the reference node can be calculated. Then, wireless network was used to transmit node identity and coordinate to coordinator.

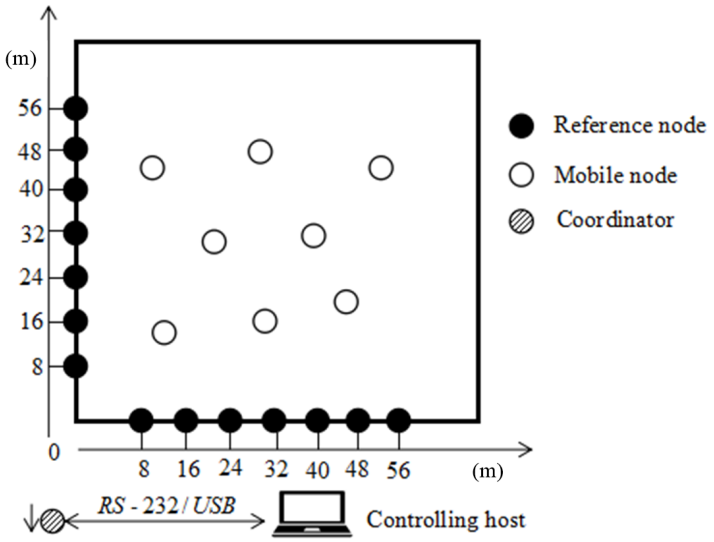

Fig. 1. System principle simulation

Inference for core algorithm of locating: given transmitted power of transmitting module was Pf; receiving power of receiving module was Ps; straight-line distance between those two modules was L and propagation factor was n. According to RSSI ranging principle that strength of transmitting signal decreases regularly with the increase of distance, the relations between transmitted power and receiving can be shown as $Ps = Pf/Ln$. Long-distance Path Loss Model was adopted and the logarithm was taken as $10 \lg Ps = 10 \lg Pf - 10n \lg L$. Transmitted power Pf of transmitting module was given as A because it is a constant; thus $10 \lg Ps = A - 10n \lg L$. Received signal strength was RSSI, thus, it can be interference that RSSI $= A - 10n \lg L$ (units: dB m). Through equivalent variation of mathematical formula, the range formula can be shown as $L = 10(A - \text{RSSI})/(10n)$.

3.2. Hardware platform design and implementation

Hardware circuit was mainly made up of two modules, wireless communication interface module and function module. Wireless communication interface module can receive and send information data among modules, which was the core component of the hardware platform. Function module was mainly made up of power circuit, serial circuit, indicating circuit and keying circuit.

3.2.1. CPU module: An enhanced 8051 CPU kernel of 8 bytes was integrated by CC2430, whose instruction execution speed was faster than that of standard

8051. There was a wireless module in CC2430. Position module was involved, for which Received Signal Strength Indicator (RSSI) of inserted CC2430 was intensively studied. Value of RSSI was a signed binary complement of 8 bytes, which can be read in registers such as RSSIL and RSSI_VAL. Within 8 symbol periods of 128 us, expected values equals to value of RSSI. Gain P of RSSI register value such as RSSIL and RSSI_VAL in RF can be calculated using the formula

$$P = RSSI\_VAL + RSSI\_OFFSET \text{ [dbm]} \tag{1}$$

RSSI_OFFSET was estimated value of pre-gain based on practical situation during system developments. Generally, RSSI_OFFSET was approximate to -45. Given RSSI register was read as -20. Then, actual input power of RF was approximate to -65 dBm. Figure 2 shows a typical relation graph of input power and RSSI_VAL. Thus, linear performance of RSSI value read in CC2430 was well and its dynamic range was about 100 dB.

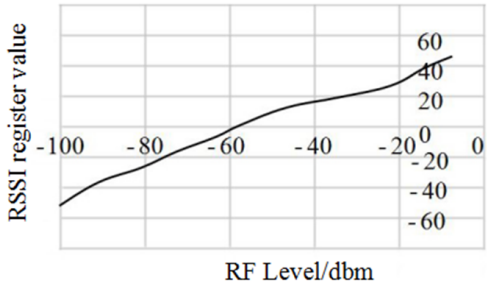

Fig. 2. Relation between RSSI value and input power

3.2.2. Design of backstepping controller: A two-line interface was provided by debugging interface of CC2430 to system on chip debugging. Through this debugging interface, on-chip Flash can be programmed and memorizer and register can be read [6]. In the debugging mode, Pin P2_1 of I/O was changed into debugging data cable and P2_2 was changed into clock line of debugging. Figure 3 shows sequence diagram of debugging interface.

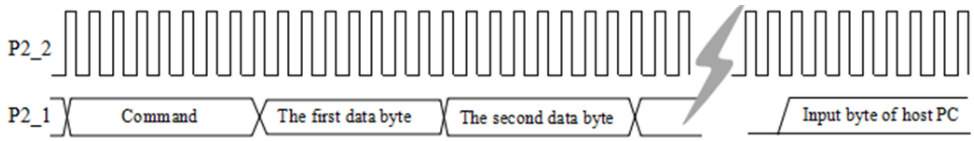

Fig. 3. Sequence diagram of debugging interface

It can be seen from Fig. 3 that SPI of two-line interface was used by debugging interface and data was driven onto pin of two-way debugging data in order to sampling on positive and negative edge of debugging clock. Debugging time was determined by debug command sent by external PC which command was made up of 1 to 4 input bytes (includes command byte) and an optional input byte read by host PC.

The first byte of debug command was command byte whose coding scheme is:

1. 7–3 bytes were instruction code;
2. 2–1 bytes were return input bytes to host PC;
3. 1–0 bytes were number of bytes of command bytes of host PC.

Debugging interface would be limited under certain circumstance though it can operate under all power modes. Under certain power mode, power consumption would be much higher than expected value because system was operating under normal mode with digital voltage regulator in operation. When debugging power mode was in 2 and 3 states, chip would stop operation when the system awoke. Thus, command of HALT and RESUME was need to make sure software would work continuously. When chip was awaken in power mode 1, system will continuously to work.

3.2.3. CC2430 peripheral equipment:

1) Power management clock

Power management controller (PMC) of CC2430 was studied. Power module was closed to avoid static power loss and achieve Ultra lower power run (VLPR). In the other hand, the lowest dynamic consumption can be achieved by clock gating and closed oscillator. Table 1 can be used to analysis influence of power mode to system operation and relations between power conditioner and oscillator.

Table 1. Power modes

Power mode	High-frequency oscillator	Low-frequency oscillator	Digital power regulator
Configuration	A: NO, B:32MHz crystal oscillator, C:16MHz RC oscillator	A:no, B:32.753kHz RC oscillator, C:32.768kHz crystal oscillator	NO
PM0	B,C	B or C	Open
PM1	A	B or C	Open
PM2	A	B or C	Closed
PM3	A	A	Closed

2) CC2430 Reset

There are four reset reasons for CC2430, including entry pin RESET_N into low level forcibly, power-on reset, Brown-out restoration, watchdog reset [7]. There are 4 initial states after restoration:

- Set I/O pin as input and pull up.
- Counter of CPU program was set as 0x0000 at which position program starts operation.
- All peripheral registers were initialized as restoration value.
- Watchdog timer was forbidden to work.

When equipment is on, there is a power on reset (POR) providing properly ini-

tialization in CC2430. In the meanwhile, Brown-out detection (BOD) working with adjusting 1.8 V digital power supply can ensure memorizer was integrated though changing supply voltage would cause adjusting 1.8 V power lower than that of Flash memorizer and the lowest level regulated by SRAM [8]. For CC2430, before starting power-on initialization, power-on reset and brown-out detection will keep equipment in reset state until supply voltage was higher than that of power on reset and brown-out detection.

In Fig. 4, working state of POR/BOD of typical 1.8 V adjusting power supply voltage with positive reset signal BOD_RESET and BOD_RESET can be observed. Reset cause for system's last can be read in register SLEEP.RST.

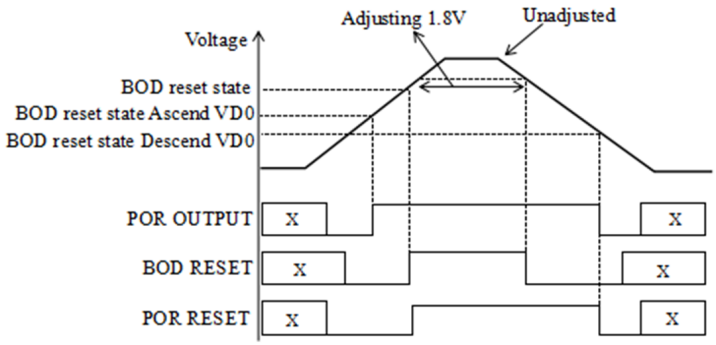

Fig. 4. Relations between power-on reset and brown-out detection

3) Others

There are 21 digital I/O pin, which can be configured as GPIO interface or used as external I/O signal to connect peripherals such as ADC, UART or timer by configuring register.

Direct memorizer access (DMA) controller was inserted in CC2430, with which CPU was basically not involved in data processing such as transmit data from ADC and RF to peripheral. DMA controller had to coordinate all DMA data transfer task to ensure DMA request and CPU access were working according to priority sequence. Data of memorizer was transferred by programming DMA path with software under DMA control. Actually, DMA controller also controlled other data transfer besides data in external data memory space.

There are two serial communication interfaces (SCI) in CC2430, T0 and USART1. Those two interfaces have two modes with some same functions, one was asynchronous serial mode and the other was synchronous serial peripheral interface.

There are two low voltage stabilizers those mainly for providing 1.8 V voltage and using as analog and digital power source. Besides, voltage stabilizers should not be used to supply power to external circuit because capacitance of power supply was limited and voltage stabilizers would produce noise which would influence stability of electric circuit.

3.2.4. Design of circuit schematic diagram: Figure 5 shows specific circuit schematic diagram.

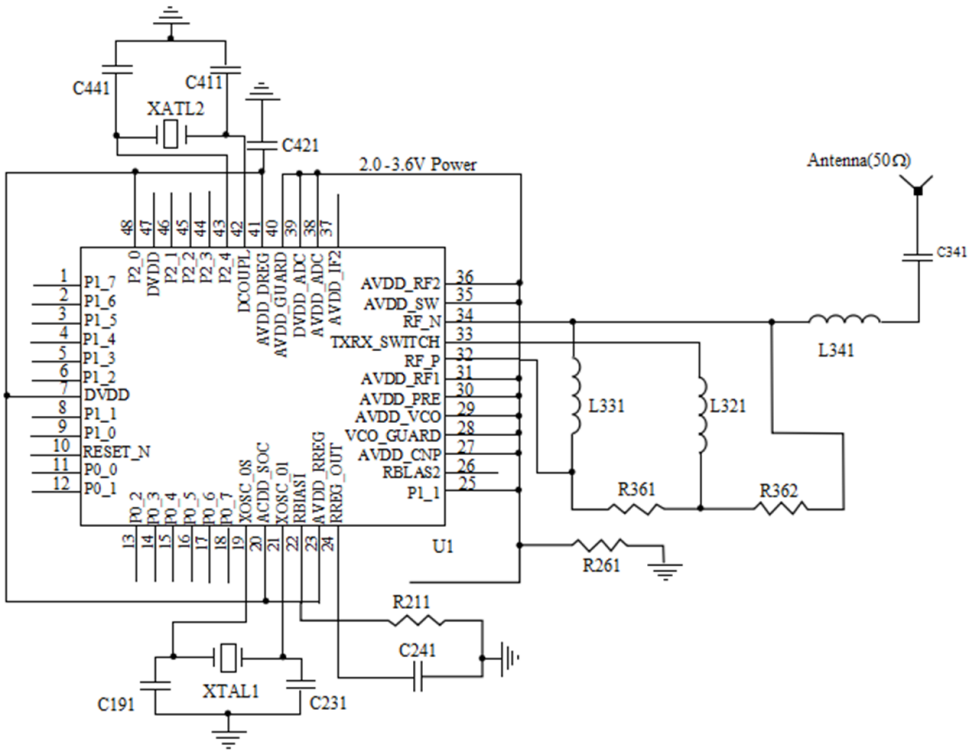

Fig. 5. Design of typical circuit schematic diagram

However, for the layout of PCB, size of decoupling capacitor of power supply, circuit layout and filtering of power supply should be well designed in order to achieve well performance. Decoupling capacitor should be close to pin for power supply and via hole should be designed separately for connecting ground plane of PCB panel. When designing external digital facilities of high speed, it should avoid disturbing RF circuit. Figure 6 shows specific PDB graph.

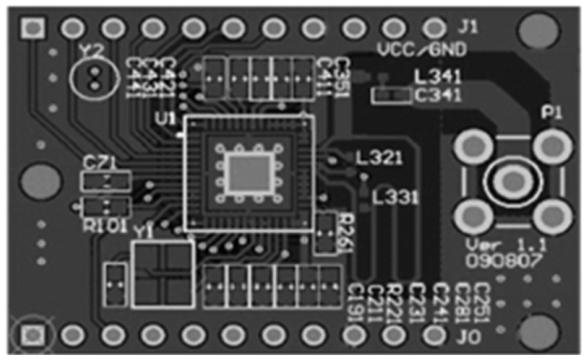

Fig. 6. PCB graph of CC2430

3.3. Software design

Software development platform IAR of ZigBee and ZStack protocol stack were used to develop software. OSAL was used to allocate tasks, which will form a simple and practical multi-task operating system through certain ways. In original state, OSAL will initialize system software and system resources. Objects of study have to be located, thus detailed analysis and study about it to be made. Code of ZigBee wireless position was based on Profile document that involves three parts, reference node, location node and coordinator. Those three parts represents three equipments and certain application range and serial ID function for equipments were identified.

XY-RSSI request: a response message will be triggered after sending serial ID 0x0011. Accepting equipment would return this XY-RSSI response message after receiving it. Location node would send this respond to reference node. Expected value calculated using collected signal strength and coordinate of X and Y will be sent by reference node to location node.

XY-RSSI response: serial ID 0x0012 was used to answer request of XY RSSI. RSSI of request information was included in expected value of RSSI. Those receipt response signal that made up of 5 bits would be stored for calculating coordinate, see Table 2 below.

Table 2. XY-RSSI information

Bit	Function
0, 1	X coordinate of reference node
2, 3	Y coordinate of reference node
4	Broadcast average value of RSSI value to itself of all reference nodes

Discovery request of location node: serial ID 0x0013 was used to locate with location node forcibly. When sending this ID, few of irrelevant content should be included. This ID can be read at location node and then coordinate of location node was achieved with a calculation. Answer to location node discovery: serial ID 0x0014. Table 3 shows ID information.

Table 3. Discovery requests of location node

Bit	Function	Value	Bit	Function	Value
0	State	0or1	6,7	Short URL of recent reference node	NO
1, 2	X coordinate calculated by location node	NO	8, 9	X coordinate of recent reference node	NO
3, 4	Y coordinate calculated by location node	NO	10, 11	Y coordinate of recent reference node	NO
5	Number of reference nodes	0∼8	12	RSSI value of recent reference node	NO

Unicast of reference node configuration: serial ID 0x0015 was sent to reference node configuration and answer request of reference node configuration. This information was obtained from PC. After this step, coordinate of reference nodes X and Y were set. Table 4 shows the configuration information.

Table 4. Configuration information of reference node

Bit	Function
0,1	X coordinate of reference node
2,3	Y coordinate of reference node

Unicast of location node configuration: serial ID 0x0016 can be used to configure location node which include A-parameter, A-parameter, running mode, information collecting time and cycle length. This information was gained from PC upper computer. Table 5 shows specific configuration information.

Table 5. Configuration information of mobile node

Bit	Function	Remark
0	A-parameter of mobile node	Intensity of electrical signal within the circumstance of 1 m around emission node was sampled
1	N-parameter of mobile node	Intensity of electrical signal within the circumstance of 1 m around emission node was sampled
2	Running mode	0: Waiting for discovery or response of information request; 1: Discover information or response automatically
3, 4	Waiting time before collection	Waiting time (ms) after sending request information
5, 6	Period	Time for one discovery under Automatic mode
7, 8	Short URL	Destination address of automatic mode to location node response. In contrast, request address.
9	Ref.end	NO
10	The minimum number of reference node	The minimum node involved in calculation

Reference node request configuration broadcast: serial ID 0x0017 was sent to the reference node to be configured. Through this command, all configuration information about position in reference node can be got and configuration broadcast of request in location node can be known whose main content was about serial ID 0x0018 which can be sent to mobile node to request node configuration information. Thus, all parameters about location node were obtained. Serial ID 0x0019 was sent several times to reference node within a given distance. Expected level of

RSSI information can be obtained with reference node. After configuring location information, software was built through hardware platform.

4. Result and analysis

A test area of 16×16 was set in basketball court (see Figs. 7 and 8) in which 6 reference nodes were set. Coordinates of these 6 reference nodes are A(0,4), B(0,8), C(0,12), D(4,0), E(8,0) and F(12,0). Three mobile nodes (a, b, c) were moving randomly in the test area and upper computer monitoring software was used to locating, tracking and analyzing theses three mobile nodes. Meanwhile, estimated positions were shown in software and marked as a1, b1 and c1.

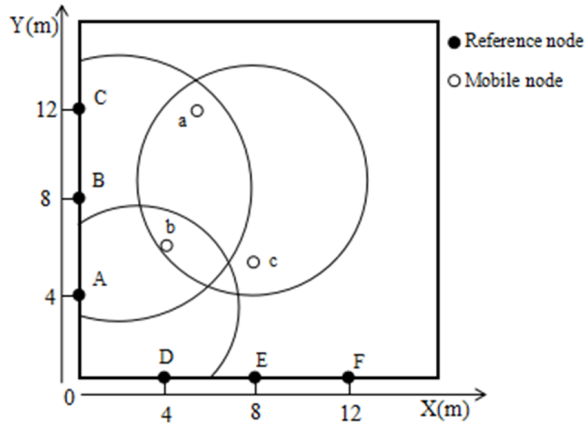

Fig. 7. Practical distribution map of mobile node at time T

Practical and estimated distribution maps of mobile node were shown in Figs. 7 and 8. Table 6 shows comparison of nodes' practical and estimated coordinates. For test result, precision analysis on location error was made, whose equation is

$$\text{error} = \sqrt{(x - x1)^2 + (y - y1)^2}\,, \tag{2}$$

where x, y are the practical coordinates and $x1$, $y1$ are the location coordinates of a point.

Table 6. Comparison between nodes' practical and estimated coordinates at time T

Type	A	B	C
Practical coordinate (m)	(6.00,12.00)	(4.00,6.00)	(8.00,5.00)
Location coordinate (m)	(6.18,11.78)	(4.13,6.35)	(8.23,4.88)
Location error (m)	0.284	0.373	0.259

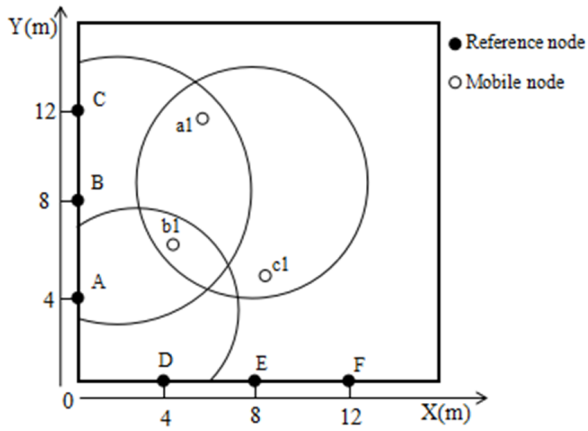

Fig. 8. Estimated distribution map of mobile node at time T

In practical, short URL of two nodes sometimes would be the same, which was tackled through repeated experiments. To sum up, method studied was proved to be feasible and effective by experimental testing.

5. Result and analysis

After analyzing existing wireless location technology, some classic location techniques of wireless local area network and specific functions provided by ZigBee technique, design scheme was put forwarded whose hardware was based on core chip of CC2430 and CC2431 and software was using Z-Stack protocol stack. Running position of football players on court were objects for study location technology based on ZigBee network. Study method that used was proved to be feasible and effective by experimental testing. There are many obstacles in this study, some of which were tackled by repeated experiments while some need further improvement.

References

[1] C. S. Ricci, J. F. Moreira, F. E. Yoshimura, M. C. S. Pontoglio: *Legitimizing the coaching profession in the dispute for symbolic capital in football in Brazil.* Sports Coaching Review *5* (2016), No. 2, 202–204.

[2] Y. J. Mon: *The research on temperature monitor by using microcontroller unit and ZigBee Wireless Sensor Network (WSN).* Advanced Science Letters *18* (2012), No. 1, 221–224.

[3] G. Y. Huang: *Win CE and ZigBee Wireless Sensor Network-based design.* Applied Mechanics and Materials *411–414* (2013), 844–849.

[4] J. Y. Guan, Y. C. Xu, W. Y. Zhang: *Acoustic target location algorithm based on ZigBee Wireless Sensor Network.* Applied Mechanics and Materials *340* (2013), 783–786.

[5] X. Hou, W. Hu, L. Zhang: *Design of altimeter and barometer module monitor system based on CC2430.* Computer Measurement & Control *19* (2011), No. 09, 2300-2299.

[6] X. Zhang, J. Fang, X. Yu: *Design and implementation of nodes based on CC2430 for the agricultural information wireless monitoring.* Proc. IEEE International Conference on Computer and Automation Engineering (ICCAE), 26–28 February 2010, Singapore, China, *5* (2010) 255–258.

[7] X. H. Ren, L. F. Liang, S. X. Jia, T. W. Wang: *Design of the remote control door for car based on ZigBee chip CC2430.* Microcomputer Information *25* (2009), No. 20, 220–222.

[8] Y. Y. Liu, W. W. Shi: *The design of wireless sensor network for monitoring temperature and humidity based on CC2430.* Microcomputer Information *25* (2009), No. 10, 130–131.

Received May 7, 2017

Acta Technica *62* No. 3A/2017, 13–20

Physiological indexes collection system for multifunctional gyms based on FFT and photoelectric sensor

Xiao Yang[1]

Abstract. Pulse oximetry is a continuous and noninvasive instrument that is convenient to detect arterial oxygen saturation. Because of its defects in system design and signal processing, there is a need for us to discuss and improve its measurement accuracy, repeatability and stability. In this paper, we propose a kind of multifunctional fitness monitor based on FFT and photoelectric sensor. It can analyze the blood oxygen saturation and heart rate of human body by adapting pulse noninvasive oxygen saturation detection method. Through collecting finger absorbed dose for red and infrared light, and amplifying it by controllable gain amplifier, then we can get the amplitude and frequency of AC electrical signal by the FFT. Firstly, we can complete the function of signal acquisition and automatic gain judgments as well as signal processing by using PIC24FJ128GA010. Finally, we need to demarcate the result by pulse blood oxygen simulator. In addition, the system also introduces the pedometer function based on acceleration sensor MMA7260 in order to enhance the practicability of fitness monitor. At the same time, the system also can obtain the dynamic physiological signs during the fitness process.

Key words. Fourier analysis, oxygen saturation, signal processing.

1. Introduction

Pulse oximetry has been widely used in clinical practice and becomes an indispensable clinical diagnostic device [1]. Its convenient operation and non-intrusive real-time measurements have essentially replaced the traditional blood measurement in vitro. Pulse oximetry can be used for continuous oxygenation estimation, especially in the operation of critical patients. It can quickly provide blood oxygen information and avoid the potential risk with arterial jacking method. In the emergency room, if the oxygen saturation can be continuously monitored by oximeter, then the ventilation can be conducted safely and alternately. In the treatment of patients requiring continuously adjuvant oxygen therapy, the pulse oximeter is often used to determine the oxygen requirement [2]. For patients with chronic obstructive

[1]Shaanxi University of Science and Technology, Shaanxi, 710021, China; E-mail: xxiaoyangsxust@163.com

tracheal disease, due to sleep apnea syndrome or nocturnal hypoxia saturation, they often require oxygen oximetry for sleep oxygen saturation study [3]. It is very difficult to collect neonatal blood, so no-damage blood oxygen meter is useful for the neonatal monitoring. It can avoid the damage to brain, lung and eye by adjusting oxygen therapy. Currently, most of the fitness products on the market are only used to detect the specific physiological parameters of the body or just have completed the detection of sports data. It did not combine the two projects, so it cannot achieve a reasonable fitness effect.

Based on this background, this article designed a multi-functional fitness monitor to guide the user's fitness by a scientific way. This monitor takes the oxyhemoglobin saturation and heart rate of human as the fitness index by calculating user's physical activity.

The hardware is a oxygen saturation detecting system composed of photoelectric sensor and corresponding conditioning circuit and the micro-controller PIC24FJ128G A010. There is a good development in the aspects of pass-filter and the controllable gain to obtain physiological signals by transmission-type pulse method. We can obtain the physiological information of body's blood oxygen saturation and heart rate using the built-in high-speed A/D of PIC24FJ128GA010 SCM to collect signals and adopt micro-controller signal sampling, and using FFT algorithm to analyze the obtained data.

In addition, the system also implements the pedometer function. The speed sensor MMA726 gets the acceleration characteristics during exercise, then it will gain some fitness information such as the step number, time and distance through software calculation.

2. Theoretical basis and algorithm of blood oxygen saturation measurement

2.1. Lambert-Beer's law

Lambert-Beer's Law reflects the optical absorption law, it means that material absorbance is proportional to its concentration at a certain wavelengths [4]. The meaning of Lambert-Beer's Law is that only we choose a appropriate wavelength and measure its absorbance, then we can figure out the concentration of solution. According to Lambert-Beer's law, formula (1) shows the relationship between the incident light intensity and the absorption layer thickness as well as the concentration of the absorbent

$$I = I_0 \mathrm{e}^{-acl} \,. \tag{1}$$

In the above formula, I_O is the input intensity, I is the transmitting intensity, a is absorptivity of absorptiometic matter, c is the concentration of absorptiometic matter, and l is the trans-missive distance (optical path) of absorptiometic matter.

2.2. The measurement principle of oxygen saturation

When the incident light passes through a certain uniform and non-scattering solution, its light absorption characteristics follow the Lambert-beer law. It can be described by formula

$$A = -\lg \frac{I}{I_0} = 2.303acl\,, \tag{2}$$

where A is the absorbance.

3. Design for measuring oxygen saturation

3.1. Hardware structure for measuring oxygen saturation

The hardware part is mainly composed of microprocessor, lighting drive, fingertip photoelectric sensor, amplifier, baseline adjustment circuit, high-speed A/D, D/A conversion and display. Pulse oximetry hardware principle diagram is shown in Fig. 1.

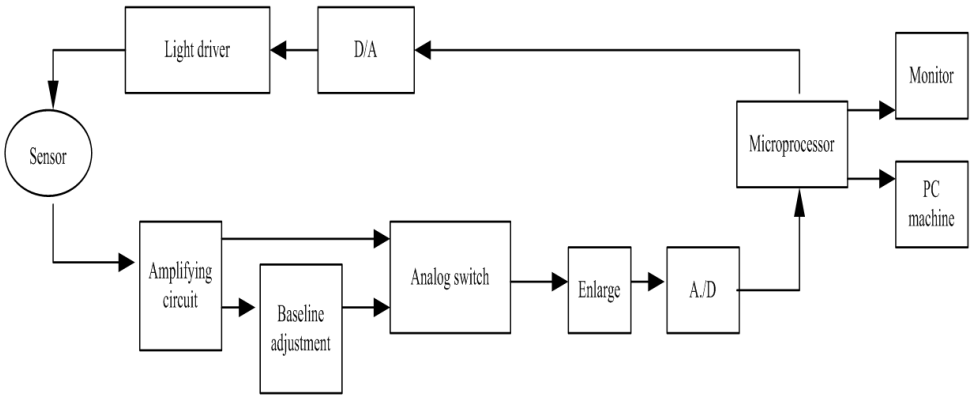

Fig. 1. Oxygen saturation detection block diagram

It will appear a driving signal with 660 nm and 940 nm infrared light through D/A conversion to the light source drive circuit. The light source drive circuit amplifies the signal and sends it to the red and infrared light emitting diodes placed side by side on the upper arm, sending optical pulse. The photoelectric detector on lower arm will transform it into electrical signals through the red light and infrared light on finger artery vessel. The intensity of the photoelectric signal detected by the photodetector is related to the size of the degree of absorption which the light signals penetrates the finger portion and is absorbed by the tissue, bone and blood.

Because the concentration of HbO_2 and Hb in blood changes cyclically with the pulse of the blood, so their absorption for light is also changing, thereby the output signal intensity of the photodetector also change with the concentration of HbO_2 and Hb in the blood. The light absorption curve of HbO_2 and Hb is shown in Fig. 2.

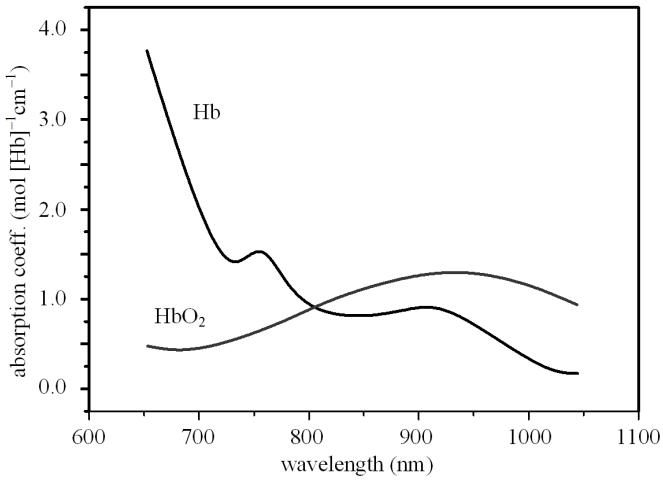

Fig. 2. Light absorption curve of HbO_2 and Hb

3.2. Software design

The system's software includes control software of non-invasive pulse oximeter microprocessor and analysis software achieved intelligent monitoring for oxygen saturation on PC. Here is no longer discussed in detail about the former.

The development of portable medical equipment and PC interface software can not only expand its function, but also achieve desktop or composite functions combined with PC. The system uses the powerful function of VC6.0 to develop and design the interface software of PC and oximeter and the data analysis software based on PC. It has the functions of data communication, intelligent analysis, storage, display and print result report [6].

4. Realization of blood oxygen saturation with Fourier analysis algorithm

The blood oxygen saturation algorithm proposed in this paper is mainly composed of three parts: signal acquisition, automatic gain judgment and Fourier signal analysis.

1. Signal acquisition: signal acquisition is mainly responsible for the LED tube drive and signal acquisition and conversion, in which the signal acquisition and conversion use the 10-bit high-speed A/D converter in microcontroller PIC24FJ128GA010. We can get the AC and DC signals with oxyhemoglobin saturation and heart beat through the A/D conversion [7].

2. Automatic gain judgment: because the degree of attenuation of the specific light through the fingertips varies from person to person, in order to enhance the versatility, the system uses the controllable gain amplifier to amplify the AC signal.

The system dynamically adjusts the gain of the controllable gain amplifier by judging the difference between the maximum value of the AC signal and the reference positive level (Vcc) of the A/D converter, and then makes sure the final data accounting for more than 2/3 of the Vcc to improve the system accuracy [5].

3. Results calibration: According to Lambert-Beer's law, when it is thought that the change of the attenuation of the light at the fingertip is mainly caused by hemoglobin, its transmitted light intensity can be expressed by the following the formula

$$I = I_0 \times \mathrm{e}^{-K_0 L_0 C_0} \times \mathrm{e}^{-K_{\mathrm{HbO_2}} L C_{\mathrm{HbO_2}}} \times \mathrm{e}^{-K_{\mathrm{Hb}} L C_{\mathrm{Hb}}} . \tag{3}$$

The attenuation of light is caused by other tissues on the optical path. The absorbance of this part of the tissue does not change with the pulse. Symbols K_0, C_0 and L_0 denote the total absorption coefficient, material concentration of light absorption and the optical path length.

5. Results and discussion

In this paper, we use pulse-type non-invasive blood oxygen saturation detection method to collect the absorption of red light and infrared light through photoelectric sensor, and then we can get the digital information about oxygen saturation and heart rate through hardware filter, amplification and Fourier analysis algorithm of software. The step-by-step circuit system composed of acceleration sensor have achieved the pedometer function. The detection signals of blood oxygen saturation and heart rate information is shown in Figs. 3 and 4.

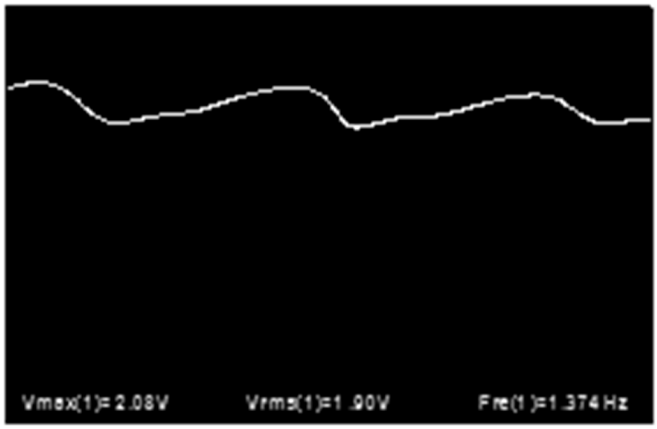

Fig. 3. Overlay chart after the filter

The sensor module generates a current signal with a degree of light attenuation, and converts the D/A into a voltage signal to form an AC/DC superimposed signal as shown in Fig. 3. After sampling for this signal, we can get the DC value corresponding to red (infrared) through a software filter. Through the bandpass filter,

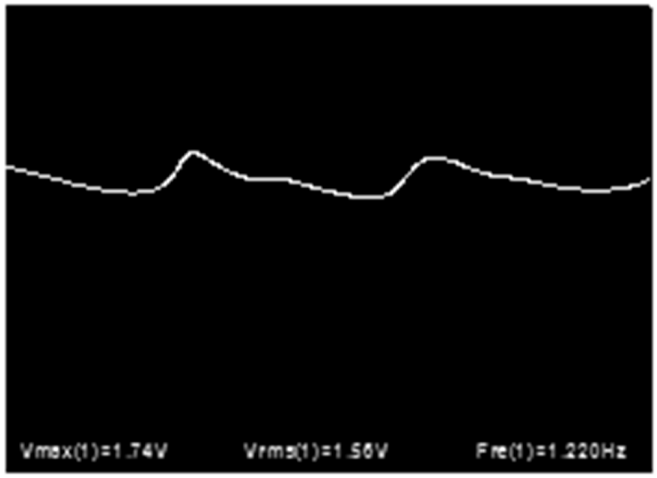

Fig. 4. Non-amplified AC signal chart after separation

superimposed signal forms a waveform shown in Fig. 4.

6. Conclusion

The multifunctional fitness monitor designed in this paper is mainly composed of two parts: the oxygen saturation, the heart rate acquisition and processing module and the step-by-step control analysis module based on the acceleration sensor. Using the photoelectric sensor, the acceleration sensor MMA7260 and the 16-bit microcontrollers PIC24FJ128GA010, etc., constitute the hardware system of this design that can analyze human signals through FFT analysis, adaptive step algorithm and digital filtering. Physical test results show that oxygen saturation accuracy proposed in this paper reach to more than 95 %, heart rate reach to 0.01 Hz. In this paper, the design of multi-functional fitness monitor has achieved the combination of physiological indicators and sports information and has provided a guiding basis for scientific movement.

References

[1] C. De La Merced Díaz-González, M. De La Rosa Hormiga, J. M. Ramal López, Y. Déniz Rivero, M. S. Marrero Morales: *Concordance among measurements obtained by three pulse oximeters currently used by health professionals.* Journal of Clinical and Diagnostic Research *8* (2014), No. 8, 211–220.

[2] S. Garcia-Gutierrez, A. Unzurrunzaga, I. Arostegui, C. Esteban: *The use of pulse oximetry to determine hypoxemia in acute exacerbations of COPD.* Journal of Chronic Obstructive Pulmonary Disease *12* (2015), No. 6, 613–620.

[3] A. V. Dunaev, V. V. Sidorov, A. I. Krupatkin, I. E. Rafailov, S. G. Palmer, N. A. Stewart, S. G. Sokolovski, E. U. Rafailov: *Investigating tissue respiration*

and skin microhaemocirculation under adaptive changes and the synchronization of blood flow and oxygen saturation rhythms. Physiological Measurement *35* (2014), No. 4, 607–621.

[4] A. Kachko, L. V. van der Ham, L. F. G. Geers, A. Huizinga, A. Rieder, M. R. M. Abu-Zahra, T. J. H. Vlugt, E. L. V. Goetheer: *Real-time process monitoring of CO_2 capture by aqueous AMP-PZ using chemometrics: Pilot plant demonstration.* Industrial & Engineering Chemistry Research *54* (2015), No. 21, 5769–5776.

[5] P. Chen, D. G. Zhao, D. S. Jiang, J. J. Zhu, Z. S. Liu, J. Yang, X. Li, L. C. Le, X. G. He, W. Liu, X. J. Li, F. Liang, B. S. Zhang, H. Yang, Y. T. Zhang, G. T. Du: *The thickness design of unintentionally doped GaN interlayer matched with background doping level for InGaN-based laser diodes.* AIP Advances *6* (2016), No. 3, paper 035124.

[6] R. Di Capua, F. Offi, F. Fontana: *Check the Lambert–Beer–Bouguer law: A simple trick to boost the confidence of students toward both exponential laws and the discrete approach to experimental physics.* European Journal of Physics *35* (2014), No. 4, paper 045025.

[7] J. Yan, G. Bin: *Research on an anti-motion interference algorithm of blood oxygen saturation based on AC and DC analysis.* Technology and Health Care *23* (2015), No. S2, 285–291.

Received May 7, 2017

Acta Technica *62* No. 3A/2017, 21–28

Portable muscle fatigue analysis system for sports training

Yuefeng Liu[1], Xiaodi Cai[1,3], Yu Fu[2]

Abstract. Portable muscle fatigue analysis system for sports training is to be studied. The portable muscle fatigue analysis system consists of hardware and software. Hardware system is made up of three modules: signal collection and wireless transmission module, data processing module and result display and data storage module. Software and its corresponding hardware module were used to code corresponding function modules. Then, system is detected by muscle fatigue analysis experiment on dumbbell lateral raise. Test results shows that there is the same variation tendency for parameters of bicipital muscle of arm and degree of muscle fatigue when doing dumbbell lateral raise. However, there are significant individual differences for muscle fatigue parameters. In conclusion, the portable muscle fatigue analysis system is verified reliable for sports training.

Key words. Sports training, muscular fatigue analysis, surface electromyographic signal, FPGA, portable muscular fatigue analysis system.

1. Introduction

When muscle motion function level was lowered by sports to a degree of insufficient energy for sports, it can be recovered by taking a long rest. This phenomenon was called muscle fatigue [1]. Muscle fatigue measurement was widely applied in various fields, such as sports field. Injury caused by excessive exercise can be avoided by assessing and monitoring muscle fatigue [2]. In human engineering field, muscle fatigue measurement can be used to avoid musculoskeletal fatigue related to working. In rehabilitation medicine field, muscle fatigue measurement and assessment can be used to guide recovering movement for rapid recovery [3]. Electromyographic signal was taken as parameter to study muscle fatigue in physical exercise. Automatic system was used as fatigue warning device for training to remain a best non-fatigue state and avoid muscle injury caused by excessive exercise.

It was convenient to acquire human electromyographic signal because surface

[1]Institute of Physical Education of Xinjiang Normal University, Urumqi 830054, China
[2]Sias International University, Zhengzhou, Henan, 450000, China; E-mail: siasyufu@yeah.net
[3]Corresponding author

electrode was featured noninvasive. Thus, surface electromyographic signal was frequently used for analyzing muscle fatigue [4]. There were many studies focused on this aspect at home and abroad. ICA and neural network was adopted by A. Subasi et al. [5] to identify and classify muscle fatigue. Median frequency of eletromyographic signal was calculated by Kang to measurement of human muscle fatigue [6]. Nowadays, off-line process has been adopted by most studies on muscle fatigue analysis. Generally, electromylgraphic collecting device could not analyze muscle fatigue [7], thus, it was inconvenient for daily muscle fatigue assessing and monitoring. Therefore, a practical portable real time muscle fatigue analysis system with low power dissipation was design based on surface electromyogram for daily training.

2. Hardware design for portable muscle fatigue analysis system

2.1. Signal collection and wireless communication module

In the system designed, Ag-AgCl electrode was used to collect electromyographic signal. Surface electromyographic signal was a weak bio-electricity signal of alternating current, whose signal frequency energy was 20–500 Hz. Thus, enlargement and filtering was needed and the magnification factor was set as 500. To meet above requirement, the system was designed based on electromyogram transducers of AD8220 and OPA349E. And circuit of the transducer was shown in Fig. 1.

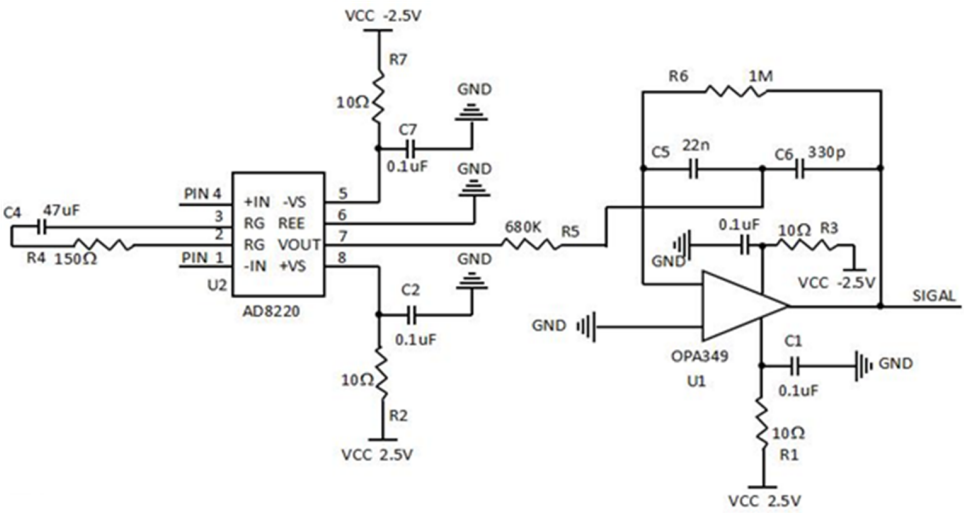

Fig. 1. Circuit diagram of enlargement and filtering

Synchronous sampling of 8 channels and delta-sigma analog-digital converter ADS 1198 of 16 bytes produced by TI company was selected. CSRBluetooth2.0 chip was used for wireless transmission. C8051F410 control center produced by Silicon Labs company was used for MCU control center. ADS1198 was used to connect

C8051F410 and SPI bus. UART was used to connect C8051F410 and wireless Bluetooth module. C2CK and C2D were used to connect C8051F410 and debugging tool. Meanwhile, in order to use as less devices on circuit board as possible, positive voltage of all devices in this system was set as 2.5 V. Thus, only one stability chip was needed for the whole system. Negative voltage corresponding to amplifier was –2.5 V, which can be obtained by voltage converter to convert 2.5 V.

2.2. Data processing module

Data processing module have to receive electromyographic signal of 6 channels and calculate parameters relevant to muscle fatigue in real time. To achieve this, FPGA was used to control this module and process signal. Core chip of FPGA chip was XC3S500E chip, whose configurable I/O pin was up to 232 which meet the requirement of system for multiply I/O interfaces. In order to achieve the best result of XC3S500E chip, supply voltages of 3.3 V, 2.5 V and 2 V should be inputted. Power supply chip AMS1117-1.2, AMS1117-2.5 and AMS 1117-3.3 V was adopted in this module, which greatly reduced circuit size and miniaturized system. For XC3S500E, there was a specified four-wire interface JTAG which can be used under any setting pattern when electrifying with XC3S500E.

2.3. Result display and data storage module

Result was displayed by LCD touch screen which also displayed variation tendency of muscle fatigue parameters in graphics. Data was stored in SD card for user to read. Chip of kernel series ARM 11 was selected for putting operation system conveniently. Data interface pin of SD card was connected to 10 K resistance and 3.3 V power supply then it was connected directly to data interface pin corresponding to S3C6410. Voltage of LCD touch screen was 5 V and electric current for driving LCD screen was around 1 A, a relatively large current value. For stabilize voltage and heat dissipation, LM2576 chip was used, whose power supply was shown in Fig. 2.

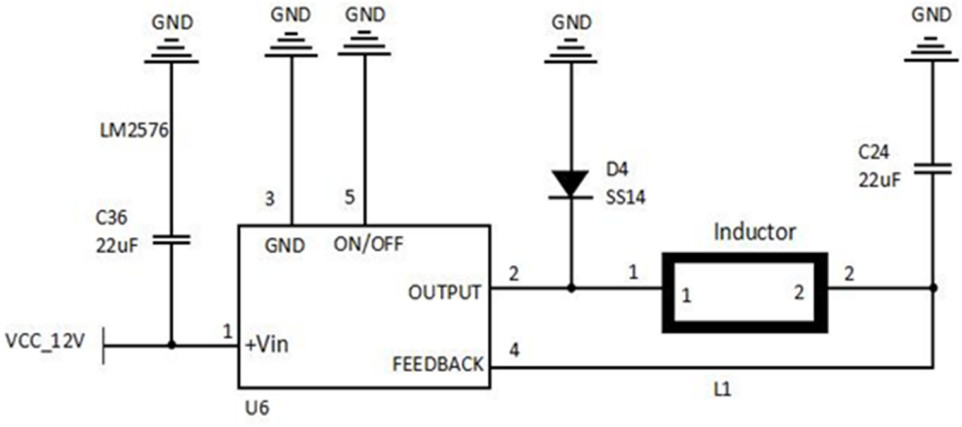

Fig. 2. LCD power supply

3. Software design for system

3.1. Signal collection and wireless transmission module

Surface electromyographic signal collected by transducer was converted into digital signal by ADS1198 which was controlled by C8051F410 through SPI bus. Then, digital signal was transmitted to wireless Bluetooth module through DART bus. This was the whole collection process. Finally, code was sent. Flow chart of the module was shown in Fig. 3.

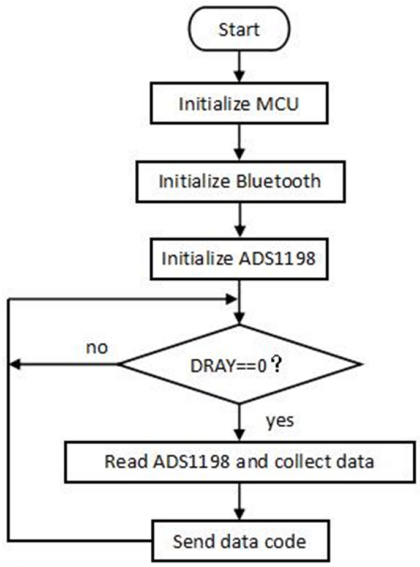

Fig. 3. Flow chart of data acquisition and wireless transmission module

3.2. Data processing module

Software in this module was made up of data receiving, data processing and data transmission. Data receiving was used to receive and parse data and extract original electromyographic signal of those 6 channels. Data processing was used to calculate data and parameter relevant to muscle fatigue. Data transmission was used to process the result and send original electromyographic signal code to display and storage module for storage. Software framework was shown in Fig. 4.

3.3. Result display and data storage module

Embedded operating system Windows Embeddd CE 6.0 was put into this module to display and storage data. Windows Embeddd CE 6.0 was featured good hardware compatibility, well reliability, strong communication ability, advanced power management system, friendly development environment and high security. Interface of

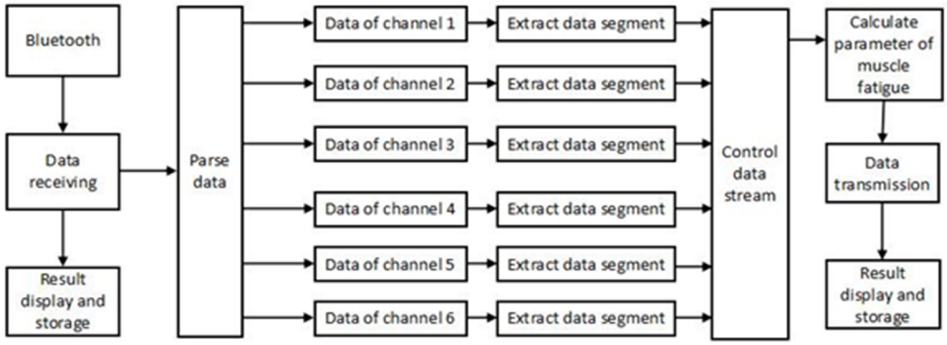

Fig. 4. Software framework of data processing module

serial device of Windows CE was a combination of communication-related function and drive program function for streaming I/O. In data display and storage module, data was received through two-way serial port- serial port COMl was responsible for receiving original eletromyographic signal and serial port COM2 was responsible for receiving data and processing parameter. There were buffer pools of 1024 bytes for those two serial ports, which was used to store those unread data in case it was lost. Totally, there were six channels for signal collection and six muscle fatigue parameters for each channel. Individual setting and display was adopted for user's convenient reading, which was achieved by drawing mechanisms of Windows CE. Besides, two documents were used to record original electromyographic signal and muscle fatigue analysis result respectively. And those documents were saved as format TXT.

4. Experiment of muscle fatigue analysis based on portable muscle fatigue analysis system

4.1. Experimental subject and method

20 males with no medical history of muscle and skeletal muscle, no muscle injury lately, no unhealthy drug taken, no smoking history and no special preparation were selected as experimental subject and they were numbered from 1–20. Their basic information was shown in Table 1.

Table 1. Basic information of experimental subject for dumbbell lateral raise

Age (years)	24.72±2.35
Height (cm)	172.4±9.12
Weight (kg)	67.02±6.59
Body index (kg/m^2)	24.37±2.81

This was a static continuing contraction mode. Before experiment, place to put electrode should be swabbed by alcohol. Then, electrode was put on their bicipital muscle of arm. During the whole experiment, all experimental subjects should stand holding 2 kg dumbbell with forearm parallel to shoulder and their forearm should be vertical to their body. The experiment was finished once they failed to do the exercise properly.

4.2. Experimental result and analysis

To quantizing relation of parameter and muscle fatigue, linear correlation analysis was conducted to all parameters. Function of linear relation was defined as $y(x) = ax + b$. Here, $y(x)$ denoted parameter value of the xth data segment, a denoted the slope of fitting straight line and b denoted intercept of straight line. Correlation coefficient was identified as function 1, for which x' denoted mean value of x and y' denoted mean value of y. Correlation coefficient r reflects the degree of fitting of straight line, through which monotonicity of data can be evaluated.

$$r = \frac{\sum_{i=1}^{n} \left(x_i - x^{'}\right)\left(y_i - y^{'}\right)}{\sqrt{\sum_{i=1}^{n} \left(x_i - x^{'}\right)^2} \sqrt{\sum_{i=1}^{n} \left(y_i - y^{'}\right)^2}} \,. \tag{1}$$

Analysis result of fatigue of bicipital muscle of arm shown that slope of ZCR and MPF was negative and presented a downward trend for all experimental subjects except number 7. And slope of ZCR and MPF for number 7 was positive. Slope of RMS and IEMG was positive and showed rising trend for all experimental subjects. Slope of MDF was negative and showed a downward trend for all experimental subjects except number 7 and number 12. Slope of MDF for number 7 and number 12 was positive. Slope of Fl2 was positive and showed a rising trend for all experimental subjects except number 5. And slope of Fl2 for number 5 was negative. Thus, it can be concluded that this muscle fatigue analysis system was suitable for most people because 6 parameters related to muscle fatigue showed the same tendency in the fatigue process. However, it can be seen from above experiment that there were individual differences for muscle fatigue, which may be related to experimental subject's skin, muscle and power generation mode.

5. Conclusion

A portable muscle fatigue analysis system based on surface electromyopgram was developed by experimental, which was featured low cost, small in size and convenient to operation. Hardware and software design for this system was almost elaborated. This system was proved reliable by muscle fatigue experiment on dumbbell lateral raise. Not all degrees of muscle fatigue can be evaluated accurately because there were relative major individual differences, which should be improved in the future study.

References

[1] L. Kahl, U. G. Hofmann: *Comparison of algorithms to quantify muscle fatigue in upper limb muscles based on sEMG signals.* Medical Engineering & Physics *38* (2016), No. 11, 1260–1269.

[2] G. Venugopal, S. Ramakrishnan: *Analysis of progressive changes associated with muscle fatigue in dynamic contraction of biceps brachii muscle using surface EMG signals and bispectrum features.* Biomedical Engineering Letters *4* (2014), No. 3, 269–276.

[3] K. Ito, Y. Hotta: *Surface electromyogram-based detection of muscle fatigue during cyclic dynamic contraction under blood flow restriction.* Proc. Annual International Conference of the IEEE Engineering in Medicine and Biology Society, 26–30 August 2014, Chicago, IL, USA, (2014), 2205–2208.

[4] D. Roman-Liu, P. Bartuzi: *The influence of wrist posture on the time and frequency EMG signal measures of forearm muscles.* Gait & Posture *37* (2013), No. 3, 340–344.

[5] A. Subasi, M. K. Kiymik: *Muscle fatigue detection in EMG using time-frequency methods, ICA and neural networks.* Journal of Medical Systems *34* (2010), No. 4, 777–785.

[6] K. M. Chang, S. H. Liu, X. H. Wu: *A wireless sEMG recording system and its application to muscle fatigue detection.* Sensors *12* (2012), No. 1, 489–499.

[7] J. R. Octavia, P. Feys, K. Coninx: *Development of activity-related muscle fatigue during robot-mediated upper limb rehabilitation training in persons with multiple sclerosis: A pilot trial.* Multiple Sclerosis International (2015), paper ID 650431.

Received May 7, 2017

Acta Technica *62* No. 3A/2017, 29–36

Effects of friction property on biomechanics of lower limbs of table tennis players

Xuefeng Yan[1]

Abstract. Friction property is an important property of sports shoes. In this paper, we studied the changes of lower limbs biomechanical characteristics of athletes between the soles and the surface of the site under different friction property conditions. Eight college students who majored in table tennis were selected as the subjects. Subjects were wearing two pairs of table tennis shoes respectively and completed the stepping forward and hitting the ball action under two angles on the surface of the three sites. The joint and kinematics data of the lower limbs were collected to analyze the effects of the friction property between the athletic shoes and the surface of the site on the biomechanical characteristics of the lower limb. The results showed that with the increase of the friction coefficient, the knee flexion angle at the peak of the ground vertical force decreases and the minimum value of the knee joint flexion angle during batting tended to decrease.

Key words. Sports shoes, friction property, table tennis, biomechanics.

1. Introduction

Table tennis players always suddenly start, stop, move and twist when they are in the squat state in the training and competition, and the knee and ankle loads are great. For different levels of athletes, the risk of injury also increases with the increase of exercise intensity and requirements, as well as the growth of training life [1]. In addition to the training and competition, the venue and equipment are parts of the factors causing the sports injury. Some studies think that the complex structure and function of foot and ankle make the footwork of table tennis players more important. And the high injury rate of the ankle and foot shows that players need to pay more attention in training, but also need to choose the right sports shoes carefully.

At present, there is no standard instrument and test method to measure the coefficient of friction. The research on friction performance of sports shoes is not

[1]Xi'an Vocational and Technical College, Shaanxi, 710077, China; Email: yanxftechnology@163.com

deep enough. It mainly focuses on the comparison of the friction coefficient between different soles and surfaces of the ground. The study on the effect of the friction property on the movement is relatively lacking. The effect of the friction property between the sports shoes and the surface of the ground will affect the biomechanical characteristics of the lower limbs of the table tennis players and this effect is a potential factor to increase the injury of the lower limbs of the players, which need to be verified experimentally. In this paper, we mainly aim at the effect of friction property on the knee joint of table tennis players [2].

2. Subjects and methods

2.1. Research objects and equipment

Eight male college students who are the table tennis players are selected as experimental subjects. They are all right-handed and have taken the second grade. Subjects have no history of serious injury to the lower limbs and did not engage in vigorous exercise 24 hours before the experiment [3]. The basic information of the subjects is shown in Table 1.

Table 1. Basic information of subjects ($n = 8$)

Height (cm)	Weight(kg)	Age (year)	Sports level
173.1±4.2	62.8±2.7	21.9±1.1	Second

The Kistler three-dimensional force platform (Model 9281CA) made in Switzerland was used to collect the ground reaction force and related parameters during the stroke. The frequency of collecting was 1000 Hz. The kinematic data of the lower limbs of the subjects were collected by the Motion infrared high speed motion capture system made in US.

The two pairs of shoes used in experimental test were table tennis shoes of two sports brands respectively, which were new N table tennis shoes and the used O table tennis shoes. The upper structure is basically the same. Subjects were wearing two pairs of shoes and uniform socks for testing.

2.2. Definition and calculation of kinematic index

The kinematic parameters are buffer time, COMx, COMy, the three-dimensional angle of the right-sided knee joint at the peak of the ground vertical impact force and the three-dimensional angle extremum of the right knee joint during the whole stroke [4]. The COMx refers to the distance between the center of gravity at the peak of the ground vertical impact and the heel in the sagittal plane, that is, the X-coordinate of the heel point minus the X-coordinate of the center of gravity [5]. The COMy refers to the distance between the center of gravity at the peak of the ground vertical impact and the heel in the frontal plane. COMx and COMy are divided by height, standardized as the multiple of the height [6]. The right pelvic

coordinate system is:

$$j = \frac{r_{\text{RASIS/MIDASIS}}}{\left|r_{\text{RASIS/MIDASIS}}\right|}, \quad k = \frac{r_{\text{MIDASIS/MIDPSIS}}}{\left|r_{\text{MIDASIS/MIDPSIS}}\right|}, \quad i = j \times k\,, \tag{1}$$

where $r_{\text{RASIS/MIDASIS}}$ is the vector quantity of the midpoint of the left and right anterior superior iliac spine pointing to the right anterior superior iliac spine, and the $r_{\text{MIDASIS/MIDPSIS}}$ is the vector of the posterior superior iliac spine pointing to the midpoint of the left and right anterior superior iliac spine.

The right foot coordinate system is:

$$k = \frac{r_{\text{RTOE/RCANKLE}}}{\left|r_{\text{RTOE/RCANKLE}}\right|}, \quad j = k \times \frac{r_{\text{RCANKLE/ROANKLE}}}{\left|r_{\text{RCANKLE/ROANKLE}}\right|}, \quad i = j \times k\,, \tag{2}$$

where $r_{\text{RTOE/RCANKLE}}$ is the vector of the right ankle joint pointing to the head point of the right foot, and $r_{\text{RCANKLE/ROANKLE}}$ is the vector of the right lateral malleolus pointing to the center of the right ankle joint.

3. Results and analysis

3.1. Division of the action

The two movements selected in this paper are the common stepping and batting movements in table tennis. Like tennis, table tennis batting action is generally divided into: backswing stage, batting stage, waving stage and the reduction phase. The Motion system and the force platform collect the data simultaneously, so the data collected by the two systems is the corresponding. Figure 1 shows the curves of the vertical force during the movement of a subject [7].

3.2. Kinematics time-space parameters analysis

The interaction of the friction coefficients and movement on the buffer time, COMx and COMx was no significant difference, and there was no significant difference in the three friction coefficients between the three variables. COMx had a significant difference between the two actions (as shown in Figure 2), COMx is positive at 180 ° step, and negative at 45 ° step. The time-space parameters analysis results are shown in Table 2.

3.3. Analysis of three-dimensional angles of knee joint

Statistical methods were analyzed by repeated measures of variance analysis. The results of the knee flexion angle at the peak of the ground vertical impact showed that there was no interaction between the action and the friction coefficient, the action had no significant effect on the flexion angle, and the single factor of friction coefficient was significant. The results showed that the knee flexion angle under the friction coefficient H was significantly smaller than the knee joint flexion angle

under friction coefficients L and M. The adduction/abduction angle and medial rotation/external rotation angle of the knee joint were not affected by the action and friction coefficient at the peak of the ground impact force. Table 3 showed the results of the three-dimensional angle of the knee joint at the peak of the impact.

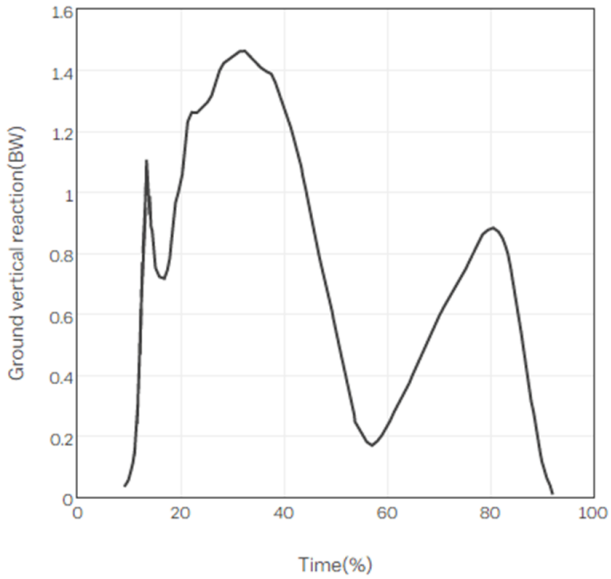

Fig. 1. Ground vertical reaction force curve of stepping and batting movement

Table 2. Time-space parameter analysis results ($n = 8$)

		Buffer time (s)	COMs (HT)	COMy (HT)
180 ° step	Friction coefficient L	0.043±0.019	0.48±0.20	2.56±0.35
	Friction coefficient M	0.057±0.029	0.55±0.24	2.70±0.24
	Friction coefficient H	0.047±0.022	0.49±0.32	2.77±0.24
45 ° step	Friction coefficient L	0.040±0.018	-0.61±0.24	2.55±0.34
	Friction coefficient M	0.043±0.010	-0.53±0.47	2.61±0.32
	Friction coefficient H	0.037±0.008	-0.62±0.35	2.59±0.30
P		0.352	0.796	0.327
Friction coefficient	*action	0.560	0.982	0.467

In the table, symbol P denotes the difference of the same index of the two movements in the three kinds of friction coefficient. Friction coefficient *action is the P value under the interaction of the friction coefficient and the action. Symbol * indicates that the significant level $P < 0.05$.

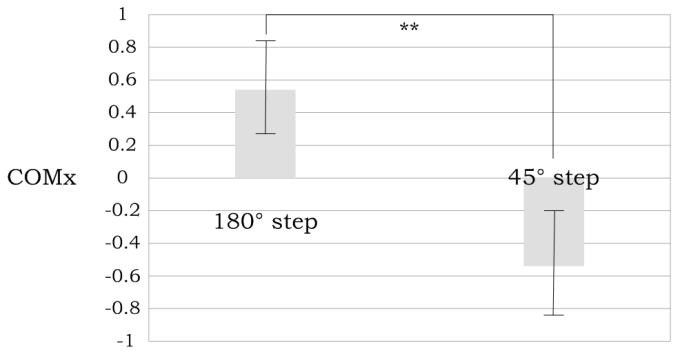

Fig. 2. Differences of COMx between the different actions (** represents $P < 0.01$, and the difference is significant)

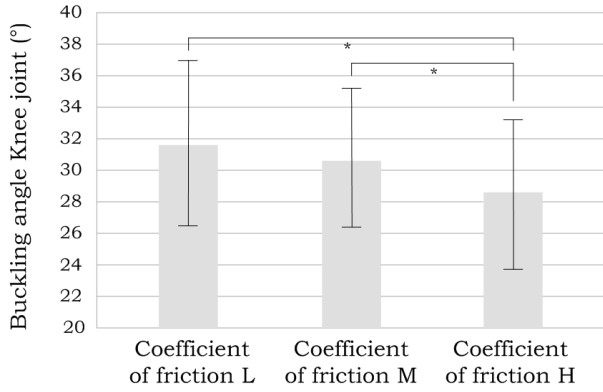

Fig. 3. Difference of the knee flexion angle at the peak of vertical impact force in the different friction coefficient (* represents $P < 0.05$, and the difference is significant)

4. Conclusion

In this paper, we aimed at the effect of friction property on the lower limbs biomechanics of the table tennis players, mainly studied the kinematic index of the athletes' lower limb. In this experiment, we took 8 table tennis students in a university as test objects. The participants completed the step and batting action under two angle with two pairs of table tennis shoes respectively on three kinds of site surfaces. The kinematic data of the knee joints of the lower limbs was collected

by the Kistler three-dimensional force platform and Motion infrared motion capture system. The following conclusions were obtained: the friction coefficient affected the kinematic characteristics of the knee joint during step and batting. With the increase of the friction coefficient, the knee flexion angle at the peak of the impact force and the minimum value of the knee joint flexion angle during batting tended to decrease.

Table 3. Analysis results of the three-dimensional angle of the knee joint at the peak of the impact ($n = 8$, unit: degrees)

		Flexion angle	adduction/ abduction angle	Medial rotation/ external rotation angle
180 ° step	Friction coefficient L	33.6±6.0	-0.02±4.07	7.5±6.5
	Friction coefficient M	32.8±4.9	-0.02±4.22	9.2±8.0
	Friction coefficient H	30.2±6.2	-0.38±4.73	10.3±6.4
45 ° step	Friction coefficient L	29.9±4.8	-1.06±3.96	5.7±7.2
	Friction coefficient M	29.6±3.8	-0.07±4.34	6.7±5.9
	Friction coefficient H	27.3±3.2	0.01±4.31	10.3±9.1
P		0.026*	0.602	0.292
Friction coefficient	*action	0.949	0.078	0.517

In the table, symbol P denotes the difference of the same index of the two movements in the three kinds of friction coefficient. Friction coefficient *action is the P value under the interaction of the friction coefficient and the action. Symbol * indicates that the significant level $P < 0.05$.

References

[1] C. Starbuck, V. Stiles, D. Urà, M. Carré, S. Dixon: *Biomechanical responses to changes in friction on a clay court surface.* Journal of Science and Medicine in Sport *20* (2016), No. 5, 459–463.

[2] T. Shimazaki, E. de Almeida, F. M. Vanderlei, Dino de Aguiar Cintra Filho, L. C. M. Vanderlei, C. M. Pastre, F. N. Bastos: *Exploration of risk factors for sports injuries in athletes of table tennis.* Fisioterapia e Pesquisa *19* (2012), No. 2, 158–164.

[3] G. Munivrana, J. Paušić, M. Kondrič: *The incidence of improper postural alignment due to the influence of long-term table tennis training.* Kinesiologia Slovenica *17* (2011), No. 2, 47–58.

[4] M. Kondrič, G. Furjan-Mandić, V. Hadžić, E. Dervišević, B. Matković, N. Ochiana: *Injuries in Slovenian table tennis players compared with injuries of some of the best Slovenian tennis players.* Gymnasium. Revista de educatie fizica si sport *8* (2008), No. 13, 73–85.

[5] W. K. Hong, C. G. Lee, D. S. Ko: *Effect of thigh muscle fatigue on the biomechanical factors of the lower limbs when walking in a squatted position.* Journal of Physical Therapy Science *28* (2016), No. 3, 1007–1011.

[6] M. Kondrič, B. Matković, G. Furjan-Mandić, V. Hadžić, E. Dervišević: *Injuries in racket sports among Slovenian players.* Collegium Antropologicum *35* (2011), No. 2, 413–417.

[7] C. Starbuck, L. Damm, J. Clarke, M. Carré, J. Capel-Davis, S. Miller, V. Stiles, S. Dixon: *The influence of tennis court surfaces on player perceptions and biomechanical response.* Journal of Sports Sciences *34* (2016), No. 17, 1627–1636.

Received May 7, 2017

Acta Technica *62* No. 3A/2017, 37–44

Design and implementation of competitive basketball wheelchair based on ergonomics

Hui Wang[1]

Abstract. Wheelchair basketball, as one of sport-assisted wheelchairs, can help handicapped people play special basketball games on the playground. For the athletes who join wheelchair basketball sports event, it is necessary for them to have basketball wheelchairs. Because this sports event has a strong confrontation, athletic wheelchairs are frequently collided, even tip-over. Therefore, athletes would be hurt to large extent, and got secondary damage. Thus, it is of prime importance to add ergonomics to the design of basketball wheelchair. The existing basketball wheelchair is made a new project design based on ergonomic theory. Deficiencies in different parts are improved, and analysis determination is made to some static sizes of the new-design basketball wheelchair seat. Improvement project is fundamentally completed. It is positively significant to improve the performance of basketball wheelchair and develop the sports for the disabled.

Key words. Basketball wheelchair, ergonomics, static size, sports injury.

1. Introduction

In every country, the existence of handicapped people is an unavoidable real issue [1]. Inconvenience brought by physical disability makes their sports become unusual [2]. Although handicapped people have some irretrievable deficiencies in their physical bodies, their hearts are eager to get understanding and respect like normal people. Therefore, auxiliary equipment, especially wheelchair series, is significantly important for physical and mental recovery of handicapped people. As one of sports event that handicapped people can take part in, wheelchair basketball game has a twenty-year development history in China, but the development of basketball wheelchair in China is far lower than international standard. If it is unable to keep pace with the development of basketball wheelchair, this game in China would be influenced in the long term and is harmful for handicapped people to recover their sports [3]. So it is essential to design and research basketball wheelchair.

[1]Xinxiang Vocational and technical college, Henan, 453000, China; Email: joehuiwang01@yeah.net

Foreign research on competitive basketball wheelchair, such as A. Faupin et al. [4] meticulous researches are made to obliquitous parameters of basketball wheelchair; D. Y. Vanlandewijck et al. [5] and others make relative research on correlation between the design of basketball wheelchair and injury of players. However, organizations that research this type of basketball wheelchair is still very rare in domestic, which makes many participating teams use imported wheelchairs to join games. The existing sports wheelchairs in domestic are reformed from ordinary wheelchairs by manufacturers combining with previous wheelchair experience. Without scientific development and experiments, there are still obvious deficiencies in some aspects such as security, cushioning and comfort [6]. For the above situation, some deficiencies of the existing basketball wheelchair are improved and a new design plan of basketball wheelchair is put forward. And analysis determination is made to some static sizes of the new-design basketball wheelchair seat, which contributes to its meagre strength for the development of handicapped sports.

2. A design of basketball wheelchair based on ergonomics

2.1. Ergonomic theory in basketball wheelchair

The design philosophy of ergonomics puts the factors related to human first, highlighting the interdependent relationship between users, industrial products, used circumstances and society [7]. So, from the perspective of ergonomics, the design process of basketball wheelchair can be regarded as "integration between human and machine and environment". Among them, "human" refers to the user of basketball wheelchair; "machine" is basketball wheelchair; and here "environment" means a working place of games for basketball wheelchair users. Based on satisfying ergonomic performance, the design of basketball wheelchair is human-centered. Not only should all the properties of components be researched, but also the overall property is paid more attention. So the optimal result of system can be acquired.

2.2. Design requirements of basketball wheelchair based on ergonomics

In the design of basketball wheelchair, several parts of basketball wheelchair that touched with human need to be adjusted in terms of human body. It tries its best to make users fell convenient and comfortable when they manipulate the wheelchairs. More specifically, according to ergonomic theory, there are some points need to be abided by:

1. Manipulation of basketball must be simple, so the users can quickly master the skills.

2. Basketball wheelchairs must have adjustability, so all different people can adapt to the driving space.

3. Apart from asking basketball wheelchairs to satisfy the basic requirements, it also needs to meet nimble and convenient requirements.

4. The basketball wheelchair should have comfort whose boundary dimension

also should roughly meet the requirement of human body.

3. Improvement plan of the existing basketball wheelchair

3.1. Improvement plan between principal axis, foot plate and barycenter of basketball wheelchair

In the wheelchair basketball training and games, it often occur phenomenon that principal axis of wheelchair is out of shape, even dehiscent. It makes basketball wheelchair not meet training and match requirement, but does harm to athletic body. A solution to this problem is that finite element analysis is made to choose a better twice bending method. Besides, highly adjustable model is designed for and adjustable range is fixed between 0 and 110 mm. in the training and matches, basketball wheelchairs are always in fast forward and backward as well as instantly revolving states. From the perspective of physics, gravity center of human body is properly moved back to make the gravity center of wheelchair closer to gravity center of two bull wheels, which increases the stability of wheelchair.

3.2. Improvement plan between principal axis, foot plate and barycenter of basketball wheelchair

A redesign is made for hand wheel of basketball wheelchair, adding a hand protection tile between hand wheel and bull wheel, which properly increases the contact area between palm and hand wheel. So players can save labor to manipulate the wheelchair, and their discomfort in hands is relieved, and unnecessary damage is avoided. The existing basketball wheelchair is equipped with stainless steel spoke of wheel cobwebbing. This spoke easily causing bending or broken-off situations without impact-resistance,which does harm to handicapped players. So the new designed wheel spoke uses composite material that is made from flame core injection process. Compared with common steel wire, it has high corrosion resistance, good quake-proof circle effect, strong hardness and better recoverability. The specific wheel pattern is shown in the following Fig. 1.

3.3. Improvement plan about quake-proof circle of basketball wheelchair

In the designing scheme, as a dismountable single component, quake-proof circle uses shock absorber to connect with frame theme. Quake-proof circle is improved its impact-resistant intensity in order to have an equal force, so its exterior shape adopts stream-line pattern. In addition, intensity of quake-proof circle is matched with its stand intensity as much as possible. And reasonably intensifying stand intensity is helpful to increase collision avoidance system to absorb collision energy. A damper spring is loaded in joint between quake-proof circle and car body in order to minimize shake when wheelchair is collided directly. Accordingly, it can guarantee the handicapped player's comfort and protect their injured body from second injury. And the specific pattern is shown in the following Fig. 2.

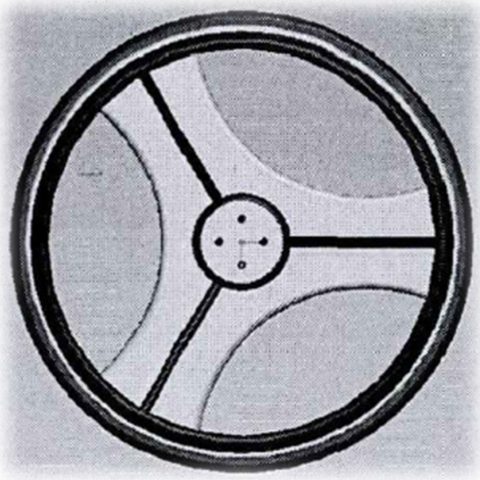

Fig. 1. Improved wheel

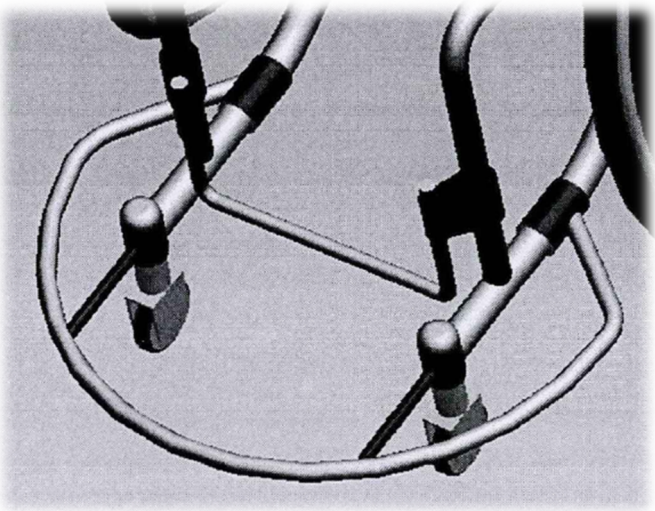

Fig. 2. Improved quake-proof circle

4. Ensuring some static sizes of basketball wheelchair seat

4.1. Size design of seat width and chair surface

Before making sure its specific sizes, an analysis is made for human body sitting postures from age group between 18 and 38. And the result is expressed in following Table 1. The design of seat width must meet people with large figures, so No. 95 percentile size data of shoulder breadth between sitting posture and two elbows is

selected with the addition of function correction value. And the length of seat width is (387+13) mm. The length of chair surface is designed according to sitting size. The seat depth of No. 5 percentile female is selected as size gist and added posture correction. Thus, the length of chair surface is (401+44+13) mm.

Table 1. Human body sitting postures size (unit: mm)

Measurement project	Female percentile				Male percentile			
	5	50	90	95	5	50	90	95
Shoulder breadth	344	375	397	403	320	351	371	377
Hip breadth	282	306	327	334	290	317	340	346
Shoulder breadth between sitting posture and two elbows	371	422	473	489	348	404	460	478
Sitting hip breadth	295	321	347	355	310	344	374	378
Sitting height	809	855	891	901	858	908	947	958
Sitting elbow height	215	251	277	284	228	263	291	298
Sitting thigh thickness	113	130	146	151	112	130	146	151
Sitting knee height	424	458	485	493	456	493	523	532
Shank and foot height	342	382	399	405	383	413	439	448
Seat depth	401	408	461	469	421	457	486	494

4.2. Size design of seat surface angle

Inclination angle of seat surface refers to this angle cannot be too big or too small. It is a reasonable range from four degree to eight degree under normal circumstance. Body pressure distribution is one of key factors to choose inclination angle of seat surface. According to numerous experiment data, it is known that when human sits straight, the pressure under ischium is biggest. With the expansion of pressure point, body pressure is gradually decreased out from ischium. It reaches the smallest pressure until thigh. It is a reasonably ideal pressure distribution of sitting posture that is specifically shown in the following Fig. 3. Finally, evaluated and compared by ergonomics, it is closest to ideal body pressure distribution when inclination angle of seat surface is 5 degree under no-cushion circumstance. So inclination angle of seat surface with 5 degree is finally selected.

4.3. Size design of foot plate and hand rail

The product's design purpose is suitable for operating requirements of most people, so foot rest of basketball can be designed as zoom mode. And its size can be determined by shank and foot height data of No. 95 male percentile and No. 5 female percentile in Table 1. The correction of foot plate is not considered because of its adjustability. The adjustable length of foot plate is 0–(448–342) mm. Due to the

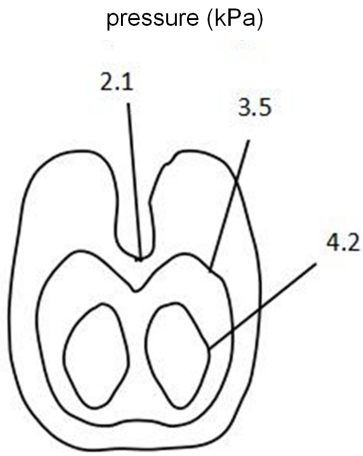

Fig. 3. Body pressure graph of sitting posture in ideal state

particularity of basketball wheelchair, the range of choice is from 0 to 110 mm. In the design of basketball wheelchair, strict design of hand rail is made according to relevant size of body tercile. The part's size takes median value from No. 50 male and female terciles as setting reference, and the height of hand rail is $(263 + 251)/2 - 13$. Because handrail height of public chair should be slightly lower than this height, the handrail height is selected as 240 mm.

5. Conclusion

With numerous research analyses, an analysis is made for design requirements of basketball wheelchair based on ergonomics and a new design is made for competitive basketball wheelchair. In response to the problems of existing wheelchairs in principal axis, foot plate, hand wheels and quake-proof circle, analysis is made and relevant solutions are put forward, which improves security, cushioning and comfort of basketball wheelchair to some extent. Besides, from body characteristics, analysis determination is made for some static sizes of basketball wheelchair, making the overall design of new plan more reasonable.

References

[1] M. Oliver, C. Barnes: *Disability studies, disabled people and the struggle for inclusion.* British Journal of Sociology of Education *31* (2010), No. 5, 547–560.

[2] D. Howe: *Chapter 2 - A social history of sport for the disabled.* Routledge online studies on the Olympic and Paralympic Games *1* (2012), No. 4, 1–12.

[3] L. Croft, S. Dybrus, J. Lenton, V. Goosey-Tolfrey: *A comparison of the physiological demands of wheelchair basketball and wheelchair tennis.* International Journal of Sports Physiology & Performance *5* (2010), No. 3, 301–315.

[4] A. Faupin, P. Campillo, T. Weissland, P. Gorce, A. Thevenon: *The effects of*

rear-wheel camber on the mechanical parameters produced during the wheelchair sprinting of handibasketball athletes. Journal of Rehabilitation Research & Development *41* (2004), No. 3B, 421–428.

[5] D. Y. Vanlandewijck, D. Theisen, D. Daly: *Wheelchair propulsion biomechanics: Implications for wheelchair sports.* Sports Medicine *31* (2001), No. 5, 339–367.

[6] A. Iturricastillo, C. Granados, A. L. Arcos, J. Yanci: *Objective and subjective methods for quantifying training load in wheelchair basketball small-sided games.* Journal of Sports Sciences *35* (2017), No. 8, 749–755.

[7] N. A. Stanton, R. Stewart, D. Harris, R. J. Houghton, C. Baber, R. McMaster, P. Salmon, G. Hoyle, G. Walker, M. S, Young, M. Linsell, R. Dymott, D. Green: *Distributed situation awareness in dynamic systems: Theoretical development and application of an ergonomics methodology.* Ergonomics *49* (2006), Nos. 12–13, 1288–1311.

Received May 7, 2017

Acta Technica *62* No. 3A/2017, 45–54

Research on tennis judgment system based on hawk-eye technology

Jiafu Feng[1]

Abstract. To design a set of fast-response and high-accuracy Hawk-eye judging systems for tennis games. Method: Quantum particle swarm optimization is used to calibrate the camera to take pictures of tennis movement, and then these pictures are matched with three-dimensional. Finally, the motion trajectory of tennis is reduced by Gaussian fitting. In the 100 sets of data, the accuracy rate of the system judged within 5 cm from the border line was about 80 %, and the accuracy rate of other regions was more than 95 %. The average time of the system was also within 10 s. The Hawk-Eye system based on quantum particle swarm optimization calibration camera has the advantages of fast response and high accuracy of judgment, which is suitable for high-level tennis game.

Key words. Hawk-eye, tennis competition, quantum particle swarm optimization.

1. Introduction

With the development of society, science and technology are also constantly moving forward. Tennis players' own physical fitness and technology as well as their own equipment are increasing, and the speed of tennis also will be accelerated, even to the speed that people is difficult to see clearly with the eyes. So, there are inevitable erroneous judgments and commutations in the tennis game. Especially in high-level events, the game decision made by the information observed by the chief umpire in accordance with the naked eye at the scene is difficult to make the game fair. Because there are limits and blind spots in human vision. Hawk-eye technology tracks the path of the tennis movement through the camera, and calculates and synthesizes a series of collected data, and then clearly shows the audience the final movement path of the tennis and landing point. It can overcome the blindness of the human eye so that the audience can watch the game from more angles, while making the referee's decision more accurate to ensure the interests of the players [1]. The accuracy of the Hawk-eye system should be as high as possible in order to make the game fairer. The response speed of the Hawk-eye system should be as

[1]Xi'an Physical Education University, 710068, Shaanxi, China; E-mail: jff_jiafufeng@163.com

fast as possible in order not to interrupt the continuity of the game. Based on this purpose, we studied and designed the tennis Hawk-eye system based on the quantum particle swarm optimization by using the virtual instrument platform and the image processing and simulation technology.

2. Theoretical review

2.1. Hawk-eye system

The Hawk-eye is an instant replay system invented by Britishman Paul Hawkins to help the audience overcome many of the blind spots in the viewing angle, enabling viewers to clearly watch the multi-perspective tennis game process through the playbacks provided by the Hawk-eye technology [2]. So, for the audience, the Hawk-eye technology has given them a good visual experience. The set of Hawk-eye technology is very precise. The whole system has 8 or 10 high-speed cameras, which divides the three-dimensional space of the entire competition venues into multiple areas that the measurement units is millimeter with the help of the computer. So, it can capture the basic data of the trajectory of tennis on the field from different angles through high-speed camera, and will observe the blind spot and dead angle that the human eye cannot see. The Hawk-eye technology system also has four computers and a large screen. The captured data will be drawn as a three-dimensional image after computer calculates, and the tennis line and placement will be presented in the big screen to the audience by using the timely imaging technology. Hawk-eye technology is very efficient, the process from the collection of data to demonstration of the results only takes less than 10 seconds. Therefore, the Hawk-eye system is now widely used in a variety of television broadcasts.

2.2. Particle swarm optimization

Particle Swarm Optimization (PSO) [3] is an evolutionary computing technique and derives from the study on the prey behavior of birds. It is a kind of optimization tool based on iteration, which is similar to genetic algorithm. The system is initialized to a set of stochastic solutions, and it interactively searches for the optimal solution. The birds in the population are abstracted as "particles" without quality and shape. We find the optimal solution in the complex solution space through the cooperation and information sharing of these "particles".

In the PSO, the solution to each optimization problem can be considered as a bird in the search space. We call it "particles." All particles have a fitness value determined by the optimized function, and each particle has a velocity that determines the direction and distance they fly, and the particles will search following the current optimal particle in the solution space.

PSO is initialized to a group of random particles, and then find the optimal solution through iteration. In each iteration, the particle updates itself by tracking the two extremes. One is the best solution that the particle finds by itself, called the individual extremum pbest; the other extreme is the optimal solution gbest of

all the particles in the whole particle population, which is the global extreme value. In addition, we cannot use the entire population but only a part to be the neighbors of the particle, then the extreme value among all neighbors is the local extreme [6]. At the same time, each particle constantly changes its speed in the solution space to determine its own direction and flight distance, and "fly" towards the area that the pbest and gbest point to as far as possible.

In the mathematical model of the PSO algorithm, the bird is abstracted as a "particle" without mass and volume. The solution group is equivalent to a bird group, the "good news" is equivalent to the optimal solution of the evolution of each generation, the food source is equivalent to the global optimal solution, and the migration from one place to another is equivalent to the evolution of solution group. The evolution or evolution of the whole system includes the emergence and differentiation of the new levels and emergence of diversity, and the emergence of new themes.

2.3. Quantum particle swarm optimization

After the PSO algorithm, scholars have also carried out a lot of work on improving the convergence and diversity of the algorithm. Even though a variety of improved algorithms are proposed on the basis of the PSO algorithm, the PSO algorithm itself is flawed, and the most fundamental of these is that it has been proved not a globally convergent algorithm [5]. The authors put forward quantum particle swarm optimization algorithm on the basis of PSO algorithm in order to solve this problem. The properties of it is completely different from the particles in the quantum space. It can be searched in the whole feasible solution space, so the global search performance of the quantum particle swarm optimization is much better than that of the general PSO algorithm.

Quantum Particle Swarm Optimization (QPSO) follows the PSO. The state of the particle is no longer expressed by the position vector and the velocity vector in the quantum space, but is described by the wave function. Owing to the uncertainty principle, the position and velocity of the particles cannot be accurately determined at the same time. Particles can be examined in the spatial representation without considering the velocity. The probability that a particle appears at position x is represented by a probability density function that is not limited to a given orbital function [4].

3. Method

3.1. Calibration of the camera

The camera is the front end of the whole system, and the information quality has great influence on the subsequent image processing and 3D construction. In the calibration process of the camera, the quantum particle swarm optimization algorithm is introduced to overcome the problem that the system is easy to fall into local small and the error is large, and the venue location of the camera is shown in

Fig. 1.

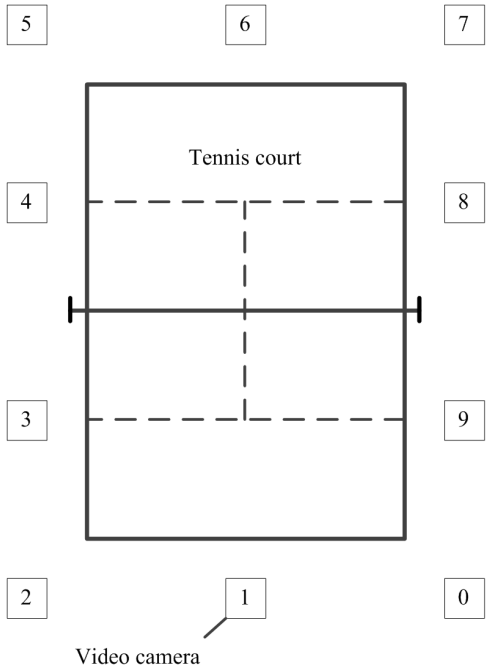

Fig. 1. Plan view of the camera arrangement

The relationship between the 3D point M and the 2D point m is:

$$s\tilde{m} = A[Rt]\tilde{M}\,, \tag{1}$$

$$s\begin{bmatrix} u \\ v \\ l \end{bmatrix} = A[r_1, r_2, r_3, t]\begin{bmatrix} x \\ y \\ z \\ 1 \end{bmatrix} = A[r_1, r_2, t]\begin{bmatrix} x \\ y \\ 1 \end{bmatrix}\,. \tag{2}$$

Here, A is the camera parameter matrix, $\tilde{M}$ is the homogeneous matrix of the three-dimensional point, $\tilde{m}$ is the homogeneous matrix of the two-dimensional point, and r_1, r_2, r_3, t is the rotation matrix and translation of the camera relative to the world coordinate system. When $Z = 0$, then

$$H = [h_1, h_2, h_3]\lambda K[r_1, r_2, t]\,, \tag{3}$$

$$r_1 = \frac{1}{\lambda}K^{-1}h_1\,, \quad r_2 = \frac{1}{\lambda}K^{-1}h_2\,. \tag{4}$$

From the properties of the rotation matrix, the constraints of the camera param-

eter matrix are

$$h_1^{\mathrm{T}} K^{\mathrm{T}} K^{-1} h_2 = 0, \quad h_1^{\mathrm{T}} K^{\mathrm{T}} K^{-1} h_1 = h_2^{\mathrm{T}} K^{\mathrm{T}} K^{-1} h_2 \,. \tag{5}$$

When the number of captured images is greater than 3, K can be solved linearly to obtain the internal parameters. The quantum particle swarm optimization equation is

$$v_i(t+1) = v_i(t) + c_1 \mathrm{rand}_1[p_i(t) - x_i(t)] + c_2 \mathrm{rand}_2[p_g(t) - x_i(t)] \,, \tag{6}$$

$$x_i(t+1) = x_i(t) + v_i(t+1) \,. \tag{7}$$

Here, i is the index of the particle, t is the evolution time, and rand_1, rand_2 are the random functions. Symbol c_1 is the optimal step size of the particle itself, c_2 is the global optimal step size of the particle, and v_i is the velocity of the i-th particle.

Then the evolution equation is obtained through the basics of the quantum mechanics, and the final global limit is the optimal value of the camera calibration.

$$\begin{aligned} & x_i(t+1) = p_i \pm \beta \left| m_{\mathrm{best}} - x_i(t) \right| \ln(1/\mu) \\ & p_i = \tfrac{\mathrm{rand}_1 \cdot p_i + \mathrm{rand}_2 \cdot p_g}{\mathrm{rand}_1 + \mathrm{rand}_2} \\ & m_{\mathrm{best}} = \textstyle\sum_{i=1}^{n} p_i / n = \sum_{i=1}^{n} p_{i1} / n = \ldots = \sum_{i=1}^{n} p_{i\mathrm{D}} / n \end{aligned} \tag{8}$$

3.2. Two-dimensional detection and tracking of tennis

The two-dimensional detection of tennis is achieved by the background difference method. In order to reduce the influence of noise, illumination and so on, the Gaussian template is used to extract the background. First, the component has the background model $A[x, y, t] = \left| \mu \left| \sigma^2 \right| \right|$ of the Gaussian distribution, μ is the average value of the pixels, and σ^2 is the variance. The pixel in current frame of camera is set as $I[x, y, t]$, and transform according to the following equation

$$\mathrm{Acc}[x, y, t] = (1 - a)\mathrm{Acc}[x, y, t-1] + aI[x, y, t] \,, \tag{9}$$

The constant a is 0.5, after the accumulation, the value of a pixel in current frame is larger than the past weight.The MATLAB image processing tools in the subtraction is used, and the image is binarized by rgb2gray function. Then the subtraction operation is carried out through the current frame and background image, and then is threshold segmentation, you can extract the target parameters, such as coordinates, length and width [7].

In the dynamic tracking of tennis, the CAMshift method is used, and the video image is transformed into color probability distribution according to the YUV information. The tennis characteristic parameters obtained by the difference method are taken as the initial parameters of the search, and set as $I[x, y]$, to calculate the zero order matrix, the first order matrix M_{01}, the second order matrix M_{02}, M_{20}

and M_{11}, and then calculate the current centroid position as

$$(x_{\mathrm{c}}, y_{\mathrm{c}}) = \left[\frac{M_{10}}{M_{00}}, \frac{M_{01}}{M_{00}}\right]. \tag{10}$$

The result is taken as the center of the search window in the next frame, and then the size of the search window is adjusted according to M_{00}:

$$\begin{aligned} l &= \sqrt{\frac{(a+b)+\sqrt{b^2+(a-c)^2}}{2}}, \\ w &= \sqrt{\frac{(a+b)-\sqrt{b^2+(a-c)^2}}{2}}, \end{aligned} \tag{11}$$

where l is the length of the search window, w is its width, $a = M_{20}/M_{00} - x_{\mathrm{c}}^2$, $b = 2[M_{11}/M_{00} - x_{\mathrm{c}}y_{\mathrm{c}}]$, $c = M_{02}/M_{00} - y_{\mathrm{c}}^2$. Calculating according to this cycle until the distance between center of mass and the core is less than the threshold, one can get the moving target parameters.

3.3. Reconstruction of three-dimensional points

It needs at least two different angles of the image in order to achieve the three-dimensional world coordinates of the positioning sphere. The 3D point is reconstructed in the ideal state from the projection point of the pixel coordinates, as shown in Fig. 2.

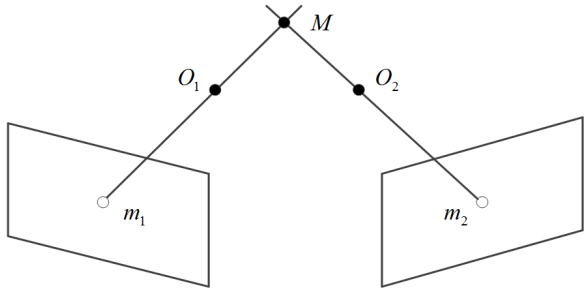

Fig. 2. Ideal 3D point reconstruction

The optical center O_1 through the camera can draw a ray to the space from the projection points m_1 and m_2 of the first image point of space. The optical center O_2 through the camera can draw another ray to the space from the projection of the second image point of space. The intersection point of the different rays drawn from different dimensions is the space point in the real world [8]. However, as shown in Fig. 3, because the images of different angles have image noise and camera calibration error, so that the intersection point on the space does not exist, and the three-dimensional reconstruction of the point problem turns into the problem about selecting the optimal solution in the point space. There are many mature algorithms for this optimal solution problems, such as the least squares method, it can be achieved by using iterations.

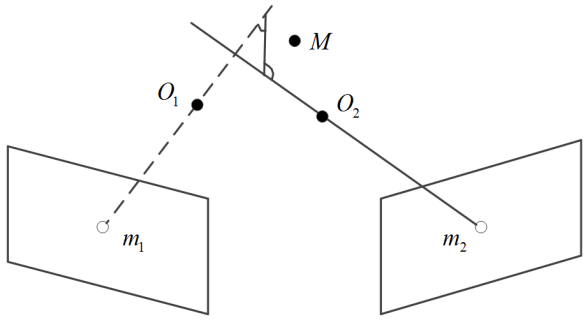

Fig. 3. Real 3D point reconstruction

After the coordinates of the spatial points are obtained, these discrete points need to be fitted. The Gaussian fitting is used to fit the corresponding points of the image using Matlab ImageProcessing. The larger area is the intersection of the centerline and the edge. The system chooses 10 pairs of points and executes TFORM = cp2tform (input points, base-points, transfromtype), B = imtransform (A, TFORM), A, B are different camera images. The curve fitting principle is the least squares method, and the curve with the quadratic sum of the distance of the given point is the smallest, and one can get the trajectory by using Matlab toolbox Gaussian.

4. Results

We create the three-dimensional space with three-dimensional coordinates by using Grid Properties.vi, and take XY plane as the ground, and create ball of the tennis through Create Sphere.vi and Create object.vi. The ball is running in accordance with the fitting track. We selected 50 points to simulate the ball running trajectory in order to make the display more coherent, and created another scene display to show the top view. In the top view, the audience can clearly see the tennis landing point, and the coordinates of the landing point and the tennis ball radius are same. When it beyond the border, it is judged out of bounds, determining the bottom line $Y = 0$. If the coordinates of the tennis landing point on the X axis, then it is positive, and the ball is in bounds. If it is negative, then it is judged the ball is outside the bounds.

100 sets of measurement data were selected for testing in order to verify the correctness of the system. The results show that the average response time of the system is 9.12 s, and some results are shown in Table 1.

The relationship between the correct rate judged by system and the distance from the boundary is shown in Fig. 4.

From the above results, the correct rate judged by the system was 80 % when it is -5∼5 cm from the border, and other places have reached more than 95 %, and the average processing time of 10 s. The decision and the processing time meet the design requirements.

Table 1. Test results

Groups	Actual distance (cm)	Actual judgments	Distance obtained by system (cm)	Judged by system
1	9.3	No	9.5	No
2	10.2	No	10.1	No
3	–7.1	Yes	–7.4	Yes
4	4.8	No	5.1	No
5	12.4	No	12.7	No
6	–15.1	Yes	–14.8	Yes
7	–0.4	Yes	0.2	No
8	5.9	No	6.2	No
9	13.8	No	13.5	No
10	3.2	No	3.5	No
⋮	⋮	⋮	⋮	⋮
95	10.2	No	9.9	No
96	7.9	No	7.8	No
97	–8.5	Yes	–8.3	Yes
98	–6.3	Yes	–6.4	Yes
99	4.9	No	4.7	No
100	–8.2	Yes	–8.3	Yes

5. Conclusion

The camera calibration based on p quantum particle swarm optimization can overcome the shortcoming that the system is easy to fall into the local small and the back-projection error is large, and the calibration precision of the camera is improved. Based on this algorithm, the tennis Hawk-eye system can track all the trajectories of tennis movement and the accurate track of the landing point of the tennis ball. It can determine the result, its level of visualization is high, the speed of judgment is fast and the result is accurate, so it can meet the design requirement.

References

[1] S. Mecheri, F. Rioult, B. Mantel, F. Kauffmann, N. Benguigui: *The serve im-*

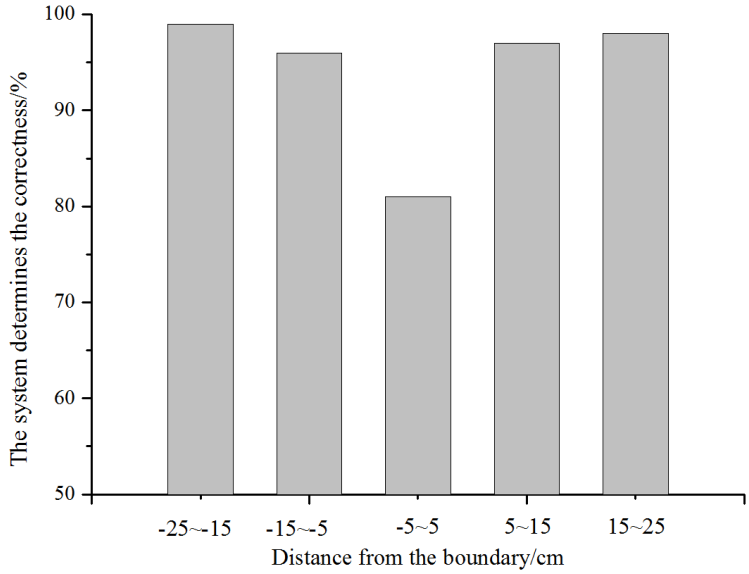

Fig. 4. Relationship between the correct rate judged by system and the distance from the boundary

pact in tennis: First large-scale study of big Hawk-Eye data. Journal Statistical Analysis and Data Mining *9* (2016), No. 5, 310–325.

[2] J. Cui, Z. Liu, L. Xu: *Modelling and simulation for table tennis referee regulation based on finite state machine.* Journal of Sports Sciences (2016), 1–9, paper 1241417.

[3] J. Kennedy: *Particle swarm optimization.* Encyclopedia of machine learning, Springer US (2011), 760–766.

[4] Y. F. Ji, C. L. Wang, Z. H. Shi, J. Ren, L. Zhu: *Table tennis service umpiring system based on video identification—for height and angle of the throwing ball.* Wearable Sensors and Robots, Springer, Singapore, Lecture Notes in Electrical Engineering *399* (2017), 495–509.

[5] Y. Hao, Z. Hao, H. Yang: *Table tennis placement is determined based on artificial intelligence.* Journal of Residuals Science & Technology *13* (2016), No. 5, 16.1–16.3.

[6] D. Wang: *Application of simulation technology in table tennis flight theory model.* Journal of Computational and Theoretical Nanoscience *13* (2016), No. 12, 9793–9797.

[7] C. Brechbuhl, G. Millet, L. Schmitt: *Accuracy and reliability of a new tennis ball machine.* Journal of Sports Science & Medicine *15* (2016), No. 2, 263–267.

[8] P. Karuna, M. Preeti: *Global plagiarism management through intelligence of hawk eye.* Indian Journal of Science and Technology *9* (2016), No. 15, 1–10.

Received May 7, 2017

Acta Technica *62* No. 3A/2017, 55–66

Design study of an integrated test system of free combat training aids based on singlechip

Nongxuan Mao[1]

Abstract. Functions of current free combat training aids are unitary. Thus based on the MSP430 singlechip, this study designed a kind of integrated test system for free combat training aids, aiming to provide a versatile exercising and test platform for athletes. First of all, the adopted software and hardware in design were introduced. Then the design of hardware circuit and the program flow of software design were elaborated. Finally, the whole system was debugged. The designed integrated test system in this study was mainly composed of MSP430F247 singlechip, an ultrasonic wave sensor module and a liquid crystal module, etc. The system collected signals through the ultrasonic wave sensor and the air pressure sensor. The MSP430F247 singlechip was responsible for data calculation as well as displaying results through liquid crystal. The wireless communication module was connected with the upper computer and the user database was constructed for data management and query. Tests of modules and the whole system indicated that, the designed free combat system met ideal requirements, which also made up for the deficiency of current free combat training aids and improved the practicability and maneuverability.

Key words. MSP430 singlechip, free combat training system, sensor, upper computer, system debugging.

1. Introduction

Free combat training aids are popular in gyms. Follows aspects should be considered in selection of exercise equipment. Firstly, it should be popular. Secondly, it should be safe that exercisers will not be injured during exercising. Thirdly, it is reasonably priced and does not occupy much space [1–2]. Therefore, this study aims to design a kind of free combat training equipment that is perfect for gym.

[1]Martial Arts Department of Xi'an physical Education University, 710068, China; E-mail: nongxuanmao1980@aliyun.com

2. Literature review

Modern free combat training aids are integrated by exercising and testing. The back of the target surface of free combat training aid is connected with a air cylinder. When the surface is hit by users, the air is compressed and the target moves backward, thus a distance of buffer is formed, which can protect the fist [3–4]. The boxing strength can be reflected by changes of the air pressure in air cylinder. Signals of the air pressure changes are collected by air pressure sensors. After analog to digital (A/D) conversion, the boxing strength can be known [5]. In the designed system in this study, ultrasonic wave sensors were installed on top of the target, thus to detect the distance between the fist during boxing through reflected waves. Thus the speed could be calculated according to the specific value of distance difference of every two measurement and the time used. Among various speed values obtained, the maximum value was defined as the boxing speed. Therefore, the free combat training aid designed in this study could not only be used for boxing training, but could be used to test the reaction time, boxing speed and boxing strength. Such system overcame shortcomings of traditional free combat training aids, and its gas buffer could protect users.

3. Research method

3.1. Design of hardware circuit

The system designed in this study was mainly composed of MSP430 singlechip, MPS20N100D-S air pressure sensor module, SC63X75 air cylinder, HC-SR04 ultrasonic wave sensor module and 12864 liquid crystal module. MSP430 singlechip was the core module of the whole system, as shown in Fig. 1.

Ultrasonic wave sensors were responsible for collection of distance signals and air pressure sensors mainly collected air pressure signals. Collected signals were sent to the singlechip for calculation of boxing speed and strength. Meanwhile, the reaction time was obtained by timer B in the singlechip. The MSP430 singlechip not only stored measurement data in FLASH, but also sent them to 12864 liquid crystal module for display. Operating principles of the system are shown in Fig. 2. Overall structure of the free combat training aid is shown in Fig. 3.

3.1.1. Design of power circuit: As shown in Fig. 3, MSP430 single chip as well as the amplifier in differential amplification circuit requires ± 5 V of power supply. Therefore, 220 V of alternating current power supply was not suitable in the circuit design and should be used after coherent processing. Design principles of the power circuit is shown in Fig. 4.

LM7805 was a $+5$ V integrated regulator and its maximum output current was 1 A. According to the law of conservation of energy, the input and output power of power supply stays the same in ideal conditions. However, the output power is usually smaller than the input power in real life due to the loss caused by each component.

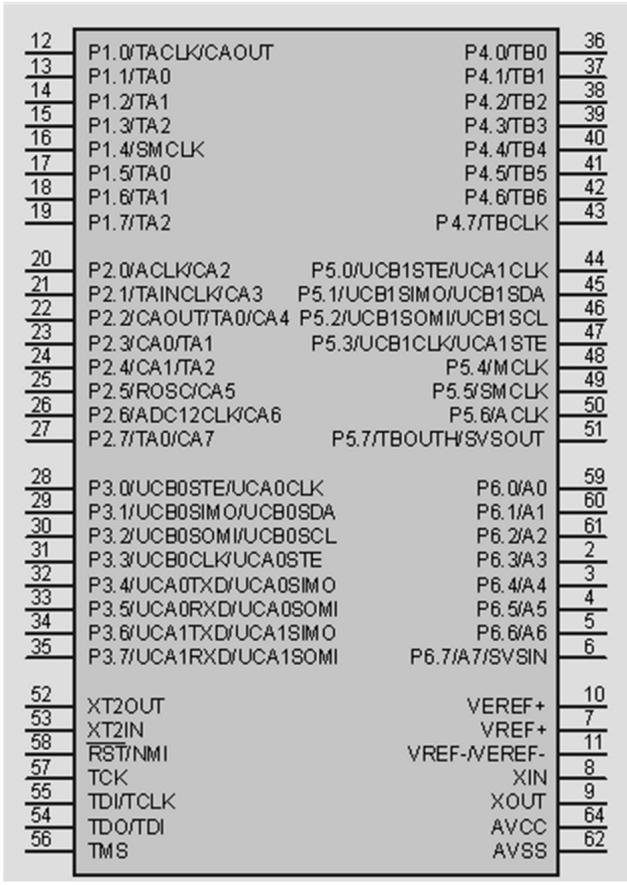

Fig. 1. Pin figure of MSP430F247 singlechip

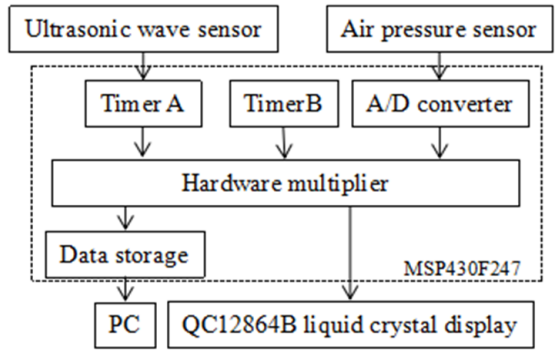

Fig. 2. Working principles of the free combat training system

The differential pressure of direct current between LM78 and LM79 before and after voltage stabilization was 2∼3 V. Thus, under positive and negative dual power,

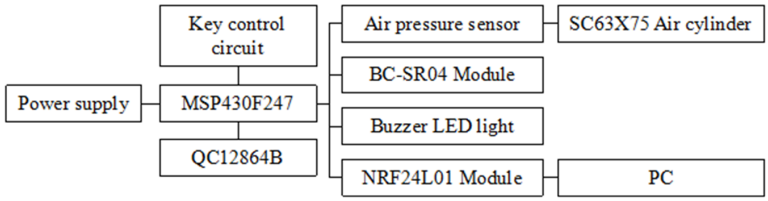

Fig. 3. Structure of the free combat training aid

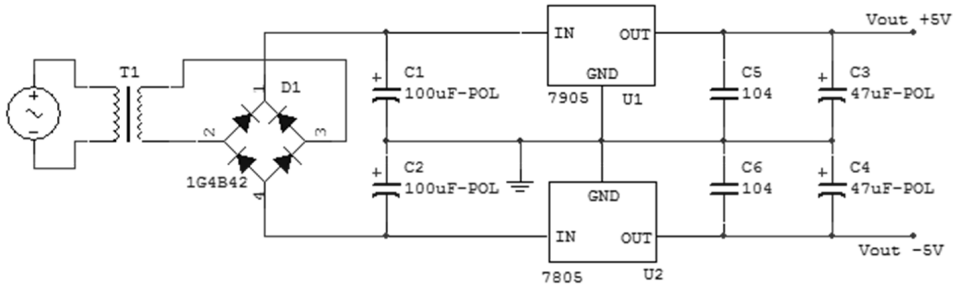

Fig. 4. Design principles of the power circuit

it should be 5∼6 V. Connection of the output end with capacitance could eliminate the ripple, thus the output direct current could be relatively stable. In addition, it had buffer effect on impact load.

3.1.2. Design of peripheral auxiliary circuit: Peripheral auxiliary circuits should be designed before the usage of MSP430 singlechip, such as reset circuit and clock circuit etc., in which the clock circuit was used to produce clock signals. The singlechip contained a low-speed crystal oscillator (LFXT1) and a high-speed crystal oscillator (XT2). Its external circuit is shown in Fig. 5.

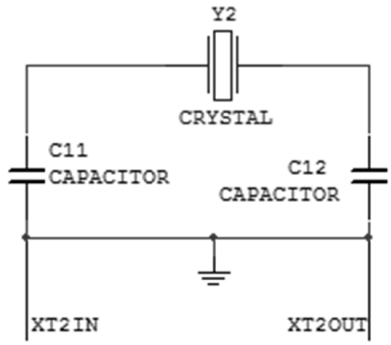

Fig. 5. Crystal oscillating circuit

MSP430 singlechip had two kinds of signals that could reset and initialize the equipment, which are power on reset (POR) signals and PUC signals. When the

MSP430 singlechip was powered on, the singlechip could produce POR signals if the reset pin RST/NMI was added with low electrical level. MAX708 was a kind of control chip of power supply for microprocessor, which could simultaneously output high level effective and low level effective reset signals [6]. Besides, MAX708 could monitor power supply signals and provide early warning of voltage drop for the singlechip. Thus the outage could be safe and parameters could be stored. The scheme of the reset circuit is in Fig. 6.

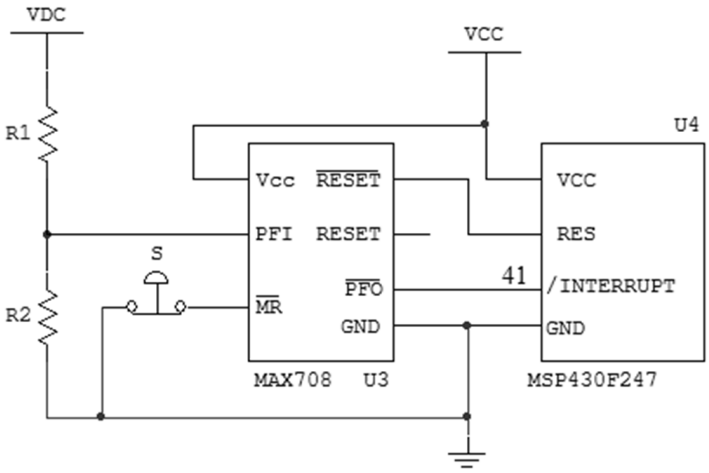

Fig. 6. Reset circuit

3.1.3. Circuit design of speed measurement: Ultrasonic waves are characterized by strong directivity and slow energy decrement and can propagate for a long distance [7]. Therefore, distances were measured using ultrasonic waves in this study. In the design, HC-SR04 ultrasonic wave sensor was used for speed measurement and the measurement accuracy reached 3 mm. The HC-SR04 distance measurement module included an ultrasonic wave emitter, a receptor and a control circuit. Its basic operating principles included three steps. Firstly, TRIG was used through input/output port to measure distances. Secondly, the module automatically emitted eight square waves in 40 kHz and it was automatically detected whether there was signal return. Thirdly, if there was signal return, a high level was output through the input/output port. The time of duration of high level was the time of ultrasonic waves from emitting to return. The measurement distance = high level time × sound velocity (340 m/s)/2. Wiring of the ultrasonic wave sensor is shown in Fig. 7.

3.1.4. Circuit design of boxing strength measurement: In measurement of boxing strength, the air pressure sensor was used to detect the voltage change in air cylinder. The maximum pressure air cylinder could bear was 320 kg; the boxing strength of normal people was around 250 kg. During boxing, the air was pressed while the piston would not rebound immediately, thus the maximum air pressure in the air cylinder could be maintained for a period of time. Thus the air pressure sensor had enough time of reaction.

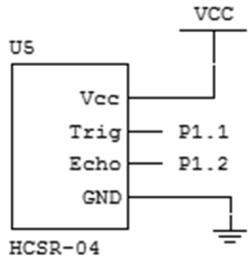

Fig. 7. Wiring of the ultrasonic wave sensor

The air pressure sensor used in this study was a SMD packaging product, which had good repeatability and long-time stability. Its internal circuit structure is shown in Fig. 8.

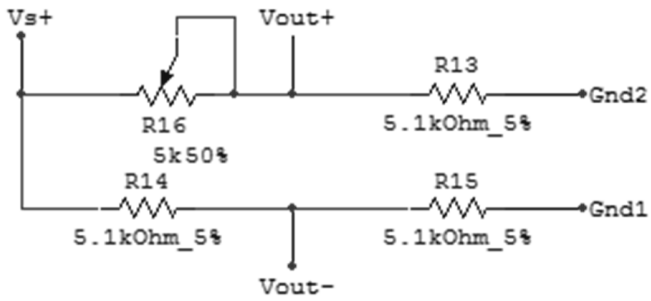

Fig. 8. Internal circuit of MPS20N1000D-S

Hardware circuit of the air pressure sensor is shown in Fig. 9. Output signals of Vout+ and Vout- were differential signals. Because signals were in millivolts, samples should be selected and amplified. Obtained positive analog signals were input in P6.0 port for analog-digital conversion. Thus the pressure value could be obtained after relevant calculation.

3.1.5. Analysis of sensor errors: Sensors were used in several parts of the designed free combat system in this study. Changes of factors, such as temperature, humidity and pressure, etc., could result in certain measurement errors. Therefore, analysis and adjustment of measurement errors in the design could reduce errors and improve accuracy, thus to further improve the systematic stability.

Propagation velocity of ultrasonic waves was mainly affected by temperature. Thus temperature correction was required for measurement of ultrasonic wave speed:

$$v = 331.4 \times \sqrt{T/273 + 1} \approx 331.4 + 0.067T \,\mathrm{m/s}\,.$$

In the above equation, v refers to the propagation velocity and T is the air temperature. Calibration curve could be used for error correction of pressure sensors.

First of all, standard weight was added on the target surface and multiple times of measurement was performed. Then standard input-output curves were drawn to obtain a characteristic curve:

$$F(x) = \frac{y_2 - y_1}{x_2 - x_1} x = kx\,.$$

In practical measurement process, the standard output could be obtained by substituting the input value to the input-output function

$$F(x_0) = kx_0\,.$$

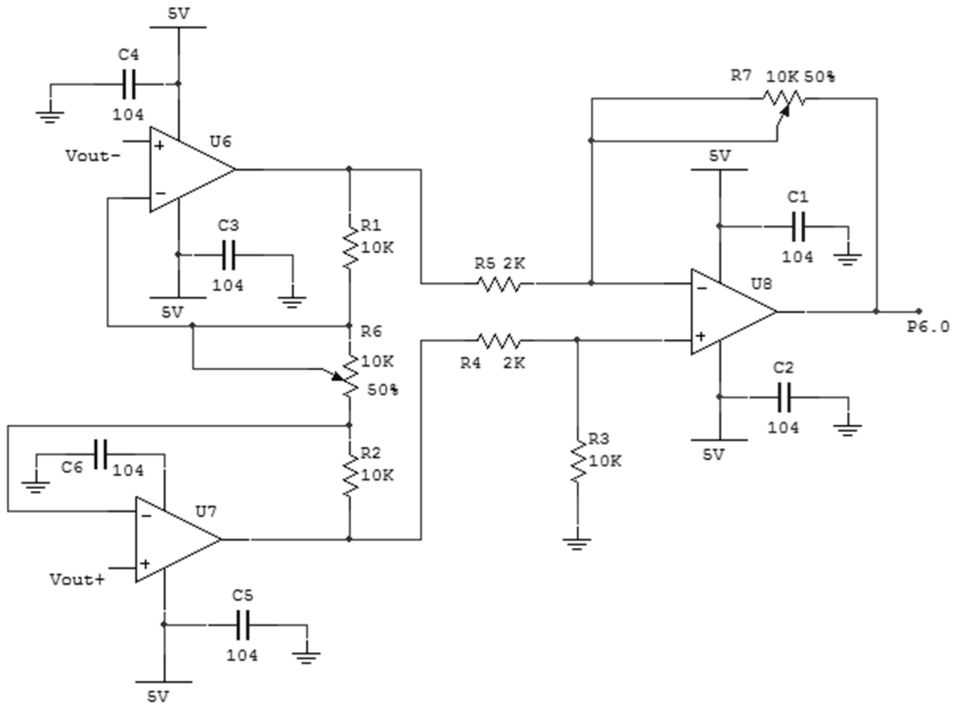

Fig. 9. Differential amplification circuit

3.1.6. Design of display circuit: QC12864B liquid crystal was used in the display module. 12864 refers to the number of lattice of 128×64 lattice liquid crystal module; its resolution ratio was 128×64. The function of key reminder circuit was to control the whole test process. Design principle of the key reminder circuit is shown in Fig. 10. As shown in the figure, the key was driven by P3.0 port and connected with a pull-up resistor. The electrical level of P3.0 port was continuously examined by the scan-round program. When low electrical level occurred, the key was pressed.

Serial peripheral interface (SPI) bus was used for central processing unit (CPU)

and peripheral equipment in this study. The SPI bus of singlechip supported the host mode and the slave mode, and it had independent shifting register, bumper and interrupt functions in receiving mode and sending mode. It could programme and control the polarity and phase of clock as well as the frequency of clock under the state of host mode [8].

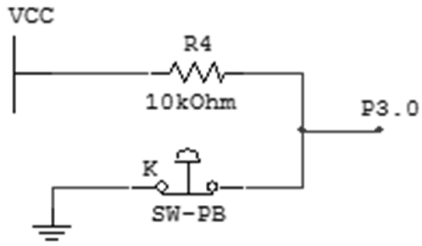

Fig. 10. Wiring diagram of the key

Communication between the system and PC was through the nRF24L01 module, which was a monolithic wireless transceiver chip operated in 2.4∼2.5 GHz general ISM frequency band. The wireless communication module included emission and reception these two parts and the operating principles are shown in Fig. 11.

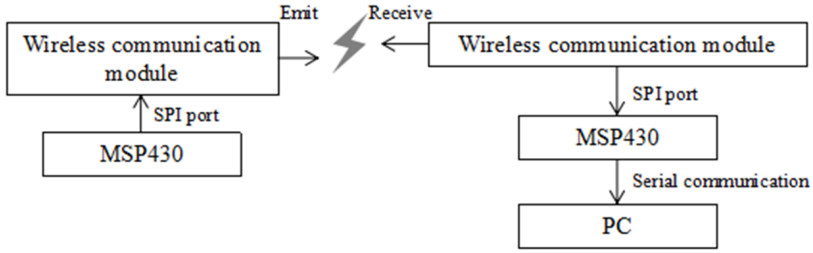

Fig. 11. Operating principles of wireless communication

3.1.7. Software design: IAR FOR MSP430 was a kind of programming and debugging environment that could be used in MSP430 singlechip. Developers could connect target boards through JTAG and the program could be debugged directly in IAR environment. Register values could be checked at any time and programming windows of C language and assembler language could switch at any time, etc.

Modularized programming concepts were used in the design. Consistent program interfaces were beneficial for debugging, correction and maintenance of the program. C language was mainly used for programming in the design of free combat training system. Besides, IAR program compiler was used for editing, debugging and compiling of C language. MSP430 singlechip emulator was used for simulation of the program.

The software part in the system was mainly composed of the main program and several interrupt service subroutines. The flow chart of the main program is

shown in Fig. 12. The interrupt service subroutine was composed of following parts: the subroutine of ultrasonic speed measurement; the subroutine of boxing strength measurement, which collected the variable quantity of air pressure; a timing program of timer; the subroutine of wireless communication. Besides, there was also a display subroutine. Design texts of subroutines were not further elaborated in this study.

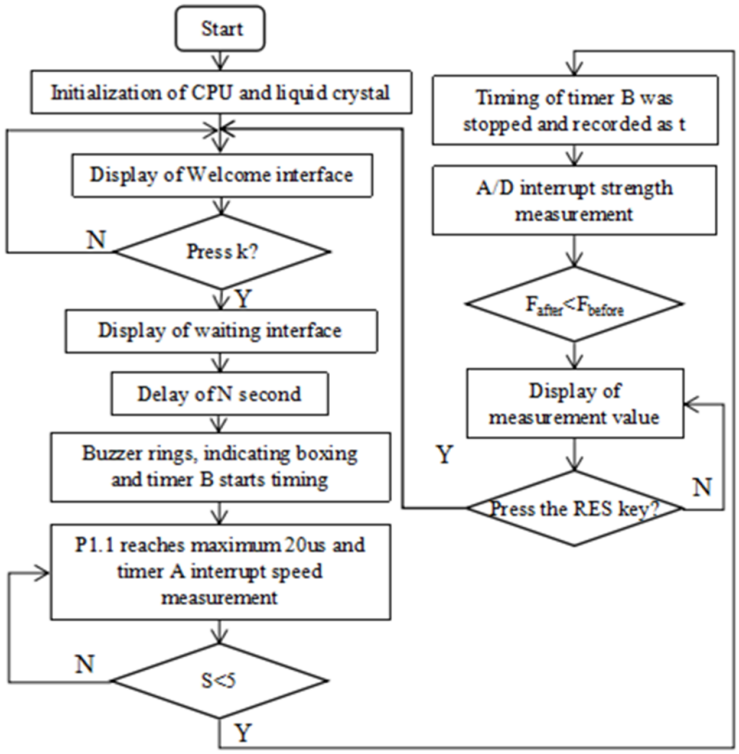

Fig. 12. Flow chart of main program

4. Debugging results and analysis

4.1. Configuration of development environment

IAR software was installed in computer and then set up. Specific steps are as follows:

IAR software was started and a new project was constructed according to Project> Create NewProject. Then in pop-up dialog box, address that should be stored was selected and then a new project was constructed.

Then the Workspace window was entered and the Debug configuration was defaulted. No correction was needed, or the program debugging could not be performed.

After that, a new file was built according to File>New>File and then saved for programming.

Finally, project options were set up and Projects>Options was selected after the finish of programming. Under the option of Device of General Options, the MSP430F247 singlechip was selected; then FET Debugger was selected under the option of Driver of Debugger for hardware simulation.

In MSP430 target board, debugged source program was loaded and hardware circuit was connected and checked. After that, mechanical framework was installed and fixed, i.e., the whole system could be tested.

4.2. Debugging and debugging result analysis

Firstly, the system was powered on. Then the display of Welcome interface could be seen. The k button was then pressed and the program entered the waiting time. After N seconds, the buzzer hinted boxing and the tester could prepare for the boxing at that time. At that moment, contents of liquid crystal display are as shown "Acousto-optic hint will be prompted after 3 second, please prepare to punch".

When the buzzer rang, the tester began to punch. During that that, the reaction time, boxing speed and boxing strength of the tester were test at the same time. The test was over when the fist hit the target surface. Test performance was then displayed, as shown in Fig. 13.

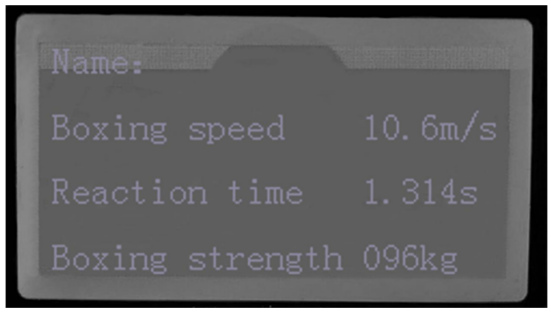

Fig. 13. Display interface of test performance

After the interface of test performance, it was also displayed that, Press RES to retest, reminding the tester to perform another test.

5. Conclusion

On the basis of theories of singlechip as well as the design methods of traditional free combat aids, we have basically understood design theories and principles of the free combat training system. Through the design of the integrate test system of free combat training, advantages and deficiencies are discovered to improve the ability of solving problems. Moreover, through module test as well as the test of the whole system, appropriate components are selected to improve the measurement accuracy, thus to improve the maneuverability and practicability of the training equipment.

References

[1] H. Chow: *Outdoor fitness equipment in parks: A qualitative study from older adults' perceptions.* BMC Public Health *13* (2013), No. 1, 1216.

[2] F. Lin: *Fitness equipment brings business opportunities.* Chinas Foreign Trade (2011), No. 11, 49–51.

[3] S. A. Combs, M. D. Diehl, W. H. Staples, L. Conn, K. Davis, N. Lewis, K. Schaneman: *Boxing training for patients with Parkinson disease: A case series.* Physical Therapy *91* (2011), No. 1, 132–142.

[4] M. J. Matthews, P. Comfort: *Applying complex training principles to boxing: A practical approach.* Strength and Conditioning Journal *30* (2008), No. 5, 12–15.

[5] L. F. M. Teixeira, V. J. De Godoi, A. Beghelli, M. Conte, P. Marchetti, M. C. Uchida: *Training cadence: New insight into boxing training.* Medicine & Science in Sports & Exercise *43* (2011), Suppl No. 1, 946.

[6] H. Wang, W. Zai: *Design and analysis of digital sensor pulse width modulation control scheme of brushless DC motor drive.* Sensor Letters *13* (2015), No. 2, 138–142+5.

[7] E. M. Shakshuki, X. Xing, T. R. Sheltami: *Fault reconnaissance agent for sensor networks.* Mobile Information Systems *6* (2010), No. 3, 229–247.

[8] M. Hutter, P. Schwabe: *Multiprecision multiplication on AVR revisited.* Journal of Cryptographic Engineering *5* (2015), No. 3, 201–214.

Received May 7, 2017

Acta Technica *62* No. 3A/2017, 67–84

RFID positioning equipment of track-and-field athletes based on VIRE algorithm

Wei Li[1]

Abstract. With the rapid development of the Internet of things technology, radio frequency identification (RFID) technology has been applied more and more widely. In this paper, for faster and accurate position of track-and-field athletes in track test, we proposed a VIRE algorithm using quadratic interpolation. The improved VIRE algorithm has good positioning effect. In addition, we applied the algorithm to a timing system design scheme based on active RFID, to determine the end point timing, and according to the system error analysis, we obtained effective error accuracy.

Key words. Radio frequency identification technology, VIRE algorithm, timing system.

1. Introduction

The concept of the Internet of things (IOT) was proposed by the Massachusetts Institute of Technology Auto-ID research center (Auto-ID Labs) in 1999. Its original meaning referred to connect all the items through radio frequency identification (RFID) and other information sensing equipment with the Internet, to realize intelligent identification and management [1, 2]. In order to meet the needs of modern logistics industry, it is continuously developed and considered as the third wave of the world information industry after the computer and the Internet [3]. With the popularization and development of mobile Internet, cloud computing, big data and so on technologies, the Internet of things technology has been applied in the warehouse management, security management, logistics management and other fields, making people's life more convenient, automatic and intelligent. It is also the core of technical reform in China's educational reform to make educational examination reform by means of information technology [4]. In consequence, the Internet of things technology is also expected to become the core technology means to support the education strategy.

In the practical examination in sports, whether it is 100-meter track and 800-

[1]Huazhong Agricultural University, 430070, Wuhan, China; E-mail: dr_weiliweili@163.com

meter track, or shot game or three steps, are involved in a large number of outdoor positioning. These positioning can be personnel positioning, and also the test equipment positioning. This positioning is conducive to the management of the examination room, exercise time and so on. The RFID technology is a non-contact automatic equipment technology, having the characteristics of small volume, wide range of reading and writing, long service life, strong anti-interference ability and so on, and the applications of supporting fast reading, mobile identification, multi-target identification, and unique identification [5, 6]. Compared with GPS and other mature positioning technologies, RFID is more suitable for small local and low-cost positioning systems. At the same time, the active RFID labels, compared to passive label recognition, the distance is farther and the storage capacity is also greater. We can see that the research of positioning system based on active RFID helps realizing more real-time and accurate personnel management, object positioning and other functions in sports skill examination, so as to achieve fair and just sports skill examination, having great social significance in the selection of personnel.

2. Method

2.1. VIRE algorithm

It is assumed that the coordinate of virtual label is (p, q), and the coordinate of actual reference label is (a, b). RSSI value of the label of the coordinate (x, y) is defined as $S_k\left(T_{x,y}\right)$, and then RSSI of the label can be calculated using formulae.

$$S_k\left(T_{p,b}\right) = S_k\left(T_{a,b}\right) + p \times \frac{S_k\left(T_{a+n,b}\right) - S_k\left(T_{a,b}\right)}{n+1}, \tag{1}$$

$$S_k\left(T_{a,q}\right) = S_k\left(T_{a,b}\right) + p \times \frac{S_k\left(T_{a,b+n}\right) - S_k\left(T_{a,b}\right)}{n+1}. \tag{2}$$

The coordinates of the label to be measured are calculated by weight.In order to improve the accuracy of VIRE algorithm, two weighting factors are introduced, the weighting factors w_{1i} and w_{2i} being given as

$$w_{1i} = \sum_{k=1}^{k} \frac{\left|S_k\left(T_i\right) - S_k\left(R\right)\right|}{k \times S_k\left(T_i\right)}, \tag{3}$$

$$w_{2i} = \frac{p_i}{\sum_{i=1}^{n_a} p_i} = \frac{n_{ci}}{\sum_{i=1}^{n_a} n_{ci}}. \tag{4}$$

In the above equations, k represents the reader, $S_k\left(T_i\right)$ suggests the label RSSI value remained to be measured read by the reader k, and $S_k\left(R\right)$ refers to RSSI value of virtual reference label. As a result, w_{1i} indicates the relationship between the virtual reference label RSSI value and the actual label RSSI value to be measured; n_a is all the selected virtual reference label areas, and n_{ci} represents the selected virtual reference label continuous area (the area connected together in the grids).

In consequence, w_{2i} suggests the ratio of virtual label continuous area to the whole selected area. And the weight $w_i = w_{1i} \times w_{2i}$, and the coordinate of the final label to be measured can be calculated as

$$(x, y) = \sum_{i=1}^{n_a} w_i \left(x_i, y_i\right) . \tag{5}$$

Although the VIRE algorithm improves the positioning accuracy and does not improve the system equipment cost, there are also shortcomings: VIRE uses linear interpolation method, and in the actual environment, electromagnetic wave RSSI exists loss, and it is not proportional to the distance; secondly, two weighted factors introduced by VIRE algorithm will be affected by the threshold set by removing the wrong coordinate.

2.2. Improved VIRE algorithm

The improved algorithm is based on the deficiency of VIRE algorithm. VIRE algorithm adopts a linear interpolation method in the reference label, which has a large error in practice, because the actual distance loss of RSSI is nonlinear. To this end, this paper uses the nonlinear interpolation method - quadratic interpolation (parabolic interpolation).

First of all, we assume that the coordinate of virtual label is (p, q), and the label RSSI value of the coordinate (x, y) is defined as $S_k\left(T_{x,y}\right)$, then the label RSSI value can be calculated with the following steps.

Assuming that in the rectangular coordinate system, the coordinates of three actual reference labels with the same known vertical coordinate are (x_1, b), (x_2, b), and (x_3, b). Then RSSI values of the reference label are $S_k\left(T_{x_1,e}\right)$, $S_k\left(T_{x_2,e}\right)$, and $S_k\left(T_{x_3,e}\right)$. Construct parabolic equation $f(x) = ax^2 + bx + c$, then we can get the column equation groups:

$$\begin{cases} S_k\left(T_{x_1,e}\right) = ax_1^2 + bx_1 + c, \\ S_k\left(T_{x_2,e}\right) = ax_2^2 + bx_2 + c, \\ S_k\left(T_{x_3,e}\right) = ax_3^2 + bx_3 + c\,. \end{cases} \tag{6}$$

The overall relative error of the quadratic interpolation is less than that of linear interpolation, and the interpolation error is smaller near the actual reference label. In some places, there will be an error greater than linear interpolation error, but those places with greater errors is usually found to be the places where the RSSI attenuation is particularly severe, and the impact on the system positioning is smaller.

3. Results

3.1. System design

When the athletes start to run, there will a corresponding starting sensor or directional antenna to sense athletes starting, and record the starting time; when the athletes reach the end point, and enter the antenna range, it will be perceived by the system and recording the perception time, so as to calculate the time performance of athletes. But for this kind of timing systems, the antenna requires to provide directional function, so the antenna cost is too high, the deployment of the antenna is more complicated, and the antenna is vulnerable to damage. In this paper, a RFID timing system for track-and-field athletes based on VIRE algorithm is proposed. The system does not need to deploy the array antenna. The system structure of the timing system is shown in Fig. 1. The whole system is divided into five modules: data storage module, positioning algorithm module, configuration management module and device communication module, and application API interface module.

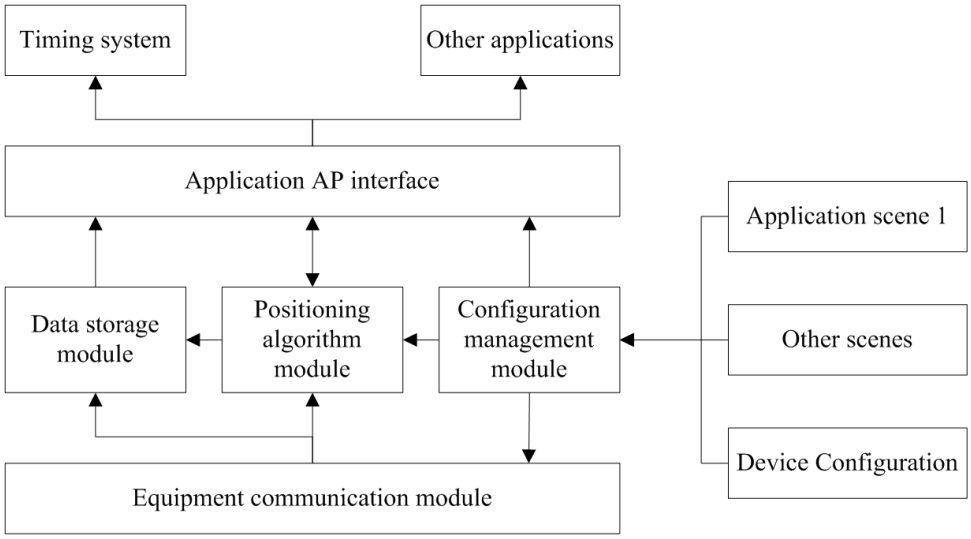

Fig. 1. Structure of timing system

3.2. Determination of the terminal point

How to determine the time at which the player is at the finish line is what a system needs to consider. When the athletes will arrive at the end point and enter the reader reading and writing range, according to the transmitting frequency of active RFID label signal, the system will continuously record a plurality of time and location information of the active RFID label into the scope of the reader, until the label leaves the read range of the reader, or when the reader collects enough reading and writing times and does not need to read any more.

As shown in Fig. 2, assuming that the t-moment label location is the solid point $P\,(x, y)$. In the following coordinate system, the distance d from the label to Y axis (the end line) is $|x|$, and the dotted line is the possible position locus of the label. In the process of athletes running to the destination, the location P of athletes will correspond to a moment t. While what the timing system requires is the moment of athletes at the terminal line, namely the moment of $d = 0$ (horizontal coordinate of P is 0).

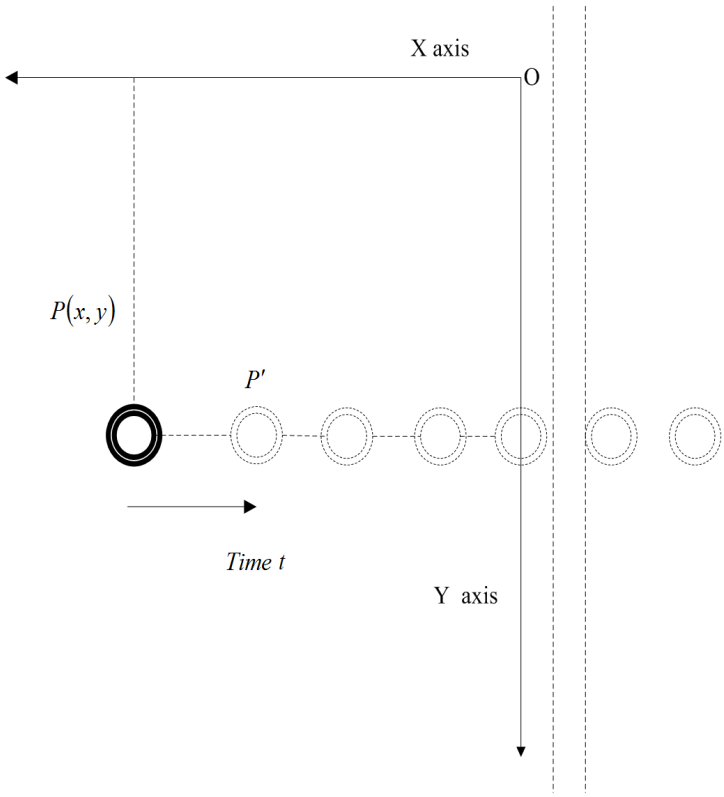

Fig. 2. Locations of athletes

From the above analysis, there is a certain functional relation between the label position P and distance $d\,(|x|)$ of the end line and the time t, and the continuity is maintained. Through the reader, although we can collect some points on the curve function, because the process of athletes before running to the end point is not a uniform motion (deceleration process), it is difficult to get a clear function equation. The approximate function curve is shown in Fig. 3. Symbol Δt is the emission time interval of the label (the reciprocal of the transmitting frequency).

For determining the time t of $d = 0$, in allusion to different cases, adopt the following methods:

The closet distance threshold $d_{\min}$ was selected, and in the position and time data read by the reader, choose the one whose distance is less than or equal to the

set threshold $d_{\min}$ and the one with the minimum distance, then the time that the distance corresponds to is the time for the label to arrive at the terminal point; in this way, because the time for athletes carrying labels to enter the reader reading range is not fixed, it may occur the situation that it does not exist points less than the threshold. In view of this situation, the second method is proposed.

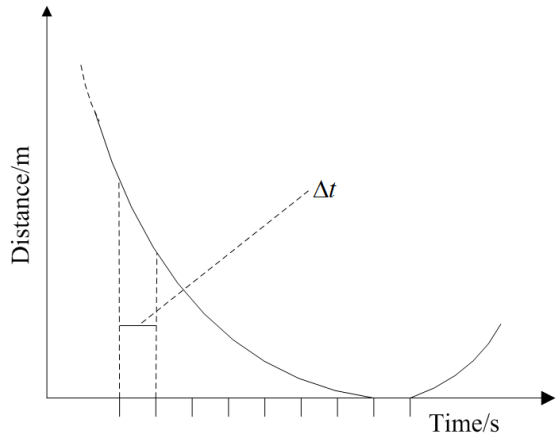

Fig. 3. Function relationship between distance and time

3.3. Theoretical error analysis

VIRE algorithm in the environment of 3 m × 3 m, when the label is divided into the grid 30 × 30, at the same time, the environment of the algorithm is bad, and in the case of severe impact on positioning accuracy, the average error of the VIRE algorithm is about 0.5 m. As a result, we assume that the positioning error E after using the algorithm is 0.5 m, then E is the distance between the actual location of the label and the measured position of the system. Theoretical error analysis is shown in Fig. 4.

In the above figure, the center is the actual position, and the error is taken as the radius to make a circle, the error distributed in it. It can be seen that the point with the maximum distance to the actual position error is in a circle, the closer to the center, the closer to the actual position distance, but this is not our focus for analysis. The key point is the vertical distance from the error point to the terminal line. As can be seen from the figure, the two blue ends of the circle are perpendicular to the terminal line. The distance to the terminal line is equal to the radius, which is the maximum.

4. Conclusion

According to the shortcomings of great actual error of VIRE algorithm using linear interpolation to calculate the virtual label RSSI value, we used nonlinear

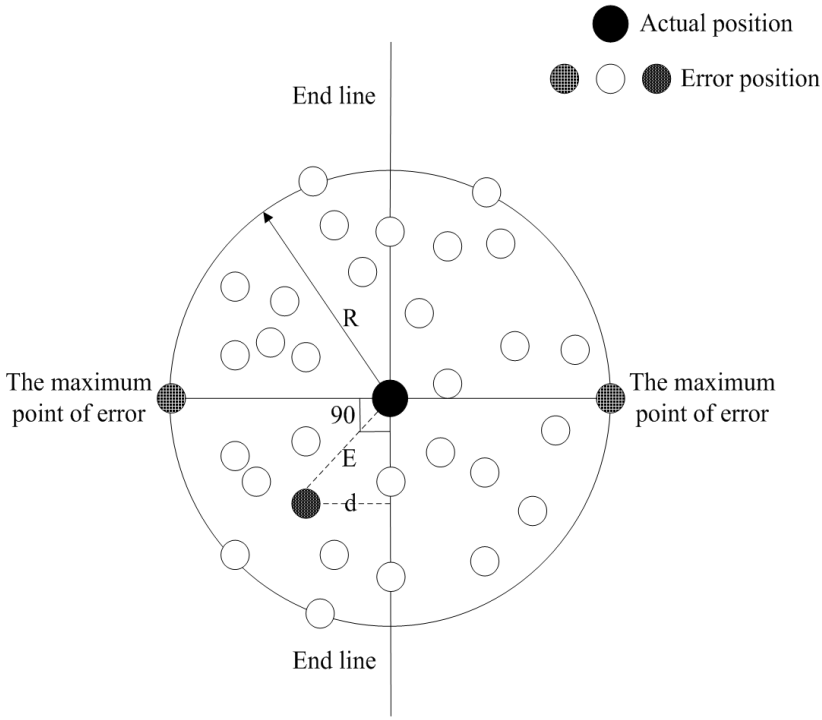

Fig. 4. Timing system error analysis

quadratic interpolation VIRE positioning algorithm, to helpto improve the accuracy of positioning, and combined with active RFID positioning technology, apply it to track-and-field athletes track timing system. First of all, we introduced the general structure of the timing system, then determined the timing method of the final position by the positioning algorithm, and finally gave the theoretical error analysis of the system. At last, the timing precision can reach 0.065 up to 0.09 seconds, suitable for 100-meter race with timing accuracy of 0.01 s.

References

[1] D. Miorandi, S. Sicari, F. De Pellegrini, I. Chlamtac: *Internet of things: Vision, applications and research challenges.* Ad Hoc Networks *10* (2012), No. 7, 1497–1516.

[2] C. S. Wang, L. P. Hung, N. Y. Yen: *Using RFID positioning technology to construct an automatic rehabilitation scheduling mechanism.* Journal of Medical Systems *40* (2016), No. 1, 4.

[3] Y. T. Liao, T. L. Chen, T. S. Chen, Z. H. Zhong, J. H. Hwang: *The application of RFID to healthcare management of nursing house.* Wireless Personal Communications *91* (2016), No. 3, 1237–1257.

[4] N. B. Aldin, E. Erçelebi, M. Aykaç: *Advanced boundary virtual reference algo-*

rithm for an indoor system using an active RFID interrogator and transponder. Journal Analog Integrated Circuits and Signal Processing *88* (2016), No. 3, 415–430.

[5] E. Miyamoto-Mikami, H. Murakami, H. Tsuchie, H. Takahashi, N. Ohiwa, M. Miyachi, N. Fuku: *Lack of association between genotype score and sprint/power performance in the Japanese population*. Journal of Science and Medicine in Sport *20* (2017), No. 1, 98–103.

[6] C. M. Roberts: *Radio frequency identification (RFID)*. Computers & Security *25* (2006), No. 1, 18–26.

Received May 7, 2017

Acta Technica *62* No. 3A/2017, 75–84

Flexible force sensor for data extraction and dynamic identification of calisthenics' footprint

Zhenzhen Bie[1,2], Minchao Shou[1]

Abstract. Gait tactile information includes footprint information and dynamic plantar pressure distribution, which is mainly used in fields such as gait identification, sports science and gait analysis. A flexible force sensor-based method for footprint data extraction and dynamic identification was put forwarded, which was mainly made up of data filtering for plantar pressure, cluster segmentation for single step footprint pressure and dynamic single step footprint identification. Among them, connected domain-based image segmentation method was used to clustering analyze plantar pressure data and single step footprint was identified according to foot anatomy principle. Research results have verified that when walk normally, accuracy rate of data extraction algorithm for single step footprint put forwarded was up to 99 % and recognition rate of dynamic identification method was up to 97 %. Besides, accuracy rate of the algorithm studied for single step footprint extraction of calisthenics was up to 95 %, which was with good robustness.

Key words. Flexible force sensor, calisthenics, footprint data extraction, dynamic identification, cluster analysis.

1. Introduction

With the development of science and technology, method for obtaining plantar pressure information have been developed from footprinting to pressure sensing measurement which used flexible force sensor. Flexible force sensor in large scale can obtain static and dynamic state of plantar pressure, thus no specific steps were needed and walk freely was enough [1]. Plantar pressure data obtained by flexible force sensor was more accurate and practical.

[1]Tongji University, Shanghai, 200092, China
[2]Corresponding author; E-mail: zhenzhenbie1011@126.com

2. Literature review

Nowadays, flexible force sensor in large scale was used by researchers at home and abroad to obtain static and dynamic plantar pressure data in order to study gait. Flexible force sensor in large scale was used by Yi Xia et al. [2] to study characteristics such as feet Cop track. However, this method was only suitable for identifying footprint of normal walk and not suitable for identifying footprint of dance gait. Pressure measuring insole was used by Christian C. B. Redd et al. [3] to collecting plantar pressure data of feet, with which footprint extraction and dynamic identification was not needed because relevant label has already marked on the hardware of pressure measuring insole. Thus, it processed data rapidly and was free from site limitation.

There were many advantages of collecting plantar pressure data with flexible force sensor in large scale, for example [4] it can collect plantar pressure data of each step of movement and compute time parameter and spatial parameter of gait. Difficulty of this technology was how to process the acquired plantar pressure data. Footprint extraction and dynamic identification of plantar pressure data collected by flexible force sensor in large scale was indispensable. A flexible force sensor-based method for footprint extraction and dynamic identification was put forwarded to tackle above problems, such as limited application fields.

3. Research method

3.1. Platform construction

Platform for obtaining plantar pressure data was designed based on up-to-date data acquisition and control technology. STM 32F single chip was core of hardware acquisition circuit for flexible force sensor, which was mainly responsible for driving linear array canning, controlling sample of analog-digital converter (ADC) and compressing plantar pressure data transmission. Sampling frequency of flexible force sensor was up to 100 Hz. And Ethernet bus mode was adopted to transmit plantar pressure data of lower computer and CMD command of upper computer because a large volume of data was to be transmitted.

Module splicing was adopted to design rectangle platform with length and width measured 8×8 for acquiring plantar pressure data. This rectangle platform was made up of sensor modules of an area of $80\times80\,\mathrm{cm}^2$ on which there were 140×140 pressure sensitive spots in length and width. Every module was an independent sub-system. Data were transmitted through network (Gigabit Switch) to remote PC for processing.

Software for acquiring and analyzing plantar pressure data with flexible force sensor in large scale was designed based on Visual Studio10 development platform. In actual testing, a large volume of data was collected by flexible force sensor. Besides, good real time performance was needed for transmitting, processing and displaying data. Thus, multithread programming was used to program software.

3.2. Method for footprint extraction and dynamic identification

It can resolve (see Fig. 1) plantar pressure data when acquiring it. Mainly, there were 3 steps: filtering plantar pressure data, extracting single step footprint and dynamic identifying single step track. After those steps, plantar pressure data of every step was obtained and parameters such as time, space, movement and dynamics were calculated.

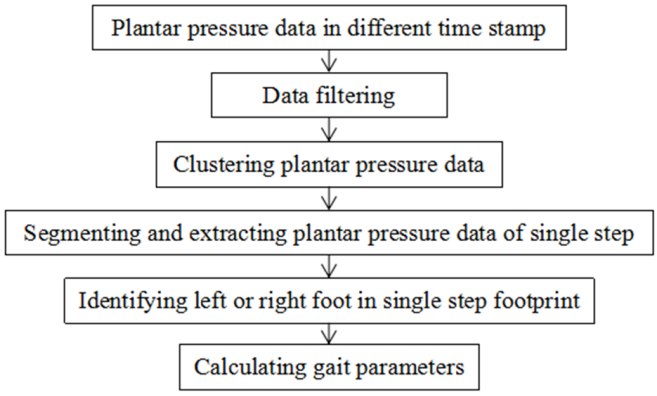

Fig. 1. Resolving steps for plantar pressure data

3.2.1. Filtering plantar pressure data: There was noise jamming during plantar pressure data-acquiring process, which was shown as data noise [5]. Before resolving plantar pressure data, those noises should be filtered out in order to reduce its influence on plantar pressure data. Pressure values on flexible force sensors were classified into 256 grades in order to corresponding it to RGB values. The larger pressure on sensor, the darker color displayed. On the contrary, the smaller pressure on sensor, the lighter color displayed.

Spatial domain filtering, transform domain filtering and morphology noise method were common methods for image denoising. Among them, spatial domain filtering was directly used on original images to tackle gray value of pixel, which included linear filtering, nonlinear filtering, mean filtering, improved mean filtering (MTM), median filtering, and improved median filtering (IMF). Based on MTM algorithm and IMF algorithm, time window [6] conception was introduced to put forward a new filtering algorithm. Principle of the new filtering algorithm was: isolated noise should be deleted using pre-and post-pressure data and IMF filtering algorithm was used to filter the remained plantar pressure data. Flow chart of this algorithm was shown in Fig. 2.

This algorithm was used in filtering experiment for plantar pressure data, and signal noise ratio (SNR) of image [7] was adopted to prove its filtering performance. Thus,

$$\mathrm{SNR} = 10\lg \frac{\sum_t \sum_{\mathrm{row}} \sum_{\mathrm{col}} (\mathrm{Image}_{\mathrm{output}} - \mathrm{Image}_{\mathrm{original}})^2}{\sum_t \sum_{\mathrm{row}} \sum_{\mathrm{col}} (\mathrm{Image}_{\mathrm{addnoise}} - \mathrm{Image}_{\mathrm{original}})^2}\,. \tag{1}$$

In this equation, $\text{Image}_{\text{output}}$ denotes output image after filtering, $\text{Image}_{\text{original}}$ denotes original noise-free image, and $\text{Image}_{\text{addnoise}}$ denotes artificial noise added-image.

Percentage p of impulse noise and Gaussian noise whose standard derivation was σ and mean value was 0 were added to each image. Image SNR was calculated by MTM, IMF and the proposed algorithm and the results are shown in Table 1.

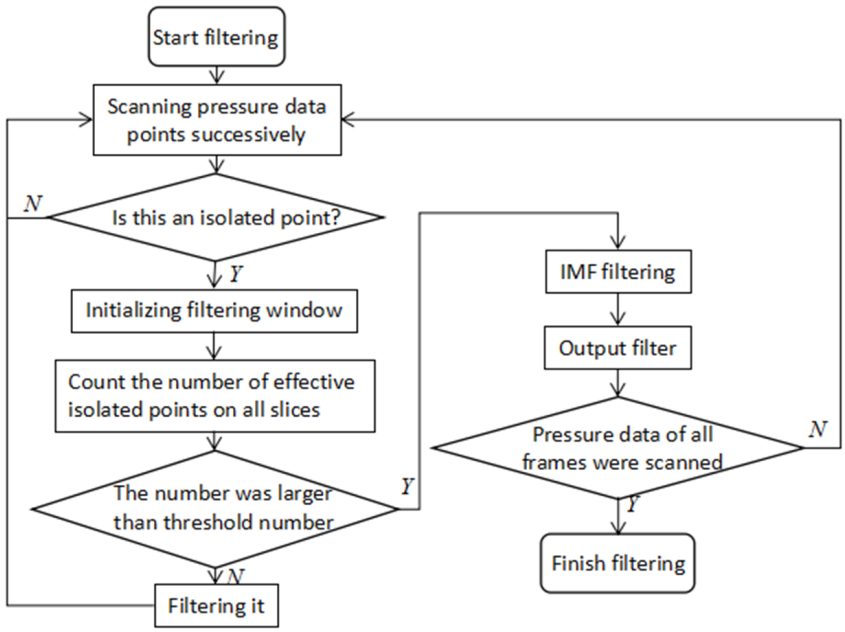

Fig. 2. Flow chart of filtering

Table 1. Denoising effect comparison

Algorithm	MTM	IMF	The algorithm proposed
SNR (dB), $p = 3$, $\sigma = 4$	–8.66	–9.21	–11.82
SNR (dB), $p = 4$, $\sigma = 8$	–9.97	–11.12	–12.51

It can be seen from Table 1 that SNR value of algorithm added with time window was lower than other algorithms, which verified that this algorithm could eliminate noise effectively, save useful data well and avoid useful data be filtered by mistake to some degree.

3.2.2. Data extraction of single step footprint: Plantar pressure data was widely used in fields such as gait analysis and sports science. The key for apply plantar pressure data was extracting gait data accurately. Thus, clustering algorithm was used to extract pressure data of single step footprint. Human normal walk was regular in the aspects of step speed, step length and step width. Plantar pressure

data was clustering segmented based on this rule.

Condition 1: In normal walk, step length and step length was changing within a reasonable range;

Condition 2: Feet length and width of normal people was within a reasonable range;

Condition 3: In normal walk, data frame of the same footprint should be within a reasonable range.

Flow chart of segmentation for plantar pressure data is shown as Fig. 3:

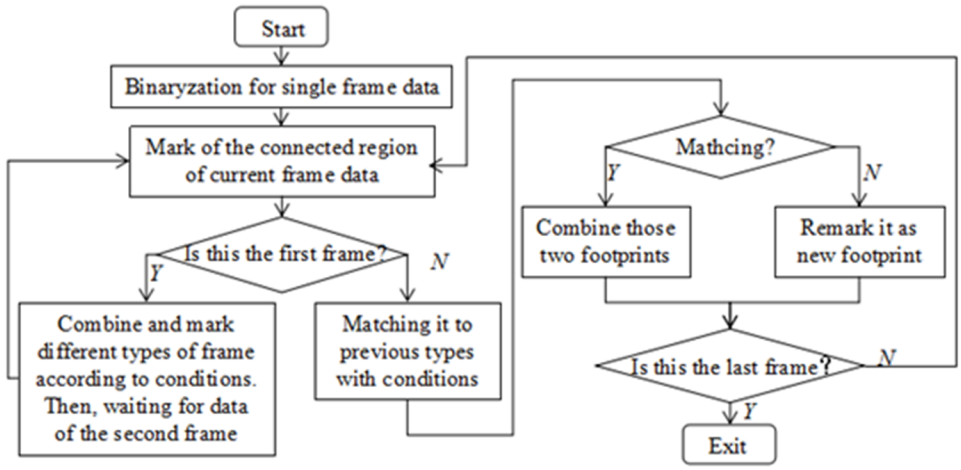

Fig. 3. Flow chart for data clustering

3.2.3. Dynamic identification method for single step footprint: A dynamic footprint identification algorithm based on plantar pressure and footprint outline was put forwarded. The identification steps were shown as follows:

1. Bilinear interpolation algorithm was used to enlarge the original image and median filtering it.

2. Convex hull was used to identify the minimum enclosing rectangle for images in step 1. Included angle of horizontal and vertical direction of footprint was calculated.

3. Image obtained in the step 2 was rotated according to nearest neighbor interpolation, and the long axis was the rotation axis.

4. Morphological processing was applied to the obtained image, which mainly including dilation or erosion action. Then, smoothing filtering was applied.

5. Edge of image obtained in step 4 was extracted with Canny edge detecting algorithm. Convex hull algorithm was reused to calculate the minimum outside envelope rectangle frame.

6. Outside envelope rectangle frame in step 5 was scanned along the direction of long axis. Footprint width in the short-axis and upper and lower boundary points in the vertical direction was recorded. Quartic polynomial data filtering was applied. Besides, regard the upper boundary of the minimum outside envelope as benchmark to record the pixel distance between upper and lower boundary of footprint and the

upper boundary of the minimum outside envelope rectangle frame.

7. In order to highlight crest and trough of fitted curve, range of horizontal axis and vertical axis was compressed to footprint size-long and width.

8. Left or right foot was identified because there were extreme values in footprint width curve and curve of footprint upper and lower points.

Given f_{w}, f_{u} and f_{d} denoting feet width curve, coordinates curve of upper boundary points and coordinates curve of lower boundary points. Local search method was used to solve distribution of extreme value of f_{w}, f_{u} and f_{d}. Given horizontal and vertical coordinates x and y satisfying $y = f(x)$. Steps for searching the extreme points are as follows:

1. $f(x)$ should be calculated from $x = 0$. $f(x + \Delta x)$ should be calculated with step length $\Delta x = 0.02$. Then, curve tendency can be judged.

2. Values of $f(x)$ and $f(x)+\Delta x$ are compared and then $x = x+\Delta x$. If the curve tendency was the same as that of step 1, repeat step 2. If the curve tendency is different from that of step 1, it means there is an extreme point. Record the number of extreme points and their values. Then, $f(x)$ is to express (no accurate value is needed as long as it is near the extreme points) and repeat step 2 until $f(x) = 0$.

3. As for curve f_{w}, the first maximum value f_1 and the second maximum value f_2 should be compared. If $f_1 < f_2$, it means the widest place of footprint is at right. In another word, tiptoe is toward right. If the inequality is opposite, the tiptoe is toward left.

As for curves f_{u} and f_{d}, the number of extreme points should be counted. If the number is 3, it means that there is a great fluctuation in this boundary and it is at the side of medial longitudinal arch. If the number is 1, it is at the side of lateral longitudinal arch. Footprint is identified as long as there is information about the footprint direction and the number of extreme points. The specific computing method is as follows

$$\mathrm{Right} = \begin{cases} f_1 < f_2 \&\& N_{\mathrm{u}} = 3 \&\& N_{\mathrm{d}} = 1, \\ f_1 > f_2 \&\& N_{\mathrm{u}} = 1 \&\& N_{\mathrm{d}} = 3, \end{cases} \tag{2}$$

$$\mathrm{Left} = \begin{cases} f_1 < f_2 \&\& N_{\mathrm{u}} = 1 \&\& N_{\mathrm{d}} = 3 \\ f_1 > f_2 \&\& N_{\mathrm{u}} = 3 \&\& N_{\mathrm{d}} = 1, \end{cases} \tag{3}$$

where N_{u} represents the number of the extreme points on the upper boundary, and N_{d} represents the number of the extreme points of the lower boundary.

4. Experiment and result analysis

4.1. Verification test for extraction accuracy of single step footprint data

Mainly, starting and ending time of single step footprint and coordinates range of single step footprint indicated accuracy single step footprint parameter. Thus, footprint data segmentation experiment for normal walk and calisthenics was designed, and this experiment was divided into normal walk group and calisthenics group.

A line (or list) was randomly chosen on field, on which several rectangle blocks larger than footprint were marked. Besides, distances between rectangle blocks were close to that of step length and step width. The whole test procedure was filmed by vidicon. It was difficult to extract single step footprint data of calisthenics because it was featuring strong rhythm and fast movements. Threshold value for clustering was altered and adjusted correspondingly before extract calisthenics' footprint because there were great different between calisthenics and normal walk. Testing time for calisthenics group was 46 s (a 5 s prelude was included). Testers of normal walk group should step on the rectangle blocks in turn during the test. After acquisition, camera was used to extract, record, and analyze differences between landing time and off-ground time and those filmed by vidicon. In order to further verify the accuracy of the starting and ending time of footprint after partitioning, clustering segmentation algorithm for single step footprint data was used to calculate the starting and ending time of all footprint sequence. The calculated starting and ending times were compared to that of footprint in the video. Then, the frame number of incorrect segmentation was counted and accuracy rate of clustering algorithm was calculated (see Table 2). Footprint segmentation data of normal walk group is shown in Table 3.

Table 2. Footprint segmentation results

Groups	Time	Sampling frame number	Frame number of incorrect segmentation	Accuracy rate
Normal walk group	3 min	18000	96	99.47 %
	5 min	30000	143	99.52 %
Calisthenics group	41 s	4100	162	96.05 %
		4100	168	95.90 %
		4100	170	95.76 %

It is seen from Table 2 that the largest error between footprint range calculated by clustering segmentation for single step footprint data and the pre-planned footprint range was 2 cm, which was within reasonable limits. It also can be seen from Table 2 that in the 3min- and 5min- test for normal walk group, correct system segmentation rate of was up to 99 %. Compared with normal walk group, accuracy rate of footprint data extraction of calisthenics group was relatively lower. Analysis showed that error rate of each step was 1–2 frames because of fast movements of calisthenics. Compared with mean frame number of single step, this error was within the acceptable range because mean frame numbers of each step was 43. It was verified that the put forwarded clustering segmentation algorithm for single step footprint data can identify the starting time, ending time and coordinate range of each step accurately. Plantar dynamics- and connected area-based branching algorithm was suitable for extracting footprint data of normal gait.

Table 3. Footprint segmentation data of normal walk group

Step number	Planned footprint location $(x, y), (x, y)$	Location calculated by system $(x, y), (x, y)$	Starting and ending time of video (ms)	Starting and ending time of system calculation (ms)
1	(10,10),(20,35)	(11,9),(19,36)	1100,2200	1110,2220
2	(45,75),(55,100)	(46,74),(56,99)	2110,2800	2100,2810
3	(15,130),(25,155)	(15,132),(23,157)	2660,3340	2680,3350
4	(45,165),(55,180)	(45,164),(53,188)	3240,3840	3250,3850
5	(15,215),(25,240)	(16,216),(23,243)	3720,4360	3730,4370
6	(40,265),(50,295)	(42,272),(48,298)	4250,4930	4260,4930
7	(15,315),(25,340)	(13,317),(23,343)	4780,5480	4770,5480

It can be seen from Table 2 that the largest error between footprint range calculated by clustering segmentation for single step footprint data and the pre-planned footprint range was 2 cm, which is within reasonable limits. It also can be seen that in the 3 min- and 5 min- test for normal walk group, correct system segmentation rate of was up to 99 %. Compared with normal walk group, accuracy rate of footprint data extraction of calisthenics group was relatively lower. Analysis showed that error rate of each step was 1–2 frames because of fast movements of calisthenics. Compared with mean frame number of single step, this error was within the acceptable range because mean frame numbers of each step was 43. It was verified that the put forwarded clustering segmentation algorithm for single step footprint data can identify the starting time, ending time and coordinate range of each step accurately. Plantar dynamics- and connected area-based branching algorithm was suitable for extracting footprint data of normal gait.

4.2. Verification experiment for dynamic identifying speed of single step footprint

Relevant speed experiments such as fast walk, slow walk, normal walk and walk with variable speed were designed to verify accuracy rate of algorithm for identifying left or right foot. 19 people, walk normally, ranging from 19 to 24 years old were involved in this experiment. All testers were required to walk normally, walk slowly, walk fast and walk in random direction, pose and speed in turn on plantar pressure data acquiring platform. In order to validate the data, this experiment was repeated 4 times. Below it can be found the evaluation criterion.

$$\mathrm{WR}_{(i,j)} = \frac{\mathrm{TR}_{(i,j)}}{\mathrm{FL}_{(i,j)} + \mathrm{TR}_{(i,j)}}\,, \tag{4}$$

$$\mathrm{WL}_{(i,j)} = \frac{\mathrm{TL}_{(i,j)}}{\mathrm{FR}_{(i,j)} + \mathrm{TL}_{(i,j)}}\,, \tag{5}$$

$$\mathrm{W}_{(i,j)} = \frac{\mathrm{TR}_{(i,j)} + \mathrm{TL}_{(i,j)}}{\mathrm{FL}_{(i,j)} + \mathrm{FR}_{(i,j)} + \mathrm{TL}_{(i,j)} + \mathrm{TR}_{(i,j)}}\,. \tag{6}$$

In this equation, $\mathrm{WL}_{(i,j)}$ and $\mathrm{WR}_{(i,j)}$ denote accurate rate of identifying left or right foot when sample i was walking along the jth way. $\mathrm{W}_{(i,j)}$ denotes accurate rate of identifying left or right foot when sample i is walking in the jth way. $\mathrm{TL}_{(i,j)}$ and $\mathrm{TR}_{(i,j)}$ denote correct times of identifying left or right feet, respectively, when sample i is walking along the jth way. Symbols $\mathrm{FL}_{(i,j)}$ and $\mathrm{FR}_{(i,j)}$ denote incorrect times of identifying left or right feet when sample i was walking along the jth way.

As $\mathrm{WL}_j = \frac{1}{N}\sum_1^N AL_{(i,j)}$ and $\mathrm{WR}_j = \frac{1}{N}\sum_1^N WR_{(i,j)}$ are the identification rates for left or right feet when walking along the jth way, $\mathrm{W}_j = \frac{1}{N}\sum_1^N W_{(i,j)}$ denotes mean identification rate of left and right feet when walking along j way. Data acquired when those 19 testers walking according to above process are shown in Table 4.

Table 4. Footprint identification rate

Walking manner	1	2	3	4
AR_j	0.980	0.987	0.975	0.963
AL_j	0.987	0.992	0.975	0.962
A_j	0.983	0.989	0.975	0.963

It can be know from Table 4 that left foot identification rate, right foot identification rate and mean identification rate of left and right foot was relatively high when walking along the first 3 ways. However, when walking along the 4th way, identification rate of left and right foot was relatively lower than that of others walking ways. The reason was that when walking along the 4th way, heel of the testers would sometime off-ground which would influence identification accuracy rate.

Gait characteristic parameters of single step data such as landing time, off-ground time and footprint area were calculated by segmenting, extracting and identifying single step plantar pressure data. Parts of footprint sequence-relevant parameters that calculated with researched method were shown in Table 5.

The study results showed that the researched method featuring high efficiency, high intelligentization and well robustness, identified left and right foot and data fast and accurately.

5. Conclusion

Data about acquiring and applying plantar pressure distribution were analyzed based on flexible force sensor. Besides, plantar pressure data segmentation and

dynamic footprint identification method was put forwarded, through which data of left and right feet were accurately segmented and identified and gait analysis and evaluation were more convenient. Further improvement was needed for the researched clustering analysis algorithm and method for identifying left and right feet, such as improved footprint identification rate and clustering conditions.

Table 5. Part of relevant parameters of each step in footprint sequence

Steps	Left/right foot	Landing time (ms)	Off-ground time (ms)	Footprint area (cm^2)	Hang time (s)	average pressure value of single frame (N)
1	Left	770	1650	145	0	604.5
2	Right	1510	2170	150	0	574.8
3	Left	2080	2710	148	0.42	576.1
4	Right	2700	3210	154	0.42	557.9
5	Left	3050	3720	148	0.37	612.1
6	Right	3590	4210	146	0.38	580.2
7	Left	4090	4800	150	0.35	596.2
8	Right	4580	5180	149	0.36	587.0

References

[1] C. H. Chuang, Y. R. Liou, M. Y. Shieh: *Flexible tactile sensor array for foot pressure mapping system in a biped robot.* Smart Structures and Systems *9* (2012), No. 6, 535–547.

[2] Y. Xia, Z. M. Yao, X. J. Yang, S. Q. Xu, X. Zhou, Y. N. Sun: *A footprint tracking method for gait analysis.* Biomedical Engineering: Applications, Basis and Communications *26* (2014), No. 01, 1450011.

[3] C. B. Redd, S. J. M. Bamberg: *A wireless sensory feedback device for real-time gait feedback and training.* IEEE/ASME Transactions on Mechatronics *17* (2012), No. 3, 425–433.

[4] L. K. Fong, K. F. Lee, C. Y. Li: *Analysis of the flexible PDMS capacitive microsensor for the 3-axis force measurement.* Micro and Nanosystems *4* (2012), No. 3, 208–213.

[5] B. Khorsandi, L. Mydlarski, S. Gaskin: *Noise in turbulence measurements using acoustic doppler velocimetry.* Journal of Hydraulic Engineering *138* (2012), No. 10, 829–838.

[6] S. Chacko, J. Jayakumar: *Directional Gaussian filter with variable filtering strength and variable window size for deblocking digital images.* International Journal of Information and Communication Technology *7* (2015), Nos. 4–5, 425–436.

[7] L. I. Weia, S. Zhang: *An improved thresholding segmentation algorithm of ball grid array X-ray digital image.* Acta Photonica Sinica *40* (2011), No. 7, 1046–1050.

Received May 7, 2017

Acta Technica *62* No. 3A/2017, 85–94

Application of EMG fatigue detection algorithm in portable DSP system

Jianyun Han[1]

Abstract. Surface muscle fatigue detection is widely used in many fields, such as kinematics, rehabilitation medicine and muscle damage diagnosis. Muscle fatigue testing can provide reliable analysis data to determine the state of human muscle, so as to provide an effective analytical method for rehabilitation assessment, physical exercise and intelligent analysis. Surface electromyography has the advantage of being noninvasive, objective and convenient, so it has become a reliable tool for people to study surface electromyography. In the full understanding of the state of muscle fatigue, people can effectively avoid the damage caused by muscle fatigue. In this paper, the real time TMS320C6748 DSP was used instead of Matlab to collect and analyze the surface electromyography (SEMG), so as to realize the real-time detection of electromyogram (EMG) parameters. We use the frequency domain feature extraction method to analyze the muscle fatigue, and study the effectiveness of the EMG fatigue analysis. It is concluded that the TMS320C6748 floating point DSP can be used as a monitoring device, which can monitor the muscle fatigue status of the athletes and some patients who need to restore muscle strength.

Key words. Muscle fatigue testing, DSP, real-time detection.

1. Introduction

In recent years, with the deep research of electromyogram (EMG) acquisition and processing methods, the real-time requirement of EMG acquisition system is getting higher and higher. The real-time equipment can effectively capture the changes in EMG signals, so as to achieve real-time monitoring of the state of the human muscle, and to understand the state of their muscles. In the process of exercise, some muscle fatigue can be perceived from the body's own muscle discomfort, and some muscle fatigue cannot be perceived. In the absence of awareness, excessive exercise can lead to muscle strain or other body damage [1]. Therefore, it is necessary to monitor the EMG in real time. In addition, some of the hemiplegia patients such as stroke, they need to do the right body movement to promote muscle activity, and the normal movement of the upper limb for a person's rehabilitation is particularly important

[1]Zhengzhou Institute of Technology, Zhengzhou, Henan, 450000, China; E-mail: hanjianyun_edu@163.com

[2].

Therefore, the scientific development of rehabilitation programs and real-time monitoring of patients with muscle status can effectively promote its muscle recovery. And for some athletes, if they can plan a good training program, and real-time understanding of the state of their muscles, they can not only make each piece of muscle have been trained, but also can effectively avoid the excessive training caused by muscle strain and other conditions [3]. In this paper, we use the advantage of the floating point DSP processor TMS320C6748 which can do high-precision floating-point operation, and design the algorithm on DSP to process the data collected by EMG and compare with the MPF value obtained by Matlab. Take the place of Matlab to do algorithm processing in a certain range, and analyze the fatigue state of the electromyogram, which can make people understand their own muscle state, so as to make a scientific exercise program according to their own characteristics.

2. Acquisition and algorithm design of face trial EMUs

2.1. Surface EMG signal acquisition

Surface electromyrography (SEMG) signal is a kind of weak and non-stationary bioelectrical signal, and its effective range is concentrated at 20 Hz∼500 Hz [4], and it is collected by Ag-AgCl electrode. Before the experiment, use alcohol to clean the collection site, remove the surface dead skin and oil, and apply the conductive paste evenly to cover the contact surface.

The placement of the electromyor electrode is divided into two kinds of reference electrode placement and test electrode placement. The placement of the reference electrode is mainly to exclude the non-human self-generated voltage, and it can be placed in the body surface of the bony mark or placed in the test muscle that does not participate in muscle tendon. In the test, the reference electrode cannot collect the electric signal of autonomous motion. In this experiment, we use the wrist as the reference electrode. The test electrodes are placed parallel to the direction of the muscle fibers. In this experiment, we have to collect extensor communis digitorum, musculus biceps brachii and musculi extensor carpi radialis longus.

2.2. Feature extraction of surface electromyography

The method of surface electromyography is divided into time domain method, frequency domain method and time domain combined method [5]. The commonly used time domain analysis method includes measuring integral myoelectric value (iEMG), zero crossing point (zc), variance (VAR), etc. [6].

Time domain method is very simple to extract features of SEMG, but with the change of muscle contraction force, a lot of time domain parameters change greatly. However, after the Fourier transform in frequency domain, the change of the waveform is very small, so it has good stability in frequency domain. The commonly used frequency domain analysis method includes the mean power frequency (MPF) and

the median frequency (MF) of the SEMG power spectrum, which are defined as

$$\mathrm{MPF} = \frac{\int_0^{+\infty} f \cdot P(f)\,\mathrm{d}f}{\int_0^{+\infty} P(f)\,\mathrm{d}f}\,. \tag{1}$$

In this equation, $P(f)$ is the power spectral density function of the signal.

The median frequency can be solved by equation

$$\int_0^{\mathrm{MF}} P(f)\,\mathrm{d}f = \int_{\mathrm{MF}}^{+\infty} P(f)\,\mathrm{d}f = \frac{1}{2}\int_0^{+\infty} P(f)\,\mathrm{d}f\,. \tag{2}$$

The time frequency domain analysis method can combine the time domain and frequency domain analysis methods, and the time-frequency domain analysis method applied to SEMG mainly includes short-time Fourier transform, Wigner-Ville distribution, Choi-Williams distribution, wavelet transform and so on [7].

Compare the three kinds of analysis methods, the time-frequency joint analysis method has the unique advantages in the SEMG analysis, which can reflect the information of the time domain and the frequency domain [2]. However, for surface EMG analysis, MPF and MF in the frequency domain have been able to well reflect the difference between normal and fatigue in the muscle, and many studies have shown that the average power frequency is more sensitive in reflecting muscle activity and functional status. Therefore, this paper uses frequency domain analysis method to obtain MPF values and perform algorithm implementation.

3. Algorithm implementation

3.1. Algorithm implementation method

Algorithmic implementation usually has two methods: direct implementation and indirect implementation. The direct implementation methods usually need to consider the following questions:

1. DSP system processing capacity.
2. The support of the storage space and the corresponding library
3. Keyword matching and other issues.

And then through the DSP to program the algorithm needs to implement, so that it is consistent with the results before and after implementing the error within the allowable range. The specific steps of direct implementation are:

1. We have a more comprehensive understanding of the implemented algorithm, so as to ensure that its Matlab, VC platform or other platforms have been able to operate, and the results are accurate.

2. We have a comprehensive assessment of the degree of difficulty of the implemented algorithm and estimate the possible problems.

3. Compare the results of the program before and after implementation, so as to ensure that the results of the program before and after implementation error within the allowable range, and carry out program optimization for the parts that do not

meet the requirements.

4. In the premise of not affecting the accuracy of the program, we strive that it works in real time and is efficient.

The indirect implementation is a method that can be simplified by Matlab to simplify the programmer's algorithm,and it requires users to install the full version of Matlab or install components in the installation of Matlab Coder components. The specific steps are as follows: First, the algorithm needs to be implemented into function. Second, call it in the command window. After the test is successful, use the Matlab Coder component to write the M file into a C language source file that can be called by the DSP. Finally, open CCS, copy the Matlab build file to the CCS project directory, add the reference path to the header file, and write the calling program. This method can reduce the difficulty of programming, but not all of the function can be converted into the target source file through this method, because some functions do not correspond to the C language library, so it needs to be further improved.

Based on the two methods of implementation, the second method is simple, but there is no C language function library corresponding to this article. In this paper, the algorithm is implemented to Matlab to DSP hardware platform, and the purpose of this paper is to get rid of the upper computer and improve the real-time requirement of signal processing. The TMS320C6748 floating point DSP has the advantages of high processing accuracy and good real-time performance, and it has little effect on the results of the collected surface EMG signal processing, so it is more practical to choose direct implementation.

3.2. DSP algorithm implementation

For the surface of the EMG signal fatigue analysis, we need to carry on the frequency domain FFT processing to the EMG signal in DSP, and then calculate the MPF value after each experiment. It should be noted that, in Matlab, in order to meet the FFT transformation requirements, the system will not meet the 2 N-side data to take the automatic zero processing, making it meet the computing requirements, and the DSP also has this function. However, it requires the user to define a buffer area that is large enough to accommodate the collected data. The system will automatically zero the memory bits that are not defined by the user. The error in the processing result is relatively small, and it can ensure the integrity of data collection.As the collected EMG signal data is generally relatively large, so this article through the following methods to store the data in the definition of the data cache, and then processed by FFT.

3.3. Matlab to DSP algorithm implementation

From Matlab to DSP algorithm migration, there are usually two ways. One is the indirect generation of executable code through Matlab software for DSP reference, and the other is directly through the C language to program the function in the DSP. For the first method, we first program the algorithm that needs to implement

into a function, and through the Matlab command window call to verify whether the algorithm is executable. Then, through the Matlab Coder component, convert the M file into a c language source file that can be called by the DSP. At last, open the CCSV5.5, copy the Matlab generated file to the CCS project directory, and write the call code.This method can save programming time, but not all functions can be written as source files for CCS use. Because some functions do not have a corresponding C language library, so its use is limited obviously. The second method is to write the program directly in the DSP. It should be noted that in Matlab, some functions need to be replaced by the corresponding c language function, in order to achieve the same effect. Although this method looks more complex than the first method, for this experiment, the second method is more applicable.

4. Results and discussion

First, the MPF value of the EMG signal is calculated by Matlab, and then calculated by DSP. The calculation results are shown in Table 1 and Table 2, and they are expressed as double real numbers. (where M represents the MPF value obtained by Matlab processing, D represents the MPF value after DSP processing, QXL, LL is female, GJ, YY is male, the following table is not indicated and the units are Hz).

Table 1. QXL experimental data Matlab processing results

Collection site	M first time	M second time	M third time	M fourth time	M fifth time	M sixth time
extensor communis digitorum	0.220374	0.229343	0.219162	0.211829	0.208613	0.198264
musculus biceps brachii	0.243682	0.244132	0.241766	0.240734	0.220412	0.202575
musculi extensor carpi radialis longus	0.243537	0.243614	0.242489	0.240247	0.228134	0.207103

It has been proved through the analysis of experimental data that the error of Matlab processing result and DSP processing result is 0 0.000002 Hz, and the error is within the allowable range. Therefore, the use of frequency domain calculation MPF value is suitable for implement to the DSP. After finishing the four subjects' EMG signal MPF values, their line charts are shown in Figs. 1–4.

As shown in Figs. 1–4, the MPF values of the four subjects show a significant downward trend after treatment. The spectral values are shift to the low frequency region, and the slope MPF is negative, which is consistent with the results of other researchers. And the absolute value of the slope increases, especially after the fourth and fifth times, the absolute value of the slope value is significantly increased. For different individuals, the beginning of the MPF value corresponding to the slope is

relatively flat.

Table 2. QXL experimental data DSP processing results

Collection site	M first time	M second time	M third time	M fourth time	M fifth time	M sixth time
extensor communis digitorum	0.220178	0.219383	0.219183	0.211579	0.208815	0.198604
musculus biceps brachii	0.244559	0.244146	0.241462	0.242354	0.222615	0.200739
musculi extensor carpi radialis longus	0.243443	0.253466	0.242269	0.240244	0.228333	0.205131

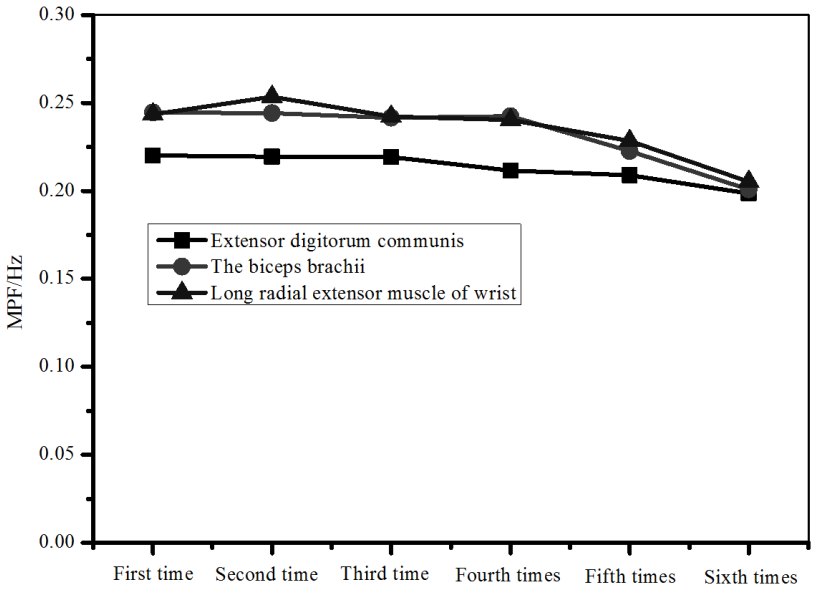

Fig. 1. Subjects QXL surface EMG signal processing MPF value line chart

After a period of exercise, subjects YY, LL after the third experiment, they have appeared the situation of the slope increased,and the other two subjects have also appeared this situation after the fourth time, which indicates that the four subjects have shown a muscle fatigue state at this time. The time of occurrence is different due to individual differences in muscle fatigue, and it is related to the fat content of each individual, people who exercise regularly have relatively low levels of fat, so the EMG signal conduction velocity is significantly faster than that of the subjects with relatively little exercise. And for the placement of the electrode, we

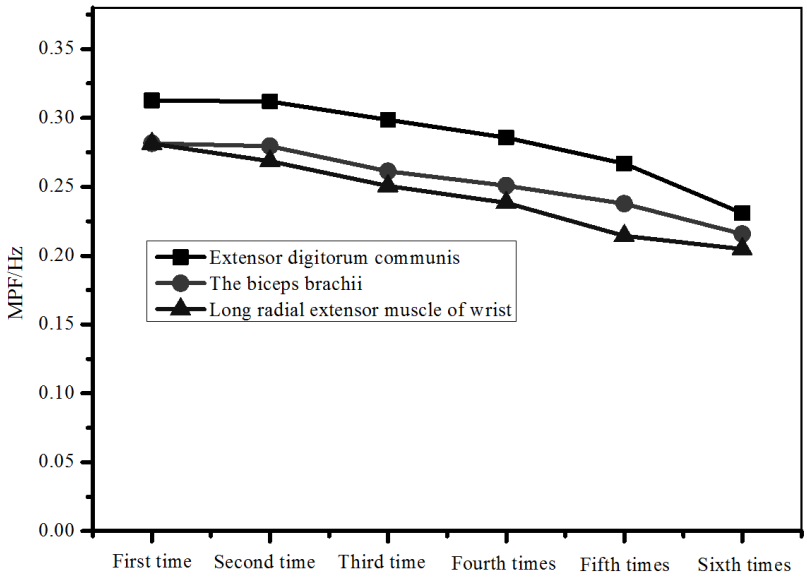

Fig. 2. Subjects LL surface EMG signal processing MPF value line chart

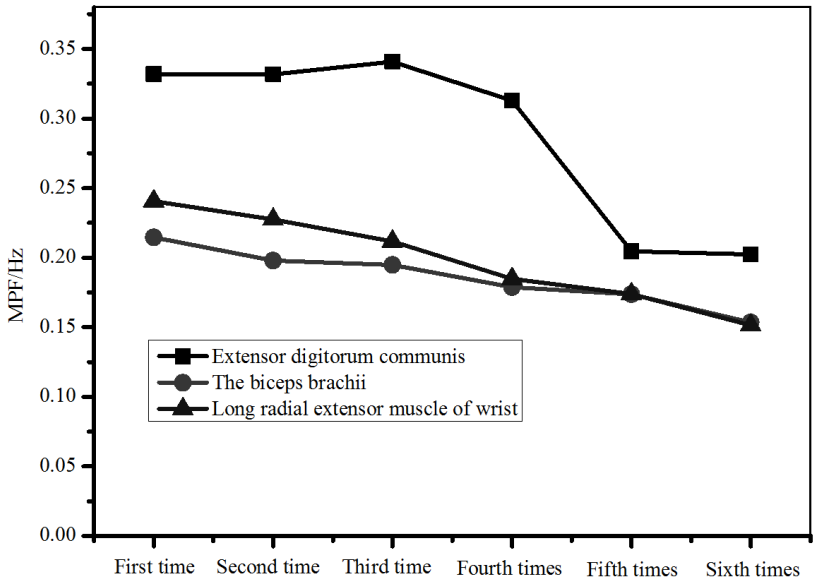

Fig. 3. Subjects GJ surface EMG signal processing MPF value line chart

cannot guarantee absolute accuracy, and only to determine the approximate location of the region where the muscles are, so it will also have a certain impact on the experiment. The size of the specific MPF value is caused by individual movement

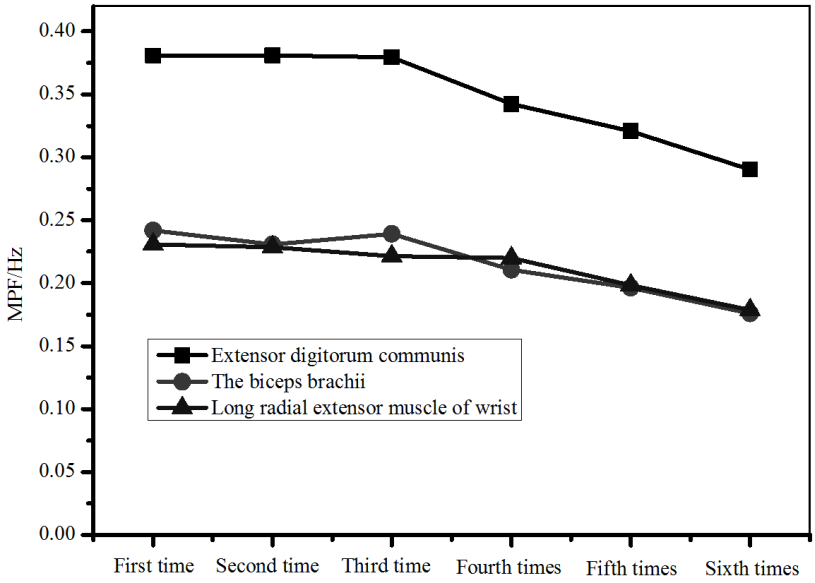

Fig. 4. Subjects YY surface EMG signal processing MPF value line chart

force. For different subjects, some people exercise force frequency is faster, so the experimental collection is relatively fast, which will have a certain impact on the experiment.

5. Conclusion

In this paper, through comparing the line charts and MPF values which are obtained by TMS320C6748 and Matlab processing EMG data, we can see that the use of TMS320C6748 can effectively deal with EMG signals. Through the analysis of the surface EMG data, it can be seen that the slope of the electromyogram MPF increased significantly after a certain period of motion, which indicates that the fatigue state of the muscle is further deepened. In the future, we can use DSP visualization to further analyze the EMG fatigue, and supplement and improve the research.

References

[1] Y. Nagano, A. Higashihara, M. Edama: *Change in muscle thickness under contracting conditions following return to sports after a hamstring muscle strain injury–A pilot study.* Asia–Pacific Journal of Sports Medicine, Arthroscopy, Rehabilitation and Technology *2* (2015), No. 2, 63–67.

[2] G. X. Ouyang, X. Y. Zhu, Z. J. Ju, H. H. Liu: *Dynamical characteristics of surface*

EMG signals of hand grasps via recurrence plot. IEEE Journal of Biomedical and Health Informatics *18* (2014), No. 1, 257–265.

[3] O. Paiss, G. F. Inbar: *Autoregressive modeling of surface EMG and its spectrum with application to fatigue.* IEEE Transactions on Biomedical Engineering *BME–34* (1987), No. 10, 761–770.

[4] G. Wang, X. M. Ren, L. Li, Z. Z. Wang: *Multifractal analysis of surface EMG signals for assessing muscle fatigue during static contractions.* Journal of Zhejiang University - Science A: Applied Physics & Engineering *8* (2007), No. 6, 910–915.

[5] M. A. Haque, R. Irani, K. Nasrollahi, T. B. Moeslund: *Facial video-based detection of physical fatigue for maximal muscle activity.* IET Computer Vision *10* (2016), No. 4, 323–329.

[6] S. Shim, H. Kim, J. Jung: *Comparison of upper extremity motor recovery of stroke patients with actual physical activity in their daily lives measured with accelerometers.* Journal of Physical Therapy Science *26* (2014), No. 7, 1009–1011.

Received May 7, 2017

Acta Technica *63* No. 3C/2017, 95–106

Control system of fitness equipment for physiological index monitoring with Bluetooth

Yunan Jin[1]

Abstract. A treadmill system communicating with Bluetooth was built to study control system of fitness equipment based on monitoring physiology parameters. First, physiology parameters and movement data collected and recorded for a long time were analyzed. To collect heart rate data, Bluetooth 4.0 of few relative interference and heart rate chest belt and normal hand-holding heart rate sensor was used. Then, practical suggestions was made for physical condition, exercise effect and fitness scheme according to analytic results. For one-time exercise, parameters of exercise effect and physical reserves evaluation were given according to body builder's dynamic physiological parameter and movement data. Thus, body builder knows better about his physical condition and exercise effect, which helps improving exercise effect and avoiding over-exercise and hypomobility.

Key words. Bluetooth 4.0, physiological index, fitness equipment, heart rate monitoring, control system.

1. Introduction

Muscle and bone can be strengthened by running. With the improvement of material life, more emphasizes were put on physical conditions. Thus, monitoring and recording basic physiological parameter and its change were significant to medical science when diagnosing, treatment and nursing clinically. Basic physiological parameter includes blood pressure, pulse and body temperature [1], which was the first to be abnormal when people being ill or injured [2]. In conclusion, monitoring basic physiological parameter was crucial to improve people's quality of life. Therefore, health monitoring technology was used to collect various physiological parameters in order to evaluate users' movement conditions when workout on a treadmill.

[1]Hangzhou Vocational and Technical College, Hangzhou, 310018, China; E-mail: yunanjinhangzhou@126.com

2. Literature review

At first, treadmill was of single function- running. With the development of science and technology, there were many additional functions for treadmill such as speed display, slope adjustment and heart rate monitoring [3]. Besides, treadmill was developing from heart rate monitoring to heart rate control [4] and some electronic treadmills were already with heat rate control function. However, there were also some transitional fitness systems which formulated personal fitness program according to height, weight and age. And those transitional fitness systems were unscientific because it did not take individual differences and dynamic change of physiological parameters into full consideration.

Thus, below fitness system was designed: collecting and recording physiological parameter (heart rate) and movement data (speed, distance, slope and time) in a long period. Parameter definitions and corresponding formula for health keeping, weight control, aerobic exercise and sports training according to single movement were put forwarded in order to evaluate exercise effect. Besides, a filtering algorithm that put forwarded according to wire and wireless heart rate data acquired a relatively ideal effect, which applied interpolation operation at first and then weight compares mean value.

3. Research method

3.1. Overall structure

Hardware was made up of treadmill hardware, upper computer main board, cardiotachometer, frequency converter, display, keyboard and mobile terminal. The structure is shown in Fig. 1.

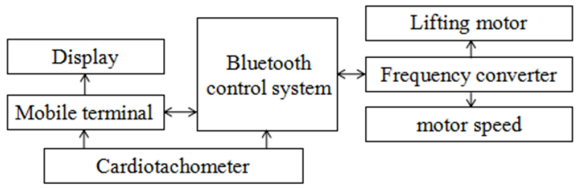

Fig. 1. Diagram of overall structure

Treadmill hardware was mainly made up of motor, belt and metal framework. And the core device motor was mainly used to adjust speed and slope. Bluetooth 4.0 was used to communicate with mobile terminal wirelessly. Upper computer was the bridge between mobile terminal and frequency converter, which was used to transmit status of frequency converter to mobile terminal and transmit order of mobile terminal to frequency converter. And frequency converter was mainly used to control speed and slope of the treadmill. Cardiotachometer was the feedback signal of physical condition, which was directly related to exercise intensity, energy consumption, respiratory degree and physical condition. When buying electronic

fitness equipment, people regarded performance of heart rate measurement system as one of the important reference standards. Hand-held heart rate sensor and wireless heart rate chest belt were popular in modern industry. Bluetooth 4.0 with low power dissipation protocol was used to achieve above functions such as control and display.

3.2. Model selection of heart rate sensor

Principle of heart rate sensor to collect heart rate [5]: heart was like a power supply, through which blood circulates around body to maintain normal activity. Complex weak currency was produced by cardiac muscle during heart beat, and the currency was transmitted to different tissues. Because distances between heart and different tissues was varied and tissue in different body part was different, electric potential varies in different body parts. Weak electrocardiosignal can be collected by two different electrodes that randomly put on the human body surface.

Hand-held heart rate sensor, wireless heart rate chest belt and Bluetooth 4.0 with low power dissipation were popular in modern fitness industry. Hand-held heart rate sensor compatible with Bluetooth 4.0 chest belt were chosen instead of common wireless heart rate chest belt with relatively loud noise.

3.3. Filtering processing for heat rate data

Filtering processing was needed again because there were noises for most signals outputted by heart rate module (wireless heart rate and wire heart rate). Heart rate data was collected by electrocardiogram (ECG) which contained physiological information that reflecting performance of cardiac system [6]. Standard electrocardiogram (ECG) is shown in Fig. 2.

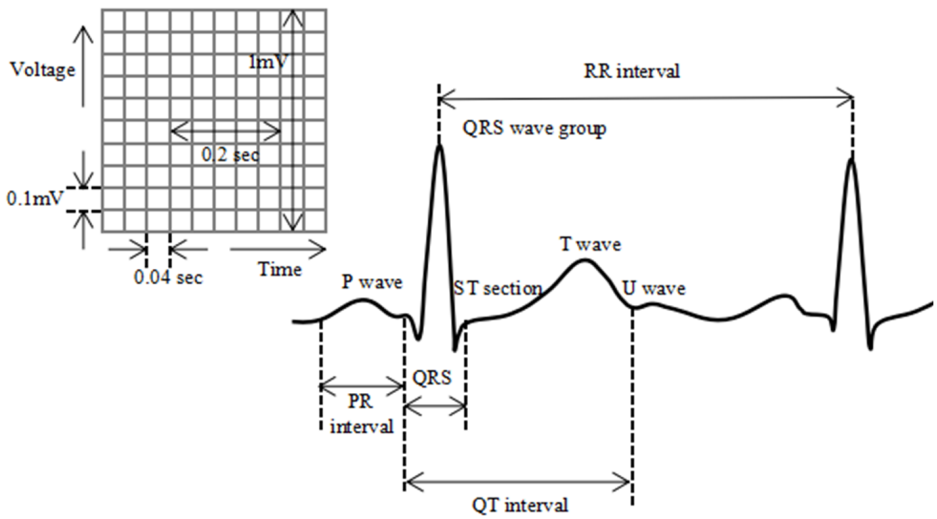

Fig. 2. Standard electrocardiogram

Most of the frequency spectrums of weak electrocardiosignal collected from human body was varied from 0.05 to 100 Hz and amplitude rage was around 10 uV-4 mV. Feature of electrocardiosignal was demonstrated by waves with bandwidth of 0∼8±3 Hz, 0∼11±2 Hz and 0∼55±19 Hz. Besides, electrocardiosignal was vulnerable to external factors, such as power line interference, electrical interference, base line drift and electromagnetic interference.

Flow for signal acquisition is shown in Fig. 3.

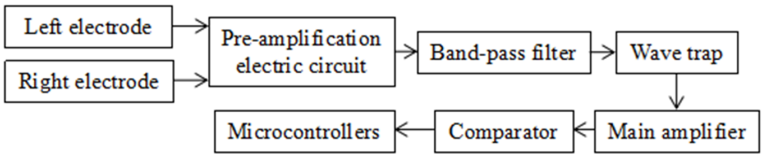

Fig. 3. Signal acquisition flow

Electrocardio energy normally worked at 17 Hz, whose frequency was around 0.05∼100 Hz and range was 5 mV. Besides, frequency of 0.5∼30 Hz was regarded as useful monitoring frequency. Butterworth band-pass filter of forth order that consisted of general operational amplifier LM324 whose bandwidth was 15 Hz and frequency was 17 Hz was used to test. After filtering, around 0.5 V electrocardiosignal can be obtained by reverse phase proportional amplification in 100 amplification times which was made up of LM324. Band elimination with relatively narrow bandwidth was named wave trap circuit. Generally, double T band-block filter circuit featuring low cost and well performance was used, which was mainly used to elimination signal at a certain frequency band and power line interference of 50 Hz.

Existing filtering algorithm for heart rate was made up of median filtering, mean filtering and slicing filtering. For mean filtering, filtering effect was well with stable data while in vigorous exercise with unstable data, filtering effect was poor. Under circumstance of poor contact and interference, filtering effect of mean filtering was better than that of median filtering though there were certain of fluctuation. Slicing filtering can effectively overcome impulse interference caused by chance factor. However, it could not restrain seasonal interference and poor smoothness [7].

Besides, another two filtering algorithm was put forwarded, interpolation operation method and method of weight comparing mean value.

1. Interpolation operation. If interval time between two pulses was close enough, median value can be eliminated. Normal heart rate of 45∼180 times/min was used in experiment and the corresponding time interval was 1.33∼0.33 ms. If time interval was longer than 1.33 ms, a pulse should be added. If time interval was shorter that 0.33 ms, comparing the two time interval next to it and found out which one was shorter. Then the time interval should be included into the shorter one. With this method, it can avoid missing pulse and collecting noise of the wrong pulse.

2. Method of weight comparing mean value. Principle of this method was comparing to the neighboring points. Weights were given according to the difference value between those neighboring points and the mean value. Then, mean value was calculated. Given filtering window was 9 and the collected original data was $a_1, a_2, \cdots, a_9$ ranged according to time sequence. Value of a_5 was to be solved.

First, mean value $\bar{a}$ should be calculated. Then, absolute differences between those neighboring points and average value were calculated: $K_n = |a_n - \bar{a}|$. If K_n was large, it meant difference between this point and the other 8 points was large. Thus, weight of this point should be lowered. Given weight of this point was $1/K_n$, and formulation of normalization constant was identified as $1/\alpha = \sum_{n=1}^{9} 1/K_n$. Thus, the value of this point was $\alpha' = \alpha \cdot \sum_{n=1}^{9} (\alpha_n K_n)$. Calculating the mean value with this method results in effective elimination of the influence of noise to mean value. It can be seen from Fig. 4 that weight comparing mean value can effectively eliminate noise and achieve accurate value.

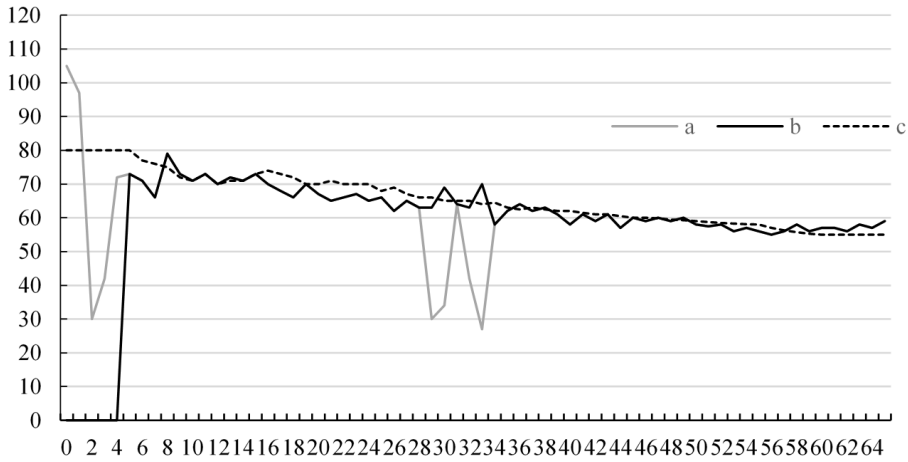

Fig. 4. Filtering effective diagram of weight comparing mean value (a was original data, b was data obtained after margin calculation, c was data obtained after mean value filtering)

3.4. Software design

CC2540 chip from Texas Instruments Company was used in lower computer studied (see Fig. 5).

Comparing to Bluetooth 3.0 version, Bluetooth 4.0 with low power dissipation protocol was featured low cost, low latency of 3 millisecond and AES-128 encription [8]. Bluetooth 4.0 can be widely applied to fields such as pedometer and heart rate monitor. There would be a heavy demand for Bluetooth 4.0 in the next 5 years. However, single mode was incompatible to classic Bluetooth device. There are two wireless technologies for Bluetooth standard 4.0, basic rate (BR, also called BR/EDR, enhanced data rate) and Bluetooth lower power dissipation (BLE). Equipment that supports both BR and BLE was called double module device. BLE protocol stack was shown in Fig. 6.

Lower computer should be able to connect to upper computer to transfer orders from upper computer to frequency converter and collect state of frequency converter.

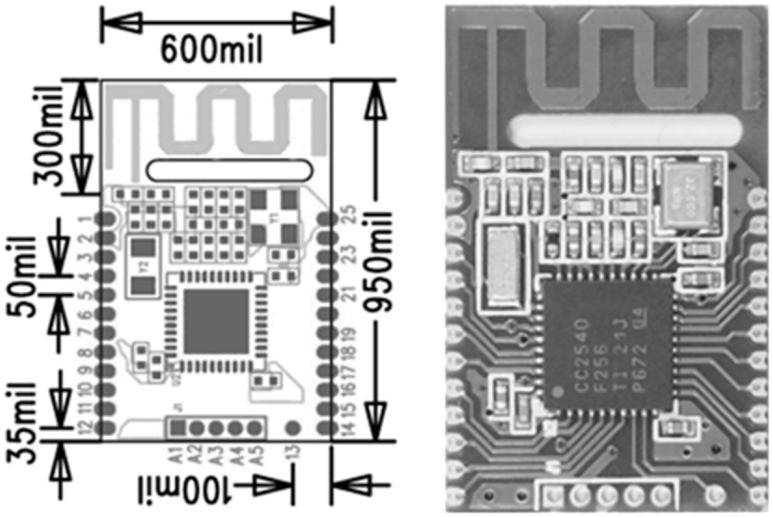

Fig. 5. CC2540 chip

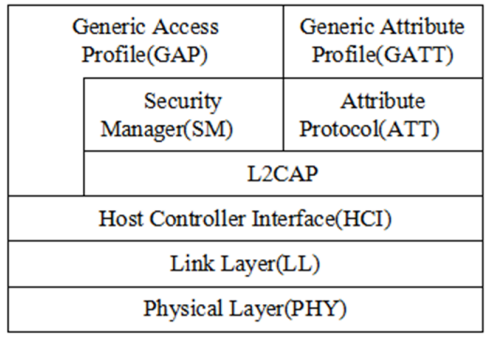

Fig. 6. Structure chart of BLE protocol stack

Thus data of computation speed, slope, and distance were transferred to the upper layer computer. Besides, lower computer can collect wire heart rate and transfer those data after in Fig. 7.

The protocol should include speed, slope, heart rate, fan, safety switch and send or accept. Protocol establishment is shown in Table 1.

3.5. Hardware design

CC2540 chip was adopted in wireless communication technology of lower computer and interface of module was shown as following:

Power interface: providing 5V direct-current supply to module.

Serial interface: for communicating with frequency converter. Serial interface was mainly used to lifting and drop treadmill and transfer state of treadmill to CC2540 chip.

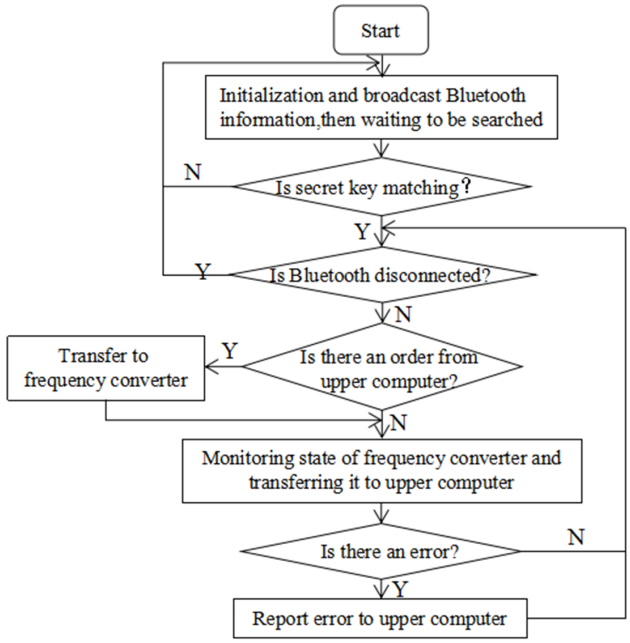

Fig. 7. Design flow chart of lower computer

Table 1. Protocol establishment

Bytes	Orders	iPad → Lower computer	Lower computer → iPad
0	Message header	FF	FF
1	Command number	00	11
2	Data 1	High speed	High speed
3	Data 2	Low speed	Low speed
4	Data 3	High slope	High slope
5	Data 4	Low slope	Low slope
6	Data 5	Heart rate: value of Bluetooth chest belt received by iPad	Heart rate: hand-held heart rate
7	Data 6	Fan(0∼255)	Fan(Retain)
8	Data 7	Safety switch(00 Open)	Safety switch(01 Close)
9	Data 8	0(Retain)	0(Retain)
10	Checksum	Checksum	Checksum
11	Data 10	00	00

Wire heart rate interface: collecting heart rate signal through wire heart rate

module and transferring it to CC2540 chip after process.

Safety switch interface: monitoring state of safety switch. When safety switch was opened, safety switch would transfer this information to master chip. This interface was adopted to transfer the stop information to frequency converter and upper computer (iPhone and iPad) when user stopped it urgently.

Bluetooth wireless interface: mainly used to transfer data to upper computer (iPhone and iPad) wirelessly.

3.6. Experimental design

This experiment was designed based on IOS system and Xcode development environment and its specific design was shown as following.

1. Convert speed and slope to distance and calorie Distance increased = Speed * Time, and Total distance: $S = \int \mathrm{d}S$, whose code was

   float mDistIntervalKm = 0;// Distance increased

   mDistIntervalKm=((double)[self GetSpeed])*(mIntervalMS/60. 0/60. 0/1000. 0);

   m_Distance+=mDistIntervalKm;// Calculate distance

   Calorie increased:

   Calorie= Speed × Weight/(1.3×(38-Slope)×150×0.45)×Time.

   Among which, speed unit was km/h, weight unit was kg (defaulted as 60 kg) and slope was integer within 0–20. Total calorie: $Q = \int \mathrm{d}Q$ and the corresponding code was:

   float m_Energy;// Total calorie M_Energy+=

   =DistIntervalKm*3.6*1000.0*60/ (1.3*(38-selfGetSlope)*150*0.45)*0.3;

2. Evaluation for effect of single exercise: American College of Sports Medicine (AcsM) put forward that it was obtained by using this equation: limiting value of heart rate in each minute = 220−actual age. If heart rate was higher that this value, it was deemed to be harmful and may be dangerous. This value was regarded as one of the most important indicator for exercise program. Target heart rate can be simplified according to Cassette formula as follows:

   The maximum heart rate 50——60,% Keep fit.

   The maximum heart rate 60——70,% Weight control.

   The maximum heart rate 70——80 % Aerobic exercise.

   The maximum heart rate 80——100 % Sport training.

   It was known that the effect of single exercise can be evaluated by detecting heart rate proportion in every section. When one was under the same exercise intensity, the larger the heart rate, the poorer the physical reservation. When different people were under the same exercise intensity, the larger proportion

of actual heart rate to the maximum heart rate means the poorer physical reservation.

Thus, a variable reflecting physical reservation L was given

$$L = 1 - \frac{1}{P_{\max}} \int P \, \mathrm{d}t \, .$$

When under the same amount of exercise, value L can reflect people's physical reservation.

Open software on the iPad, the main operation interface would show 6 buttons, such as accelerate, decelerate, increase the slope, decrease the slope, start, and stop. Besides, it also displayed value of speed, slope, distance, time, calorie, and heart rate. What's more, two icons were displayed, speed table and slope table. Bluetooth connection interface was made up of two buttons, one progress bar, two switches and a table, which was used to search and connect to treadmill. Data analysis interface was made up of function buttons such as velocity curve, heart rate curve, distance, time, calorie, and evaluations and an icon, which was used to display those recorded historical data. Interface design would not be described.

4. Result and analysis

Control variate method was adopted. Four experimenters were requested to jogging 20 min (male: 6 km/h, female: 5 km/h) at 5:00 p.m. every day. Change of heart rate curve was analyzed and physical reservation and exercise effect were evaluated. Those were required for one month.

Data and analysis results on 14th August, 2016 were selected, which was shown as below.

Experimenter A: male, 25 years old in good health, sometimes outdoor exercise.
Experimenter B: male, 44 years old in good health, hardly outdoor exercise.
Experimenter C: female, 22 years old in good health, hardly outdoor exercise.
Experimenter D: female, 41 years old in good health, sometimes outdoor exercise.

Table 2. Experimental data

Experimenter	Physical reservation parameters	Keep fit	Weight control	Aerobic exercise	Sports training
A	0.28	4.7 %	24.9 %	66.2 %	0.8 %
B	0.22	5.5 %	0.5 %	31.7 %	57.2 %
C	0.32	3.4 %	34.6 %	59.8 %	0.0 %
D	0.27	3.2 %	28.7 %	53.5 %	12.3 %

It can be known form Table 2 that different experimenters were different in physical reservation. Experimenter B was in poor physical reservation because of no

regular exercise and relatively older that the other experimenters. Experimenters A and C was in good physical reservation because of young. Experimenter D who was relatively elder than the other experimenters was in middle level of physical reservation because of regular exercise.

Besides, it can also evaluate their exercise effects by comparing it to the expected ones. Physical reservation of experimenter A in August, 2016 is shown in Fig. 8.

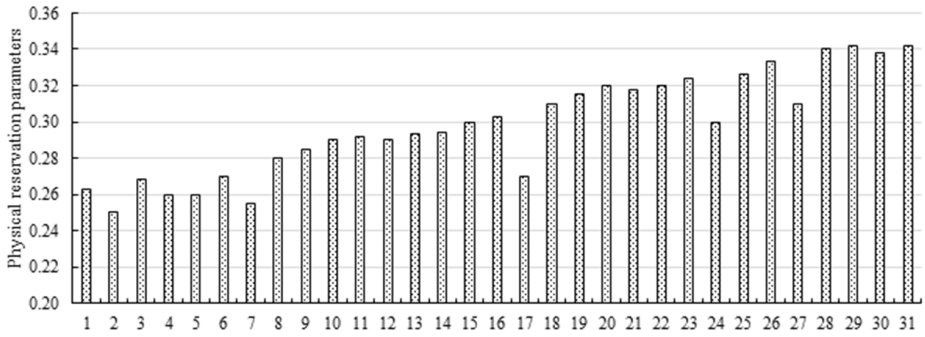

Fig. 8. Physical reservation of experimenter A in August, 2016

It can be known that after a long-term exercise, experimenter's physical reservation was improved, which meant his physical reservation was enhanced. This was comforted to human physiological feature and proved that those physical reservation parameters were reasonable.

5. Conclusion

Based on hardware and communication technology of traditional treadmill, hardware device Bluetooth 4.0 of lower power dissipation was designed, which was able to control treadmill and communicate with iPhone. IOS Client software was developed to store, operate and display relevant data. By dividing heart rate section, users can check effect of each exercise at a glance. Besides, physical reservation parameter concepts was put forwarded and was proved with a month's experiments.

References

[1] T. Bossmann: *Effects of an ultra-long distance running on selected physiological and psychological parameters as possible markers of overtraining.* Schweizerische Zeitschrift fur Sportmedizin und Sporttraumatologie *60* (2012), No. 1, 21–25.

[2] J. A. Bragada, P. J. Santos, J. A. Maia, P. J. Colaço, V. P. Lopes, T. M. Barbosa: *Longitudinal study in 3.000 m male runners: Relationship between performance and selected physiological parameters.* Journal of Sports Science & Medicine *9* (2010), No. 3, 439–444.

[3] Ł. Dziuda: *Fiber-optic sensors for monitoring patient physiological parameters: a re-*

view of applicable technologies and relevance to use during magnetic resonance imaging procedures. Journal of Biomedical Optics *20* (2015), No. 1, paper 010901.

[4] J. Del Coso, C. González, J. Abian-Vicen, J. J. M. Salinero, L. Soriano, F. Areces, D. Ruiz, C. Gallo, B. Lara, J. Calleja-González: *Relationship between physiological parameters and performance during a half-ironman triathlon in the heat*. Journal of Sports Sciences *32* (2014), No. 18, 1–8.

[5] P. G. M. da Rocha, J. L. Lopes, S. M. F. de Moraes: *Effect of environment alteration in psychological components and physiological parameters during the treadmill running in athletes*. Psicologia: Teoria e Pesquisa *26* (2010), No. 2, 381–386.

[6] A. Stankus, V. Stankus, R. Didziokas, G. Varoneckas: *High frequency filtering of 24-HOUR heart rate data*. European Journal of Scientific Research *9* (2013), No. 33.

[7] A. Jóśko, P. Irzmański, P. Figoń: *Classic, adaptive filtering techniques in the ECG signal enhancement*. Przegląd Elektrotechniczny *91* (2015), No. 7, 11–12.

[8] J. F. Ensworth, M. S. Reynolds: *Every smart phone is a backscatter reader: Modulated backscatter compatibility with Bluetooth 4.0 Low Energy (BLE) devices*. Proc. IEEE International Conference on RFID (RFID), 15–17 April 2015, San Diego, CA, USA, IEEE Conference Publications (2015), 78–85.

Received May 7, 2017

Acta Technica *62* No. 3A/2017, 107–114

System research on pressure source's prediction and analysis for athletes with improved hierarchical K-Means algorithm

Huichao Li[1]

Abstract. With the development of competitive sports, psychological factors become the key to success or failure of athletes. The feasibility of predicting and analyzing the pressure source of athletes based on improved hierarchical K-Means algorithm is explored. Firstly, hierarchical clustering is used to obtain the results of initial pressure source clustering. Secondly, the K-Means algorithm is used to continue clustering. The improved algorithm has high speed and efficiency as well as good clustering effect. Meanwhile, this algorithm is viable to predict and analyze athlete's pressure force.

Key words. Data mining, hierarchical clustering algorithm, athletes, pressure source, predictive analysis.

1. Introduction

With the development of competitive sports, the scale and number of spectators are gradually expanded, and the intensity of competition on the sports field is also increasing. These will have some psychological impact on the athletes' psychological pressure. Stress response has become a serious problem in today's competitive sports. If athletes want to do best in stadium, they have to overcome psychological factor. Therefore, many scholars and experts pay more attention to the research field of competition pressure.

Generally, the traditional psychological counseling is usually conducted through the inquiry of psychological professionals, or some questionnaires are provided to evaluate the psychological status of athletes. However, this method has poor efficiency and cannot give effective suggestions. Through participating in the development of "Athletes Race Stress Management System" from scientific research project of the General Administration of Sport, it is known that this traditional method is

[1]Civil Aviation University of China, Tianjin, 300300, China; E-mail: huichaolicivil@163.com

applied to the competitive pressure guidance in sports field. The method of data mining is applied to cope with psychological pressure. It cannot only solve the situation of large number of athletes and complicated psychological conditions, but also effectively solve the problem of coping with stress [1].

Cluster is an unsupervised method of machine learning. It aggregates data items, observation value or feature vectors into groups. At present, clustering technology has experienced rapid development. As an important branch technology of data mining, clustering technology has a variety of applications in various fields such as machine learning, data mining, information retrieval, picture segmentation and pattern classification. It even involves biology, psychiatry, archaeology and other fields. Cluster, as one of the steps of exploratory data analysis, always has been researched and discussed by many experts in many fields. This reveals the facts that cluster have a broad appeal and practicality [2]. But, there is not a general concept and method to evaluate the cluster because of the differences between different disciplines. Clustering analysis is particularly suited to explore the internal relations within the data set and the structure evaluation due to its feature. Stream data mining is a more active research direction in data mining field. Recently, clustering algorithm is widely applied in streaming data research. Generally, streaming data is a data generated by a lot of dynamic such as network data stream [3]. Some scholars put forward an improved K-Means algorithm called - Stream KM++ algorithm. This algorithm achieves convection data mining algorithm through improving data structure and distance formula, and it also obtains a good result [4].

Therefore, clustering algorithm and content-based recommendation algorithm are applied to competitive stress psychology analysis and recommendation. After clustering, the corresponding coping strategies of the athletes are obtained, which can improve the mental state of the athletes when facing the pressure. The athletes have the ability to resist compression, and the psychological level is improved when they suffer setbacks.

2. Improved K-Means algorithm

For sports competition pressure source data, it has a small data size and large data feature. If only use the K-Means algorithm, it is found that there exist many problems in early experiment and no good discrimination. Therefore, in the cause analysis, the small amount of data and more data dimensions are considered, which may affect the clustering results. According to the characteristics of the competitive pressure source data, the improved algorithm is considered [5].

In order to obtain a better initial center and time complexity, an improved hierarchical K-Means algorithm is proposed for the traditional hierarchical K-Means algorithm. It is assumed that X is $[x_1, x_2, \cdots, x_n]$ and it is a data in n R-dimensional spaces. In view of the need to determine the K value problem ahead of time, the algorithm firstly uses a silhouette coefficient to confirm the number of cluster [6]. When reaching this level after using hierarchical clustering, the number of clusters and the initial center of the iteration are locally adjusted. In this way, it greatly saves the computation for multi-layered cluster. In addition, the criterion of intra class

similarity is adopted when the initial centers are adjusted locally. It decomposes the smallest cluster into two new clusters. In this way, a partial adjustment is carried out for the cluster with poor condensation and misclassification. This will make the choice of the initial center more reasonable and also facilitate the operation [7].

Step 1: The original data is processed and the contour coefficient is calculated by formula (1). This value is used as the initial value when the K value is the maximum

$$s(i) = \frac{b(i) - a(i)}{\max\{a(i), b(i)\}}. \tag{1}$$

Step 2: The agglomerative hierarchical clustering algorithm is used to merge adjacent two clusters to form new clusters.

Step 3: The new cluster centers of the merged clusters are calculated, and the average values of the two cluster hearts in the upper layer are calculated.

Step 4: Step two and three are repeated until the number of cluster reaches $(K - R)$ $(0 \leq R \leq K - 2)$. If $K = 2$, then $R = 0$.

Step 5: The intra cluster similarity of all the assigned clusters is calculated.

Step 6: The cluster within smallest cluster similarity is selected, that is the cluster within largest class-radius. The cluster is divided, while the cluster center c_i and the farthest sample point x_{i1} are found. In the cluster, the farthest sample point x_{i2} from x_{i1} is selected.

Step 7: Points x_{i1}, x_{i2} and other cluster center are selected as the new cluster center to do the K-Means clustering again.

Step 8: If the center of mass changes, then it returns to step 6; otherwise the algorithm ends and outputs the result.

It is observed that hierarchical clustering algorithm is used to cluster the original data first from step one to four. And then the process enters the K-Means cluster from step five to six. The number of clusters is reselected according to the number of clusters calculated by the previous hierarchical clustering algorithm. In addition, the initial clustering center of K-Means algorithm is also selected. From step 7 and 8, it enters K-Means algorithm to perform twice clustering.

The improvement of this algorithm:

1) Because the small sample data has a small size, it will male big error if we directly do K-Means algorithm. It is bad for us to analyze and decide data. Therefore, cluster is used to combine the hierarchical clustering and $-$Means.

2) The initial clustering center of K-Means algorithm no longer does random selection, and it will confirm the operation situation of former hierarchical clustering. Divide the cluster with lowest cluster similarity to save the operation time.

In order to verify the effectiveness of the algorithm, Iris Data, Breast Cancer Data and Abalone data from UCI database are selected. The data set number and characteristic number are shown in the following table. The experiment test is carried out in a PC computer (2.4 GHZ Intel CPU. 2 G Memory, Windows system).

In order to compare the algorithm performance, the K-means algorithm and the improved $H - K$ algorithm are used to cluster the data downloaded from the UCI website. The results of clustering are compared from the aspects of efficiency and

aggregation. The run time contrast time of the CPU is shown in Fig. 1.

Table 1. List of test data set

DSN Data set name	Date set size	Cluster number
Iris	150	3
Breast cancer Wisconsin	286	2
Abalone data	4177	29

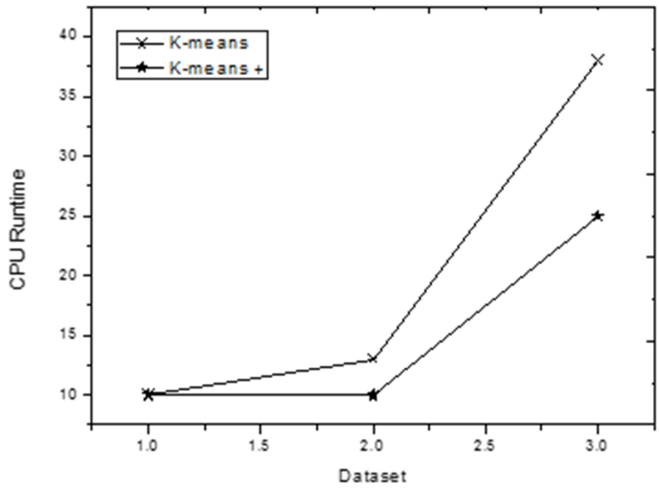

Fig. 1. CPU run time contrast broken line graph

From the above figure, as the number of data sets increases, the running time of CPU is significantly increased. the improved hierarchical K-Means clustering algorithm has a more development on run time compared to traditional K-Means algorithm, and the increasing range is obvious. Because the improved algorithm estimates the value of K in advance by using silhouette coefficient, it only optimizes the small range near the K value, which effectively reduces the time complexity of the algorithm.

In addition, in order to show the cluster degree, the accuracy rate is used to evaluate the algorithm efficiency, while iris data is used to verify cluster effect. The details are shown in Table 2.

Table 2. Accuracy comparison of two algorithm in Iris data set (%) run time

	Cluster 1	Cluster 2	Cluster 3
K-Means	100	94	72
Improved H-K	100	96	76

From above, improved $H-K$ algorithm has a high accuracy compared to traditional K-Means algorithm. Although it has a little increase, the effect is closer. It

shows that the improved algorithm has great development on efficiency and accuracy to small sample data set.

3. Application of improved K-Means algorithm in sports competition pressure source data

According to improved algorithm, it is known that cluster analysis is needed after data cleaning and transformation. Firstly, silhouette coefficient is used to work out the general cluster number K. Figure 2 shows the contour coefficient (re) value curve when K values range from 2 to 100. It is known that silhouette coefficient obtains the maximum value when cluster number reaches 2. It means that the number of clusters is better at 2, but this is not the final result. Based on hierarchical clustering algorithm, the cluster is carried out first. Then the next initial clustering center of K-Means is figured out according to the improved algorithm, which is convenient for later calculations.

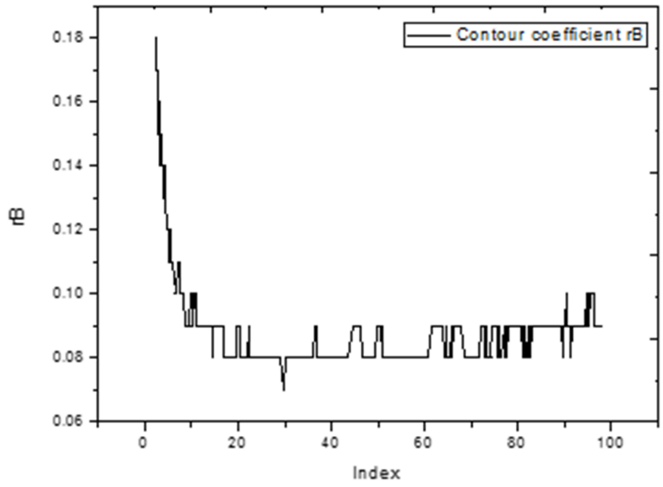

Fig. 2. Silhouette coefficient graph

The improved hierarchical K-Means algorithm is adopted to cluster the data set, clustering the 22 dimension such as competition pressure source, social support and athlete burnout. The final cluster center is shown in Fig. 3.

The overall similarity between the first classes (Series 1) and the second (Series 2) is relatively large, and parts of the property are different. The third class (Series 3) accounts for less than the total number, but it is significantly different from the first and second classes. It means this kind of athletes have a poor psychological level (low overall score shows that the pressure source is non-conformance and they have less pressure).

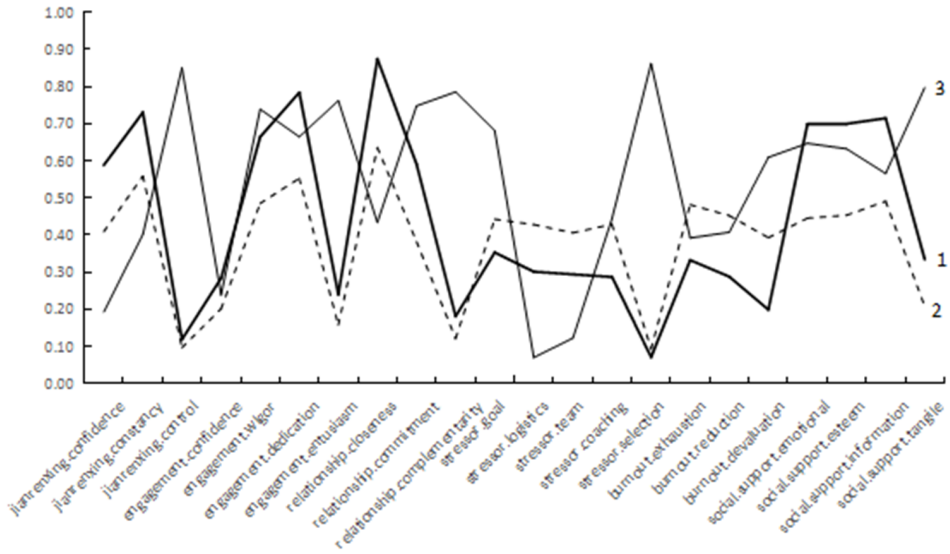

Fig. 3. Sketch map of final clustering center

4. Conclusion

In this paper, the improved K-Means algorithm will be applied to the data of sports competition pressure source. Firstly, the experiment determines the cluster number of initial hierarchical cluster according to the contour coefficient and makes first hierarchical clustering. Secondly, the initial clustering center of new K-Means algorithm is figured out again according to the improved algorithm. Finally, the K-Means algorithm is used to cluster the data sets, and the clustering results are obtained. In a word, improved algorithm has high speed and efficiency as well as good clustering effect. The improved hierarchical K-Means algorithm is feasible for predicting the pressure source of the athlete.

References

[1] Y. Xiong, J. Yang, Y. Li: *Price and carbon emission decisions under pressures of consumer, regulator and competition.* International Journal of Manufacturing Technology and Management *30* (2016), Nos. 1–2, 87–115.

[2] Y. Ding, R. Ma: *Hidden Markov model based time-series images clustering algorithm and its application in sports image processing.* Recent Advances in Electrical & Electronic Engineering (Formerly Recent Patents on Electrical & Electronic Engineering) *9* (2016), No. 1, 44–52.

[3] L. Zhang, F. Lu, A. Liu, P. Guo, C. Liu: *Application of k-means clustering algorithm for classification of NBA guards.* International Journal of Science and Engineering Applications *5* (2016), No. 1, 1–6.

[4] D. M. McMillan, D. J. Irschick: *Experimental test of predation and competition pressures on the green anole (Anolis carolinensis) in varying structural habitats.* Journal of Herpetology *44* (2010), No. 2, 272–278.

[5] N. N. Astakhova, L. A. Demidova, E. V. Nikulchev: *Forecasting method for grouped time series with the use of K-means algorithm.* Applied Mathematical Sciences *9* (2015), No. 97, 4813–4830.

[6] R. G. Negri, W. B. da Silva, T. S. G. Mendes: *K-means algorithm based on stochastic distances for polarimetric synthetic aperture radar image classification.* Journal of Applied Remote Sensing *10* (2016), No. 4, paper 040501.

[7] J. D. Rose: *An efficient association rule based hierarchical algorithm for text clustering.* International Journal of Advanced Engineering Technology *7* (2016), No. 1, 751–753.

Received May 7, 2017

Acta Technica *62* No. 3A/2017, 115–126

Data acquisition system for football based on ZigBee

Qing Ning[1]

Abstract. More and more attention is paid to football player's scientific training and ways to collect their movements' data, thus team skills and tactics are improved. Ways to achieve a better result is now a popular research topic among many professional football players. Wireless network is built based on ZigBee technology in order to collect movement data of football players in the field. Centroid locating algorithm and trilateration algorithm are studied from the aspect of location, thus improved location algorithm-centroid multilateral algorithm is put forwarded. Based on this algorithm, football players' movements' data are collected and analyzed by k-means clustering. Therefore, players' running ability are analyzed. Movement data of players in 5 groups are taken as sample data and above method is used to analyze the relevant data. Experiment verifies that this method is good for analyzing football players' physical power and the corresponding strategic cooperation.

Key words. ZigBee, location algorithm, k-means, movement data, application.

1. Introduction

Wireless data-built network is made up of nodes with signal acquisition ability, transmittability and data-handling capacity. Those node are used for monitoring observing zone as much as possible, thus smart task can be completed. All nodes are made up of data acquisition module, data receiving and storage module, data transmitting module and battery module. ZigBee is widely applied because of its low-power dissipation, networking and good expansibility. One of its significant advantages is that it can be used to build large network freely, whose coverage area is enormous.

Comparing to other network construction mode, ZigBee-based network has more practical functions than others. However, its construction is also more complex. Manufacturer who thinks highly of ZigBee technology, chip maker and soft giant establishes a technical alliance in order to standardize ZigBee technology.

Advantages of ZigBee can be summarized as (1) low power consumption because

[1]School of Physical Education, Henan University of Science and Technology, Luoyang, 471000, China; E-mail: qnqingning@126.com

ZigBee node is of short working time and low transmission rate; (2) reliable signal data transmission because mechanism of TCP signal transmission is reliable; (3) 8 bits kernel-needed because requirement of hardware storage is relatively low; (4) relatively short corresponding time for different states; (5) large network capacity and many sub-ZigBee network can be added in one area; (6) improved network security because encryption algorithm of 128 bits can be used to set security level at will.

2. Literature review

After the introduction, practical ZigBee technology was applied to many fields of production in a short period of time [1]. Comparing to other countries in the world, ZigBee was introduced to China very late. For ZigBee network, data collected by sensor were analyzed and transmitted by ZigBee controller [2]. ZigBee is a wireless communication technique which is often compared to WIFI technology. WIFI technology is of great transmittability [3] in a limited time because of large power dissipation. Corresponding standards for physical layer and network layer in network structure construction were established by ZigBee technology. In physical layer, wireless transmission function was achieved by enable control [4] and network layer was used to construct and allocate resource of ZigBee network [5].

Appropriate network topology was needed when constructing network. Generally, star topology featuring simple construction, easy networking and convenient adding or deleting node [6] was used as long as site area was not too large. Though it is of low practical security, practical security of star topology is higher than that of mesh topology structure. Network constructed with star topology was coordinately working with nodes. Nodes were equal, thus, data can transmit among different nodes [7]. When designing hardware of ZigBee network based on node, embedded single chip microcomputer (SCM) of CC2530 [8] or DHT11 type [9] can be used as control chip. As for software, IAR compiler [10] was adopted, which supported different types of single chip computer.

Wireless location technology can be used to collect data once ZigBee network was built. Location technologies based on ZigBee can be classified into ranging and range-free [11] according to whether it was related to measuring distance or not. Trilateration of ranging algorithms and centroid locating of range-free algorithms were selected as the research objects. Considering that trilateration was demanding for hardware and centroid locating was demanding for signal quantity, centroid multilateral algorithm was put forwarded which integrated the advantages and disadvantages of these two algorithms.

3. Research method

3.1. Network covering football court built based on ZigBee

Star topology (see Fig. 1) was adopted to construct network before acquiring data when the running range of football players was relatively small. This network was made up of a main coordinator and several terminal nodes. Coordinator (hereinafter referred to FFD) was core of the network, which was used to receive data transmitted from different terminal nodes. Generally, FFD was located near to terminal node for the sake of convenient networking and maintaining. Terminal nodes (hereinafter referred to RFD) were used to assist coordinator to collect data acquired from football players and sent signals to players' sensor in order to interact with them.

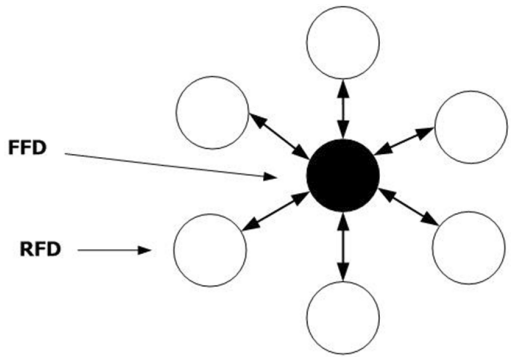

Fig. 1. Star network

One of the biggest advantages of star topology structure was easy management because its structure was simple and total path direction was relatively less. In order to cover the whole football court, several star ZigBee networks were set (see Fig. 2). Coverage area of star network was relatively more concentrated than the others'. Every football players in the field was carrying a small signal tracker, thus RFD can track their movement trail, collect their movement data and send those data back to coordinator. Then, all data received will be sent to PC by coordinator.

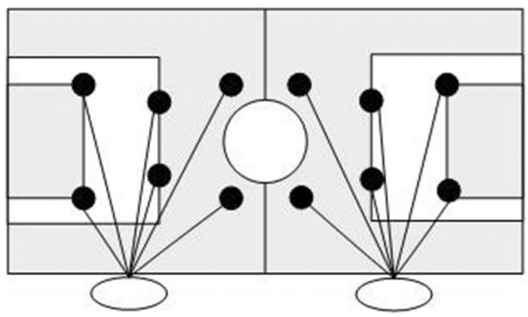

Fig. 2. Layout of ZigBee nodes

Hardware can be classified into coordinators, terminal nodes and PC processing and display terminal. For coordinator, CC2430 single chip microcomputer (SCM) was used as core control unit to receive data from network built by ZigBee and those data were transmitted to PC centralized controller through corresponding communication port (see Fig. 3), thus network was maintained in real time. These data collected was sent to CC2430 processor. ZigBee technology was used to communicate with surrounding terminal nodes (see Fig. 4) and DHT11 chip was used by terminal nodes to collect movement data of players those send by their sensors. Generally, this sensing device was used together with CC2430 single chip microcomputer (SCM).

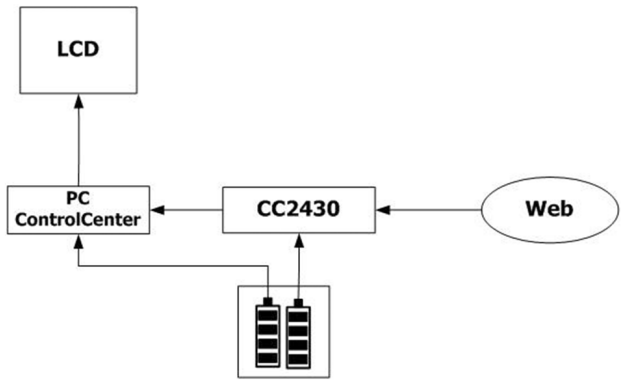

Fig. 3. Master node structure

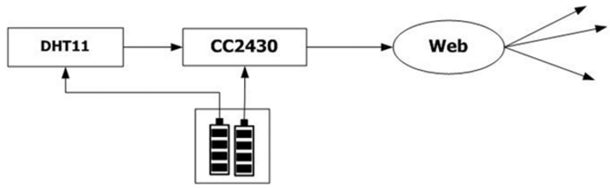

Fig. 4. Slave node structure

CC2430 was used as control chip for coordinator because it had many advantages of ZigBee technology, such as communication technology module of standard IEEE802.15.4 is included.

CC2430 single chip microcomputer (SCM) was also featured: (1) high signal receiving sensitivities; (2) low power dissipation in non-working state and RTC was used to start it; (3) CSMA/CA communication standard was supported; (4) lowered energy consumption because supply voltage relocatability is good; (5) easy to analog signal receiving because port of 14 bits was integrated in CC2430 chip to change modulus.

Terminal node was used to collect players' movement data, which was embedded with DHT11 chip. Because serial bus communication was used in DHT11 chip, number of IO port was reduced and transport protocols was simple. When transmitting

signals through DHT11 sensing device, coordinator was used to send request signal. After around 40 microseconds, Response signal at terminal node was read. If signal status bit was 0, it means Response signal has been sent by sensing device; when it was sending, the status bit will be changed into 1. Thus, data can be transmitted between terminal induction system and coordinator. When transmitting data and status bit of data package was start from 0, high level signal was sent, which means DHT11 equipment was abnormal and examination was needed.

3.2. Location algorithms

Given X, Y and Z as fixed nodes, corresponding coordinates are (t_X,f_X), (t_Y, f_Y) and $(t_Z,\ f_Z)$. Distance between those three nodes and destination node D were Length_X, Length_Y and Length_Z, respectively. Given center of a circle with coordinate of $D(t,f)$ and radius was distance between node and node, the below equations can be obtained

$$\text{Length}_X = \sqrt{(t - t_X)^2 + (f - f_X)^2}\,, \tag{1}$$

$$\text{Length}_Y = \sqrt{(t - t_Y)^2 + (f - f_Y)^2}\,, \tag{2}$$

$$\text{Length}_Z = \sqrt{(t - t_Z)^2 + (f - f_Z)^2}\,. \tag{3}$$

According to equations (1–3), the coordinate of the destination node D can be given as:

$$\begin{bmatrix} t \\ y \end{bmatrix} =$$

$$= \begin{bmatrix} 2(t_X - t_Y) & 2(f_X - f_Z) \\ 2(t_Y - t_Z) & 2(f_Y - f_Z) \end{bmatrix}^{-1} \begin{bmatrix} t_X^2 - t_Z^2 + f_X^2 - f_Z^2 + \text{Length}_Z^2 - \text{Length}_X^2 \\ t_Y^2 - t_Z^2 + f_Y^2 - f_Z^2 + \text{Length}_Z^2 - \text{Length}_Y^2 \end{bmatrix}. \tag{4}$$

Range-based localization algorithm was of high accuracy and hardware requirement is demanding. From the point of cost and power dissipation, some algorithms irrelevant to ranging were studied by many scholars. This Range-based localization algorithm, different to ranging-based algorithm, does not need ranging information and localizes node based on network connectivity.

Centroid locating method, one of the typical algorithms, was put forward by scholar of University of Southern California. This algorithm was easy to apply because it was to solve mean value of corresponding polygon vertices of polygon geometry area. This algorithm scene was facing a similar network structure. In this structure, a signal was sending signals around continuously. When the corresponding destination node received this signal up to a certain amount or a certain period of time, this destination node was regarded as within the communication range. Meanwhile, when destination node received a certain amount of signal that distributed in several geometry areas, corresponding centroids can be calculated. And those cen-

troids can be used to locating destination node. There are obvious drawbacks in this algorithm. For example, though layout of signal range was reasonable, insufficient signal number would cause sparse area and decreasing number of centroid. Thus, locating accuracy would be lowered.

Two above algorithms were typical for ranging algorithm and range-free algorithm, respectively. In complex engineering, locating algorithm was based on trilateration, so trilateration was widely applied. However, this algorithm was limited by hardware of node and odds power dissipation. Generally, expected locating result cannot be achieved when measuring distances between destination node and three or more fixed node. Centroid locating algorithm based on centroid has a relatively low hardware requirement and communication overhead but requires a certain number of signals. Based on those two algorithms, centroid multilateral algorithm was put forwarded.

This ranging-based algorithm was similar to trilateraion in many aspects. However, it can be seen form Fig. 5 that this algorithm was different to trilateraion because regions were used in this algorithm.

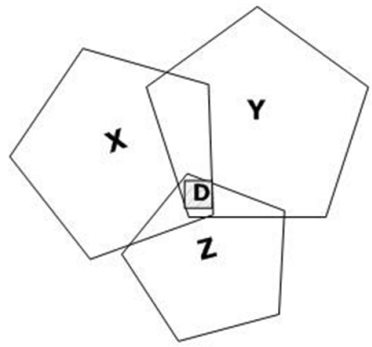

Fig. 5. Multilateral algorithm

In this figure, X, Y and X are fixed nodes and D is the destination node. Distances between the destination node and these fixed nodes XD, YD and ZD can be measured by trilateraion and these were expressed as Lx, Ly and Lz. Under ideal condition, X, Y and Z are the centers of three polygons that mutually intersect. The intersection area was simplified into a small rectangular area (see shadow area in Fig. 5). Centroid of the rectangular area are regarded as destination node D, and the coordinates of destination node D are identified.

The algorithm is based on finding intersections of several polygons, so this can be simplified by solving rectangle intersection of two polygons. Given two polygons and rectangles T1 and T2 correspond to these two polygon intersections. Four vertex coordinates of rectangles T1 and T2 were marked. The reason for simplifying these two polygons as rectangle was that calculation can be much easier than used to because less vertex coordinates mean less calculation. According to the vertex coordinates, the larger value of the X-axis was obtained by comparing the left margins of T1 and T2; the less value of X-axis was got by comparing right margins of T1 and T2; the less value of Y-axis was got by comparing upper boundaries of T1

and T2 and the larger value of Y-axis was got by comparing lower boundaries of T1 and T2. Thus, location of the rectangular region is defined using these four values.

Given four vertexes of T1 and T2 distributed according to 2×2 and described by two-dimensional array, the vertex coordinates of the rectangle can be described as

$$R_{\mathrm{T1}} = \{(X_{\mathrm{T11}}, Y_{\mathrm{T11}})\,(X_{\mathrm{T12}}, Y_{\mathrm{T11}})\,(X_{\mathrm{T11}}, Y_{\mathrm{T12}})\,(X_{\mathrm{T12}}, Y_{\mathrm{T12}})\}$$

$$R_{\mathrm{T2}} = \{(X_{\mathrm{T21}}, Y_{\mathrm{T21}})\,(X_{\mathrm{T22}}, Y_{\mathrm{T21}})\,(X_{\mathrm{T21}}, Y_{\mathrm{T22}})\,(X_{\mathrm{T22}}, Y_{\mathrm{T22}})\}$$

Based on solving method for solving the above question, the larger or lesser value can be calculated by comparing the corresponding sides of the two rectangles. Thus, location area of R_{T1} and R_{T2} is shown as $\{(X_{\mathrm{Z11}}, \mathrm{Y_{Z11}})\,(\mathrm{X_{Z12}}, \mathrm{Y_{Z11}})\,(X_{\mathrm{Z11}}, Y_{\mathrm{Z12}})\,(X_{\mathrm{Z12}}, Y_{\mathrm{Z12}})\}$

$$\begin{cases} X_{Z11} = \max(X_{\mathrm{T11}}, X_{\mathrm{T21}}), \\ X_{\mathrm{Z12}} = \min(X_{\mathrm{T12}}, X_{\mathrm{T22}}), \\ Y_{\mathrm{Z11}} = \min(Y_{\mathrm{T11}}, Y_{\mathrm{T21}}), \\ Y_{Z12} = \max(Y_{\mathrm{T12}}, Y_{\mathrm{T22}}). \end{cases} \tag{5}$$

Coordinates of these three fixed nodes are $X(a_1, b_1)$, $Y(a_2, b_2)$ and $Z(a_3, b_3)$ The distances between these three fixed nodes and destination node were Lx, Ly and Lz, which were calculated by the same method as before. Thus, the corresponding vertex coordinates of rectangles Rx, Ry and Rz corresponding to the three polygons can be expressed as

$$Rx = \{(a_1 - Lx, b_1 + Lx),\ (a_1 + Lx, b_1 + Lx),\ (a_1 - Lx, b_1 - Lx),\ (a_1 + Lx, b_1 - Lx)\},$$

$$Ry = \{(a_2 - Ly, b_2 + Ly),\ (a_2 + Ly, b_2 + Ly),\ (a_2 - Ly, b_2 - Ly),\ (a_2 + Ly, b_2 - Ly)\},$$

$$Rz = \{(a_3 - Lz, b_3 + Lz),\ (a_3 + Lz, b_3 + Lz),\ (a_3 - Lz, b_3 - Lz),\ (a_3 + Lz, b_3 - Lz)\}.$$

Intersection rectangles of two rectangle areas were solved and marked as $Z_{\mathrm{Ri,Rj}} = (a_{11}, b_{11}), (a_{12}, b_{11}), (a_{11}, b_{12}), (a_{12}, b_{12})$. For rectangle $Z_{\mathrm{Ri,Rj}}$, left margin was expressed as a_{11}, right margin was expressed as a_{12}, upper boundary was expressed as b_{11} and lower boundary was expressed as b_{12}. The intersection rectangle of Rx and Ry was derived according to the above solution method and equation (5).

$$\begin{cases} a_{11} = \max(a_1 - Lx, a_2 - Ly) \\ a_{12} = \min(a_1 + Lx, a_2 + Ly) \\ b_{11} = \min(b_1 + Lx, b_2 + Ly) \\ b_{12} = \max(b_1 - Lx, b_2 - Ly) \end{cases} \tag{6}$$

The area of the location rectangle can be obtained as long as the same calculation was made in the other polygon areas based on equation (5).

3.3. Analysis to movements data based on K-Means

Motion trail of football players in court was obtained by the designed location algorithm. Those data including position coordinates based on which data mining can be used to obtain speed and running range. There were many algorithm cat-

egories and clustering algorithm was one of the typical algorithms. In clustering algorithm, every record was seen as an integral whole and several records formed as a set. Thus, clustering algorithm was about a process for dividing this set according to a certain standards.

One of the widely used clustering algorithms (see Fig. 6) was partial clustering. Under partial clustering, all records were divided into clusters, thus set of center points were obtained. Every record was then put into appropriate set of center points. Center points would be re-calculated by subset and all records would be divided by new set of center points. This was a process of repeated iteration which stops when the center points would not change when iterating. Take K-Means algorithm as an example, and Mahout algorithm for data mining (DM) was used to further analyze data.

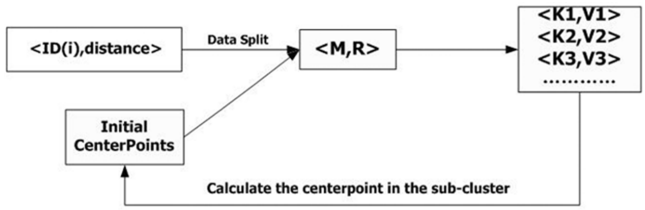

Fig. 6. Processing of K-Means with Mahout

Mahout is a machine learning library (MLL) which included many algorithms such as data mining algorithm and machine learning algorithm. Those algorithms were MapReduced to make large-scale data analysis on distributed cluster and Hadoop.

```
[root@newHad1 ~]# mahout kmeans \
> -i /mahout/kmeans-ex/reuters-sparse/tfidf-vectors \
> -c /mahout/kmeans-ex/reuters-clusters \
> -o /mahout/kmeans-ex/reuters-kmeans \
> -k 10 \
> -dm org.apache.mahout.common.distance.CosineDistanceMeasure \
> -x 10 –clustering -ow
```

Here, the operating parameters (-i) and (-o) denote input, parameter (-c) denotes information of initial center point, parameter (-k) denotes cluster numbers after dividing and parameter (-x) denotes the maximum number of iterations.

With K-Means cluster, running range and physical power of players in court can be obtained by analysis. According to previous location algorithm, players' data can be obtained, which is shown as follows.

Wang Ming: (15.063, 17.042, 5.64, 10.85, 11.75, 16.95, 30.45, 42.75.....)

Li Liang: (4.953, 7.102, 6.75, 5.47533, 6.12, 8.745, 7.11, 8.175.....)

These are the movement data of players at a certain position. All center data of players and distance between players and center can be obtained through K-Means, thus:

Wang Ming: (c: 18.811875, 1:3.748875, 2:1.769875, 3:13.171875, 4:7.96175.....)

Li Liang: (c: 6.8037912, 1:1.850791, 2:0.208208, 3:0.0537812, 4:1.32846.....)

Parameter c denotes the mean distance of movement distances and after being analyzed with K-Means, it can be know that Wang Ming's running range was larger and mean movement distance was longer while Li Liang's mean movement distance was much shorter. Thus, Li Liang should have more physical training.

4. Experimental results and their analysis

4.1. Transmission performance of ZigBee

Reliability of data transmission and acceptance of wireless network built based on ZigBee was tested in different speed and different numbers of data packages-sent.

Given the sent data package was fixed, transmission distance was progressively increasing, data units- sent were initially set as 2000 and sensor carried by players sent 5 times per minute. Area of football court was 50 m×95 m, thus two subnets of star topology were set to collect data. The principal data concerning the wireless transmission is in Table 1.

Table 1. Wireless transmission 1

Transmission distance	Data units sent	Data units received	S-R efficiency
15	10000	10000	100 %
25	10000	9989	99.8 %
30	10000	9965	99.6 %
40	10000	9932	99.32 %
50	10000	9875	98.75 %

It can be seen from Table 1 that data acceptance efficiency was not lower than 90 %. In the longest transmission distance, such as 50 meters, successful rate of data transmission can be further tested by changing sending rate of sensor.

Under the premise of same transmission distance (see Table 2), acceptance efficiency was reduced with the increasing number of data units- sent. Sending times of sensor was set less than 25, thus collection of players' movement data would not be influenced and acceptance efficiency was ensured no lower than 80 %.

4.2. Analysis to location algorithm

Central positions of different rectangles were obtained through simulation. Based on the improved centroid multilateration algorithm, the experiment verified that the central position of rectangle was at the centre of intersection area. However, there are errors in practice. Provided the maximum rectangle included in intersection area is $A'B'C'D'$, the test position is the midpoint of corresponding crosswire which is marked as O.

Practical center point is around point O and point P is defined as the maximum

error. Rectangle $A'B'C'D'$ and centroids X, Y, Z of three different polygons were put in a plain domain F1F2YD. Point Y is centroid of the larger polygon. F1F2 parallel to point O is the shortest side of rectangle $A'B'C'D'$. Line L is constructed vertically to F1F2. Make a line across centroid Y and vertical to line L and their point of the intersection is marked as point D. Thus, trapezoid F1F2YD is built (see Fig. 7).

Table 2. Wireless transmission 2

Transmission distance	Data units sent	Data units received	S-R efficiency
	20000	19654	98.27 %
	30000	26864	89.54 %
	40000	35345	88.36 %
	50000	41752	83.5 %
	60000	47531	79.21 %

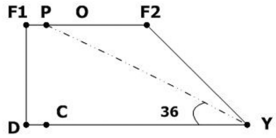

Fig. 7. Scope of F1F2YD

In practical calculation, it is hard to perform calculations based on rectangle $A'B'C'D'$ because of these errors and calculation time is quite long. After a simple logical derivation, absolute error point is located around point P on F1F2.

$$\text{Deviation} : e = PO = \text{F1}O - \text{F1}P\,. \tag{7}$$

Make a line crossing point P and vertical to line DY, which intersects line DY at point C. Thus, the below equation can be obtained

$$\text{F1}P = CD = YD - YC\,. \tag{8}$$

Given $YD = 2\text{F1}D = 2d$, the below equation can be obtained

$$\text{F1}P = 2d - 2d \times \cos(\overrightarrow{PYD})\,. \tag{9}$$

Lines F1D and YF2 intersect at point T. Thus, there is an imaginary triangle DYT. According to theories relevant to centroid, the following equation was deduced.

$$\text{F1F2} = YD \times (1/2)\,. \tag{10}$$

According to equations (9) and (10), we get the relation

$$\text{Deviation} : e = YD * (1/2) \times (1/2) - \text{F1}P \approx 0.12d\,. \tag{11}$$

After deduction, it can be seen that the error value is in direct proportion to distance between the fixed nodes. In other words, if positions of the fixed nodes are identified, there would be an error.

After analyzing the error value, the maximum location range of players is set as 2 m×2 m. The average error and standard deviation of three location algorithm in different coordinate range are compared. In Table 3, TM denotes trilateration, LC denotes locating centroid algorithm and TC denotes centroid multilateration algorithm.

Experiment was made in the maximum range of 2 m×2 m to collect movement coordinates of players. Tape was used to record actual position of players and several points were selected in each area. Signal was received at each point and these three algorithms were used to locate. Location times were not less than 50 times. Average error and standard deviation (see Table 3) were obtained according to errors between coordinates and practical results. Thus, it was known that centroid multilateration algorithm was more accurate than that of trilateration and locating centroid algorithms.

Table 3. Test results of 2 m×2 m

Coordinates (m)	Algorithms	Average coordinates (m)	Error	St. deviation
(0.46,0.18)	TC	(0.67,0.157)	0.280	0.09
	LC	(0.69,0.07)	0.521	0.360
	TM	(0.73,0.13)	0.476	0.22
(1.78,1.05)	TC	(1.50,0.88)	0.241	0.129
	LC	(1.76,0.82)	0.359	0.322
	TM	(1.65,0.82)	0.257	0.307
(1.32,1.89)	TC	(1.54,1.52)	0.380	0.036
	LC	(1.79,1.58)	0.560	0.128
	TM	(1.70,1.70)	0.442	0.136

5. Conclusion

ZigBee technology was used to collect data of players in the field and two subnets were built under new topology to cover the whole court. Area of Football court was 50 m×95 m, and the maximum movement range of players were set as 2 m×2 m. Each player was carrying a sensor. More accurate centroid multilateration algorithm that covered wider range was put forwarded based on improved trilateration and locating centroid algorithm. Running distance of players and their physical abilities were

analyzed based on collected data. Thus, reasonable tactics were identified.

References

[1] F. Cuomo, A. Abbagnale, E. Cipollone: *Cross-layer network formation for energy-efficient IEEE 802.15.4/ZigBee wireless sensor networks.* Ad Hoc Networks *11* (2013), No. 2, 672–686.

[2] P. S. Purnima: *ZigBee and GSM based patient health monitoring system.* Proc. IEEE International Conference on Electronics and Communication Systems (ICECS), 13–14 February 2014, Coimbatore, India, IEEE Conference Publications (2014), No. 2, 1–5.

[3] J. Wang: *ZigBee light link and its applicationss.* IEEE Wireless Communications *20* (2013), No. 4, 6–7.

[4] N. Baker: *ZigBee and Bluetooth strengths and weaknesses for industrial applications.* Computing & Control Engineering Journal *16* (2005), No. 2, 20–25.

[5] H. C. Tung, K. F. Tsang, K. L. Lam, H. Y. Tung, B. Y. S. Li, L. F. Yeung, K. T. Ko, W. H. Lau, V. Rakocevic: *A mobility mnabled inpatient monitoring system using a ZigBee medical sensor network.* Sensors (Basel) *14* (2014), No. 2, 2397–2416.

[6] M. Dai, Y. H. Wang, Q. Y. Pan: *A design for smart home system based on ZigBee.* Computer Measurement & Control *21* (2013), No. 03, 706–708.

[7] M. J. Huang, T. Wang: *Self-healing research of ZigBee network based on coordinator node isolated.* Applied Mechanics and Materials *347–350* (2013), 2089–2094.

[8] W. Zheng, Z. M. Li, D. H. Luo: *Design and implementation of wireless network in smart home.* Video Engineering *37* (2013), No. 21, 56–59.

[9] L. X. Wu, J. Zhan, W. Shi: *The low power study based on ZigBee network.* Proc. IEEE International Conference on Wireless Communications, Networking and Mobile Computing WiCOM '08, 12–14 October 2008, Dalian, China, IEEE Conference Publications (2008), 1–4.

[10] D. S. Yun, S. H. Cho: *A data transmission method in ZigBee networks using power efficient device.* Proc. IEEE International Conference on Advanced Technologies for Communications, 6–9 October 2008, Hanoi, Vietnam, Conference Publications (2008), 162–165.

[11] P. Kinney: *ZigBee technology: Wireless control that simply works.* Proc. Communications Design Conference, 29 September–2 October 2003, San Jose, CA, USD *2* (2003), 1–20.

Received May 7, 2017

Acta Technica *62* No. 3A/2017, 127–134

Measurement of surface electromyography characteristics of Wushu athletes in the technical movement based on telemetry EMG

Lingling Deng[1]

Abstract. The development of the martial arts movement is essentially the development of human potential. In order to improve the athletic level and to find out the shortage of athletes' martial arts, this paper intends to use the telemetry electrometer to measure the surface electromyography characteristics of Wushu athletes during the martial arts movement. Compared with the commonly used analysis method of surface electromyogram (EMG) signals, we choose the time-frequency analysis method as the index of fatigue of muscle. Then, this paper takes the Sanda movement as an example, designs the comparative experiment of the excellent athletes (group A) and the general level athletes (group B), and analyzes the EMG signals during the movement of the athletes.

Key words. Telemetry EMG, surface electromyography, martial arts movement.

1. Introduction

After the exclusion of other factors, the essence of the competitive sports development is to explore human potential. It is very difficult to achieve constant development on a high level of achievement [1]. Therefore, on the basis of respecting the laws of nature, people need to use new technology to find out the subtle problems in sports technology, and to correct them, so as to improve the level of competitive sports [2].

Based on a large number of relevant literature, this study uses surface electromyography to observe the activities of the athletes during the martial arts movement, analyzes its surface EMG characteristics, so as to improve the technology of athletes in the subtle aspects and promote the development of technology and performance [3]. Compare the main difference between the excellent athlete and the general level athlete, find out the nature of the difference, and provide the theoretical basis for

[1]Shenyang sport University, 110102, Liaoning, China; E-mail: deng_linglingdll@163.com

the Sanda athletes in order to cultivate the fast and accurate response ability under the complex game conditions, as well as providing a direct application method for the coach to carry out the scientific, targeted and effective training. It is vitally significant to elevate level of movement training and promote health of entire people.

2. 2. Methods applied to muscle fatigue assessment using surface myoelectric signals

The surface electromyogram (SEMG) is a one-dimensional time series signal that records the morphological changes of neuromuscular system [4]. There are different degrees of correlation between time-frequency characteristics and muscle activity state and functional state [5]. Surface electromyography spectrum analysis and time-frequency analysis are used to study the muscle fatigue index of athletes.

2.1. Time domain analysis

The time domain refers to the evaluation index that can reflect the change characteristics of the EMG curve in the time dimension [6]. The main indexes are integral electromyography (IEMG), mean amplitude (MA), root mean square amplitude (RMS), duration (DUR) and so on. Electromyography (EMG) is an electrodiagnostic medicine technique for evaluating and recording the electrical activity produced by skeletal muscles [7]. EMG is performed using an instrument called an electromyograph to produce a record called an electromyogram. IEMG refers to all the EMG signal rectified by the filter. The specific formula is as follows:

$$\mathrm{IMEG} = \int_{t}^{t+T} |\mathrm{EMG}(t)| \, \mathrm{d}t \,. \tag{1}$$

Here, t is the lower limit of the integral, $t+T$ is the integral line, $\mathrm{EMG}(t)$ is the time variation function of the EMG curve. Symbol MA reflects the intensity of the EMG signal and the number of units involved in the movement and the frequency of the same degree of change.

2.2. Frequency domain analysis

The frequency domain analysis refers to the evaluation of EMG signal in frequency. The main method is to pass the fast Fourier transform (FFT) of the time domain signal to obtain the spectral or power spectrum of the surface area electrical signal, which can reflect the change of the surface EMG signal at different frequency components, so it can be better to reflect the distribution characteristics of surface area of the signal in the frequency dimension [8]. The parameters commonly used for electromyography are the average power frequency (MPF) and the median frequency

(MF). The quantity MPF is given by the formula

$$\mathrm{MPF} = \frac{\int_0^\infty fP(f)\,\mathrm{d}f}{\int_0^\infty P(f)\,\mathrm{d}f}\,. \tag{2}$$

In formula (2), $P(f)$ represents the electromyogram, and f represents the frequency. Quantity MF is the intermediate value of the discharge frequency of muscle fiber in the process of skeletal muscle contraction.

3. Measurement of surface electromyography characteristics of athletes during technical exercise

In this study, we need to select the athlete's fist and leg movements in the Sanda Competition and training process to measure the surface EMG characteristics, in order to collect the EMG signals of the athletes in the fist and leg movements. All the subjects in this study are 12 boys aged about 20 years old, and they are in good health. The subjects are divided into group A and group B. The group A is 6 martial arts athletes selected from the Wushu Sanda Team of Xi'an sports institute, and the group B is the same level of 6 athletes selected from the school Wushu Sanda team.

The surface EMG test uses the German MEGA company's ME6000 16-guided telemetry EMG instrument, the instrument used to collect experimental EMG signal, and the acquisition frequency is 1500 Hz. We use Myo Research-XP software to standardize the original EMG signal to obtain the corresponding data. In this experiment, we compare the athletes of group A and group B, mainly to analyze the changes of surface electromyography of muscle during the movement of athletes, and use a variety of methods to carry out real-time synchronous monitoring of the EMG in the technical action of athletes during the whole process. The specific experimental process is shown in Fig. 1.

4. 4. Analysis of surface electromyography characteristics of athletes during technical movement

4.1. Analysis of muscle discharge duration in action

The duration of muscle activity is the time between the beginning and the end of the muscle activity, which is the duration of the muscle's discharge. During the course of the action, the coordination between the muscles is very important. If the coordination degree between muscles is high, then the muscle discharge time is neat and regular, so it can save more energy consumption in the work under the same situation, and also can be used to determine the level of training athletes. The discharge duration of straight punch muscle of group A and group B is as shown in Fig. 2.

As can be seen from Fig. 2, the discharge duration of the triceps and brachioradialis is the longest in the straight punch movement, and the discharge duration of

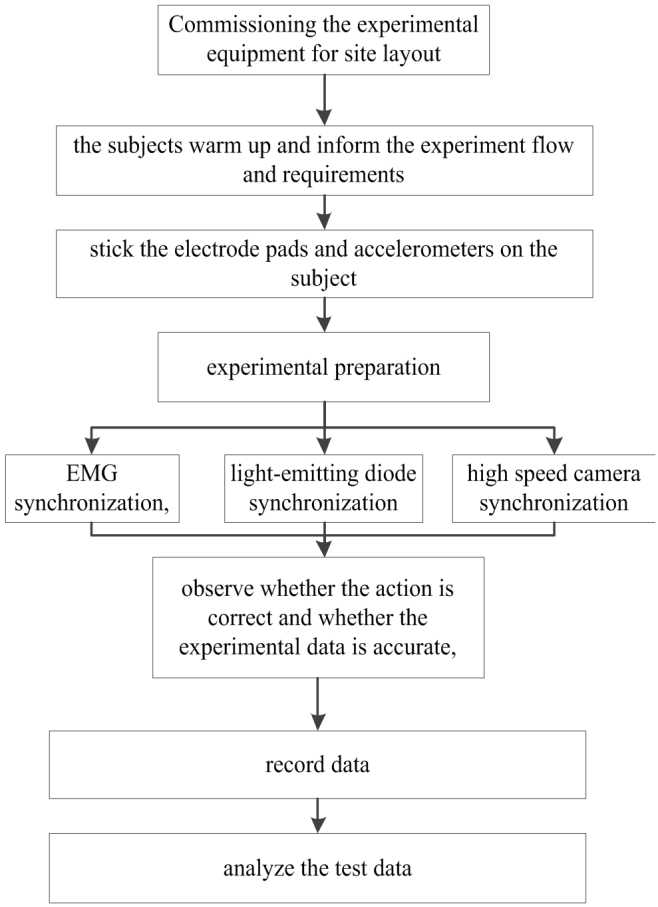

Fig. 1. Experimental process

the deltoid is the shortest. On the whole, compared with group A, the duration of the straight punch muscle of group B is relatively early, and the discharge duration is longer. The duration of the round kick muscle of the different level athletes is as shown in Fig. 3.

As can be seen from Fig. 3, the duration of the round kick muscle in group A is the longest, followed by the order of gluteus maximus, abdominal oblique and biceps femoris. The duration of the gluteus maximus muscle in group B is the longest, followed by the order of musculus obliquus externus abdominis, rectus femoris and biceps femoris. From the discharge duration, there is no difference between different levels of athletes.

For the long discharge muscles, in the usual training, we should not only pay attention to the strength of muscle exercises, but also pay attention to the duration of long muscle endurance exercises, which can give full play to the main force of muscle muscle strength, while increase the level of endurance of muscles that are

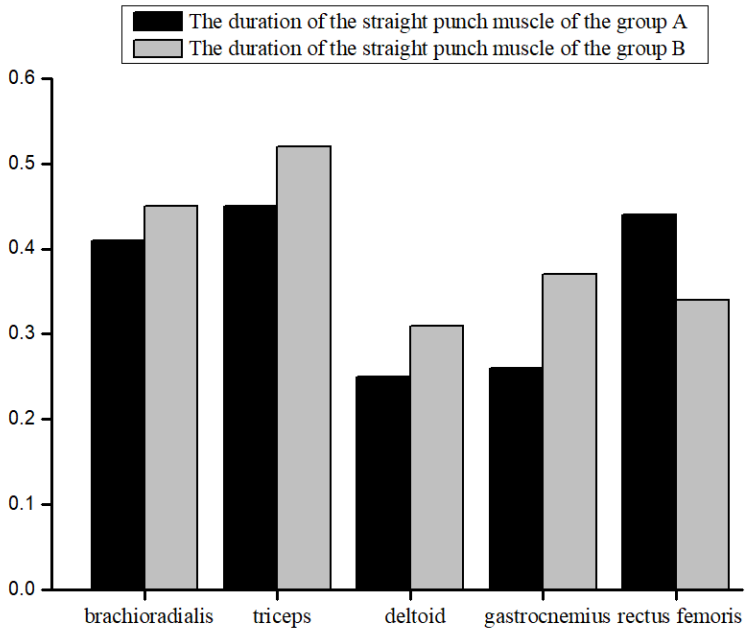

Fig. 2. Duration of the straight punch muscle of the two groups

involved in the entire movement for a long time, that is, in the usual training, we should not only pay attention to strengthen the reaction force, the greatest strength and fast strength, but also to strengthen the strength of endurance training.

4.2. Analysis of mean square amplitude in action

The mean square root values of the block muscles in the group are significantly higher than those in the group B. In the side kick leg technical action, the mean square root value of the medial muscle, gluteal muscle and femoral component muscle of group B is significantly higher than that of group A. In the group B, the medial femoral muscle discharge is larger, the root mean square value is the highest, and the discharge volume is the smallest. From the results of the root mean square amplitude data can be found that, when the athletes complete the action, the muscles should pay attention to coordination. In the case of saving energy to play greater muscle strength, and the coordination between the muscles is also very important.

5. Conclusion

Based on the important role of the reaction ability in the technical movement, this study takes the Sanda movement as an example. The results show that the duration of discharge in group A is relatively short, and has better elasticity and contractility. From the different levels of athletes' straight movements of the EMG

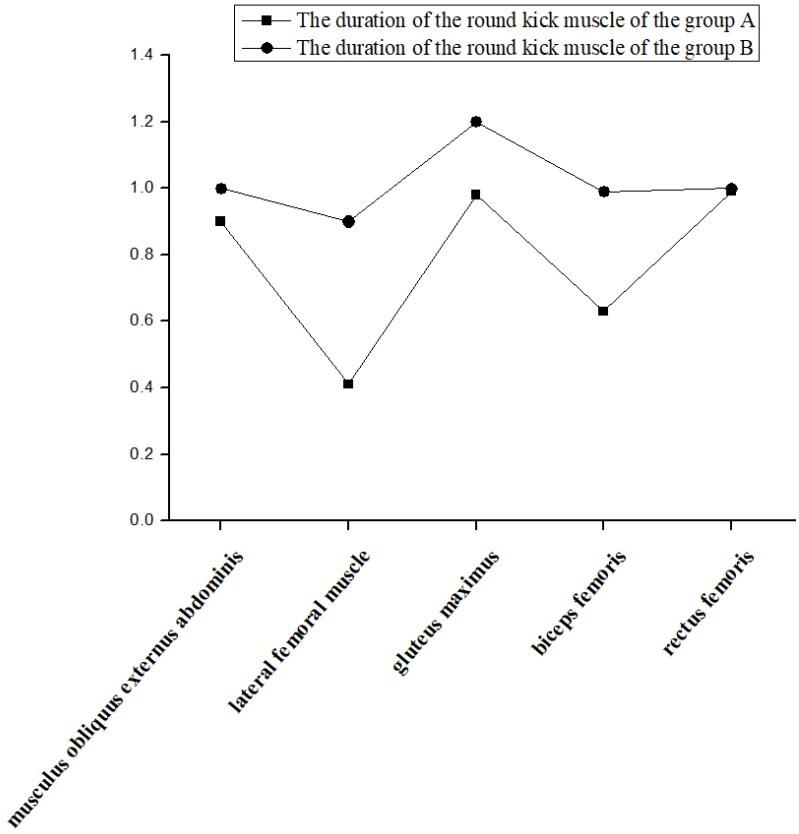

Fig. 3. Duration of the round kick muscle of the different level athletes

characteristics, which indicates that the upper limb muscle discharge is higher, and the lower limb muscle discharge is smaller, this is consistent with the principle of right straight action force. At the same time, the muscle force of the group A athletes in the side kick action is reasonable. In addition to gastrocnemius, the duration of muscle discharge in group A is shorter than that in group B, and the duration of muscle discharge in group A is shorter than that in group B in the whip legs action, which is reasonable for saving energy and a good contraction force. According to the results of the study, we understand the muscle force situation of the whip legs action, so we should carry out the specialized training to the main muscle.

References

[1] [A. Holobar, M. A. Minetto, D. Farina: *Accurate identification of motor unit discharge patterns from high-density surface EMG and validation with a novel signal-based performance metric.* Journal of Neural Engineering *11* (2014), No. 1, paper 016008.

[2] E. Martinez-Valdes, C. M. Laine, D. Falla, F. Mayer, D. Farina: *High-density surface electromyography provides reliable estimates of motor unit behavior.* Clinical Neurophysiology *127* (2016), No. 6, 2534–2541.

[3] B. T. Jeon, S. H. Moon: *Study on the rumination behaviour in spotted deer (Cervus nippon) equipped with EMG telemetry system.* Journal of the Korean Society of Grassland and Forage Science *22* (2002), No. 3, 161–168.

[4] F. Moscatelli, G. Messina, A. Valenzano, A. Petito, A. I. Triggiani, A. Messina, V. Monda, A. Viggiano, V. De Luca, L. Capranica, M. Monda, G. Cibelli. *Differences in corticospinal system activity and reaction response between karate athletes and non-athletes.* Neurological Sciences *37* (2016), No. 12, 1947–1953.

[5] G. Ouyang, X. Zhu, Z. Ju, H. Liu: *Dynamical characteristics of surface EMG signals of hand grasps via recurrence plot.* IEEE Journal of Biomedical and Health Informatics *18* (2014), No. 1, 257–265.

[6] F. Quinzi, V. Camomilla, A. Di Mario, F. Felici, P. Sbriccoli: *Repeated kicking actions in karate: Effect on technical execution in elite practitioners.* International Journal of Sports Physiology and Performance *11* (2016), No. 3, 363–369.

[7] T. Šupuk, M. Cecić: *Surface electromyography: Measurement, processing and analysis of EMG signals recorded during gait.* Proc. International Conference on Software, Telecommunications and Computer Networks, 10–13 October 2004, Venice, Italy, (2004), No. 8, 516–516.

[8] Y. Makiguchi, Y. Konno, K. Konishi, K. Miyoshi, T. Sakashita, H. Nii, K. Nakao, H. Ueda: *EMG telemetry studies on upstream migration of chum salmon in the Toyohira river, Hokkaido, Japan.* Fish Physiology and Biochemistry *37* (2011), No. 2, 273–284.

Received May 7, 2017

Acta Technica *62* No. 3A/2017, 135–142

Simulation and mathematical modeling for racket position and attitude of table tennis

Jiansi Song[1]

Abstract. Racket position and attitude of table tennis robot are studied. First, relevant knowledge and method to identify racket position and its attitude is elaborated and analyzed. Then, equation-the mathematical expression, for locating racket position and attitude is set up according to table tennis movement locus. Besides, possible racket position and attitude are analyzed with practical situations. Finally, simulation platform for table tennis robot is built. Simulation experiment verified that the studied method for identifying racket position and attitude can accurately define the dropping point of the returned table tennis ball.

Key words. Table tennis robot, racket position and its attitude, mathematic modeling, movement locus, simulation platform.

1. Introduction

Analog machine for training table tennis player was simulating opponent serve and return. In order to obtain an in-depth knowledge of opponent's strategy, table tennis player should have a long-term training about a specific technical. Using table tennis robot to have those boring training can improve sports level and technological content, save labor and enhance automation level. Racket position and attitude determines whether or not it can return the ball quickly and accurately. Study on table tennis robot mainly focused on below aspects: visual measurement and control, predicting and tracking movement locus of table tennis ball and predicting hitting point [1]. However, few studies have focused on racket position and attitude. For return the ball quickly and accurately, accurately predicted movement locus and appropriate hitting point was needed because table tennis ball was moving quickly. Besides, a specific racket position and attitude was needed. Thus, method to identify racket position and attitude was studied.

[1]Shaanxi University of Science and Technology, Shaanxi, 710021, China; e-mail: jvxrhzfp@tom.com

2. Literature review

Abroad, there were many studies on table tennis robot since 1980s. In 1983, John Billincy launched a sport of robot playing table tennis [2]. In 1987, table tennis robot developed by Russel L. Anderson from American AT&T Bell Labs made man-machine competition come true [3]. Russel L. Anderson analyzed the three parts of table tennis robot thoroughly: mechanical system, real time visual system and control system. In Oct. 2012, Katharina Muelling and her team members researched and developed a table tennis robot which could learn techniques from human coach and the opponent and adjust strategies [4]. Based on those research results, various algorithms were used domestically to improve accuracy of tracking movement locus. Hitting position and speed of table tennis ball arriving at the hitting position were studied [5].

Main purpose was to identify position and attitude of racket. First, study on table tennis robot can promote the development of theories and technologies in relevant areas such as machinery, vision and simulation. Second, table tennis ball of high-speed moving was involved in table tennis robot. Besides, study on tracking rapidly moving object, predicting track and controlling mechanical arm of robot to hit ball accurately was not only critical to research on table tennis robot but also essential to fields such as military and spaceflight. Thus, there was a promising application prospect for visual tracking and track predicting of rapidly moving objects.

3. Research method

Table tennis robot that was made up of visual system, control system and mechanical system, was for table tennis training, fitting and entertainment. Visual system was used to identify table tennis ball and predict its movement locus. Control system was used to control mechanical arm according to relevant data, thus, table tennis ball would be returned at the most appropriate time and place. Mechanical system was used to control mechanical arm, which should rotate joints and move arm quickly and identify and hit table tennis ball accurately.

Below three points were involved in predicting hitting point: distance between hitting point and ground, distance between hitting point and human body in front or back, and distance between hitting point and human body on the left or right. Hitting rate and dropping point were determined by strength, speed and arc to hit [6]. In order to hit, racket position and attitude should be adjust by moving it toward the hitting point because table tennis ball was moving at high speed. Thus, to improve accuracy and effectiveness of hitting, three-dimensional coordinates of the hitting point should be predicted quickly.

Right-hand coordinate system was used for simulation platform; its coordinate system is shown in Fig. 1.

OpenGL was adopted to design simulation platform. In order to display object in the scene better, only numerical value of object was set and no units. Thus, when it was applied practically, it can be zoomed in or out correspondingly. Parameters of objects were shown as follows:

Table tennis ball: radius 0.1, original coordinate (0, 2, 8).
Table tennis table: length 16, width 8, height 3.
Racket:1 radius 0.5, thickness 0.1, original coordinate (0, 2, –8).

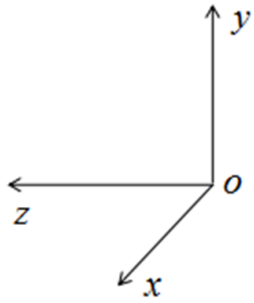

Fig. 1. Setting of coordinate system for simulation platform

There were thousands of drooping points on hall table tennis table. Table tennis robot was not as fast as players and not able to control dropping point as accurate as players, thus, a center point on the half table was set as dropping point (0, 0, 4) to determine racket position and attitude.

3.1. Determining racket position and attitude

Accurately predicted racket position and attitude and hitting point was needed to return the ball to opponent's table because table tennis ball moves quickly. Given a hitting point was known and the center point of opponent's table was the dropping point after return. Air resistance and Magnus force caused by backspin table tennis ball [7] was neglect, thus the ball was only influenced by gravity. Considering table tennis ball was moving in a two-dimensional space vertical to table and net in the middle, racket position and attitude was identified according to the known dropping point and hitting point.

3.1.1. Mathematical modeling. First, the coordinate system was set in accordance with Fig. 2.

In Fig. 2, table tennis ball was moving in plane that is parallel to plane yoz. The ball was served out from point A, reaching hitting point P after rebound from dropping point C and arrived at dropping point D after hitting. Let g denotes the gravity acceleration, H denotes the height between the point P and table tennis table, v_P denotes the ball speed at point P, β denotes included angle (the angle of incidence) between v_P and horizontal direction, S denotes the horizontal distance between point P and point D, and v_{back} denotes the speed of ball rebound from racket. Disregarding energy loss of ball rebound from racket, the formula $v_{\text{back}} = v_{\text{P}}$ was obtained. Symbol α denotes the included angle (the angle of reflection) between $_P$ and horizontal direction and T denotes the time of ball moving from point P and point D. This motion process was divided into two stages. The first stage was ball moving from point P to another point with the same height of point P and T_1 is the

time spent. The second stage was ball dropping from point at the same height of point P to dropping point D and T_2 is the time spent. Thus, the below formula is satisfied.

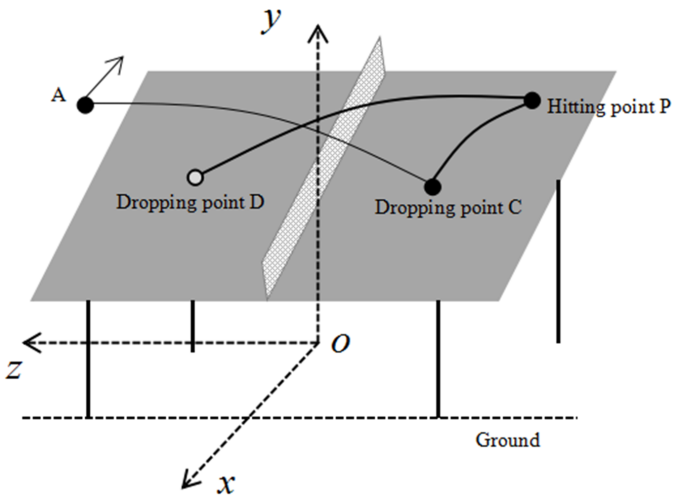

Fig. 2. Setting of coordinate system

$$S = v_{\text{back}} \cos(\alpha T), \quad 2v_{\text{back}} \sin\alpha = gT_1,$$

$$H = v_{\text{back}} \sin(\alpha T_2) + \frac{1}{2} g T_2^2, \quad T = T_1 + T_2 \,. \tag{1}$$

It can be obtained from formula (1) that

$$\frac{S^2 g^2 \tan^2\alpha}{v_{\text{back}}^2} - 2Sg\tan\alpha + \frac{S^2 g^2}{v_{\text{back}}^2} - 2gH = 0 \,. \tag{2}$$

As $\tan\alpha$ is unknown, we can determine it as follows:

$$\tan\alpha = \frac{v_{\text{back}}^2 \pm \sqrt{v_{\text{back}}^4 + 2gHv_{\text{back}}^2 - S^2 g^2}}{Sg} \,. \tag{3}$$

Put $\Delta = v_{\text{back}}^4 + 2gHv_{\text{back}}^2 - S^2 g^2$. It can be seen from formula (3) that table tennis ball can arrive at the designated dropping point D only when there was no force on racket and $\Delta \geq 0$. When $\Delta = 0$, there is only one real resolution. In this case, there is only one route that satisfies the condition and there is only one corresponding racket position and attitude. When $\Delta > 0$, there are two angles α that satisfy the condition and two corresponding racket positions and attitudes. When $\Delta < 0$, there exists no real resolution and ball cannot return to the designated dropping point. In this case, a certain amount of force should be given to hit the racket.

3.1.2. Identifying racket position and angle. It can be know from previous analysis that the prerequisite for study was the known hitting point and racket position and attitude was identified accordingly. The racket angle was identified through β and α, as can be shown from Fig. 3.

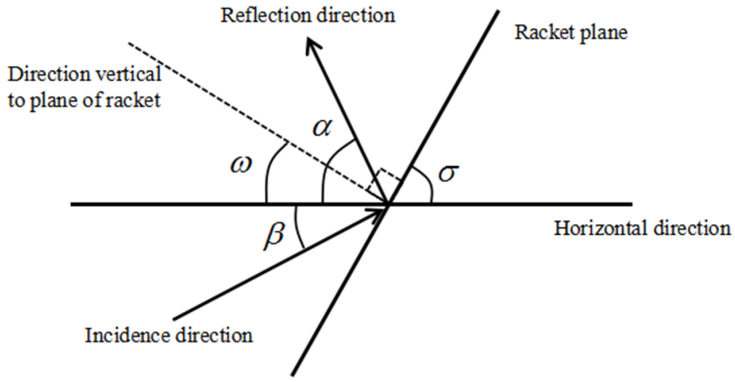

Fig. 3. Sketch map for the incidence direction and reflection direction

The figure includes acute angle σ between racket plane and horizontal direction and acute angle ω between the direction vertical to racket plane and horizontal direction. Angle $\alpha \geq \beta$ or $\alpha < \beta$, thus,

$$\omega = \frac{|\alpha - \beta|}{2}. \tag{4}$$

Thus,

$$\sigma = \frac{\pi}{2} - \omega = \frac{\pi}{2} - \frac{|\alpha - \beta|}{2}. \tag{5}$$

4. Simulation experiment and analysis of its results analysis

VC 6.0 development environment of Windows 7 operating system was adopted by the simulation platform. Single document application program was used as frame for platform and OpenGL development library was used to simulate the scene. The movement locus of table tennis ball was obtained using Runge-Kutta method [8] and shown by animation. Flow chart for simulation system is shown in Fig. 4.

After simulating the scene, program designed was operated showing the main interface of the simulation platform. For easy computing, it should be changed into front view. Then, grade of difficulty and initial parameters was set, which included initial three-dimensional coordinate of ball, initial velocity, included angle between plane of $x0y$ and $x0z$ and gravitational acceleration. Thus, simulation experiment would begin with those set initial value.

Click "hit" in the "simulation control" menu to hit the ball, thus there would be two corresponding movement locus of ball. Figures 5 and 6 are two screenshots of simulation platform for table tennis robot showing that when the designated

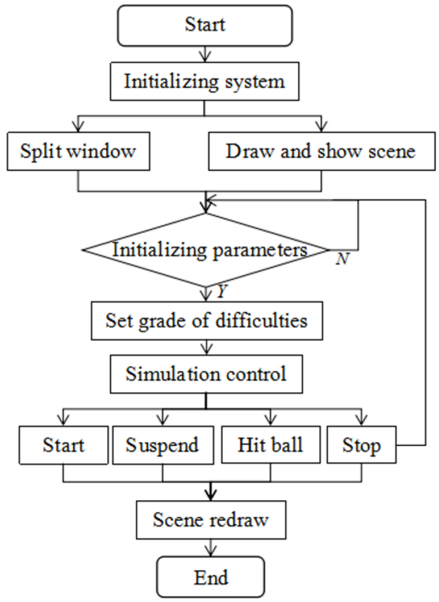

Fig. 4. Flow chart for system of simulation platform

dropping point was the same, movement locus of table tennis ball was influenced by the racket position and attitude.

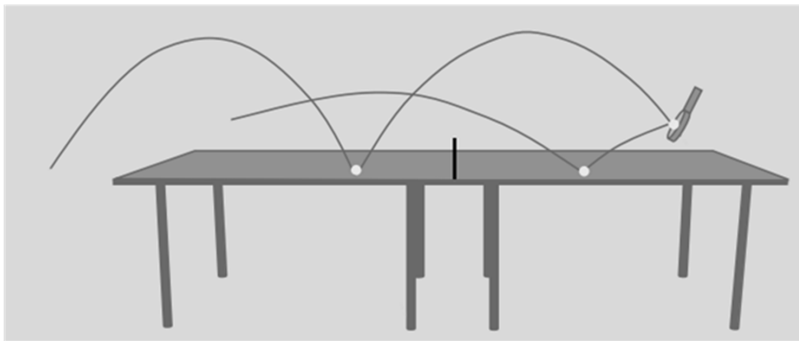

Fig. 5. Movement locus 1 for table tennis ball

In this design, it can also play, suspend, stop and draw dropping point, which is not discussed here.

5. Conclusion

Method to identify racket position and attitude of table tennis ball was studied. Mathematical modeling for racket position and attitude was built based on movement locus of table tennis ball. Thus, the method for identifying racket position

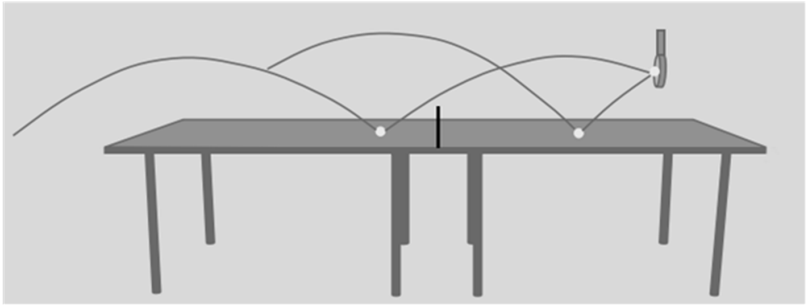

Fig. 6. Movement locus 2 for table tennis ball

and attitude was verified with simulation platform. Air resistance and Magnus force caused by backspin table tennis ball was neglected. Besides, table tennis ball movement in a two-dimensional space was studied. Therefore, three-dimensional space and those facts neglected should be included in further study.

References

[1] J. S. Tomar, D. C. Gupta, N. C. Jain: *Free vibrations of an isotropic non-homogeneous infinite plate of parabolically varying thickness.* Indian Journal of Pure Applied Mathematics *15* (1984), No. 2, 211–220.

[2] J. S. Tomar, A. K. Gupta: *Effect of thermal gradient on frequencies of an orthotropic rectangular plate whose thickness varies in two directions.* J Sound and Vibration *98* (1985), No. 2, 257–262.

[3] R. H. Gutierrez, P. A. A. Laura: *Fundamental frequency of vibrating rectangular, non-homogeneous plates.* Applied Acoustics *18* (1985), No. 3, 171–180.

[4] R. P. Singh, S. K. Jain: *Free asymmetric transverse vibration of parabolically varying thickness polar orthotropic annular plate with flexible edge conditions.* Tamkang Journal of Science and Engineering *7* (2004), No. 1, 41–52.

[5] M. N. Gaikwad, K. C. Deshmukh: *Thermal deflection of an inverse thermoelastic problem in a thin isotropic circular plate.* Applied Mathematical Modelling *29* (2005), No. 9, 797–804.

[6] S. Chakraverty, R. Jindal, V. K. Agarwal: *Flexural vibrations of non-homogeneous elliptic plates.* Indian Journal of Engineering and Materials Sciences *12* (2005) 521–528.

[7] N. L. Khobragade, K. C. Deshmukh: *Thermal deformation in a thin circular plate due to a partially distributed heat supply.* Sadhana *30* (2005), No. 4, 555–563.

[8] Y. F. Zhou, Z. M. Wang: *Vibrations of axially moving viscoelastic plate with parabolically varying thickness.* J Sound and Vibration *316* (2008), Nos. 1–5, 198–210.

Received May 7, 2017

Acta Technica *62* No. 3A/2017, 143–148

Design and application of climbing arm assist system

Xue Wang[1]

Abstract. As a new research field, the human assistance has been developed according to the needs of the application field, and has been reflected in the field of industrial and automotive engineering and rehabilitation medicine, military equipment and so on. In this paper, we take how to realize the human arm power as the research task, and through human - machine system kinematics and dynamics analysis, establish the kinematics and dynamics of mechanical system model of arm and exoskeleton. In addition, we use simulation technology to verify the correctness of the dynamic model of the arm and the exoskeleton mechanical system, which provides theoretical support for the research on tracking strategy control. We make detailed analysis of the control strategy theory, establish the expression of the assistance characteristic curve for the typical control strategy, and design the software and hardware to realize the control strategy. The data collected by prototype experiment is rationally analyzed, and the experimental results verify the correctness and feasibility of the control strategy. In addition, through the experimenter's arm assist system, we successfully complete the flexion movement of arms carrying the dumbbell. The effect is obvious and it achieves the desired objectives of the design.

Key words. Arm assist system, exoskeleton, control strategy.

1. Introduction

The human assist system is of great significance to improve the body's physical quality and break the human motion and physiological limits. As the external executive part of human in few number, its executive ability will directly affect the development of human beings and the survival ability to adapt to the harsh environment. It is the direct reason why the United States Department of Defense attaches great importance to introduce the upper limb and the lower extremity exoskeleton into the army, to assembly in each soldier's body [1]. In the future, the arm assist system can be used in the field of disaster relief and other fields, so as to improve the ability of human beings to overcome natural disasters, which has certain significance and value in saving human life and property.

[1]Zhejiang University of Science and Technology, Zhejiang, 310023, China; E-mail: dr_xuewang01@163.com

After the comparison and analysis of existing human assist mechanical system, we try using different mechanical systems, demonstrate the feasibility of the arm four-rod assist mechanical system, and conduct the mechanical system kinematics and dynamics modeling. In addition, we use Matlab software for the analysis of kinematics simulation of mechanical system, and modify the parts size of the arm four-rod assist mechanical system; moreover, we use Pro/E to complete the 3D design of the arm assist mechanical system, and introduce the 3D model into the dynamic simulation software Adams environment for the simulation. Through comparing Matlab dynamic simulation results with Adams simulation results, we manufacture the power machinery of arm assist system.

2. Mechanical system

2.1. Motion function planning of arm assist system

The previous human-assisted robot was used in medical and military applications. As it needs to consider the effect of many unknown external environmental parameters and its action function implementation in the military field, the technology is challenging and frontiering. The Honda Corporation of Japan in 2007 saw a gap in the application field, and developed a civil leg exoskeleton assist robot. The robot is placed in the motor on the leg side, which is the Honda Corporation of Japan motor R & D products: flat type brushless DC motor, quite small in the volume. The motor completes the transmission through the connecting rod connected fixedly together by the leg side [2].

In this paper, according to the different application fields of arm assist system, several action function requirements are put forward. Firstly, meet civilian needs and achieve the arm carrying heavy objects, pushing and pulling objects and further assist actions; secondly, meet the needs of the medical field and realize the auxiliary nurse nursing for the bedridden patient, patient arm rehabilitation training and further assist actions; thirdly, assist actions can be achieved in military including arm throwing objects, climbing obstacle and so on.

2.2. Mechanical system design and kinematics and dynamics analysis

After deep analyzing the characteristics and performance of the existing mechanical system, the four-bar mechanism [3] that can be analyzed by theoretical analysis, and exploratory application of new mechanism is conducted in the field.

The application of four-bar mechanism in the human arm assist system is derived from the following aspects:

First of all, in the arm assist action function defined in the paper, the tensile force of the elbow joint plays a key role, restricting the realization and effect of arm function, and even causing sports injury; in addition, the shoulder joints and elbow joints, in the upper extremity throwing motion simulation, show that the elbow joint tensile force safety limit is 3000 N, and the shoulder joint tensile force safety limit is

4500 N [4].

Secondly, movement characteristics of four-bar mechanism meet the realization requirements of arm assist action function (forearm reciprocating swings) [5]. If taking the main arm and the forearm as two hinged connecting rods, the connecting rod can achieve the swing action of the forearm, as shown in Fig. 1.

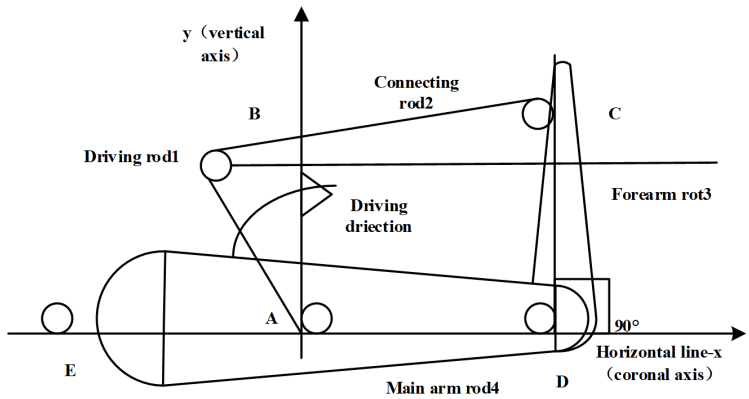

Fig. 1. A four-bar framework sketch map

Thirdly, the linkage mechanism has one of the biggest advantages. It is that the agency itself can guarantee the safety of forearm swing, through good design and size of the crank rod. Driven by a motor, the arms only repeatedly move in the range of a certain angle, and it will not cause arm dislocation or fracture accident caused by the arm movement overload because of the system and motor.

3. Dynamic modeling and simulation analysis of mechanical system

In this chapter, the relationship between the rod 3 (forearm) angular acceleration and other relevant variables and active torque M_1 of the rod 1 is established by using the Lagrange equation [6]. With the help of Adamas dynamic simulation software, the correctness of the mathematical model is verified by the simulation model of the mechanical system.

3.1. Derivation of mechanical system dynamic equation

Lagrange kinetic equation is

$$M_1 = \frac{\mathrm{d}}{\mathrm{d}t}\left(\frac{\partial T}{\partial \theta_1}\right) - \frac{\partial T}{\partial \theta_1} + \frac{\partial U}{\partial \theta_1}\,. \tag{1}$$

According to the mechanism model constructed in the paper, the quality of the connecting rod can be ignored by selecting the lightweight material and optimizing

the structural dimension, but only focusing on the quality of human forearm. And the formula for calculating the quality of forearm is:

$$m_{\text{total}} = m_{\text{hand}} + m_{\text{forearm}} = 0.247 + 0.595 = 0.842\,\text{kg}\,. \tag{2}$$

The l-hand centroid refers to the distance from the centroid the center point to elbow, and elbow centroid indicates the distance from the forearm centroid to the center point to the elbow. The data of the centroid position of each part of the arm should be transformed to the center point of the elbow joint. Symbol T is the system kinetic energy, and U denotes the system potential energy. The system kinetic energy is

$$T = \frac{1}{2}(m_2 l_{3\text{c}}^2 + J)\dot{\theta}_3^2\,. \tag{3}$$

Also, the expression of function relation is established as

$$\theta_3 = \lambda_1 \theta_1\,. \tag{4}$$

After the above kinematic mathematical analysis, it was found that θ_3 and θ_1 have an ideally linear relationship. Now, equation (1) can be rewritten into the form

$$M_1 = \frac{\mathrm{d}}{\mathrm{d}t}\left(\frac{\partial T}{\partial \dot{\theta}_3}\cdot\frac{\partial \dot{\theta}_3}{\partial \dot{\theta}_1}\right) - \frac{\partial T}{\partial \theta_3}\cdot\frac{\partial \theta_3}{\partial \theta_1} + \frac{\partial U}{\partial \theta_3}\cdot\frac{\partial \theta_3}{\partial \theta_1} \tag{5}$$

When $\theta_3 = \alpha\cdot\theta_1^2 + b\cdot\theta_1 + c$, which is a second-order interpolation function relation, then

$$M_1 = (m_3 l_{3\text{c}}^2 + J)\ddot{\theta}_3(2a\lambda_2(\theta_3) + b) + (m_3 l_{3\text{c}}^2 + J)\dot{\theta}_3(2a\lambda_2(\dot{\theta}_3) + b) +$$

$$+ m_3 g\cos\theta(2a\lambda_2(\theta_3) + b)\,. \tag{6}$$

Here, (4) may be reversely transformed as $\theta_1 = \lambda_2\theta_3$ and $\dot{\theta}_1 = \lambda_2\dot{\theta}_3$. It is necessary to choose three typical coordinates Al≡(62.5, 54.9712), A2≡(117.5, 110.4102), and A3≡(172.5, 155.2312) in allusion to the relation curve in Fig. 2(a), and the unit is the length. After the calculation, we can get $a = -0.0018$, $b = 1.3239$, and $c = -20.9162$.

3.2. Establish the M document of assist mechanism of dynamic mathematical model Matlab M

After taking $a = -0.0018$, $b = 1.3239$, and $c = -20.9162$ and the speed variation range of the rod 1 as well as the average speed l0 rad/s of the setting rod 1, the output torque changes with time, as shown in Fig. 2. The torque is negative, which is indicated by the fact that the applied torque is oriented in the clockwise direction. In 0.25 seconds or so, the rod 1 rotates about 145 degrees.

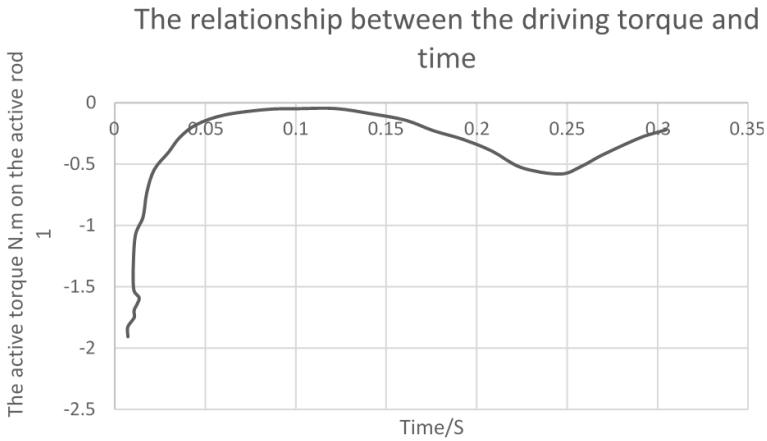

Fig. 2. Rod l active torque variety curve with l0 rad/s input

3.3. Simulation results of mechanical system model in Adams

In Adams/View, by setting the initial conditions of dynamics simulation operation, rod 1 adds a rotating Motion, the angular velocity is l0 rad/s, and the running time is 0.3 seconds, to ensure being consistent with initial conditions of the mathematical model of Matlab. The results are shown in Fig. 3 below. It is noted that the torque unit of the ordinate is in Nmm, and the simulation torque units in Matlab is in Nm. The torque value is positive in the simulation of the model, which shows that the rotational torque applied in the simulation environment is counterclockwise. There is no substantial impact on the next analysis of simulation results.

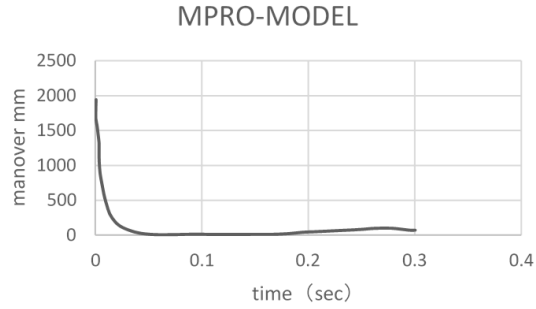

Fig. 3. Relationship between the drive torque and time of model in Adams

4. Conclusion

This paper makes full use of the dynamic simulation analysis software Adams and 3D mechanical parts design software Pro/E and takes reasonable size and shape of

the mechanism. It greatly shortens the mechanical structure design and development time, and preliminarily checks the strength of parts. Then we use mechanical parts design software Autocad2005 to design part plane processing map, and eventually process the components successfully. The hinge movement is flexible after assembly and the fixed end connection is reliable, which meets the design requirements of the mechanical devices, and provides a reliable mechanical system prototype for the experiment.

It is necessary to add how to ensure the dimensions of the rod 3 and the rod 4 in the installation process. The size of the rod 3, because of choosing 79 mm, can be achieved by adjusting the distance between the fixed position of the arm and the axis of the elbow. The rod 4 can also be implemented in the same way. The elbow axis through the elbow joint differs from man to man, needing to be measured through the actual elbow movement (the methods is to fix the main arm and make the forearm rotating in the plane). In addition, according to the traces left by the forearm in plane, judge which point position is most likely the axis of the elbow joint.

References

[1] M. Tavakoli, C. Viegas: *Analysis and application of dual-row omnidirectional wheels for climbing robots.* Mechatronics *24* (2014), No. 5, 436–448.

[2] Y. F. Wu, H. Nakamura, Y. Takeda, M. Higuchi, K. Sugimoto: *Development of a power assist system of a walking chair based on human arm characteristics.* Journal of Advanced Mechanical Design, Systems, and Manufacturing *1* (2007), No. 1, 141–154.

[3] S. K. Kerahroudi, F. Li, G. A. Taylor, M. Abbod, M. E. Bradley: *Evaluating the novel application of a class of sampled regulators for power system control.* IEEE Transactions on Control Systems Technology *24* (2016), No. 5, 1573–1581.

[4] M. E. Alfaro, D. I. Bolnick, P. C. Wainwright: *Evolutionary dynamics of complex biomechanical systems: An example using the four-bar mechanism.* Evolution *58* (2004), No. 3, 495–503.

[5] D. C. Jiao, Z. M. Li, H. F. Juan, Q. H. Zhang, J. Z. Ren, P. L. Zhou, X. W. Han: *Flat detector C-arm CT-guidance system in performing percutaneous transthoracic needle biopsy of small pulmonary lesions.* Acta Radiologica *57* (2016), No. 6, 677–683.

[6] S. Krishnaswamy, D. J. Coletti, H. Berlin, K. Friel: *Feasibility of using an arm weight-supported training system to improve hand function skills in children with hemiplegia.* American Journal of Occupational Therapy *70* (2016), No. 6, 1–7.

Received May 7, 2017

Acta Technica *62* No. 3A/2017, 149–156

Research and design on boxing-teaching robot of embedded system and pressure sensor

Zhengxian Huang[1]

Abstract. As an exercise to enhance physicals effectively, boxing is very popular. To meet market requirement of measuring punching power and interacting with boxers, boxing-teaching robot is designed based on embedded system and pressure sensor. The design process is introduced from three aspects - hardware design, embedded platform setting-up and software design. Processor S3C2440 and embedded Linux operating system are chosen and LCD touch screen is used for man-machine interaction. For setting up embedded platform, software development process and operating system of embedded Linux platform are adopted and cross-compiling environment is established. Qt/Embedded is used to design application program. Thus, five modules have been designed. Embedded database SQLite is used for data storage. The designed boxing-teaching robot promotes boxing teaching.

Key words. Boxing robot, punching power, S3C2440, embedded system.

1. Introduction

The origin of boxing dates back to a long time ago. When boxing, boxers keep jumping and think fast and thoughtful for every punch [1]. Thus, both locomotive organ and brain are trained, which results in strengthened strength and improved reaction capability [2]. However, facilities of boxing are not popularized domestically. Most boxing equipment in gym is boxing training dummy of tumbler or in shape and figure of whole human body. Those traditional boxing equipment is only for practicing punching and punching power and speed are not measured by it. Thus, it is hard for a boxer to get a well training [3]. Boxing equipment abroad is similar to that of home, which is only superior in durability and punching hand feel [4].

Electronization of sports equipment is greatly promoted by the developed modern science and technology, especially information technology and micro-electronic technique [5]. Experts and scholars at home and abroad have studied sports equip-

[1]National Police University of China, 110854, Liaoning, China; E-mail: drzhengxianhuang@yeah.net

ment electronization, most of which is on ball game electronization. For example, Y. L. Liu et al. [6] designed network communication of soccer robot achieving information passing and sharing among robots. C. Tang et al. [7] studied an algorithm of moving basketball robot based on color space and object shapes. However, there have been few studies on boxing equipment electronizing. Thus, boxing-teaching robot is designed based on embedded system, pressure sensor and computer communication technology. And its software and software have been designed.

2. Hardware design for boxing-teaching robot

2.1. General structure of system

Overall structure of the designed boxing-teaching robot was made up of boxing training dummy and man-machine interaction module. Boxing training dummy consisted of punching airbag of head and chest, corresponding pressure sensors (on the head and chest), air pump for airbag, mechanical arm, drive motor and photoelectric sensor. Man-machine interaction module was made up of LED panel, control box and voice broadcast. In terms of functions, boxing teaching system was divided into five parts such as CPU, AD data acquisition, auto-punching, air pump control and man-machine interaction. Block diagram of system functions is shown in Fig. 1.

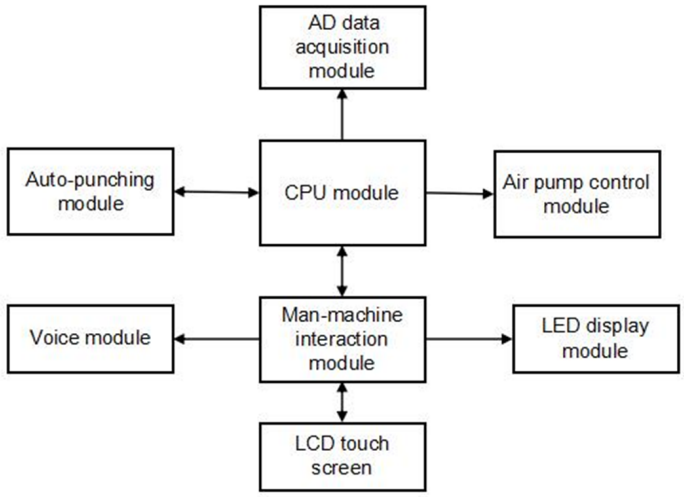

Fig. 1. Block diagram of system functions

2.2. Specific module design

S3C2440 processor of ARM9 development board was selected for CPU module. Almost all hardware components of this system were provided by this development board. Besides, this development board can operate the needed embedded Linux

operating system. The man-machine interactive module was made up of LCD touch screen, LED result display and voice broadcast. 3.4 inches ultrathin liquid crystal touch screen with resolution ratio of 320×240 and TFT true color from Samsung company were chosen, which was characterized by no heat, low-power dissipation and long working hours. Voice chip UDAl341 was used in voice module. Function of voice module was driven by compiling UDAl341 and cross compiler arm-linux-gcc3.4.1 was used here. AD data acquisition module was made up of pressure sensor and ADC converter. MPX5100SERIES pressure sensor was selected, for which 5V direct-current power supply and 100 kPa measurement range was needed. ADC converter of S3C2440 was used by AD converter. Auto-punching module was made up of photoelectric senor, direct-current dynamo, feedback switch, signal acquisition and control circuit. Signal acquisition circuit of photoelectric senor is shown in Fig. 2. Motor control circuit was made up of CD4093, optocoupler 4N26 and high-power MOS tube IRF3025. Among them, pin 1 and 2 and pin 12 and 13 of chip CD4093 were connected to pin 30 and pin 28 of processor S3C2440 respectively to control and simulate left and right punch. Mainly, air pump control module is used to re-inflate air bag, which schematic circuit diagram is shown in Fig. 3.

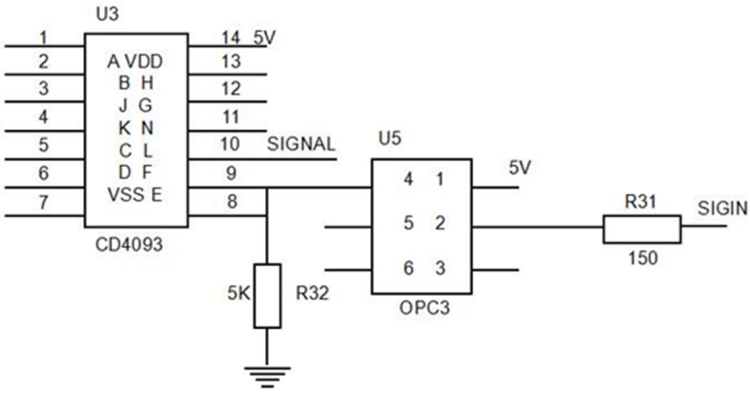

Fig. 2. Signal acquisition circuit of photoelectric sensor

3. On system of embedded software

3.1. Software development process and operating system of embedded Linux platform

Embedded software development process of Linux is divided into five parts: embedded processor and hardware platform selecting (according to users' requirement) → Boot Loader porting → kernel tailoring and compiling → appropriate file system generating → application development and system testing. Utu Linux operating system provided by YangChuang TeK featuring small kernel, high efficiency and open sources was selected. This operating system was designed based on processor supporting MMU (memory management unit). It was easy to tailor the embedded

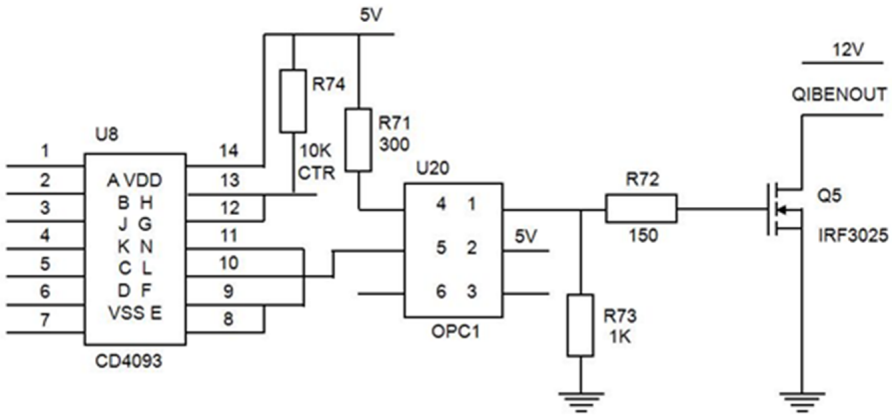

Fig. 3. Control circuit of air pump

operating system because of its dynamic module loading. Those functions related to utu Linux were also used: controlling development board with command, transmitting data through PC computer and development board and operating program automatically.

3.2. Cross-compiling environment establishment

When developing embedded system, apart from the existing development board of S3C2440 processor, a host machine with Linux operating system was needed whose corresponding development board was target board. Cross compiling was used because processors of host machine and target board were incompatible. Development environment of embedded system is shown in Fig. 4. Two things have to be done to establish a cross-compiling environment: for target machine, install Linux operating system and Qtopia bank. For host machine, install Linux operating system and tool chain arm-linux-gcc-3.4.1 and arm-linux-gcc-3.3.2 of cross compiling. Besides, Linux system sound code and Qt sound code of target machine and host machine were the same. Apart from embedded Linux operating system, Bootloader, kernel and file system provided by YangChuang TeK was selected for target board, which needed some modifications before application, such as selecting touch screen supporting 290×320 for compiling Bootloader and kernel and using touch screen as input equipment for generating file. When establishing environment for host machine, arm-linux-gcc cross compiler should be added to host machine firstly. Then, compile kernel tree which is the same version of target machine. Finally, Qtopia bank file of target machine was added to host machine [8].

4. Software design of boxing-teaching robot

Embedded system software was the key to design boxing-teaching robot, which including AD data acquisition, UI (user interface), auto-punching, SQLite database

and result display. Those five software modules were realized through multi-process.

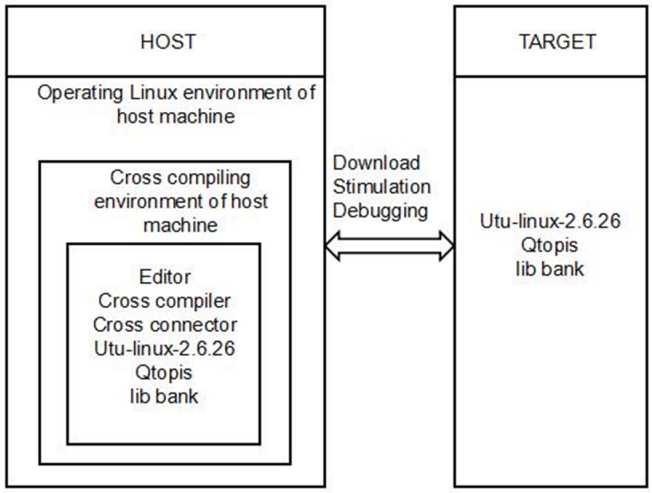

Fig. 4. Schematic diagram of embedded cross development

AD data acquisition and processing module was made up of pressure data acquisition and data processing. Data acquisition was an independent progress in the system, which computedpunching power by dynamometry, displayed it by LED display screen then wrote the power value in message queue. Data processing was mainly for converting the pressure signal collected by pressure sensor into punching power value.

Result display module was made up of voice broadcast and punching power displaying. Voice broadcast received message sent by UI module by message queue then voice broadcast it correspondingly. Punching power display function was made up of a group of Nixie tubes which was made up of LED and controlled by single chip. Single chip received punching power data that sent by ARM development board with serial port. After verified effective, those data were displayed on Nixie tubes. Punching power display module was made up of transmitting end and receiving end. Transmitting end was operating on ARM development board while receiving end was receiving data through R232 serial port and displaying it on LED display screen. Display module of punching power is shown as block diagram in Fig. 5.

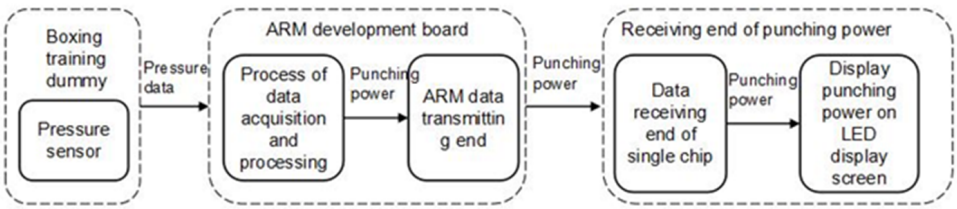

Fig. 5. Block diagram of power display module

Auto-punching module was made up of signal acquisition program of photoelectric sensor and punching control program. Signal acquisition program of photoelectric sensor was used to identify whether there was human within the effective range before boxing training dummy. After acquired signal, rand0 random function was used to determine whether simulate punching or not. If it was yes, left punch or right punch. Pause time after punching was randomly determined by the system.

Database SQLite module was used to save detailed data of boxer's each punching under fast punching module. This module was made up of data storage and data query. Data storage was used to record detailed data of each effective punching including punching position, punching time, total time and the minimum threshold value of power. Data query was used to query the data base and provide the needed data according to requirement when under demonstration mode.

In UI user interface module, LED touch screen was used for man-machine interaction, through which user can operate system. In order to make it easier, the whole system was divided into "mode selection" and "result display". There were three different modes – pressure testing, strong punching and fast punching. Result display interface showed total punching time, each punching time, total number of effective punching, each punching power and total number of punching.

5. Conclusion

The robot designed is a multi-functional integrated system with excellent hardware equipment and software platform. Punching power is computed by pressure sensor when boxers punch air bag. Thus, it is displayed in real time. Functions such as abundant voice broadcasting and practical randomly punching increase man-machine interaction, which makes the system instructs boxers well.

References

[1] P. R. Bosch, J. Poloni, A. Thornton, J. V. Lynskey: *The heart rate response to nintendo wii boxing in young adults.* Cardiopulmonary Physical Therapy Journal *23* (2012), No. 2, 13–29.

[2] A. El-Ashker, S. El-Ashker: *Cardiopulmonary effects of using mouthguards during medium and high intensities in elite Egyptian boxing athletes.* Journal of Physical Education & Sport *15* (2015), No. 1, 15–19.

[3] K. Kayahan: *Investigation of production possibilities of open area fitness equipment from wooden materials.* International Journal of Science Culture and Sport *4* (2016), No. 17, 319–328.

[4] R. Mora, G. Weisstaub: *Outdoor fitness equipment in parks in Santiago, Chile.* Revista Médica De Chile *144* (2016), No. 1, 134–135.

[5] Y. X. Wang, Y. P. Jiang: *Research on sports electronic instrument and equipment.* Applied Mechanics and Materials *484–485* (2014), No.Chapter. 4, 524–527.

[6] Y. L. Liu, Z. Z. Chen: *Design and implementation of robot soccer communication protocol based on ant colony algorithm* . Advanced Materials Research *605–607* (2013), No.Chapter. 12, 1913–1918.

[7] C. Tang, Z. H. Hu: *Basketball detection based on moving robot.* Applied Mechanics and Materials *734* (2015), No.Chapter. 4, 629–632.

[8] J. Zhao, H. Wang, B. Li: *Research and realize the key technology of the soft system for instrument platform based on the embedded linux.* IEEE International Conference on Electronic Measurement and Instruments, 16–18 August 2007, Xi'an, China, IEEE Conference Publications, (2007), 2-426–2-432.

Received May 7, 2017

Acta Technica *62* No. 3A/2017, 157–162

Research on monitoring system of physiological index of intelligent treadmill based on sensor

Yanwei Yang[1]

Abstract. Based on the study of fitness system monitoring, we have established a treadmill system through Bluetooth communication. By collecting and recording physiological parameters and motion data, we analyze the data, and use the results of the analysis to give a scientific evaluation of physical condition, fitness effect and fitness program quantification. For a single exercise, according to people's dynamic physiological parameters and exercise data, we give the fitness effect of exercise and physical reserve evaluation parameters, so as to help people to better understand their physical condition and exercise fitness effect. Therefore, people can get more scientific exercise, to prevent excessive exercise or lack of exercise and other issues, and improve fitness efficiency.

Key words. Heart rate monitoring, control system, physiological parameters.

1. Introduction

Running exercise is one of the most important activities for people to carry out physical exercise and is one of the most popular fitness activities in the world [1]. It has a high rating in the medical profession and sports field, and it is also the most effective way of exercise [2]. Running can effectively strengthen the function of limb muscles, bone exclusion, heart and lung, and it has the obvious curative effect for losing weight [3]. Due to some objective factors, such as: climate, environment, venues, etc., people are increasingly concerned about the indoor exercise, so treadmill fitness has become the preferred way of people to exercise [4].

The basic physiological parameters of the human body include blood pressure, pulse and body temperature, which are closely related to vital signs, and we can use these physiological parameters to determine the health of the human body [5]. At present, the most commonly used indoor fitness equipment is electric treadmill, and it enjoys features of small footprint, easy speed regulation and simple operations [6]. Some treadmills also support audio and video playback, with a simple heart rate

[1] Jilin Sport University, Jilin, 130022, China; E-mail: sportyanweiyang@163.com

measurement function, different environments and venues experience function, but these treadmills in the human nature has not fully reflected [7]. From the point of view of fitness, it did not achieve the best fitness effect. In view of the above situation, we combine treadmill fitness with sports health monitoring, collect and store the physiological parameters during people running. In addition, through a certain analysis and processing, we present the people's physical and sports situation in time, so people can view their current health indicators in real time, and understand their own exercise situation. Therefore, it has great application prospect and research value to record and analyze motion data for a long time.

2. The basic structure of the system

2.1. Treadmill system requirements

1) Collect and record the physiological parameters (heart rate) and motion data (velocity, distance, slope, time) for a long period of time.

2) Based on the statistical analysis of the data, we give a quantitative evaluation of the physical condition, fitness effect and fitness program.

3) Based on the statistical analysis of the data, we give guidance to people's later fitness training programs.

4) For a single movement, according to people's dynamic physiological parameters and motion data, the system can adjust the exercise intensity and exercise time in real time.

2.2. The hardware requirements of treadmill system

In hardware, the system consists of seven parts, namely treadmill hardware, frequency converter, host computer board, heart rate meter, display, keyboard and mobile phone side.

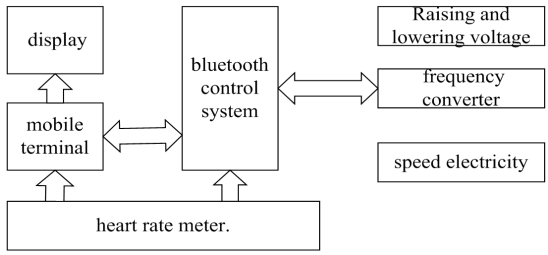

Fig. 1. System hardware requirements analysis chart

(1) Treadmill

Treadmill hardware is provided by Rizhao Kangli, mainly composed of motor, running belt and metal frame. Model: AC9000.

(2) Frequency converter

The main task of the inverter is to control the speed of the treadmill motor speed

and the size of the ramp motor, this part is the purchase of the sea frequency of the inverter, the relevant agreement has been written.

(3) Host computer

In order to communicate with iPhone and iPad, here we adopt the Bluetooth 4 communication scheme to realize wireless transmission. On the one hand, Apple released restrictions on the Bluetooth protocol, allowing programmers to add their own protocol. On the other hand, Bluetooth 4 has been popular in the new Apple and Android phones, so here we choose the CC2540 chip.

(4) Heart rate meter

Heart rate is an important feedback signal for human health. In the process of rational control of fitness, heart rate is an important part of scientific fitness. Heart rate is a relatively simple measurement of a physiological parameter, heart rate changes can directly reflect the body's exercise intensity, energy consumption, breathing and physical condition. At present, the fitness industry is using hand-held heart rate sensor and wireless heart rate chest.

(5) Mobile terminal

Here, we use the Bluetooth 4.0 low-power protocol to achieve the control and display of the above functions. This can directly be arranged through the Bluetooth 4.0 to obtain the value of wireless heart rate chest, and then directly display it. Due to the hardware limitations of Bluetooth 4, the support of system iOS7 is used.

3. Selection of heart rate sensor

3.1. Heart rate

Heart rate is an important indicator of human health feedback. In the process of exercise, the reasonable control of heart rate is an important way of scientific fitness. With the development of the heart rate measurement system, it has become an important part of fitness equipment, so the purchase of electronic control equipment is also an important reference for this. Heart rate is an important physiological parameter in the human body, heart rate changes can directly reflect the body's breathing, energy consumption, physical condition and exercise intensity.

3.2. Heart rate sensor

The principle of the heart rate sensor: the heart is like a power supply, the reason why the blood can continue to circulate in the body. As it is dependent on the rhythm of the heartbeat, people can maintain normal life activities. Electrocardiogram (ECG) signal is an important physiological signal of the human body, it contains rich physiological information, which can reflect the function of the heart system, and among them, the heart rate is an important one. Place two electrodes at any two points in the human body, we can collect the body of the weak ECG signal.

Bluetooth 4.0 technology is the rise of a wireless transmission technology in recent years. This program requires Bluetooth 4. G lungs without traffic, which has the advantages of the small interference, low power consumption and no external power

supply. It can develop their own communication protocol, and the communication can be more flexible, as well as it can communicate with iPhone and other mobile terminals, so as to save the treadmill computer research and development work. To have an integrative consideration, we give up the noise of the larger common wireless heart rate chest, and select the hand-held and Bluetooth 4.0 chest strap compatible program.

3.3. Heart rate data filtering

Heart rate is an important feedback signal for human health. In the process of reasonable control of fitness, heart rate is an important part of scientific fitness. Heart rate measurement system as an important part of improving the value-added fitness equipment, fitness equipment has gradually become an important criterion.

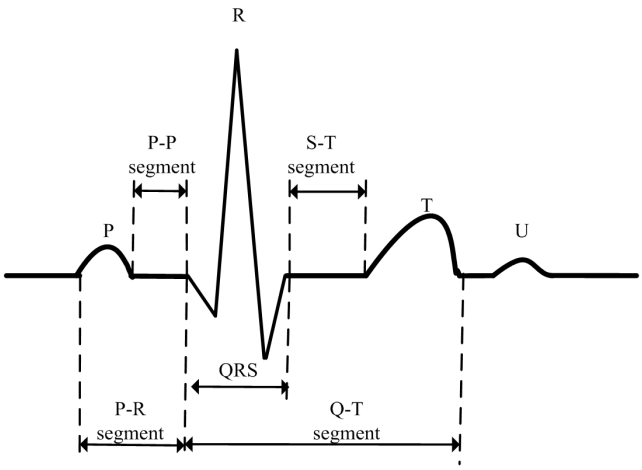

Fig. 2. Standard electrocardiogram

The standard human ECG signal waveform is shown in Fig. 3. The signal acquisition process is shown in Fig. 4.

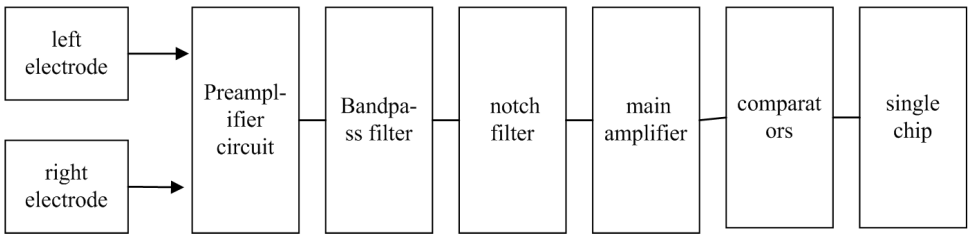

Fig. 3. Flow chart of ECG signal acquisition

The heart rate filtering algorithm: suppose that we need to find the value of a_5, where we select the filter window 9. The collected raw data by the time is in order: $a_1 \cdots\cdots a_9$. First, find the average of these nine values: $\overline{a} = 1/a \sum_{n=1}^{9} a_n$.

Then, calculate the absolute value of the difference between the average of each value: $k_n = |a_n - \overline{a}|$. The bigger the k_n, the greater the difference between the point and the 8 points around it. We need to reduce the weight of this point, where $1/k_n$ is the weight of this point. And then calculate the normalization constant. The formula is $1/\alpha = \sum_{n=1}^{9} 1/k_n$. We can calculate the value of the point: $\alpha' = \alpha \sum_{n=1}^{9} \alpha_n/k_n$. Therefore, when we calculate the average, it can effectively remove the effect of noise on the mean.

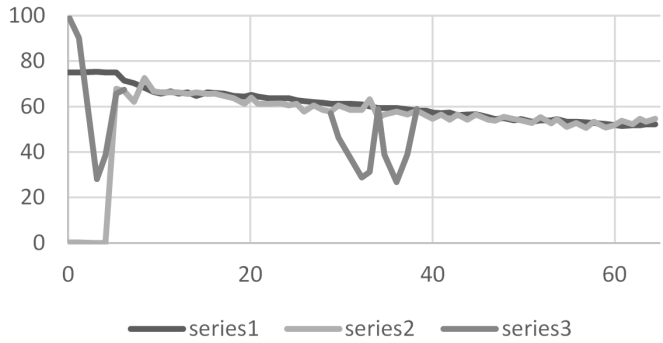

Fig. 4. Mean filtering data processing

Series 3 is the original data, series 1 is the data after the difference operation, and series 2 is the mean filtered data. The results show that the method can not only effectively filter out the noise, but also can retain the accuracy of the values.

4. Conclusion

According to the traditional treadmill industry hardware and communication methods, we design a hardware device that can control the treadmill, and it can communicate with Apple's Bluetooth 4.0 low-power transmission hardware device. This paper analyzes the characteristics of various heart rate acquisition sensors, and gives a heart rate acquisition scheme compatible with hand—held heart rate sensor and Bluetooth 4.0 wireless heart rate chest. This study improves the heart rate filtering algorithm, summarizes the predecessors' algorithms and puts forward our own algorithms.

References

[1] J. T. Black, P. S. Romano, B. Sadeghi, A. D. Auerbach, T. G. Ganiats, S. Greenfield, S. H. Kaplan, M. K. Ong: *A remote monitoring and telephone nurse coaching intervention to reduce readmissions among patients with heart failure: Study protocol for the better effectiveness after transition - heart failure (BEAT-HF) randomized controlled trial.* Trials *15* (2014), No. 1, 124–135.

[2] M. R. Cowie, S. Sarkar, J. Koehler, D. J. Whellan, G. H. Crossley, W. H. W. Tang, W. T. Abraham, V. M. Sharma, M. Santini: *Development*

and validation of an integrated diagnostic algorithm derived from parameters monitored in implantable devices for identifying patients at risk for heart failure hospitalization in an ambulatory setting. European Heart Journal *34* (2013), No. 31, 2472–2480.

[3] A. Ugwumadu: *Are we (mis) guided by current guidelines on intrapartum fetal heart rate monitoring? Case for a more physiological approach to interpretation.* International Journal of Obstetrics & Gynaecology (BJOG) *121* (2014), No. 9, 1063–1070.

[4] A. Lanata, G. Valenza, M. Nardelli, C. Gentili, E. P. Scilingo: *Complexity index from a personalized wearable monitoring system for assessing remission in mental health[.* IEEE Journal of Biomedical and Health Informatics *19* (2015), No. 1, 132 to 139.

[5] P. G. Jacobs, N. Resalat, J. el Youssef, R. Reddy, D. Branigan, N. Preiser, J. Condon, J. Castle: *Incorporating an exercise detection, grading, and hormone dosing algorithm into the artificial pancreas using accelerometry and heart rate.* Journal of Diabetes Science and Technology *9* (2015), No. 6, 1175–1184.

[6] Y. Guo, A. Q. Zhou, W. Gao, F. Li, Y. Li, J. P. Yang, M. Zhu, H. Y. Zhang : *Evaluation of physiological index on treadmill exercise testing of 294 healthy children in Shanghai area.* Zhonghua Er Ke Za Zhi (Chinese Journal of Pediatrics) *41* (2003), No. 5, 338–343.

[7] M. P. Tarvainen, J. P. Niskanen, J. A. Lipponen, P. O. Ranta-Aho, P. A. Karjalainen: *Kubios HRV – Heart rate variability analysis software.* Computer Methods and Programs in Biomedicine *113* (2014), No. 1, 210–220.

Received May 7, 2017

Acta Technica *62* No. 3A/2017, 163–172

Discussions on multi-sensor Hidden Markov Model for human motion identification

Nan Yu[1]

Abstract. Based on acceleration sensor and gyroscope data fusion, a human motion identification method was put forward for tackling the problem of large error of monitoring human motion with single sensor. Measurement accuracy of attitude angle was greatly improved by revising attitude angle collected by acceleration sensor with human motion information outputted by gyroscope and achieving information fusion for multi-sensor using Kalman filtering algorithm. Hidden Markov Model (HMM) for identifying human motion was built based on characteristics of human attitude angle. Experiment showed that to identify physical exercise was more accurate with multi-sensor HMM based-method than with single sensor.

Key words. HMM, multi-sensor, human movement identification, data fusion.

1. Introduction

A human motion model for physical education was made up of head, the upper part of the body, the upper part of big arm, the middle and lower parts of big arm, forearm, hip, thigh, shank and feet. A new type of jointing element was used among those parts. This mode was used demonstrate various exercises for students or athletes to imitate and practice [1]. Therefore, recognition algorithm of HMM was adopted to analyze angular information and extract characteristics of several basic movements. Human movement mode was analyzed and identified in real time with the matching input sequence and HMM model.

2. Literature review

Two basic approaches for identifying movement were video image-based monitoring method and wearable device-based monitoring method. To collect and analyze depth image features, video inductor was introduced to video image-based monitor-

[1]Tianjin University, Tianjin, 300072, China; E-mail: nprv5919@tom.com

ing method whose typical image processing method was based on kinect [2]. This method was featured limited monitored area, needing specific light for monitored area and unguaranteed privacy security for users. Mature technology-MEMS sensor was adopted by wearable device-based monitoring method, such as attitude detecting system made up of accelerometer, gyroscope and magnetometer were used to identify human motion information [3]. This method was featured guaranteed privacy security for users. This device was of low price and suitable for widely promotion.

Generally, acceleration sensor was used in motion detection technology because of its accurate identification in uniform variable speed [4]. However, most physical exercise was variable acceleration motion. Thus, there was large identification error because of gravitational acceleration and accelerated speed. Therefore, a wearable device was designed to collect data using acceleration sensor and gyroscope. More accurate and reliable identification information was obtained by fusing multi-source information with Kalman filtering. HMM recognition algorithm was used to analyze attitude angle and extract characteristic value of motor. Common human movement mode was analyzed and identified in real time by the matching input sequence and HMM model.

3. Research method

3.1. Data collection and fusion

A space coordinate system should be built before collecting human motion information. Performance of different body parts was very different during the same exercise because human motion was complex. Motion of the upper trunk (body parts above waist and under the neck) was relatively stable in daily activities while in walk, stand and fall down, its motion was evident. Thus, sensor was put on the upper trunk to collect data.

Human trunk coordinate system oxyz (see figure 1) was built taking place of sensor as original point. Ground coordinate system was taken as fixed Cartesian coordinate system OXYZ. When human body stood still, human trunk coordinate system oxyz was parallel to ground coordinate system OXYZ.

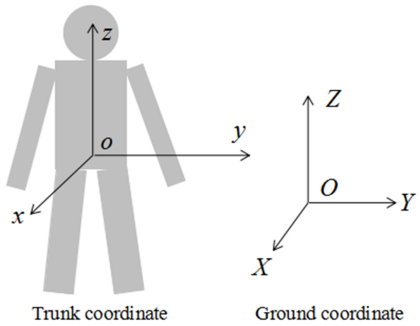

Fig. 1. Space coordinate system for human motion

3.2. Algorithm for information collection and fusion

Tri-axial digital acceleration sensor MMA7660 was used to collect human gravitational acceleration. MEMS tri-axial angular velocity sensor (gyroscope) L3G4200D was used to collect human attitude angle. Sampling frequency was set as 50Hz. The collected acceleration data and gyroscope data was transferred by information acquisition module to PC to fuse. Angular value collected by system was revised in real time by data that collected by acceleration sensor, thus deviation of attitude angle measurement caused by single sensor was addressed [5].

Given $\boldsymbol{G}$ vector value measured by acceleration sensor when exercising. Acceleration magnitudes of $\boldsymbol{G}$ in three coordinate axes X, Y and Z are G_x, G_y and G_z. Acceleration measurement should be converted to angular value and acceleration magnitude should be converted to angular value, which, in principle, is shown in Fig. 2.

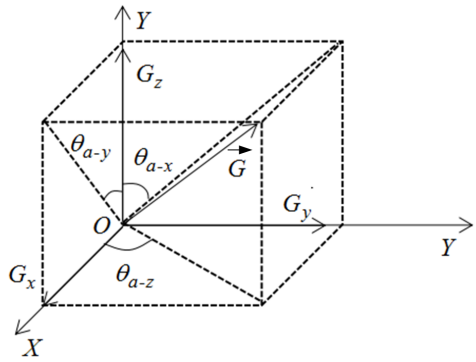

Fig. 2. Principle for measuring angular value with acceleration sensor

The given acceleration sensor was in idle state:

$$\boldsymbol{G}^2 = G_x^2 + G_y^2 + G_z^2 \tag{1}$$

First, normalize vector $\boldsymbol{G}$.

$$F_x = \frac{G_x}{|\boldsymbol{G}|},\ F_y = \frac{G_y}{|\boldsymbol{G}|},\ F_z = \frac{G_z}{|\boldsymbol{G}|} \tag{2}$$

The vector value $\boldsymbol{F}_{\mathrm{a}}$ in the direction of normalized gravity is computed using the formula

$$|\boldsymbol{F}_{\mathrm{a}}| = \sqrt{F_x^2 + F_y^2 + F_z^2} = 1\,. \tag{3}$$

Included angles $\theta_{\mathrm{a}-x}$, $\theta_{\mathrm{a}-y}$ and $\theta_{\mathrm{a}-z}$ between the gravity vector and directions of three coordinate axes were calculated with normalized vector value. Method to

calculate the included angles was shown as follows:

$$\theta_{\mathrm{a}-x} = \arcsin\left(\frac{|F_y|}{\sqrt{F_y^2+F_z^2}}\right),\ \theta_{\mathrm{a}-y} = \arcsin\left(\frac{|F_x|}{\sqrt{F_x^2+F_z^2}}\right),$$

$$\theta_{\mathrm{a}-z} = \arcsin\left(\frac{|F_y|}{\sqrt{F_x^2+F_y^2}}\right). \tag{4}$$

Given rotation angular speed measured by rotating angular velocity sensor around coordinate axes X, Y and Z of components ω_x, ω_y and ω_z. The measured angular velocity should be converted to corresponding rotation angle. According to the collected rotation angular velocity at present and system sampling period, rotation angle of gyroscope rotating around the direction of the three axes was calculated as

$$\theta_{\mathrm{g}y-x} = \int \omega_x \,\mathrm{d}t,\ \theta_{\mathrm{g}y-y} = \int \omega_y \,\mathrm{d}t,\ \theta_{\mathrm{g}y-z} = \int \omega_z \,\mathrm{d}t\,. \tag{5}$$

In the above formula, $\theta_{\mathrm{g}y-x}$, $\theta_{\mathrm{g}y-y}$ and $\theta_{\mathrm{g}y-z}$ denote corresponding rotation angles of axes X, Y and Z after calculation, respectively. Symbol $\mathrm{d}t$ denotes the sampling period of gyroscope data.

Kalman filter was used to fuse information collected by acceleration sensor and gyroscope. Regard acceleration sensor-measured value as predicted value and gyroscope-measured value as observed value. Predicted value revised by observed value was taken as the output value. Drift error b of the gyroscope estimated by the acceleration sensor was taken as the state vector, thus, the state equation and observation equation of system were shown as follows

$$\begin{cases} \begin{bmatrix} \dot{\theta} \\ \dot{b} \end{bmatrix} = \begin{pmatrix} 0 & -1 \\ 0 & 0 \end{pmatrix} \begin{bmatrix} \theta \\ b \end{bmatrix} + \begin{bmatrix} 1 \\ 0 \end{bmatrix} \omega_{\mathrm{g}y} + \begin{bmatrix} \omega_{\mathrm{g}} \\ 0 \end{bmatrix} \\ \theta_{\mathrm{a}} = \begin{bmatrix} 1 & 0 \end{bmatrix} \begin{bmatrix} \dot{\omega} \\ b \end{bmatrix} + \omega_{\mathrm{a}} \end{cases}. \tag{6}$$

In formula (6), $\omega_{\mathrm{g}y}$ denotes the angular velocity representing the output by gyroscope with fixed deviation. θ_{a} denotes the angular value of acceleration sensor after processing. Symbols ω_{g} and ω_{a} denote measurement noise of gyroscope and acceleration sensor. These two measurement noises are mutual independent. For the convenience of calculation, those two measurement noises are assumed to be normally distributed white noises. Given measurement noise of system $\omega(k)$ and sampling period is T_{s}. Thus, the state equation and measurement equation of system are as follows:

$$\begin{cases} X(k) = \begin{bmatrix} 1 & T_{\mathrm{s}} \\ 0 & 1 \end{bmatrix} X(k-1) + \begin{bmatrix} T_{\mathrm{s}} \\ 0 \end{bmatrix} \omega_{gy}(k-1) + \begin{bmatrix} \omega_{\mathrm{g}}(k) T_{\mathrm{s}} \\ 0 \end{bmatrix} \\ V_i = \begin{bmatrix} 1 & 0 \end{bmatrix} X(k) + \omega_{\mathrm{a}}(k) \end{cases}, \tag{7}$$

$$K_{\mathrm{g}}(k) = \frac{P(k\,|k-1)H^{\mathrm{T}}}{HP(k\,|k-1)H^{\mathrm{T}} + \Gamma(k)}\,. \tag{8}$$

In formula (8), $K_{\mathrm{g}}(k)$ denote the Kalman increment at time k. Symbol $P(k\,|k-1)$ denotes the covariance of system at time $k-1$. Symbol H denotes output matrix of measuring system and H^{T} denotes its transpose. $\Gamma(k)$ denotes the covariance of measurement noise. Thus, the fused attitude angle is given as follows:

$$\theta(k) = \theta_{gy}(k) + K_{\mathrm{g}}(k)(\theta_{gy}(k) - \theta_{\mathrm{a}}(k))\,. \tag{9}$$

In the above formula, $\theta_{gy}(k)$ and $\theta_{\mathrm{a}}(k)$ denote the output attitude angle of gyroscope and acceleration sensor at time k, respectively. Symbol $\theta(k)$ denotes the output attitude angle after fusion at time k and the optimal value output by the Kalman filtering at time k. The covariance of the system state at time k was calculated using the formula

$$P(k\,|k) = (1 - K_{\mathrm{g}}(k)H)P(k\,|k-1)\ . \tag{10}$$

Formulae (6)–(10) represent the whole computing process of Kalman filtering. Formulae (8) and (10) were used to guarantee recursiveness and continuity of the filtering algorithm. When received output angular velocity of gyroscope at $k+1$th time, the system would go back to formula (6). Thus, the system entered filtering algorithm at time $k+1$.

The collected multi-sensor data after fusion was more close to true value because measuring angle error of acceleration sensor was carried out. In order to explain effect of fusion algorithm, comparison charts of measurement attitude angle before and after fusion in X direction are shown in Figs. 3 and 4.

The attitude angle curve of stable walk is shown in Fig. 3. It can be seen from this figure that there is a small attitude angle change before and after data fusion. Those two curves were of high coincidence rate and data before fusion was of relatively small curve interference because measuring error of sensor was small when doing slow and stable exercise. Figure 4 shows attitude angle curve of fast walk, a strenuous exercise. It can be seen that the measured angles before and after data fusion were very different. When doing slow and stable exercise, angular value measured by sensor was of small interference and high accuracy. When doing strenuous exercise, the measured angular value was inaccurate because acceleration sensor was influenced by gravity and zero drift of gyroscope. Thus, multi-sensor data fusion was introduced to calculate the optimal estimated value in direction of motion vector, which method greatly lowered gravity vector displacement and zero drift those occurred because of interference of external force [6]. Therefore, smoothing and effective attitude angle

was obtained.

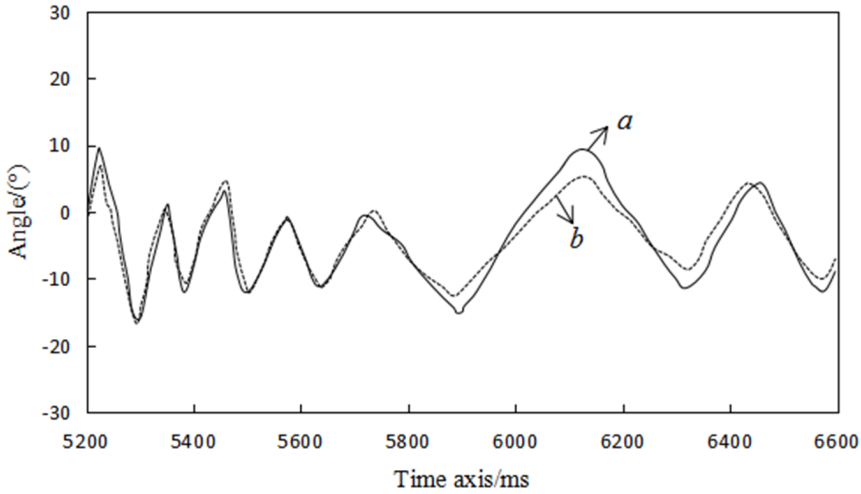

Fig. 3. Angle comparison of stable walk in X axis direction (a: before fusion, b: after fusion)

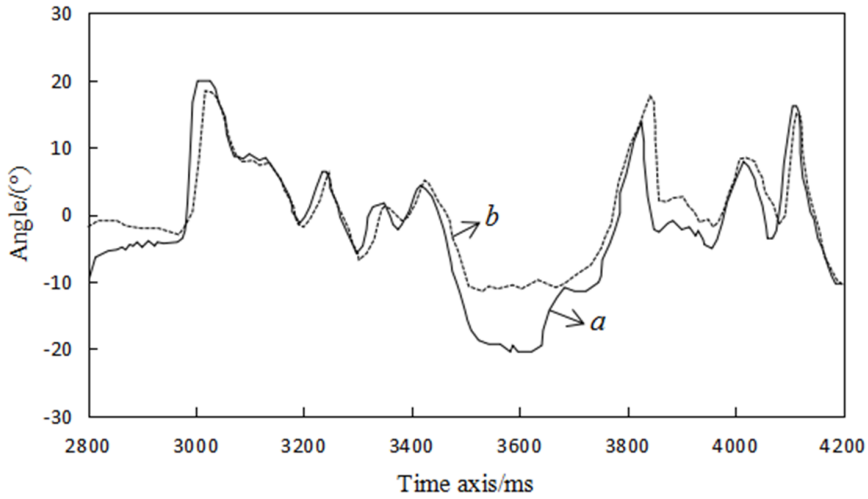

Fig. 4. Angle comparison of fast walk in X axis direction (a: before fusion, b: after fusion)

3.3. HMM model-based identification algorithm for specific motion

Markov chain is a Markov process with discrete parameters of time and state and a specific situation in Markov random process. Markov chain can be described as follows:

$$P(X_{m+k} = q_{m+k}/X_m = q_m, X_{m-1} = q_{m-1}, \cdots, X_1 =$$

$$= q_1) = P(X_{m+k} = q_{m+k}/X_m = q_m)\,, \tag{11}$$

where $q_1, q_2, \cdots, q_m, q_{m+k} \in (\theta_1, \theta_2, \cdots \theta_N)$.

Matrix of transition probability is

$$A = \begin{bmatrix} \mathrm{a}_{11} & \cdots & a_{1N} \\ \vdots & \ddots & \vdots \\ a_{N1} & \cdots & a_{NN} \end{bmatrix}$$

and

$$0 \le a_{ij} \le 1,\ \sum_{a=1}^{N} a_{ij} = 1\,.$$

Several parameters below are used to describe a Hidden Markov Model (HMM):

A: $A = a_(ij)_{N\times N}$ is the state probability transfer matrix. B: $B = b_j(k)_{N\times N}$, $j = 1, 2, \cdots, N$, $k = 1, 2, \cdots, M$ is the probability matrix forthe observed value. N: N is the state number of Markov chain in mode. Finally, π: $\pi = (\pi_1, \cdots, \pi_N)$ is the state vector of the initial probability.

Given a HMM was $\lambda = (\pi, A, B)$. In other words, HMM was made up of two parts. One Markov chain was made up of π and A, producing output state sequence. Another one was a random process described by B, producing observed value sequence.

Standard Baum-Welch algorithm [7] was adopted to estimate HMM parameter. This algorithm was featured by a high timeliness while computation complexity was low. Updating weight with recursive computation effectively reduced its complexity, thus the model parameter that explained sample sequence more accurately was obtained. The computational process of this algorithm is shown below.

Defined variable $\delta_t(i, j)$ that corresponds to observed sequence O. Given S_i and S_j as the states at time t and time $t + 1$ respectively. Thus,

$$\delta_t(i,j) = P(q_t = S_i, q_{t+1} = S_j\,|o_1, o_2, \cdots, o_T) =$$

$$= \frac{\alpha_t(i) a_{ij} b_j(o_{t+1}) \beta_{t+1}(j)}{\sum_i \sum_j \alpha_t(i) a_{ij} b_j(o_{t+1}) \beta_{t+1}(j)}\,. \tag{12}$$

Defined variable $\eta_t(i)$. Given $\eta_t(i)$ denoted probability of observed sequence being in state S_i at time t. Thus,

$$\eta_t(i) = P(q_t = S_i\,|o_1, o_2, \cdots, o_T) = \frac{\alpha_t(i)\beta_t(i)}{\sum_i \alpha_t(i)\beta_{t+1}(i)}\,. \tag{13}$$

It can be seen from formulae (12) and (13) that

$$a_{ij} = P(S\,|S) = \frac{\sum \delta_t(i,j)}{\sum \eta_t(i)},$$

$$b_j(k) = P(O\,|S\,) = \frac{\sum_{t,k} \eta_t(i)}{\sum \eta_t(i)},\ \pi_i = P(S) = \eta_t(i)\,. \tag{14}$$

In this formula, a_{ij}, $b_j(k)$ and π_i are HMM parameters after reevaluation, thus new model was obtained.

Viterbi algorithm was based on dynamic programming. The optimal status switch was obtained with the observed output sequence. Mode was identified by Viterbi algorithm which was used to calculate likelihood. The computational process of Viterbi algorithm follows:

$$\sigma_t(i) = \max P(q_1 = S_i\,|\mathrm{o}_1\,) = \pi_i b_i(o_1),\ 1 \le i \le N\,, \tag{15}$$

$$W_i = 0\,. \tag{16}$$

Formula (16) represents the the initial condition for the system. After forward recursion, the below formula can be obtained

$$\begin{aligned}\sigma_t(j) &= \max P(q_1, q_2, \cdots, q_t) = S_j, o_1, o_2, \cdots, o_t),\\ &= \max[a_{ij} b_j(o_t) \max P(q_1, q_2, \cdots, q_{t-1} = S_i, o_1, o_2, \cdots, o_{t-1})], \\ &= \max[a_{ij} b_j(o_t)\sigma_t(i)],\ 1 \le i, j \le N,\ 2 \le t \le T.\end{aligned} \tag{17}$$

Formula (17) denotes the maximum value of $\sigma_t(j)$ at time t in state i. Given,

$$P = \max \sigma_t(j),\ q_T = \arg max[\sigma_t(i)]\,. \tag{18}$$

It was obtained with recursive operation $q_{t+1} \leftarrow q_t$, $t = 1, 2, \cdots, T-1$. The motion model corresponding to the maximum probability value is taken as identification result, which means that the state motion at present is identified. Flow chart for identifying human motion model is shown in Fig. 5.

4. Experiment and analysis

Based on characteristics of several basic movements, Weizmann data base and ten common movements in this data base including bend, jack, jump, pjump, run, side, skip, walk, wave1 and wave2 were compared to motion data obtained in experiment in order to compute identification rate. Model was built based on regarding those ten motion states as target object for identification. Ten athletes, ranging in age from 22 years old to 30 years old with normal height and weight and no limb illness, was chosen as monitoring objects. Two experiments (5 people in each experimental group) were done and its results was observed and compared. Single acceleration sensor was adopted by the first experimental group to collect human motion information for identifying motion mode. Multi-sensor data after fusion was used by the second experimental group to identify motion mode. Experimenters

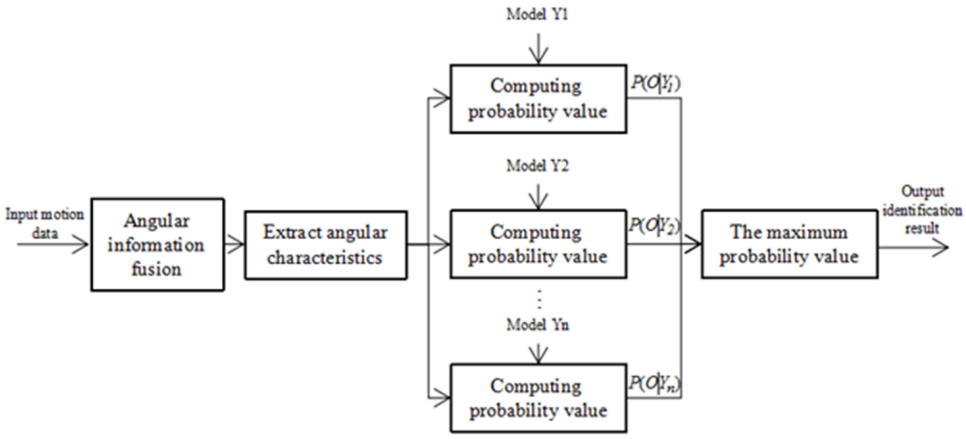

Fig. 5. Flow chart for identifying motion mode

should wear sensor across the upper limb and exercise randomly for one hour without external disturbance. Data collected by information collection module of sensor was transferred to upper computer through wireless communication module. Then, data was analyzed and motion mode was identified. Results of the experiment are shown in Table 1.

Table 1. Thermophysical properties of regular fluid and nanoparticles

State of motion	Identification rate of the first experimental group (%)	Identification rate of the second experimental group (%)
Bend	74.5	83.1
Jack	88.3	96.2
Jump	86.4	92.2
Pjump	81.3	88.4
Run	82.7	95.3
Side	75.3	82.7
Skip	86.9	91.1
Walk	83.5	92.3
Wave1	75.9	85.4
Wave2	79.1	89.7

It can be seen from Table 1 that the identification rate of the second experimental group was much higher than that of the first experimental group. Experiments verified that identifying human motion was more accurate with information fusion than with single sensor.

5. Conclusion

Acceleration sensor and gyroscope was adopted to collect changing information of attitude angle in different motion. Multi-sensor data was fused to extract characteristics of angular value. HMM motion mode was established to identify motion mode according to fusion characteristics. Experiment verified that identifying basic movements was more accurate with multi-sensor HMM based-method. Further study will be focused on classification and identification of relatively complex movements.

References

[1] K. Davids, C. Button, D. Araújo, I. Renshaw, R. Hristovski: *Movement models from sports provide representative task constraints for studying adaptive behavior in human movement systems.* Adaptive Behavior *14* (2006), No. 1, 73–95.

[2] E. C. Neto, E. S. Reboucas, J. L. de Moraes, S. L. Gomes, P. P. Reboucas Filho: *Development control parking access using techniques digital image processing and applied computational intelligence.* IEEE Latin America Transactions *13* (2015), No. 1, 272–276.

[3] F. Khoshnoud, C. W. de Silva: *Recent advances in MEMS sensor technology – biomedical applications.* IEEE Instrumentation & Measurement Magazine *15* (2012), No. 1, 8–14.

[4] F. Sadi, R. Klukas: *Reliable jump detection for snow sports with low-cost MEMS inertial sensors.* Sports Technology *4* (2011), Nos. 1–2, 88–105.

[5] A. Kubacki, P. Owczarek, A. Owczarkowski, A. Jakubowski: *Construction and signal filtering in quadrotor.* Progress in Automation, Robotics and Measuring Techniques, book series AISC *351* (2015), 153–161.

[6] B. Munoz-Barron, J. R. Rivera-Guillen, R. A. Osornio-Rios, R. J. Romero-Troncoso: *Sensor fusion for joint kinematic estimation in serial robots using encoder, accelerometer and gyroscope.* Journal of Intelligent & Robotic Systems *78* (2015), No. 3, 529–540.

[7] T. N. Sainath, D. Kanevsky, B. Ramabhadran: *Gradient steepness metrics using extended Baum-Welch transformations for universal pattern recognition tasks.* IEEE International Conference on Acoustics, Speech and Signal Processing, 31 March–4 April 2008, Las Vegas, NV, USA, IEEE Conference Publications (2008), 4533–4536.

Received May 7, 2017

Acta Technica *62* No. 3A/2017, 173–180

Research on the trajectory tracking technique of table tennis servo machine

Yu Zhang[1,2], Fanyou Meng[1], Qun Sun[1], Huan Meng[1]

Abstract. At present, the robot visual trajectory tracking algorithm can be divided into two categories: One is based on the template matching algorithm, such as histogram matching and background Gaussian estimation; the other is based on the kinematics model trajectory tracking method, such as particle filter, Kalman filter algorithm and so on. However, there are still many difficulties in the actual real-time trajectory tracking, such as the high speed of the table tennis to make the image blurred, the ball in the flight itself by the air resistance, and camera imaging distortion and other factors. It directly leads to the measurement results deviate from the real motion trajectory. On this basis, this paper presents a discrete Kalman filter estimation algorithm for adaptive measurement of covariance. In the different stages of trajectory tracking, the size of the covariance is dynamically adjusted, which not only ensures the fastness and convergence of the initial phase tracking, but also realizes the real-time and stability requirements. Finally, we carry out the experimental test, and the experimental results verify that the tracking algorithm has a good tracking effect.

Key words. Table tennis dispenser, regression tracking, Kalman filter, measurement covariance.

1. Introduction

In recent years, a novel ping pong robot has gradually become one of the research hot spots by reason of its difficulty and challenge in both real-time and intelligent design [1]. Therefore, for the robots, a high efficient vision system with real-time and adaptability for the environment is the base of the whole robot system. Visual tracking is one of the most important topics in computer vision and artificial intelligence [2]. In the target tracking system, the integration of airborne visual system and navigation is used to locate the moving target in real time [3]. Particle filter can model accurately in non-linear non-Gaussian system, and be widely used in object

[1]Mudanjiang Medical University, China
[2]Corresponding author; E-mail: yuzhangmudanjiang@163.com

tracking [4]. Along with rapid descending of computation cost, particle filter algorithm gradually becomes the mainstream [5]. At present, the robot visual trajectory tracking algorithm can be divided into two categories: One is based on the template matching algorithm, such as histogram matching, background Gaussian estimation and so on; the other is based on the kinematics model trajectory tracking method, such as particle filter, Kalman filter algorithm and so on. However, there are still many difficulties in the actual real-time trajectory tracking, such as the high speed of the table tennis to make the image blurred, the ball in the flight itself by the air resistance, and camera imaging distortion and other factors, which directly leads to the measurement results deviate from the real motion trajectory [6]. On this basis, this paper presents a discrete Kalman filter estimation algorithm for adaptive measurement of covariance. In the different stages of trajectory tracking, the size of the covariance is dynamically adjusted, which not only ensures the fastness and convergence of the initial phase tracking, but also realizes the real-time and stability requirements. Finally, we carry out the experimental test, and the experimental results verify that the tracking algorithm has a good tracking effect.

2. Methods

2.1. Modeling and discretization of table tennis movement

In the study of statistics and modern target tracking theory, based on time series analysis, people have proposed hidden Markov model. In this section, we introduce the basic principle of the hidden Markov model and the Kalman filtering method.

The object of this paper is the flight trajectory of table tennis in the air. In theory, the flight trajectory of table tennis is the continuous motion equation of time and space coordinates. That is

$$\begin{aligned} x &= x(t), \\ y &= y(t), \\ z &= z(t). \end{aligned} \tag{1}$$

After tracking the position and velocity of the moving object, the literature [7] gives an algorithm to predict the placement and bounce trajectory of table tennis. Take the x-axis direction as an example, as shown in Fig. 1, the definition of two-dimensional vector is $\boldsymbol{x} = [x, \dot{x}]^{\mathrm{T}}$, respectively, on behalf of the table tennis on the x-axis position and speed.

The continuous state equation of table tennis is described as (note that subscripts are different variables here, not time series labels)

$$\begin{bmatrix} \dot{x}_1 \\ \dot{x}_2 \end{bmatrix} = \begin{bmatrix} 0 & 1 \\ 0 & 0 \end{bmatrix} \cdot \begin{bmatrix} x_1 \\ x_2 \end{bmatrix} + \begin{bmatrix} 0 \\ 1 \end{bmatrix} \cdot a_x . \tag{2}$$

When ignoring the ideal situation of interference, table tennis in the x-axis direction to do uniform motion, obviously deterministic input $u = 0$.

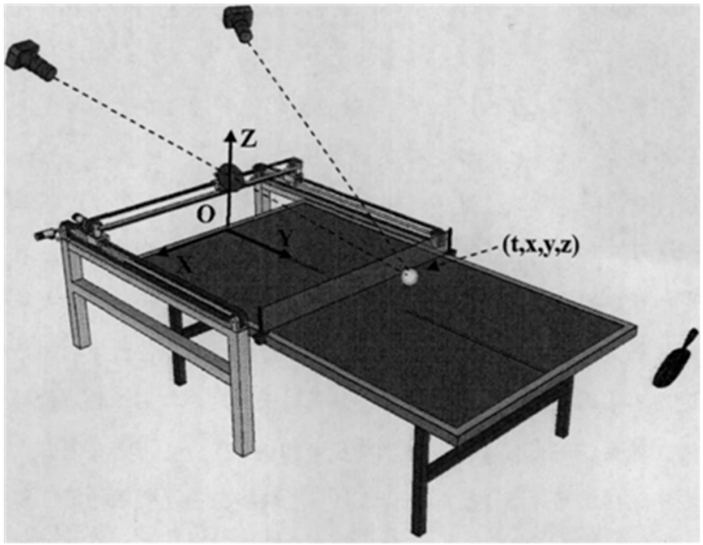

Fig. 1. A three - dimensional coordinate system of table tennis servo machine

2.2. Trajectory tracking algorithm for adaptive measurement covariance

For the elimination of noise in high-speed motion tracking, there are a lot of filtering algorithms. However, a considerable number of algorithms are using frequency domain feature filtering method. From the time domain to the frequency domain, it needs a large amount of computation and it is difficult to guarantee the real-time performance. Therefore, this paper uses a direct time domain filtering method, namely, the discrete Kalman filter.

The algorithm introduces a dynamically modified measurement covariance formula $R_k = f(d_k)$. Here, d_k represents the k-th moment, that is the distance between table tennis and binocular cameras in three-dimensional space. It is defined as follows:

$$d_k = \sqrt{(x_k - x_c)^2 + (y_k - y_c)^2 + (z_k - z_c)^2}\,. \tag{3}$$

In the above formula, x_k, y_k, z_k represent the coordinates of the three-dimensional world coordinate system of the ball, x_c, y_c, z_c represents the coordinates of the midpoint of two optical centers of the left and right cameras. In the binocular vision system used in this paper, the two cameras are placed symmetrically, so this also reflects the depth of binocular vision of table tennis.

3. Experiments and results analysis

The physical device used in this experiment is shown in Fig. 1. In the figure, we define the table tennis robot "visual world coordinate system", the z axis is vertical up, and the xy plane is the table surface. The visual system of the table tennis

robot gives the discrete (t, x, y, z) sequence by locating the spatial position of the table tennis in real time. In this experiment, the robot that we used is the second generation of binocular vision based on the development of the horizontal guide table tennis robot. Consider that the acceleration of gravity is $g = 9.8\,\mathrm{m/s^2}$, so we can set the perturbation acceleration to be $a = 0.1g$. According to the results of camera calibration, the measurement covariance R_k is usually set to the maximum error of measurement. In this experiment, the initial value of R_k is set to 10 mm, and with the decrease of d_k the value of R_k increases gradually to 40 mm.

3.1. Tracking results and contrast experiments

Figure 2 shows the results of the tracking of the axial velocity in the three-dimensional world coordinate system, where the solid line represents the output of the filter and the circle represents the result of the velocity difference directly based on the position information obtained by sampling.

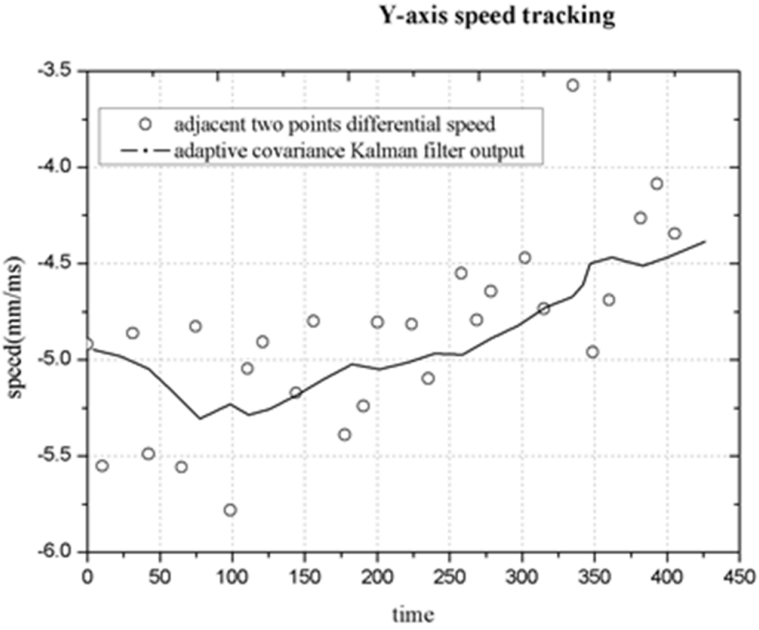

Fig. 2. Table tennis track tracking results indicate–y-axis speed tracking

3.2. Error and correction test

As shown in Figure 3, the anti-jamming performance of the filter is an important measure of real-time visual tracking. In this paper, we introduce a sliding window filtering algorithm (a dashed line) with a smaller computational algorithm, which is often used in the field of digital filtering.

The figure describes the velocity tracking curve in the case of noise interference in

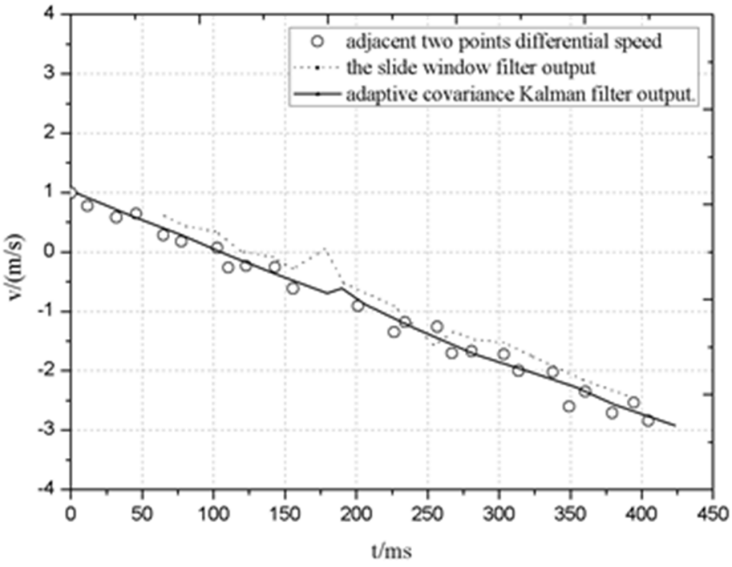

Fig. 3. Tracking results after adding noise to the measured data of z-axis

the z-axis measurement signal. As shown in the figure, a measurement noise signal is introduced near the time of 200 ms, and the measurement result deviates from the actual trajectory. The difference velocity is expressed as a large disturbance (as shown by a circle point in the figure). From the output data curve analysis of the filter, the adaptive measurement of the covariance Kalman filter (solid line) can more effectively suppress the impact of noise on the output, resulting in smaller fluctuations, and it has a large effect on the sliding window filter algorithm output (dotted line).

Due to image processing, light or occlusion and other reasons, it cannot measure the accurate information of table tennis, which means that there may be data loss situation. In this paper, we analyze and simulate the problem of data loss. Figure 4 shows the trajectory tracking results in the case of loss of trajectory measurement data on the z-axis during table tennis. In the case where the Kalman filter in the z-axis direction is between 150 ms and 210 ms and there is no measurement signal input, the track tracking result is shown in Fig. 6. From the velocity tracking curve (solid line in the figure), the adaptive measurement covariance Kalman filter algorithm (solid line) has better adaptability for the loss of data, and the output is smoother, while the sliding window filter algorithm (shown in the dotted line) output has a greater jitter.

4. Discussion of the results

The experimental results show that the initial value of the filtering algorithm has a great influence on the convergence speed. If the initial value is set to a fixed value

of $[0, 0]^{\mathrm{T}}$, and set a relatively large value P of the state covariance at the same time, the resulting tracking process will be a big fluctuation in the first 100 ms and the results of the tracking can be closed to the true value after 100 ms. Therefore, in this experiment, the actual observations are taken as the initial a priori estimates. Since it requires the initial value of the velocity, the difference in the previous two measurements of the position is taken as a priori estimate of the initial velocity. It is proved that the initial value of the measured initial value or multiple measurements is taken as the initial state estimation, so that the follow-up tracking has a better convergence effect. The effective tracking accuracy to ensure that the table tennis drop prediction accuracy is less than 8 cm, and they are all falling within the racket range. At present, the table tennis robot using this method has been able to complete more than 10 rounds of continuous hit.

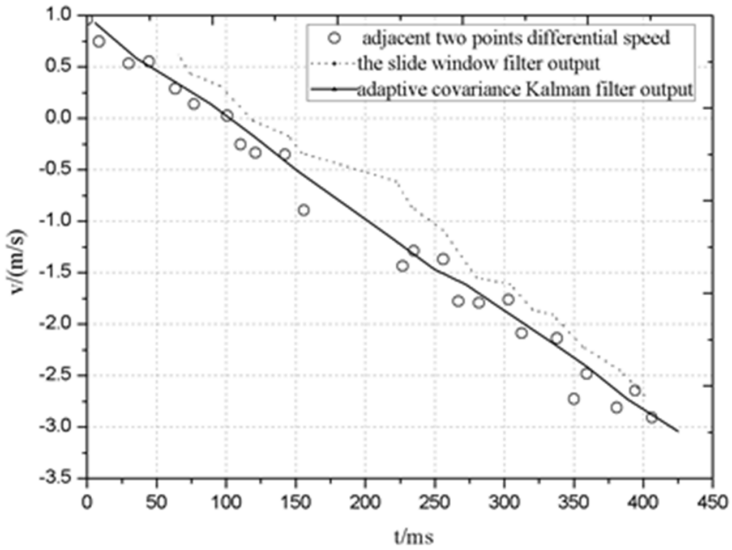

Fig. 4. Analysis of data loss occurs during the z-axis tracking process

5. Conclusion

In this paper, we use the table tennis robot as the research object, and the high-speed flight (5 m/s or more) table tennis as the tracking target, to build a self-adaptive covariance Kalman filter tracking algorithm. The experimental results show that the algorithm has good accuracy and convergence speed, and it can be applied to real-time image tracking and video processing. In real life, a large number of meaningful visual information is included in the movement, such as robot walking positioning and traffic flow detection and so on. Therefore, the real-time motion tracking method has a wider application prospect.

References

[1] Z. Zhang, D. Xu, M. Tan: *Visual measurement and prediction of ball trajectory for table tennis robot.* IEEE Transactions on Instrumentation and Measurement *59* (2010), No. 12, 3195–3205.

[2] Y. Hayakawa, A. Nakashima, S. Itoh, Y. Nakai: *Ball trajectory planning in serving task for table tennis robot.* SICE Journal of Control, Measurement, and System Integration *9* (2016), No. 2, 50–59.

[3] Y. Ren, Z. Fang, D. Xu, M. Tan: *Spinning pattern classification of table tennis ball's flying trajectory based on fuzzy neural network.* Control and Decision *29* (2014), No. 2, 263–269.

[4] Y. Tian, Z. Chen, F. Yin: *Distributed Kalman filter-based speaker tracking in microphone array networks.* Applied Acoustics *89* (2015) 71–77.

[5] N. Yubazaki, J. Yi, M. Otani, N. Unemura, K. Hirota: *Trajectory tracking control of unconstrained objects based on the SIRMs dynamically connected fuzzy inference model.* Proc. IEEE International Fuzzy Systems Conference, 5–5 July 1997, Barcelona, Spain, IEEE Conference Publications *2* (1997), 609–614.

[6] M. C. Liu, Q. Li: *Analysis on the application of region-growing algorithm in table tennis trajectory simulation.* Research Journal of Applied Sciences Engineering & Technology *5* (2013), No. 09, 2779–2785.

[7] E. Beretta, E. de Momi, V. Camomilla, A. Cereatti, A. Cappozzo, G. Ferrigno: *Hip joint centre position estimation using a dual unscented Kalman filter for computer-assisted orthopaedic surgery.* Proceedings of the Institution of Mechanical Engineers, Part H: Journal of Engineering in Medicine *228* (2014), No. 9, 971–982.

Received May 7, 2017

Acta Technica *62* No. 3A/2017, 181–186

Biomechanical analysis on force plate of aerobics shoes

Yang Yang[1]

Abstract. A pair of good shoes is essential to aerobics, especially a pair of professional aerobics shoes featuring shock absorption and injury avoiding. Huakang shoes, Reebok shoes (RBK) and gymnastics shoes are selected as experimental subjects. Experiments on force plate of shoe sole and plantar pressure are conducted to measure mean force value, FT value, PP (Peak Pressure) value and MF value of 12 female aerobics athletes and kinetic analysis is conducted to analyze those data. Thus, some useful references are provided for designing aerobics shoes. Study results show that in experiment on force plate of shoes sole, PP value and MF value of bare foot rank the first and the values of Reebok shoes rank the second among those experimental subjects. Huakang shoes are proved to be better than Reebok shoes in terms of reducing movement FT and pressure. In experiment on plantar pressure, Mean force of Huakang shoes rank the first, FT value and MF value of Reebok rank the first and PP value of bare foot rank the first among those experimental subjects. It proves that Huakang shoes are better than Reebok shoes in terms of reducing FT of ground on foot and reducing vibration during exercise.

Key words. Aerobics shoes, force plate, plantar pressure, biomechanics.

1. Introduction

Medically, feet are regarded as "the second heart" of human, thus both walk and health are influence by shoes [1]. Comprehensively, production requirement of sport shoes was the strictest one among all kinds of shoes. Modern sport shoes should not only be durable and comfortable but also should meet requirement of different sport events to improve performance of athletes [2]. Aerobics is a form of physical exercise for improving health, shaping body and entertaining [3]. With the development of competitive sports, aerobics has developed into an independent sports competition, in which aerobics shoes is of vital importance. Professional aerobics shoes are able to adjust feet load when landing and reduce impact force of athlete when landing, thus sport injury is reduced indirectly.

So far, there are many studies about shoes for basketball and football, S. Zhang et al. [4] studied influence of midsole density of basketball shoes to rebound landing

[1]Shenyang Normal University, Liaoning, 110034, China; E-mail: jack_yangyang@yeah.net

of players. E. M. Hennig et al. [5] studied athletic ability display and its injury with different soccer shoes. However,there are few studies about aerobics shoes. Even fewer studies are focused on foot injury of aerobics athletes from plantar pressure of frequent lower limb movements [6]. Huankang shoes, Reekbok shoes and gymnastics shoes are selected as experimental subjects. Experiments on force plate of shoe sole and plantar pressure are conducted to analyze characteristics of plantar pressure of frequent technical movement. Thus, plantar pressure of different technical movement and different shoes are studied to provide a biomechanical reference for designing and producing aerobics shoes.

2. Experimental subjects and method

2.1. Experimental subjects

Three kinds of shoes were selected as experimental subjects, among which two of them were domestic brands for producing professional aerobics shoes – Huakang specific-aerobics shoes for competition and Reebok specific-aerobics shoes for competition (Hereinafter referred to as Huakang shoes and Reebok shoes respectively). The other shoes were gymnastics shoes that used to simulated barefoot state and its thickness of shoe sole was around 0.1 cm. Specific style of shoes was shown in Fig. 1.

Fig. 1. Shoes for experiment

2.2. Experimental method

1) Experiment on force plate of shoe sole

Twelve females in good health and with normal feet morphologic function and similar competitiveness were selected from professional aerobics team of the Physical Culture Institute. After technical training and preliminary experiment, movements

of those 12 athletes were stable. Thus, the measured data exhibited a high reliability. Those 12 athletes were divided into 3 groups with 4 people in each group. Emed measuring system was applied to measure indexes of plantar such as Mean force, PP, FT and MF (The maximum ground reactive force) when athletes in the three groups were walking on emed force plate wearing Huakang shoes, Reebok shoes and gymnastics shoes, respectively. Before formal experiment, preliminary experiment was conducted. In processing data, standard five-area partition was selected. Detailed standard five-area partition is shown in Fig. 2.

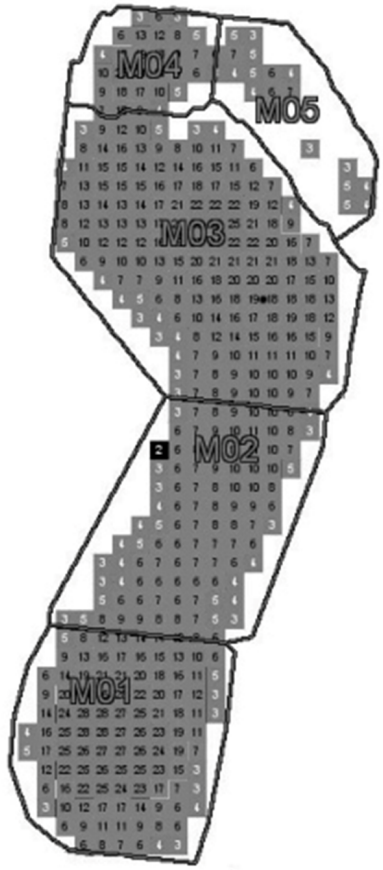

Fig. 2. Plantar-area partitioning

(2) Experiment on plantar pressure

Athletes in three groups wearing Huakang shoes, Reebok shoes and gymnastics shoes those with insole of force plate were required to complete specific aerobics lower limb movements in the set time, including knee lift jump, jumping jack and skip jump. Plantar pressure testing system of insole was used to record partial related mechanical parameter, such as Mean force value, PP value, MF value and FT value. Before formal experiment, preliminary experiment was conducted. All

data were analyzed by software "novel database essential". Besides, EXCEL 2003 and SPSS 12.0 statistical software were used for multivariate statistical analysis and statistical test.

3. Experimental results and analysis

3.1. Results and analysis of experiment on force plate of shoe sole

Four indexes of feet were tested with force plated and the results showed that there were no significant differences for the four indexes of feet. Thus, right foot data of those athletes in the three groups were selected from experiment results and analysis for further analysis. Kinetic parameter of different shoes and barefoot was tested and those data were compared in pairs, and specific results are shown in Table 1 and Table 2. It was shown in Table 1 that performance of Huakang shoes was better than that of Reebok shoes in terms of reducing movement FT and pressure. It was showed in Table 2 that there was a significant difference for Mean Force value of Reebok shoes and barefoot and of Huakang shoes and barefoot. However, there was no significant difference for kinetic parameter of three different kinds of shoes in terms of the other three indexes.

Table 1. Results analysis of kinetic parameter of walking with different kinds of shoes ($x \pm s$)

Shoes	Mean Force (N)	FT (N)	PP (N/cm^2)	MF (N)
Huakang	76.89±14.33	51.90±10.29	309.18±43.21	199.45±21.76
Reebok	80.27±13.63	60.61±19.28	313.54±32.29	258.33±73.61
Barefoot	112.38±23.65	73.63±15.17	501.32±187.25	282.67±37.90

Table 2. Difference comparison for kinetic parameters of walking with different kinds of shoes

Shoes	Mean Force (N)	FT (N)	PP (N/cm^2)	MF (N)
Huakang & Reebok	0.894	0.557	1.002	0.198
Reebok & Barefoot	0.012	0.442	0.114	0.811
Barefoot & Huakang	0.005	0.087	0.112	0.059

On "shoes-ground" surface, there was no significant difference for Mean Force and MF value of athletes in three groups wearing Huakang shoes and Reebok shoes and those values were lower than that of barefoot. It indicated that resultant force of ground cannot be changed by these two types of shoes, but Mean Force value and MF value can be lowered to a certain degree by using difference materials and structure to adjust component forces of plantar and material structure of shoes. In this case, Huakang shoes were better than Reebok shoes. Thus, it can be inferred

that there were no significant difference for active force on the ground of athletes in the three groups wearing those two kinds of shoes. Specifically, Huakang shoes can lower the maximum plantar pressure more than the Reebok shoes did. Thus, Huakang shoes were better than Reebok shoes in terms of reducing movement FT and pressure.

3.2. Results and analysis of experiment on plantar pressure

German insole plantar pressure measuring system was used for recording and difference comparing related mechanical parameters of partial plantar areas when experimental subjects were doing specific aerobics movements wearing different kinds of shoes and barefoot, and the results are shown in Table 3, Table 4 and Table 5, respectively. Data of those three tables show that for those three kinds of shoes, there were some differences but not significant among them for the four indexes. It can be inferred that Huakang shoes were better than Reebok shoes in reducing FT of the fore sole of feet, protecting feet and absorbing shock.

Table 3. Results analysis of jumping jack in different kinds of shoes ($x \pm s$)

Shoes	Mean Force (N)	FT (N)	PP (N/cm^2)	MF (N)
Huakang	148.09±42.78	207.48±88.53	418.79±83.47	352.36±102.69
Reebok	135.12±19.89	378.74±46.21	414.30±120.43	370.53±103.22
Barefoot	135.03±43.33	160.84±74.32	467.90±98.48	362.42±73.82

Table 4. Results analysis of knee lift jump ($x \pm s$)

Shoes	Mean Force (N)	FT (N)	PP (N/cm^2)	MF (N)
Huakang	145.53±46.18	156.37±198.45	374.97±94.03	328.54±132.88
Reebok	133.28±56.90	408.21±189.56	408.79±118.64	358.39±125.34
Barefoot	135.36±53.65	127.67±135.89	423.44±121.78	328.78±138.96

Table 5. Results analysis of skip jump ($x \pm s$)

Shoes	Mean Force (N)	FT (N)	PP (N/cm^2)	MF (N)
Huakang	151.53±56.09	435.61±134.37	401.53±150.02	263.34±132.74
Reebok	125.84±53.22	445.72±169.58	352.54±147.23	312.36±143.12
Barefoot	112.70±39.17	346.73±167.46	423.29±154.52	301.56±153.78

Research showed that plantar contacting area and pressure intensity of plantar areas were increasing with the increasing velocity of movement, thus, ground reactive force of plantar were increasing [7]. In jumping movement of aerobics, the fore sole

of feet played an important part in bearing. Two kinds of sports shoes studied were able be absorb shock of plantar to a different degree and reduce ground impact force for feet. Shock absorption principle was different, but generally, it was made up of shock absorption material and shock absorption structure. Mainly, the frequently used material of shock absorption for aerobics shoes is EVA material. With EVA material shoe sole, Huakang shoes are able to reduce body shock and absorb and reduce reactive force in order to protect feet.

4. Conclusion

Below two conclusions were drawn through experiment on force plate of shoe sole and on plantar pressure:

(1) Huakang shoes are better than Reebok shoes in terms of reducing movement FT and pressure.

(2) Experiments on plantar pressure shows that Huakang shoes are better than Reebok shoes in terms of reducing FT of the fore sole of feet and protecting feet.

These two experiments showed that high springback material is recommended for shoe sole of aerobics shoes because it can improve shock absorption performance. And shock absorption performance of material of the fore sole of feet should be improved when designing professional aerobics shoes.

References

[1] S. M. Abd Elkader, Y. N. Abd Elhafz, S. S. Al-Abdulrazaq: *Foot taping versus medical shoes on kinematic gait parameters in children with Down's syndrome.* World Applied Sciences Journal *27* (2013), No. 3, 311–317.

[2] M. Shieh, Y. E. Yeh: *A comparative study on perceptual evaluations of sports shoe exterior colors in Taiwan.* Color Research & Application *40* (2015), No. TOC. 2, 178 to 193.

[3] M. Héroux, I. Janssen, D. C. Lee, X. Sui, J. R. Hebert, S. N. Blair: *Clustering of unhealthy behaviors in the aerobics center longitudinal study.* Prevention Science *13* (2012), No. 2, 183-195.

[4] S. Zhang, K. Clowers, C. Kohstall, Y. J. Yu: *Effects of various midsole densities of basketball shoes on impact attenuation during landing activities.* Journal of Applied Biomechanics *21* (2005), No. 1, 3–17.

[5] E. M. Hennig: *The influence of soccer shoe design on player performance and injuries.* Research in Sports Medicine an International Journal *19* (2011), No. 3, 186–201.

[6] Q. E. Qiu, Q. L. Hu, Y. D. Gu: *Experimental study on mechanical properties of sole materials of aerobics sports shoes.* Advanced Materials Research *341–342* (2011), 77 to 79.

[7] K. Wörtler, C. Schäffeler: *Acute sports injuries and chronic overuse stress damage to the forefoot and midfoot.* Radiologe *55* (2015), No. 5, 417–423.

Received May 7, 2017

Acta Technica *62* No. 3A/2017, 187–196

Research and application of volleyball target tracking algorithm based on surf corner detection

Guowei Yuan[1]

Abstract. Real-time target tracking is a popular application in the field of computer vision, and it is also a topic of practical significance. As the requirements of tracking speed and precision in modern society are more and more high, corner point has the advantage in improving tracking precision as the key feature of image. SURF corner detection algorithm is extensible, suitable for combination with other target tracking algorithms, and it can be combined with motion detection and other tracking algorithms to improve the speed. In this paper, the SURF corners detection algorithm and target tracking algorithm are studied, and an improved method of combining the SURF corner detection with the Kalman filter is proposed. The Kalman filter prediction and updating algorithm is used to rapidly update the region of interest.

Key words. Target tracking, SURF corner detection, Kalman filter, tracking speed.

1. Introduction

In recent years, with the rapid development of surveillance system, the application of real-time position tracking of monitoring image gets more and more widely used in many areas, quantity demand also gets bigger and bigger, and the accuracy of the tracking system is getting higher and higher. However, due to the real-time tracking requirements, many tracking algorithms have to reduce the accuracy requirements, it can easily lead to tracking failure [1]. The tracking will be seriously disturbed when the tracking target is close to the target environment [2]. The corner is an important local feature of the image, also known as the feature points, the video sequences can be detected and matched. Although there is no definite mathematical definition of corners so far, corner points are usually defined as points that can contain enough information of the image, which focuses on the important shape and edge information [3]. By using the rotation invariant feature of corner point and the insensitive to light and the advantages of very few pixels, this method is applied to

[1]Physical Culture Institute, Ningxia Normal University, Guyuan, 756000, China; E-mail: guoweiyuan1982@163.com

target tracking by optimizing the speed of corner detection.

In this study, the tracking algorithm based on corner detection is applied to the volleyball test in order to track the movement of volleyball and calculate the distance. Through this study, the human error in the process of volleyball testing is solved, and the test results are more reliable.

2. SURF algorithm

2.1. SURF corner detection algorithm

There are different sizes of objects in the image. If an attempt is made to use fixed dimensions to match the same corner feature in different frames, such as the Harris operator, the strength response template will not match due to the scale change. The principle and process of SURF corner detection algorithm are described in the following.

Firstly, according to the definition of SURF corner, the algorithm uses the Hessian matrix [4] to describe the corner of the image, which is used to represent the local curvature of a pixel, that is, to find the corresponding pixel level and the vertical direction of the second-order partial derivative. It is shown in equation

$$H\left(I\left(x,y\right)\right)=\left[\begin{array}{cc}\frac{\partial^2 I}{\partial x^2} & \frac{\partial^2 I}{\partial x\partial y}\\ \frac{\partial^2 I}{\partial x\partial y} & \frac{\partial^2 I}{\partial y^2}\end{array}\right]. \tag{1}$$

In the equation, $I(x,y)$ is the pixel point in the image whose coordinates are (x,y).

According to the specificity of SURF angular scale independence, Hessian matrix needs to introduce scale variable. The so-called scale is the definition of clarity, the larger the scale, the more blurred the image, on the contrary, the smaller the scale, the clearer the image. In the field of image processing, Gaussian filtering can be used to simulate the scale. Let σ be the standard deviation of the Gaussian function, which implicitly defines the scale of the image. The filter with larger σ value smooths the details of the image. The larger the image scale, the more blurred the image. The Gaussian filtering equation is shown in (2).

$$G\left(x,y\right)=\frac{1}{2\pi\sigma^2}\mathrm{e}^{-\frac{\left(x-\frac{m}{2}\right)^2+\left(y-\frac{n}{2}\right)^2}{2\sigma^2}}. \tag{2}$$

In the equation, x,y are the coordinates of the corresponding position on the template and m,n define the Gaussian template size that is expressed as $m\cdot n$.

2.2. Optimization of SURF corner description

According to the study of corner detection algorithm in this study, the following description of SURF corner points is studied and optimized [5]. Firstly, the process of SURF corner description is described briefly. At last, the optimization scheme is

given.

(1) Determine the corner orientation:

Using the detected corner features, the principal directions of these corner points are determined, that is, the direction of the region with the largest gray-scale variation is described.

The method can be simply described as the center of the corner to calculate the radius of 6σ (σ being the corresponding scale value of the corner) within the neighborhood of pixels in the x, y directions of the Hall wavelet response. The so-called Hall wavelet response reflects the gray-scale image changes, here used Hall wavelet template side length is 4, respectively, 4×4 neighborhoods in x, y direction of gray-scale changes. Then, in the range of 360 degrees, every 60 degrees to do a Harvard wavelet response vector addition operation. And finally, select the direction of the longest vector as the main direction of the corner. That is, the main direction describes the direction of the most dramatic changes in gray, as shown in Fig. 1.

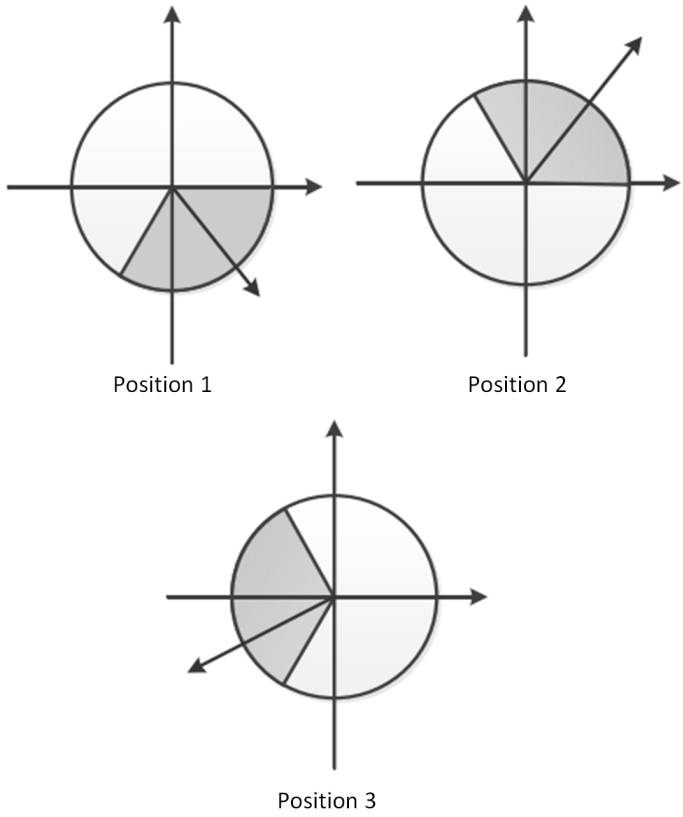

Fig. 1. Schematic diagram of main direction determination method

(2) Rotation corner neighborhood

After determining the main direction, we need to construct the descriptor of the main direction of the corner point. The method is to center the corner point, take

the square with a side length of 20σ as the neighborhood, and rotate with its main direction as the rotation angle.

2.3. Target tracking algorithm

(1) Kalman filter

Kalman filter is the most typical representative of the predictor, the so-called predictor refers to the completion of the target motion prediction method, which can accurately predict the next frame of the target state of motion. Kalman filter test phase to consider three kinds of movement [6].

(2) Optimized tracking algorithm

Based on the optimization of the SURF corner detection algorithm and the motion prediction function of the Kalman filter, a tracking algorithm combining the improved SURF corner detection and the Kalman filter is proposed. The Kalman filter is used to predict the center position and velocity of the target, and return to the possible region of interest, that is, the region of interest. The SURF corner detection is performed in the reduced area and the matching tracking is completed.

- The x_k Kalman prediction system with target state vector $\boldsymbol{A}$ is established, and the predicted position of the target can be predicted by Kalman filter. it is given by the equation (3).

$$x_k = \begin{bmatrix} x \\ y \\ v_x \\ v_y \end{bmatrix}. \tag{3}$$

  where x is the pixel abscissa of the target center in the image and y is the pixel ordinate of the center of the target in the image. Symbol v_x denotes the moving speed of the target center point in the x-axis direction of the image coordinates and v_y stsnds for the movement speed of the target center point in the y-axis direction of the image coordinates.

- The observation vector z_k of the moving object is determined, as shown in the equation (4).

$$z_k = \begin{bmatrix} z_x \\ z_y \end{bmatrix}. \tag{4}$$

  In this equation, $(z_x z_y)$ is the observed center of coordinates of the moving object.

3. Design of target tracking

3.1. Target detection design

(1) SURF corner detection

According to the study and analysis of SURF corner detection algorithm, the general steps of its implementation are shown in Fig. 2.

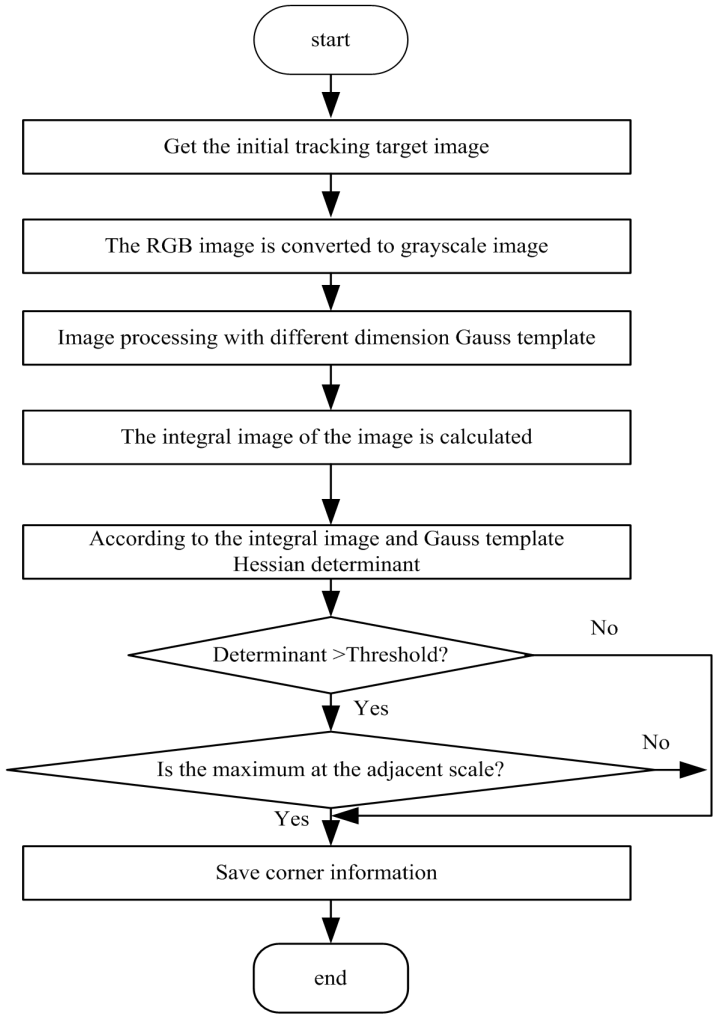

Fig. 2. SURF corner detection algorithm flow chart

(2) SURF corner description

Although the corner description process is encapsulated in the same function as corner detection, however, due to the complexity of the implementation of the corner description, the flow is described separately here. It is shown in Fig. 3.

3.2. Target prediction tracking design

(1) Target prediction

According to the optimized tracking algorithm, the realization of motion pre-

diction is the realization of Kalman filter. The realization of the specific process is shown in Fig. 4. The implementation of the prediction update of the region of interest is described in detail below.

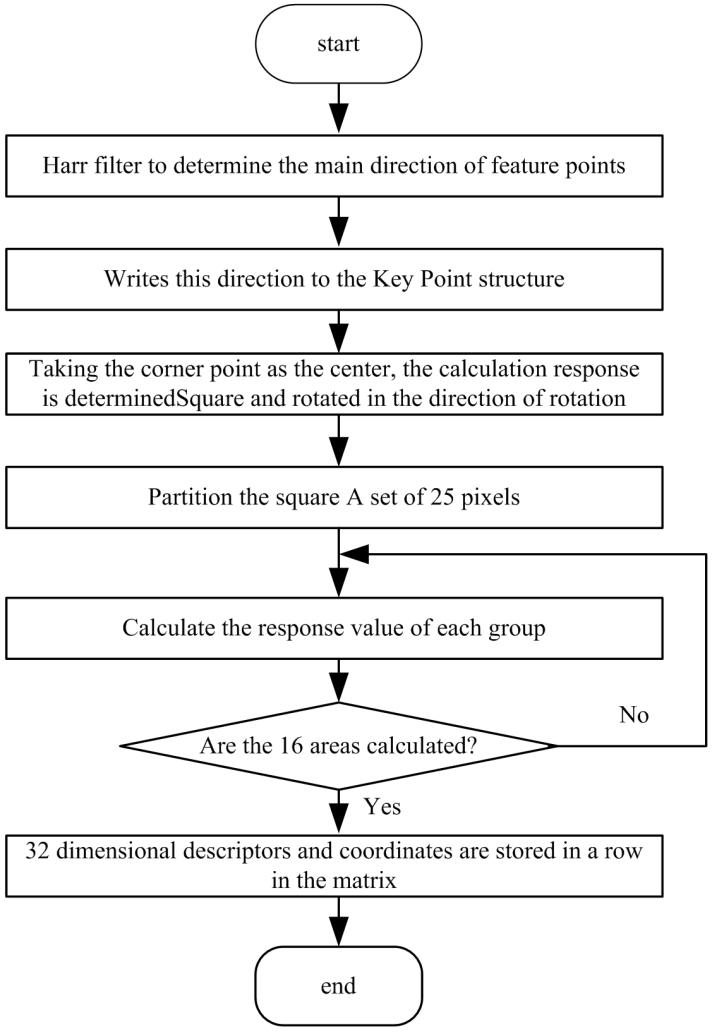

Fig. 3. Corner description implementation flow diagram

- When the tracking is started, the region of interest of the initial two consecutive frames is set to the whole tracking window. After detecting the matching to the target, the Kalman filter is initialized with its center position and velocity and the region of interest is updated.
- When there is no match to the corresponding target, the entire tracking window is set again as the region of interest and the variable representing the number

of frames is reset to zero. According to the analysis of the Kalman filter, it is necessary to set the transfer matrix F and gain matrix H, and transfer the process noise covariance matrix Q and observation process noise covariance matrix R. Matrices F and H are set as shown in equation (5).

$$Q = \begin{bmatrix} 0.01 & 0 & 0 & 0 \\ 0 & 0.01 & 0 & 0 \\ 0 & 0 & 0.01 & 0 \\ 0 & 0 & 0 & 0.01 \end{bmatrix}, \quad R = \begin{bmatrix} 0.0001 & 0 \\ 0 & 0.0001 \end{bmatrix}. \tag{5}$$

(2) Target measurement output

In the output part of the results, the system must ensure that tracking and output results are provided at the same time, that is, real-time output, which requires a refresh function, refresh once per second.

4. Results and discussion

After the optimization, the speed of 512×512 Lena RGB image is described, and the test result is shown in Fig. 4.

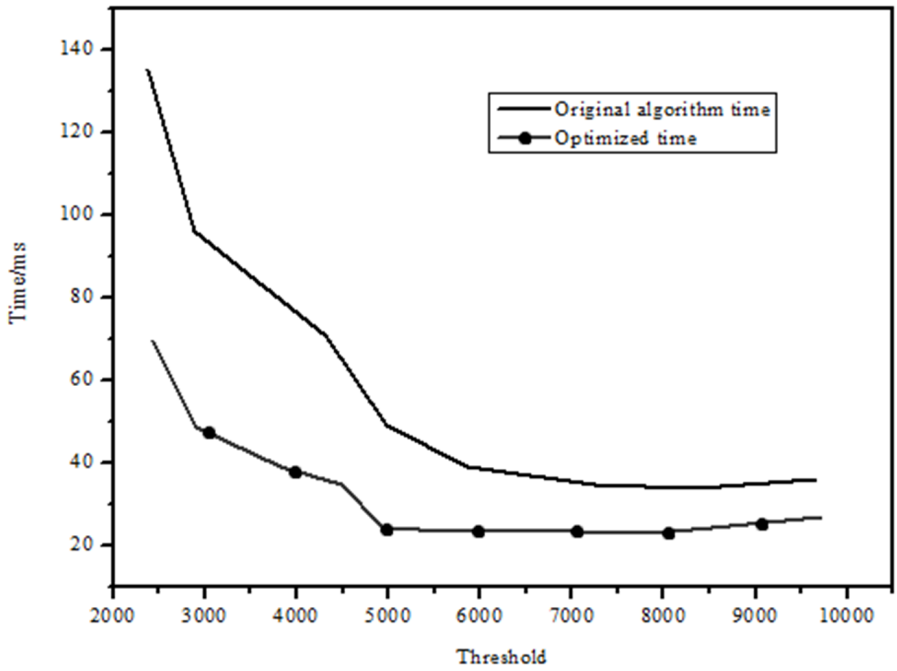

Fig. 4. Comparison of line charts of the corner description time after the optimization

It can be seen from Fig. 5 that the optimized algorithm consumes only 50 % of the

time described in the original algorithm. The speed has been significantly improved. Since the dimension of the corner vector is smaller after optimization, it will also improve the speed in tracking and matching process. In this paper, two identical 512×512 Lena RGB images are tested for matching speed. The matching method is based on the widely used Euclidean distance matching method.

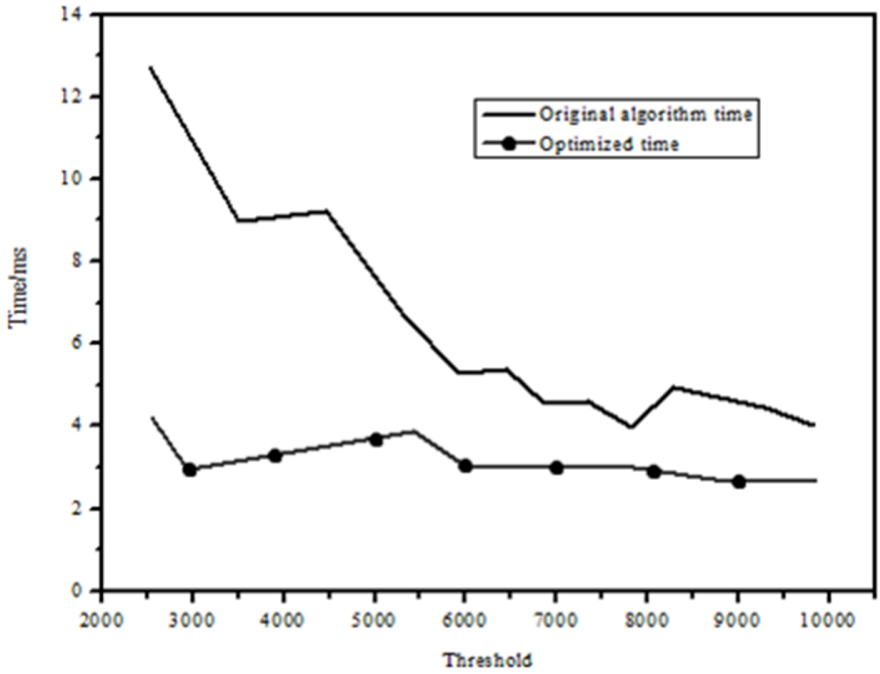

Fig. 5. Comparison of line charts of corner optimization

It can be seen from Fig. 5 that the optimized description algorithm significantly improves the speed of operations. The time in the Fig. 5 means the time required for the corner point to complete the description. It is the time taken to describe the corner points of the volleyball image shown in Fig. 5 after setting the different thresholds for corner detection. The time used is only 33 % of the original algorithm.

5. Conclusion

In this paper, based on the research of SURF corner detection algorithm, we proposed a real-time target tracking method which combines the optimized SURF corner detection algorithm and Kalman filter. The improved corner detection algorithm is applied to the volleyball test and tracking system, and the tracking effect of the system is tested by using the volleyball. It is verified that the algorithm can track the real-time moving object accurately.

References

[1] I. Kortabarria, J. Andreu, I. M. de Alegría, J. Jiménez, J. I. Gárate, E. Robles: *A novel adaptive maximum power point tracking algorithm for small wind turbines*. Renewable Energy *63* (2014), No. 1, 785–796.

[2] F. J. Hu, X. Zhen: *Robot path planning model of target gravity optimal RRT algorithm*. Revista Tecnica De La Facultad De Ingenieria Universidad Del Zulia, Technical Journal of the Faculty of Engineering *39* (2016), No. 7, 403–414.

[3] J. P. Lee, Q. Q. Wu, M. H. Park, C. K. Park, I. S. Kim: *A study on modified hough algorithm for image processing in weld seam tracking system*. Advanced Materials Research *1088* (2015), No.Chapter 10, 824–828.

[4] L. Li, Y. Hu, X. Wang: *Design sensitivity and Hessian matrix of generalized eigenproblems*. Mechanical Systems and Signal Processing *43* (2014), Nos. 1–2, 272–294.

[5] T. N. Shene, K. Sridharan, N. Sudha: *Real-time SURF-based video stabilization system for an FPGA-driven mobile robot*. IEEE Transactions on Industrial Electronics *63* (2016), No. 8, 5012–5021.

[6] Y. Wu, H. Fu, Q. Xiao, Y. Zhang: *Extension of robust three-stage Kalman filter for state estimation during Mars entry*. IET Radar, Sonar & Navigation *8* (2014), No. 8, 895–906.

Received May 7, 2017

Acta Technica *62* No. 3A/2017, 197–204

Design and research of smart boxing trainer based in physical education practice on the sensor

Zhengmao Li[1]

Abstract. Since the 20th century, boxing has developed rapidly and become popular among people. According to techniques and tactics and training requirements of all kinds of boxing, a smart boxing trainer based on the sensor is designed in the study. The system of the designed smart boxing adopts STC12C5A60S2 processing chip in hardware, including signal collection, deviation compensation, voice announcement and other modules. In terms of software, Keil μVision2 is used to realize the initialization driver to hardware modules, helping collect power signals and eliminate interference and set the time and voice modules. BSDSOI S SD voice chip is combined with Interphonic 5.0 to broadcast results of the training. Finally, the system is tested, the deviation source is analyzed and the deviation is compensated. The experiment shows the training method is effective, that the system is viable, and that the system can be used by coaches to make more targeted training plan for trainees.

Key words. Sensor, boxing training, boxing training, trainer, system calibration.

1. Introduction

Boxing is a valuable event, which can improve the coordination of human body and stabilize the respiratory system [1]. So in order to meet the requirements of training, training devices designed for boxing emerge. In China, training devices are relatively backward, which mainly includes hand target, training bag and simulated target as a result of outdated technology and knowledge. The training devices are too outdated, dull and stereotyped to systematically acquire training data [2]. Therefore, it is difficult for coaches to make horizontal and vertical comparison for trainers, which may affect their improvement. A new type of equipment, which works in collecting data and integrating teaching, training and testing, seems to be very important.

In box training, physical training device are interesting and scientific. At present,

[1]College of Sports Science, Shenyang Normal University, 110034, Liaoning, China; E-mail: zhengmaolimaoli@yeah.net

many types of training devices have produced in China, which can only record one punching position [3–4]. Training devices produced abroad have many positions and complete functions. But these devices are costly, so they cannot be generally used in China [5]. For example, linear displacement sensor of the taekwondo trainer manufactured in South Korea displays in spite of slow force, so the design of the device has weakness in measurement. The cost of the trainer itself is so high that it cannot be used widely in China [6]. Based on the above conditions, the simulated training target of the smart boxing trainer is designed according to techniques and tactics and training requirements. Computer technology is embedded in the device to control it, realizing the digitization of boxing punching information. Sensing technology is also used to exactly measure punching points and momentum and other key moving parameters. Hence, an intelligent man-machine training is realized, which makes it possible for coaches to make better plans for the trainees.

2. Hardware design of the smart boxing trainer

2.1. Realization of simulated system

Basic equipment used in the design is the primitive pile trainer currently existing in the market. And meanwhile, kennel processing control chip is also implanted in the trainer by electronic technology. Hardware function structure of the system is shown in Fig. 1. The flow chart of specific modules is shown in Fig. 2.

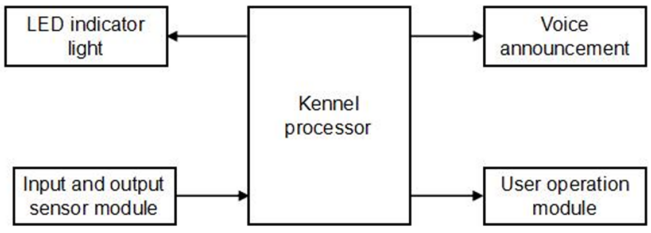

Fig. 1. Hardware function structure of the system

In the designed system, pressure transducer is voltage sensor. Signal acquisition and converter of the system are very important. The pressure sensor can convert power signals of boxing trainees into voltage signals. And these tiny voltage signals are converted into sample signals of A/D converter after amplification and wave filtering. At last, A/D converter converts these simulated voltage signals into digital signals again and send to microprocessor for processing. TH4805 pedal force sensor in the design is adopted as signal acquisition unit.

TH4805 sensor works in a strain mode, and its working principle is shown in Fig. 3.

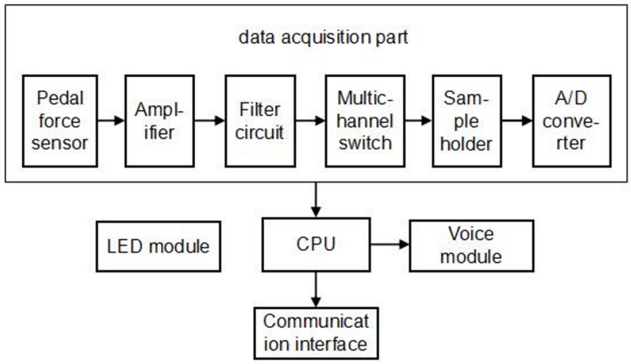

Fig. 2. Flow chart of modules data acquisition part

2.2. Realization of digital system

In designing the power module, voltage regulator in the system is LM317, enlarging the input range of supply voltage. In order to enhance the stability of circuit voltage, TL431L regulator chip is used in the system. 479 μF capacitor and 104 filter capacitor are also used in the input part of the power module so as to reduce interference. Serial communication circuits are added to the power module. Level conversion chip of MAX232 is embedded in the system in the way of RS232 bus. As for voice module, audio playback module BSD5015 SD is used. Therefore, a LM317IC chip converted by a 3.3 V voltage is employed. In terms of MCU processing module, processor chip STC12C5A60S2 is used, which has high speed, lower power consumption and strong ability of anti-interference. STC12C5A60S2 is the main control part of data collection. 8/10 bit resolution through chip integration makes analo-to-digital conversion for dynamic analog signals and sends the collected data to the control memory.

3. Software implementation of the smart boxing trainer

3.1. Power signal acquisition and interference elimination

In the process of power signal acquisition, three threshold values are set as system evaluation limits, whose determination system adopts the training quantification standard of national boxing player. The power signal is amplified 10 times, the acquired signal is sent to MCU, whose voltage signal ranges from 0 to 5 V. As 8 bit binary A/D conversion is applied in the system, the signal precision is $1/(2^8-1)$. When the binary is x after receiving A/D conversion, the corresponding voltage signal value is $5x/(2^8-1)$ and power signal value is about $5x/(2^8-1)\times 1000/5$ N. In the implementation of the program, three graders are set, standing for the grade limit of three voltage signals, namely, 0x30, 0x80and 0xCC, and their corresponding power signals are about 20 kg, 50 kg and 80 kg. The detailed data acquisition flow is shown in Fig. 4.

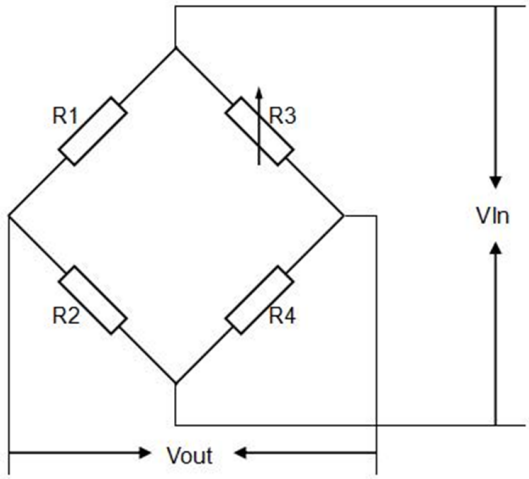

Fig. 3. Working principle of TH4805 sensor

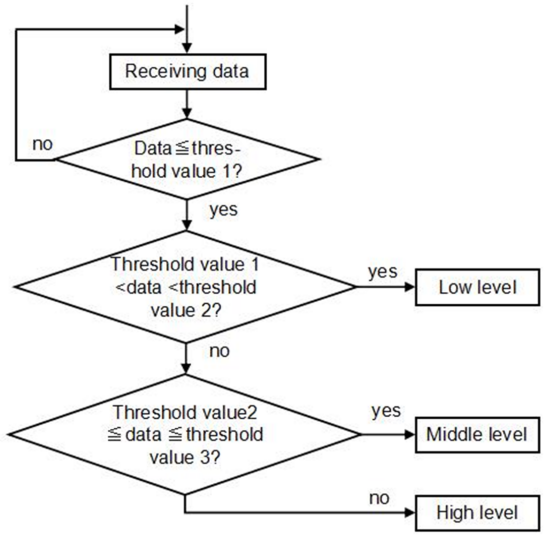

Fig. 4. Process of force data acquisition

When the trainee punches the target, it can be seen from the oscilloscope display: there is a nearly 10 ms interval from the beginning of the wave form to the maximum value. But the the precision the system requires is detecting 4 boxing data in a second (the time to do a boxing is 250 ms or so), so it takes just 200 ms to know the maximum value of voltage change. The system may be affected by glitch signal in acquiring signals, so the time for AD conversion is set 5.5 μs. And 100 conversions takes about 600 μs. The average value of 100 voltage values is taken as a signal acquisition point. It takes 200 ms to acquire 300 average values. By sequencing

these averages, the maximum value is clear so that interference in signal acquisition can be decreased.

3.2. Setting of time and voice system

It is concluded and found from the researches and experiments: in high state of rapid boxing, the high-quality boxing of common training people is mainly in the preceding 50 times. Therefore, in designing the system, 10 s is set as the round time to evaluate the performance of users. Timer 0 working mode of MCU is applied in designing the program. The crystal oscillator of MCU is 12 MHz, and its mechanical period is 50 ms, hence, the time of 200 exactly corresponds to 10 seconds. Meanwhile, voice announcement module is added in the system to report the training results of trainees. BSD5015 SD card audio playback module used in the design combines Interphonic 5 speech synthesis system made by Iflytek.

4. System detection of the smart boxing trainer

4.1. System calibration

The designed system in the study is calibrated statically and dynamically. The process of static calibration is: within the 1000 N measurement, as the amplified sensor signal is converted to 0–5 V voltage signal by AD, the correspondent pressure of each 1 V voltage signal is 200 N or so. In addition, the calibration also includes voltage detection by the potentiometer, which directly chooses the output voltage (5 V) of the chip. When it is rotated to the maximum, PI.0 port voltage of 60S2 is 4.99 V and meanwhile the power of voice announce is 996 N. The specific static calibration results are shown in Table 1.

Table 1. Static calibration

Voltage (V)	Standard pressure (kN)					
	0	c	c	c	c	c
Stroke	(1)	(2)	(3)	(4)	(5)	(6)
Forward stroke (1)	0.000	1.002	2.006	3.008	4.006	5.007
Reverse stroke (1)	0.001	1.004	2.007	3.009	4.004	
Forward stroke (2)	–0.003	1.005	2.010	3.003	4.007	5.003
Reverse stroke (2)	–0.004	0.998	2.005	3.006	4.009	
Forward stroke (3)	–0.002	1.007	2.009	3.011	4.012	5.012
Reverse stroke (3)	0.003	1.007	2.008	3.007	4.005	
Average value	–0.0012	1.004	2.007	3.007	4.007	5.008

Besides, when dynamic measurement calibration is carried on, as the human target face is installed with cushion and spring device, the deviation is higher than that of the static calibration. The whole dynamic measurement calibration work

is done according to law of conservation of momentum, and the specific method is: swing balls are placed in the same height. They are free to fall successively. The force of punching area of human target and impact force induction balance after these balls fall is collected. By comparing several experiments, it can be found that the force collected dynamically is by 30–40 N smaller than that of the standard strength under rigidity. Different trainees are in different states, the training target had better be more flexible. Under this circumstance, some deviations in dynamic state can be ignored compared with the overall effect of the system.

4.2. Deviation compensation

The sensor in the system is relatively sensitive. In real-time detection, the system automatically enters to the working statement in power-on condition and produces deviation of measurement data because the sensor is embedded inside the human target and creates mechanical pressure in fixing with the target. In order to solve the above problems, the dial switch is connected in the system to set lower threshold value under detection. The dial switch with 8 bit binary can be set to 255 to the maximum. After debugging, the compensation of 0x10 is made in the system. It is about 60 N, namely, FR (R means real value) = FA (A means acquisition) – FC (C means compensation).

5. Conclusion

After investigating the current situation and needs of boxing market at home and abroad, the creation of the study and viability are approved, which means modern electronic technology and boxing training are combined in an effective way of designing a smart boxing trainer based on the sensor. Hardware circuit module plan as well as hardware circuit controlling works of each module (acquisition module, power module and voice module) are designed, thus making it possible to acquire signal, eliminate interference and set time and voice module. In the latter stage of circuit debugging, the system is calibrated statically and dynamically, which verifies the viability of the system.

References

[1] M. Cheraghi, H. A. Alinejad, A. R. Arshi, E. Shirzad: *Kinematics of straight right punch in boxing.* Annals of Applied Sport Science *2* (2014), No. 2, 39–50.

[2] S. el Ashker: *Technical performance effectiveness subsequent to complex motor skills training in young boxers.* European Journal of Sport Science *12* (2012), No. 6, 475–484.

[3] C. Yahne, S. Jackson, K. Tollestrup: *Training teen mothers as motivational interviewers: A feasibility study.* Motivational Interviewing Training Research Implementation Practice *1* (2015), No. 3, 25–30.

[4] M. C. Chyu: *A non-competitive martial arts exercise program for health and fitness in the general population.* Journal of Human Sport & Exercise *5* (2010), No. 13, 430–443.

[5] T. W. Woodward: *A review of the effects of martial arts practice on health.* WMJ: Official Publication of the State Medical Society of Wisconsin *108* (2009), No. 1, 40–43.

[6] R. A. Fox, E. Jacewicz, F. R. Eckman, G. K. Iverson, S. A. Lee: *The effect of short-term training on production and perception of s?? by Korean speakers.* Journal of the Acoustical Society of America *126* (2009), No. 4, 2311.

Received May 7, 2017

Acta Technica *62* No. 3A/2017, 205–212212

Research on energy-saving management and control of stadiums & gymnasiums based on Android SHD

Lijing Cao[1]

Abstract. As people pay more attention to sports, the degree of participation is getting higher and higher, the large and comprehensive gymnasiums are sprung up everywhere in the country. Different from the small gymnasium, modern large-scale gym is more powerful, and the control ability is more intelligent and humane, but there are still some inadequate. For example, the control is too centralized and regardless of flexibility. Based on this, this study proposed the use of Android SHD (smart handheld device) as a mobile terminal to match with the server work, so as to further improve the system functions. This study is based on the bus of the gym intelligent lighting control system, combined with wireless technology, to establish handheld devices and server communications, to achieve the indirect control of the gym lighting equipment through the two instruction interaction. The main work of this study is to select the communication protocol, establish communication, collect the command set and design Android SHD interface and so on. Through this study, we achieve the communication between client and server, and also set a more detailed and comprehensive function for client system, and then improve the original gymnasium intelligent lighting control system functions through Android SHD with the work of the server. The energy-saving management has a great practical significance.

Key words. Android, SHD, gymnasium, low frequency, energy-saving management.

1. Introduction

As people pay more attention to sports, the degree of participation is getting higher and higher, the large and comprehensive gymnasiums are sprung up everywhere in the country. Different from the small gymnasium, modern large-scale gym is more powerful, and the control ability is more intelligent and humane. It not only provides basic sports venues for sports activities, but also can host conferences, cultural activities and exhibitions, greatly improve the comprehensive utilization of the stadium and economic usefulness. Meanwhile, it offers a more comfortable and modern place for people. Lighting, as an important manifestation of stadium function, is an important part of the stadium design [1]. At the same time, when

[1]Tianjin Vocational Institue, Tianjin, 300402, China; E-mail: lijingcaoljc@163.com

broadcasting the event, it is asked to show clear and comprehensive pictures for the television audience. And in order to achieve the above requirements, the stadium lighting should be ensured appropriate in vertical and uniform illumination, and the color, temperature, color rendering index, three-dimensional all need to achieve the standard parameter [2].

The gymnasium electric energy saving control system of this research is based on the CAN bus technology, to establish the entire communication used for gymnasium lighting, take the embedded web server as the entire intelligent lighting system control center. The user can achieve a variety of gymnasium lighting control through the image of the page in the developed server [3].

This study aims at the lack of intelligent lighting control system in modern gymnasium. This study puts forward the idea of central controller through the cooperation of mobile terminal. As Android development platform has a wealth of hardware options and a strong software framework support, so Android SHD has a wide application. Therefore, this study selects Android SHD as a mobile terminal, with the central controller to work, so as to further improve the gym energy control management research.

2. Basic communication experiment

2.1. The research of Android-based application

Before the establishment of the client and server communication, we need to build Android development platform, it includes JJDK, SDK, eclipse plug-in, and ADT plug-in. After successfully installing the above tools, you can use the AVD to develop Android application. First, we need to start Eclipse and select "File" item, then select "New", and then select "Android Application Project".

Before the establishment of the client and server communication, we need to build Android development platform, it includes JJDK, SDK, eclipse plug-in, and ADT plug-in. After successfully installing the above tools, you can use the AVD to develop Android application. First, we need to start Eclipse and select "File" item, then select "New", and then select "Android Application Project".

We need to respectively type the appropriate name on Application name, Project Name, and Package. Usually, it should be noted that Application Name and Project Name use capital letters, Package Name use lowercase letters, and the choose of SDK version according to objective conditions and practical needs Select, when we select "Finish", then a new project was born [4].

After the successful creation of Android AVD, we can test program in Android AVD, this study only created a simple TextView, Button control, and separately set their value: Hollow World, Hollow Android Activity and Hollow Android. When debugging, we select “Run” option in the menu at the top of the Eclipse main interface, in turn select "Run As", "Android Application" option. The first time it needs a long time when you start the simulator, and wait a while before the program operates successfully.

2.2. Single thread Socket communication

Single thread Socket communication is client software development. Through the learning for TCP protocol and Socket communication programming, we can achieve the basic communication and simulation between client and server programmed on the Android platform, which means the communication between mobile phone and computer-side. As the program needs to be networked, so the network privilege of system must have done before network permissions, otherwise the system will be error, so in the initial of program creation, we need to add code in Android Manifest.xml file to support the normal network access.

2.3. Multithread Socket communication

The use of multi-threaded Socket programming: there is a problem for single-threaded Socket Programming. We need to deal with the accept operation and data writhing and reading after the establishment of Socket with different threads [5]. A single thread also can deal with this problem. For the connection request of each client, after the production of Socket, the server will generate a single thread to preserve the Socket and communicate with customer, so as to improve the efficiency of the program to customers. After the end of a client communication, Socket will exit, and the thread also will withdraw [6]. It also can make a further development on reading and writing thread, so that read and write operations can be processed in parallel; client processing is similar.

3. System design

3.1. Layout of system summary

Based on the CAN bus control of gym intelligent lighting system, this study aims to improve the macro-function of gym intelligent lighting system through the implementation of Android SHD and server communications.

From the structure of the system, we can see that the system adopts the client/server structure, and has a good human-computer interaction performance. As the only server in system, the central controller server is the data aggregation in the entire system, and it is responsible for information collection and storage of lighting equipment. As a client, Android SHD can provide a good user interface so that users can control the gym lighting system flexibly through Andrews SHD.

3.2. Interfacial design of Android client

(1) User login interface

The identity of software user is divided according to the different needs for different groups in the intelligent lighting control system, the software users are divided into control and management personnel, maintenance personnel and ordinary audience. The user name and password of audience is empty, so we can login directly.

When the user logs in, the client will pass the user name and password to the server through Socket communication, and then the server will encrypt the data and store it in server within an existing user name through MD5 hash operation after receiving the data [7–8]. Different users select different options to log in different control systems, and they have different functional privileges. The related registration process as shown in Fig. 1.

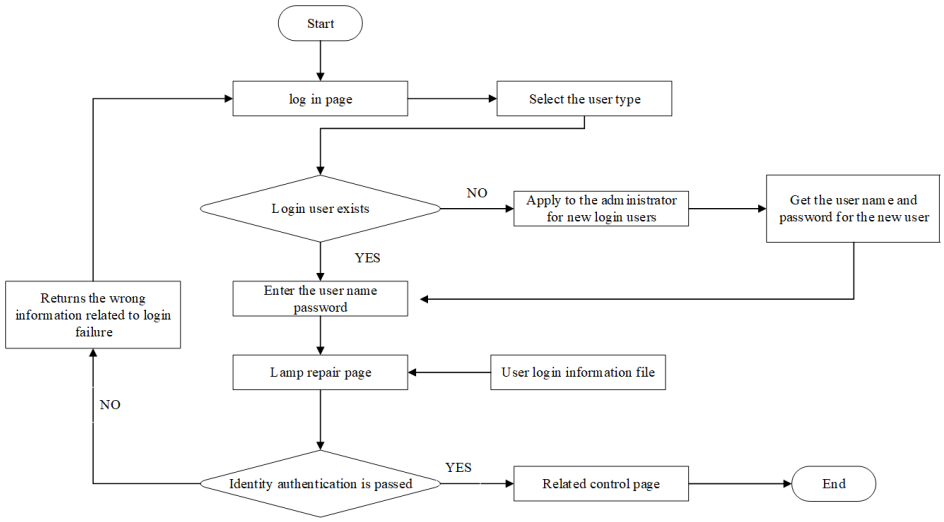

Fig. 1. Login authentication flow chart

The drop-down list shows the option entry for user's type in Login processing. When you click this option, it will pop-up four options like control personnel, maintenance personnel, professionals and system administrator.

(2) Control interface design for control personnel

According to the diversity of the function of large-scale gymnasium, the login main interface of system control personnel is divided into emergency lighting control, weather query and scenario mode selection. The flow chart shown in Fig. 2.

(3) Control interface design of maintenance personnel

Because the maintenance staff is only responsible for the maintenance of venues lighting equipment, so the system only set two simple scene mode such as the lamp full open and all closed mode, while providing the query of lamp life in order to simplify the maintenance work. In specific maintenance, the maintenance personnel firstly select the specific venue number, and click on the specific lighting options, then we can see the lamp life.

(4) User interface design for expert

Expert users can query the working smart relay combination for specific scenario and set connection with client server through the Socket communication. The client will show the display information through the List View platform. The using method is mentioned in the above, so here is not go into details. At the same time, the expert user can edit the profile, and pass the modified information to the server,

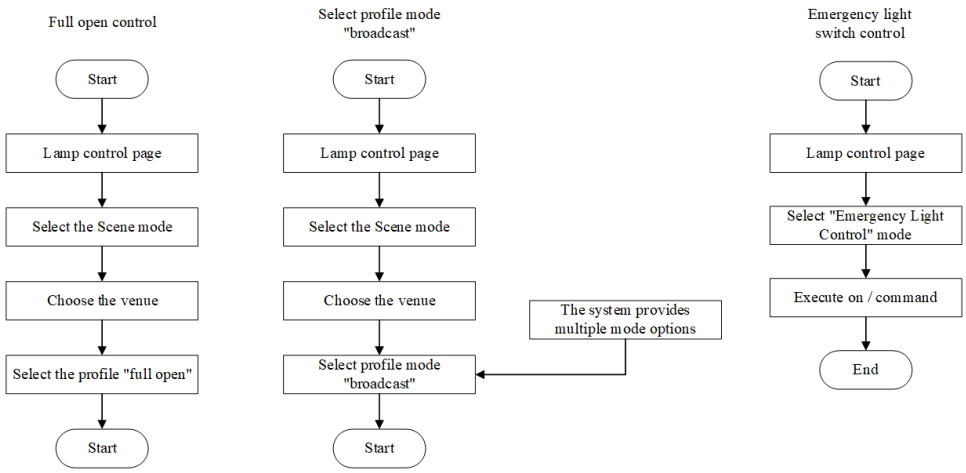

Fig. 2. Control module flow chart

then coverage the server-side data, so as to achieve the purpose of modification. Expert user clicks on the audience mode, and the server diary record the client's request, the flow chart as shown in Fig. 3.

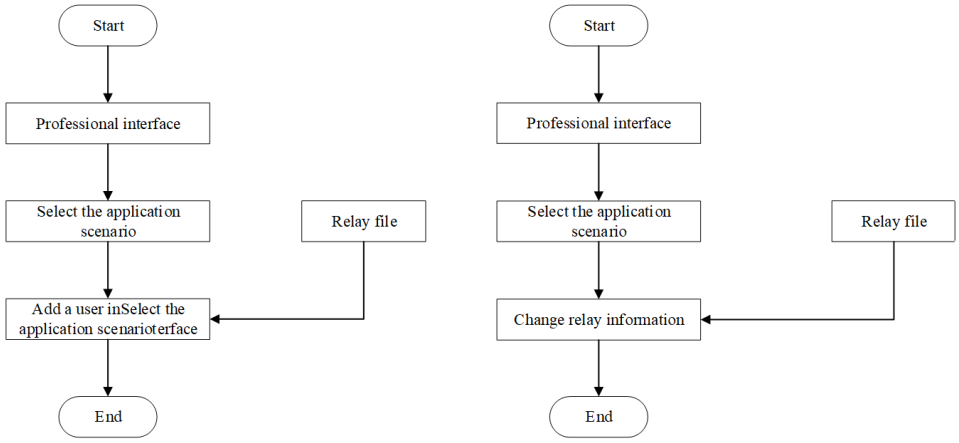

Fig. 3. Flow chart of scene editor

(5) System administrator interface design

If the user information does not exist, you need to apply a new number for the administrator. After passing application, the administrator user login system through the system management staff number, and fill in user type, user name, password and other information in the new user page. The server information file is updated after the success of new user added, and the flow chart of new user is shown in Fig. 4.

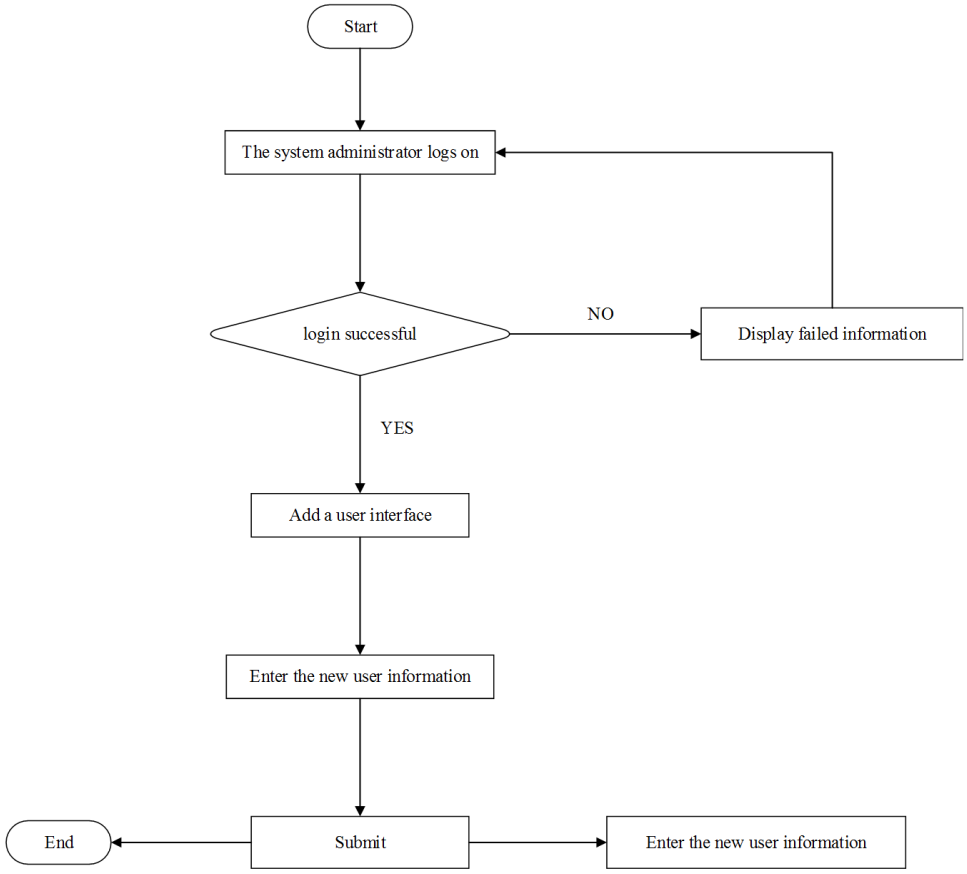

Fig. 4. Add user flow chart

4. Conclusion

In this paper, through the establishment of single-threaded client and server basic communication, we explore the multi-thread client and service-oriented basic communication technology. Through the overall framework of the system and functional analysis, we set command set of client and server according to its function. The system users are divided into control management, maintenance personnel, professionals and system management staff. Developing the software in the platform, we can achieve the control for most of lighting on the platform, and the simple and intuitive interface design brings some good feelings for user to experience the application. Based on the gym power energy management of Android SHD, management control for the stadium will be more centralized and efficient.

References

[1] A. Chiarini, E. Vagnoni: *World-class manufacturing by Fiat. Comparison with Toyota production system from a strategic management, management accounting, operations management and performance measurement dimension.* International Journal of Production Research *53* (2015), No. 2, 590–606.

[2] A. Agha: *Standing the test of time: Embankment investigations, their implications for African technology transfer and effect on African American archaeology in South Carolina.* Atlantic Studies *12* (2015), No. 3, 336–354.

[3] Y. Yu, Y. Li, D. Xiang, X. Jiang: *Making method and application of standards for energy consumption quota of civil buildings.* International Journal of Ambient Energy *37* (2016), No. 6, 548–558.

[4] T. Shin, H. T. Jeon, J. Byun: *Developing nontrivial standby power management using consumer pattern tracking for on-demand appliance energy saving over cloud networks.* IEEE Transactions on Consumer Electronics *62* (2016), No. 3, 251–257.

[5] Mohamed Afif Asyraf bin Mohamed Roshdin Murad, N. A. A. Rahman, N. I. A. Rahman, M. Haque: *Knowledge, attitude and practice regarding exercise among people exercising in gymnasium and recreational parks around Kuantan, Malaysia.* Journal of Applied Pharmaceutical Science *6* (2016), No. 6, 047–054.

[6] J. Teng, W. Lu, Y. Cui, R. Zhang: *Temperature and displacement monitoring to steel roof construction of Shenzhen bay stadium.* International Journal of Structural Stability and Dynamics *16* (2016), No. 6, paper 1640020.

[7] L. Ren, C. L. Yuan, H. N. Li, T. H. Yi: *Structural health monitoring system developed for dalian stadium.* International Journal of Structural Stability and Dynamics *16* (2016), No. 04, paper 1640018.

[8] M. Mosadeghi-Nik, M. S. Askari, F. Fatehi: *Mobile health (mHealth) for headache disorders: A review of the evidence base.* Journal of Telemedicine and Telecare *22* (2016), No. 8, 472–477.

Received May 7, 2017

Acta Technica *62* No. 3A/2017, 213–224

Study on binocular stereoscopic vision of Hawk-eye for tennis based on three-dimensional positioning

Cheng Yang[1,2], Li Guo[1]

Abstract. In the game of tennis, there always are some misjudgments or unfair penalties to players. However, "hawk-eye" system, which is brought in, can significantly help referees to make more reasonable penalties, and ensure the matches with justice and equity. A further processing is made to receive the tennis positional data with analyzing the image-forming principle of "hawk-eye" binocular stereoscopic vision, capturing the motion trail of the ball and transmitting to PC end by using wireless sensing. From the perspective of three-dimensional positioning algorithm, non-range-based positioning algorithm is firstly studied to come up with a three-moving beacon positioning algorithm, which is applied to two dimension; directing at three-dimensional space, this algorithm combined with hierarchy coordinated put forward multi-movable beacon hierarchy positioning algorithm: from the perspective of image reconstruction of binocular stereoscopic vision, camera calibration algorithm is studied and a further improvement is put forward. According to a large number of experiments, the proposed positioning algorithm has a higher accuracy. A smaller data size can reduce equipment the consumption. At the same time, the improved method imaging standardization makes a further improvement on acquiring image accuracy.

Key words.
Binocular vision, three-moving beacon positioning, multi-movable beacon hierarchy positioning, camera calibration.

1. Introduction

After a century of development, tennis [1] has become a commercial sport. Tennis players need to gain critical scores as much as possible and make sure they can win victory. However, in some critical balls, the referee may make some controversial penalties. What's more, the spectators would be disappointed by the matches with more unfair penalties. From the perspective of developing tennis and maintaining athletes' rights and interests, it is important to bring "hawk-eye" [2] system into tennis, which can identify the location precisely.

[1]Shijiazhuang Tiedao University, 050043, Hebei, China
[2]Corresponding author; E-mail: chengyang_college@yeah.net

Actually, “hawk-eye” system is an immediate playback system [3]. First, it makes a millimeter partition to the place's three-dimensional space in virtue of PC; then using camera captures the basic data of tennis movement trail from different angles; these data are received by computers to process three-dimensional images; lastly, the images are transmitted to the screen, which can be on the live television. The whole process only takes several seconds.

2. Literature review

As pattern of computer vision, binocular stereoscopic vision [4] can use camera to acquire two located images from different positions. Positioning vanishing point of imaging matching corresponded with computer also can be called anaglyph. From that, the three-dimensional information can be acquired.

Geometric model of camera imaging [5] needs to take intrinsic parameter (corresponding parameter of geometrical characteristic and optical characteristic) and external parameter into consideration. camera standardization [6], and data needs to be collected to acquire the imaging, but the location [7] is the most important step. Data is transmitted to PC end by camera with wireless network. Research on wireless network is always a hot topic, and its related algorithm can be classified into two ones: ranging and non-ranging algorithms. Based on RSS [8] is the most typical algorithm in ranging algorithms. This algorithm can get the node position through the relationship between distance and signal intensity; DV-HOP [9] is one of non-ranging algorithms, which estimates the distance among nodes by using the relationship between cop count and distance.

This paper studies the camera standardization algorithms, and we consider that camera bracket can be adjusted, the semi-auto camera standardization is proposed based on checkerboard plane template. Compared with conventional imaging algorithms, the accuracy of acquiring imaging get further improved. From the viewpoint of 3D, the DV-HOP algorithm is studied and combined with mobile beacon, and a new improved algorithms is proposed.

3. Research methods

3.1. Binocular vision image-forming theory and epipolar geometry

Generally speaking, two cameras are used in binocular vision. As shown in Fig. 1, points $C1, C2$ are respectively the optical centers of the cameras. Point T is the focal point of camera light. Points $(V1, W1)$ and $(V2, W2)$ are the light transmitting nodes $R1$ and $R2$ projected by T on the camera. Points $Q1, Q2$ are the intersections of the vertical direction corresponding to the camera optical center to surface. At the same time, points $(V1, W1)$ and $(V2, W2)$ can also be expressed as the same object T space, namely "conjugate point". Points $C1$ and $C2$ are connected by points $R1$ and $R2$, namely $R1C1$ and $R2C2$ projection lines. They are respectively

extended to point T, which can be represented as coordinates (x, y, Z)

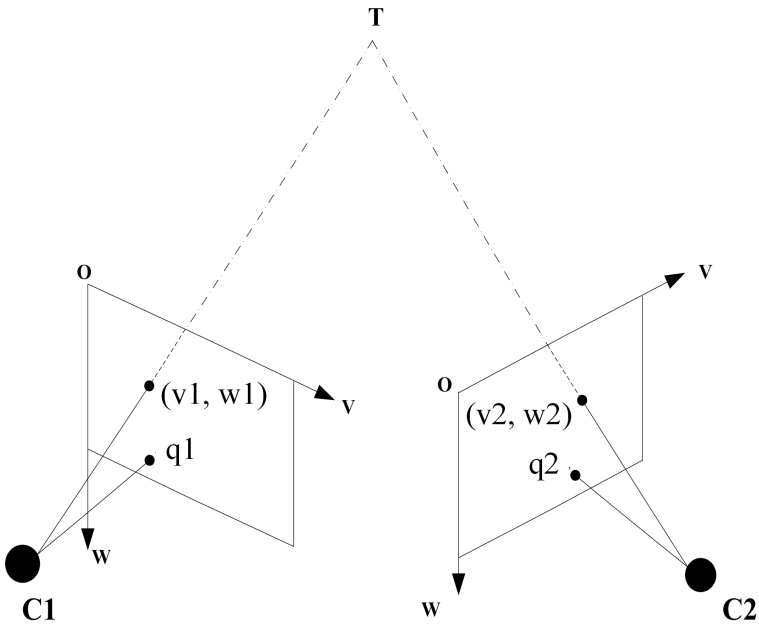

Fig. 1. The Theory of Binocular Stereo Vision

Binocular stereo vision has two structural models: one is that two cameras' optical axis are in a parallel position, which can make the imaging plane formed in the P plane. And if signature is made to camera's photo center, the corresponding baseline is also parallel to the P plane. Optical axis in the plane is perpendicular to the baseline; another is that two cameras are put in a mobile position, but the binocular stereo vision still has some common rules that are unrelated to the cameras' positioning place.

From Fig. 2, it is seen that the left coordinate system of the camera consists of $Q_1A_1B_1C_1$, and right system is composed of $Q_2A_2B_2C_2$. Symbol G in the three-dimensional space corresponds to projection starting point $< g_1, g_2 >$ in the delineation plane of the two cameras. And the two points are extended and intersected at point G in space. A further assumption is put forward. Points Q_1 and Q_2 are very close to their corresponding position. Therefore, Q_1 and Q_2 can be regarded as corresponding photo center nodes. Points C_1 and C_2 have a consistent direction vector with relative space of camera optical axis; G_1 and G_r, respectively, represent the coordinates that intersect with G; a rigid body transformation defined by a translation direction vector Tc and the orthogonal rotation matrix EC represent the geometrical relationship between G_1 and G_r, which is expressed as follows:

$$T_\mathrm{c} = Q_1 - Q_2 \tag{1}$$

$$G_{\mathrm{r}} = EC(G_1 - T_{\mathrm{c}}) \tag{2}$$

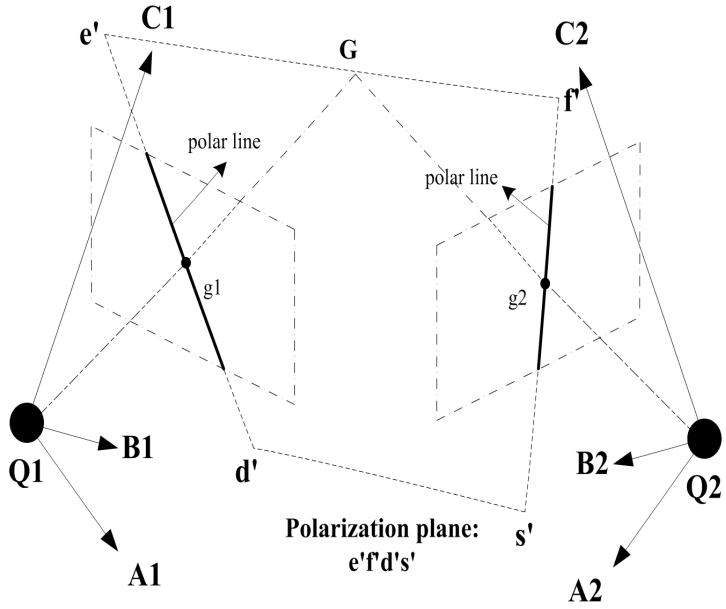

Fig. 2. Epipolar Geometry

Projection point $< g_1, g_2 >$ of two cameras is in $e'f'd's'$ plane with space intersection point, which is also called pole plane. The rest points of the space are in another plane with two projection points as well. At the same time, all the pole planes are collinear, which is called base line. It is the pole ligature. Imaging point of right camera's center Q_2 at the left image is k_l, while center Q_1's image point is k_{r}. So the line is known as $k_l k_{\mathrm{r}}$. When the spatial point G is in an unstable position, the pole plane β rotates with base line, which contributes to a gather of pole plane. In pole plane $e'f'd's'$, camera plane is vertical to optical axis and intersected with two cameras' planes, so w_l and w_{r} in the intersection plane are called polar.

3.2. Improved methods of camera calibration

Camera calibration needs to solve parameters, including internal parameters and external parameters. As shown in Table 1, the internal parameter is the setting parameter of the camera itself, affecting light capture and image focus. It mainly contains central point $< r_x, e_x >$ that is regarded as center for the captured object. However, it is affected by lens distortion and noise. Two focal distances f_s and f_z are involved in the direction of S/Z. The focal length is the distance from the theoretical center to the main focus of the camera lens, which is represented as the ratio of the focal length of the camera to the distance in the horizontal and vertical directions.

At the same time, the non-vertical factor of the camera is set to α. The external parameter is the orientation relation of the camera coordinate system corresponding to the world coordinate system, that is to say, the position relation between the rotation matrix and the translation matrix. In addition, two linear classifications of camera imaging models need to be considered. If it is a nonlinear imaging model, the change parameter of radial lens is $< v1, v2 >$ and the change parameter of the tangential lens is $< t1, t2 >$.

Table 1. Camera parameters

Parameters	Expression	Degrees of freedom
Internal parameter	$V = \begin{bmatrix} f_s & \alpha & r_x \\ 0 & f_z & e_x \\ 0 & 0 & 1 \end{bmatrix}$	5
Distortion (radial direction, tangential direction)	$< v1, v2 >,\ < t1, t2 >$	4
External parameters (rotation matrix, translation matrix)	$R = \begin{bmatrix} rm_1 & . & . & . & rm_m \\ . & . & & & . \\ . & & . & & . \\ . & & & . & . \\ . & . & . & . & rm_n \end{bmatrix},\ T = \begin{bmatrix} l_x \\ l_y \\ l_z \end{bmatrix}$	6

Considering that stand of tennis "hawk-eye" is adjustable, a semi-automatic camera calibration method based on plane template of checkerboard is adopted. A in the template space is assumed to respectively represent the camera coordinate and imaging coordinate of the projection point. In the camera coordinate system, the space coordinate is (X, Y, T, m); in the image coordinate system, the space coordinate of image point a' is (s, z, m). Symbol m is a constant, and the projection relationship between A and a' can be expressed as follows:

$$Wa' = V[RT]A\,. \tag{3}$$

In the above formula, W is a non-zero invariant and external parameter is $[RT]$. Vector $< r_x, e_x >$ serves as the central point, f_s and f_z are the effective focal lengths in the S and Z axes, and α is the non-vertical factor in the S and Z axes, satisfying the condition $\alpha \neq 0$. The intrinsic parameter V has a form of matrix

$$V = \begin{bmatrix} f_s & \alpha & r_x \\ 0 & f_z & e_x \\ 0 & 0 & 1 \end{bmatrix}. \tag{4}$$

It is assumed that the template plane is at world coordinate system $C = 0$; matrix relationship between the template and image is fulfilled. In this formula, mi $(i = 1, 2, 3)$ can express the rotation matrix R in ith row

$$W[s\ z\ m]^{\mathrm{T}} = V[m1m2m3T][XY0m]^{\mathrm{T}} = V[m1m2T][XYm]^{\mathrm{T}} \tag{5}$$

Unit matrix between spatial objects A and a' is expressed as 3×3 I-matrix, including a nonzero constant factor such that (3) is transmitted into

$$Wa' = IA,\ I = V[m1m2T]\,. \tag{6}$$

The fundamental constraint of camera intrinsic parameter needs to be counted. And I is recorded as $[I1I2I3]$, which is expressed as a product of (6)

$$[I1I2I3] = \theta V[m1m2T]\,. \tag{7}$$

In the expression, θ is a non-zero constant factor. Because the rotation matrix is characterized by orthogonality, $m1$ and $m2$ also meet orthogonality condition. The module value is equal to 1, and then intrinsic parameter of fundamental constraint is

$$\begin{cases} I1^{\mathrm{T}}V^{-\mathrm{T}}V^{-1}I2 = 0, \\ I1^{\mathrm{T}}V^{-\mathrm{T}}V^{-1}I1 = I2^{\mathrm{T}}V^{-\mathrm{T}}V^{-1}I2. \end{cases} \tag{8}$$

Here, $V^{-\mathrm{T}}V^{-1}$ is curve of the second degree, and its corresponding unit matrix has 8 degrees of freedom. In the external parameter, the rotation matrix has three parameters and translation matrix also has three parameters. As a result, in the intrinsic parameter, the matrix has 2 parameters, which means 2 constraint conditions.

3.3. 3.3 Three-mobile beacon positioning algorithm and multi-mobile beacon hierarchy positioning algorithm

Three mobile positioning methods of auxiliary beacon and non-ranging, which is combined mobile beacon with DV-Hop algorithm. Considering characters that beacon produces many virtual beacons in the movement process, one-off positioning is fulfilled. Because it has a smaller consumption and it has a higher positioning precision.

Three-mobile beacon positioning algorithm is a positioning algorithm for topological network and bouncing number accumulation. From Fig. 3, the real distance and route information of every beacon is listed, and $W1$, $W2$ and $W3$ are the beacon nodes. And the three nodes acquire their opposite position information respectively. Bouncing numbers between beacons are gained by unknown node K through collecting virtual data package.

According to distance computation formula, average bouncing distance between $W1$, $W2$ and $W3$ can be worked out. Meanwhile, all bouncing information would

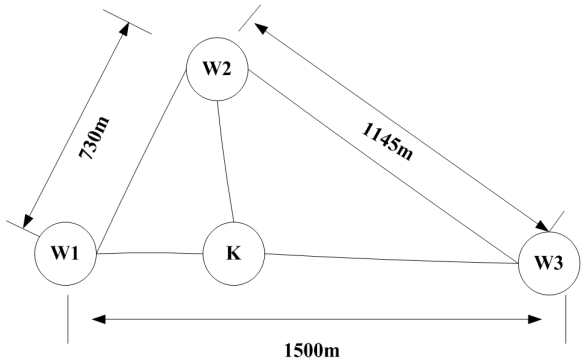

Fig. 3. TMB-DV-Hop Net Work topology

be spread in the whole network.

$$D_i = \frac{\sum \sqrt{(A_i - A_j)^2 + (B_i - B_j)^2}}{\sum f_i},\ i \neq j\,. \tag{9}$$

The distance from the node K to other nodes can be estimated according to the minimum ($Min(\sum f_i)$) and average bouncing distance D_i. This algorithm is an improvement for DV-Hop, and the average distance D_i is worked out unreasonably, especially in the different network environment.

In the two-dimensional environment, with the help of mobile beacon auxiliary, DV-Hop is improved by three-mobile beacon positioning algorithm. However, at most of time, the positioning problem needs to be considered when received data distributed in three-dimensional space. If positioning problem of three-dimensional space is stressed, there will exist a problem—"common plane", which means that four nodes are closely in one plane, and two intersection points resulting from their opposite nodes as radius. Therefore, the unknown node position cannot be estimated. In order to solve this problem, "common plane degree" concept is brought in to expand three-mobile beacon positioning algorithm to three-dimensional space. As a result, multi-mobile beacon hierarchy positioning algorithm is put forward.

Four-side positioning technology is combined with three-dimensional DV-Hop algorithm here. Three-dimensional DV-Hop algorithm also can be divided into three stages:

1) Minimum bouncing number from the beacon nodes is respectively counted by unknown node collection.

2) A minimum bouncing number multiplying average distance is considered as an estimated distance $HopSize_i$ between beacon nodes.

3) When the unknown nodes acquire more than four $HopSize_i$, the space positions of unknown nodes can be worked out.

$$HopSize_i = \frac{\sum \sqrt{(A_i - A_j)^2 + (B_i - B_j)^2 + (C_i - C_j)^2}}{\sum f_i},\ i \neq j\,. \tag{10}$$

In expression (10), $(A_i,\ B_i,\ C_i)$ are the space coordinates of the beacon node i; $(A_j,\ B_j,\ C_j)$ are the space coordinates of beacon node$j$; f_i expresses the bouncing number counted from ith node to other beacon nodes. When distances of four or more unknown nodes are known, a resolution can be carried out by multilateral measurement. If multilateral measurement is changed into four-lateral positioning method, the formulae could be expressed as follows:

$$\begin{cases} (A_1 - A)^2 + (B_1 - B)^2 + (C_1 - C)^2 = L_1^2, \\ (A_2 - A)^2 + (B_2 - B)^2 + (C_2 - C)^2 = L_2^2, \\ (A_3 - A)^2 + (B_3 - B)^2 + (C_3 - C)^2 = L_3^2, \\ (A_4 - A)^2 + (B_4 - B)^2 + (C_4 - C)^2 = L_4^2. \end{cases} \tag{11}$$

In expression (11), L_i is the distance from the unknown node to the beacon node i, which can transform the expression into the form of $XZ = Y$ and we can further get the space vector of (X, Y, Z).

4. Experiment result and analysis

4.1. Standardization simulation and analysis

In the experiment, the adopting chessboard is 10×10 Black and White. There are 81 grids in all except outermost layer. Every grid lens is 2 cm long. The camera is a specialized vidicon for tennis. Out of experimental purpose, narrow baseline configuration is adopted that is 13 cm long. The out image is set up as RGB, its resolution ratio is 640×480 and pixel size is 15(10–3 cm)×15(10–3 cm).

The appointed chessboard is placed in camera shooting scale in front of the camera; the light source is sunlight; a rotational movement is made by control templates. However, the image is not parallel to optical axis. Every time the template is rotated and standardization plank is shot by two cameras, so camera's intrinsic parameter can be counted by the three images. In order to reduce the standardization error, a lot of images should be shot from different angles.

Tool cabinet of MatLab is used to make standardization. In the standardization, the bigger error may occur. At this time, tangential or radial parameters can be imported to reduce the error, but this method has no experience to refer and the judgement is made only by naked eyes. In order not to influence the standardization precision, the tangential or radial parameters are regarded as input value of optimizing standardization algorithm to improve its precision. Table 2 and Table 3 contain the intrinsic parameter between after and before, and the optimized standardization result is more close to actual value.

Adopting default standardization and improved one acquires the corresponding result of Fig. 4 and Fig. 5. The error of extracting image is less than 0.5 pixels; and error range of improved standardization method is more concentrated, so the error is much less.

Table 2. Default internal results of left camera labeling

Parameters	Results
$< fs, fz >$	[485.45754, 483.78545]±[0.94578, 0.93542]
$< rx, ex >$	[375.45754, 342.78545]±[0.97578, 0.88542]
α	0.00000±0.00000
$< v1, v2 >$, $< t1, t2 >$	[–0.02218, 0.02358, 0.00461, –0.00204, 0.00000]
err	[0.13478, 0.0753]

Table 3. Refined internal results of left camera labeling

Parameters	Results
$< fs, fz >$	[484.45754, 482.78545]±[0.94538, 0.93552]
$< rx, ex >$	[375.42554, 340.78545]±[0.95278, 0.89542]
α	0.00000±0.00000
$< v1, v2 >$, $< t1, t2 >$	[–0.02222, 0.02358, 0.00461, –0.00210, 0.00000]
err	[0.12408,0.0621]

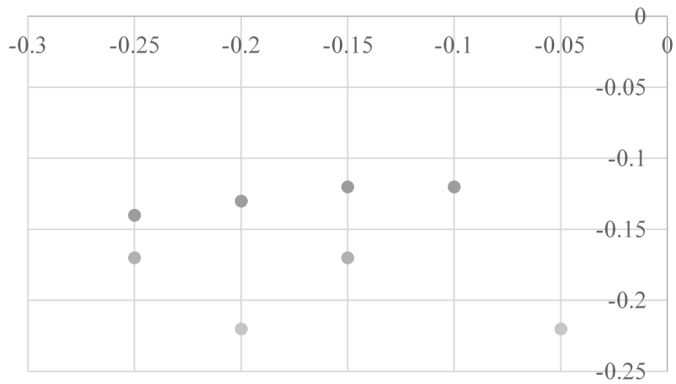

Fig. 4. Projection result 1

4.2. Positioning algorithm simulation and analysis

In every same wireless network (like Fig. 6), the three algorithms have higher positioning precision, which are all less than 0.5. Maximum and minimum average errors of three-mobile beacon positioning algorithms are in lower level, which is better than DV-Hop and MB-DV-Hop. At the same time, DV-Hop precision has

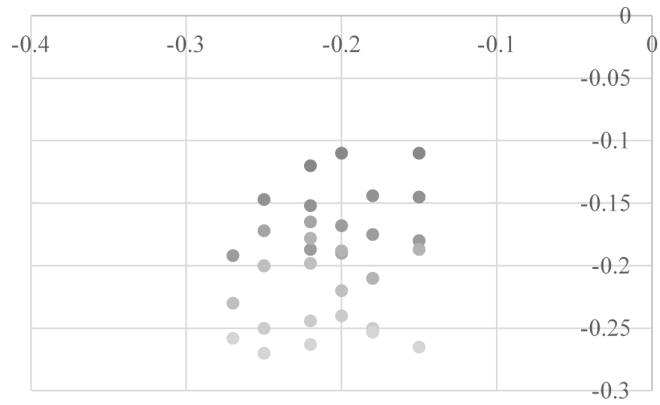

Fig. 5. Projection result 2

a huge fluctuation and its algorithm is not very stable. In the different wireless network (like Fig. 7), TMB-DV-Hop still has a higher precision and is very stable. However, DV-Hop has a huge fluctuation, hardly having any reference.

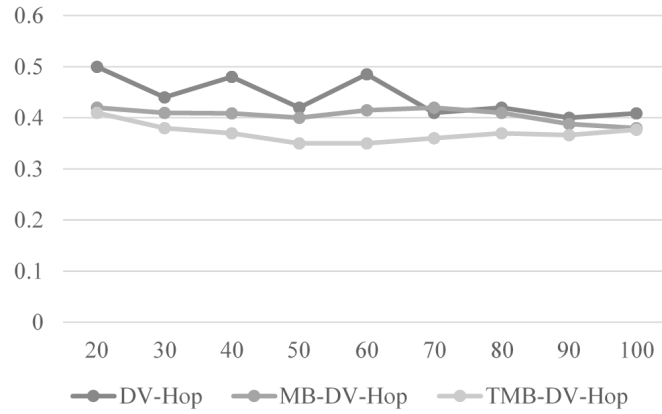

Fig. 6. Precision with XX electricity

DV-Hop in two-dimensional space is extended to three-dimensional space by multi-mobile beacon hierarchy positioning algorithm (like in Fig. 8). Compared with improved algorithm, both improved algorithms and 3D-DV-Hop have lower error. Maximum and minimum errors of multi-mobile beacon hierarchy positioning algorithms are in a lower level. Nodes in 3D-DV-Hop are set up as 10 and 20, and this algorithm precision has a huge fluctuation. As the number of nodes increases, the error is gradually reduced. Generally speaking, however, the average error of multi-mobile beacon hierarchy positioning algorithm is at a lower level and very stable.

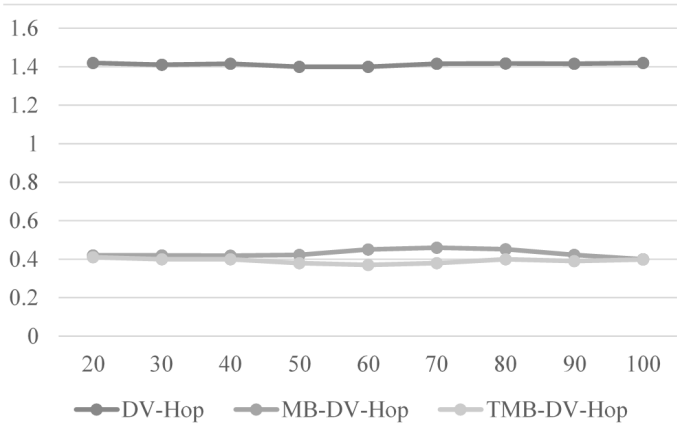

Fig. 7. Precision with XY electricity

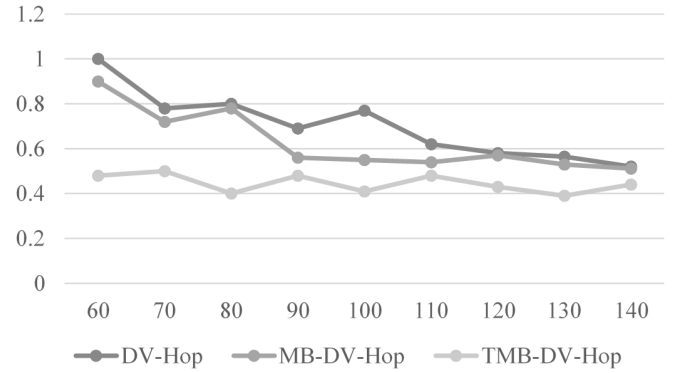

Fig. 8. Precision with 3D space

5. Conclusion

Camera imaging is disposed by binocular stereo vision. Image-forming principle of binocular stereo vision is analyzed, and epipolar geometry is studied from the optic conception. From the hardware, camera's standardization method is improved, which can improve imaging precision further. From two-dimensional plane, DV-Hop is researched and three-mobile beacon positioning algorithm is put forward by virtue of mobile beacon. It is expanded to three-dimensional plane, which results in multi-mobile beacon hierarchy algorithm. A number of experimental results show that when the beacon nodes are constantly changed, the improved algorithm has a higher precision and is in a relatively stable state with smaller data fluctuation.

References

[1] F. Alyas, M. Turner, D. Connell: *MRI findings in the lumbar spines of asymptomatic, adolescent, elite tennis players.* British Journal of Sports Medicine *41* (2007), No. 11, 836–841.

[2] Li Zhao, Ning Xia: *The volleyball movement under the "eagle eye" can see how far–On "eagle eye" effect on the development of volleyball competition system.* Contemporary Sports Technology *4* (2014), No. 20, 141–142.

[3] M. S. Y. Jong, E. T. H. Luk: *Adopting eagle eye in outdoor exploratory learning from the teacher perspective.* IEEE International Conference on Advanced Learning Technologies, 7–10 July 2014, Athens, Greece, IEEE Conference Publications (2014), 617–621.

[4] R. Xiang, H. Jiang, Y. Ying: *Recognition of clustered tomatoes based on binocular stereo vision.* Computers and Electronics in Agriculture *106* (2014), 75–90.

[5] Y. Liu, H. Y. Chen, K. Liang, C. W. Hsu, C. W. Chow, C. H. Yeh: *Visible light communication using receivers of camera image sensor and solar cell.* IEEE Photonics Journal *8* (2016), No. 1, Paper 7800107.

[6] P. Serafinavičius: *Investigation of technical equipment in computer stereo vision: Camera calibration techniques.* Elektronika ir Elektrotechnika *59* (2005), No. 3, 24–27.

[7] H. Zou, X. Lu, H. Jiang, L. Xie: *A fast and precise indoor localization algorithm based on an online sequential extreme learning machine.* Sensors (Basel) *15* (2015), No. 1, 1804–1824.

[8] M. Pajovic, P. Orlik, T. Koike-Akino, K. J. Kim, H. Aikawa, T. Hori: *An unsupervised indoor localization method based on received signal strength (RSS) measurements.* IEEE Global Communications Conference (GLOBECOM), 6–10 Dec. 2015, San Diego, CA, USA, IEEE Conference Publications (2015), 1–6.

[9] S. Kumar, D. K. Lobiyal: *An advanced DV-hop localization algorithm for wireless sensor networks.* Wireless Personal Communications *71* (2013), No. 2, 1365–1385.

Received May 7, 2017

Acta Technica *62* No. 3A/2017, 225–234

ABS anti-fatigue training detection system in classification and recognition algorithm of inertia signal detection movement training based on naive Bayesian

Haidong Yang[1], Liyan Zhang[2,3]

Abstract. The human body sensor network is the application of the traditional wireless sensor network in the monitoring of the human body. It is a completely new human body monitoring technology, which provides remote medical service of human health. Inertial signal is a common method for human body sensor network to monitor the human body. In order to further expand the application range of the human body sensor network, this paper presents a method of human abdominal training monitoring based on inertial signal. The paper takes ABS bridging exercise as a case for the study, uses Naive Bayesian classifier to identify different bridging exercises, and achieves the supervision on the double bridging movement.

Key words. Inertial signals, ABS, double movement, anti-fatigue training.

1. Introduction

The abdominal muscles are important muscle tissues of the human body, and the main function of the abdominal muscles is to bound the human spine. As a result, it is difficult to provide strong constraints on the spine in the course of the exercise, easily leading to spinal damage or other accidental injuries [1, 2]. In the process of abdominal muscle strength training, it is necessary to monitor the training actions of abdominal muscles.

Monitoring of abdominal muscle training actions can provide direct feedback information of training effect for the patients and doctors, and help doctors to adjust the treatment plan in time according to the patient's recovery situation; moreover, it

[1]Northeastern University, Liaoning, 110819, China
[2]Shenyang Normal University, Liaoning, 110034, China
[3]Corresponding author; E-mail: prof_liyanzhang@163.com

can prevent the occurrence of overtraining. As a result, it is not only not conducive to rehabilitation treatment, but also affects the progress of rehabilitation of patients. For example, studies have shown that asymmetric upper body strength training will cause asymmetric compression on the disc of the human body, and long-term asymmetric strength training will easily lead to spinal injury [3].

The use of Electromyographic (EMG) for monitoring human abdominal training actions is the most commonly used method in clinical medicine and kinematics [4]. Through the calculation of average amplitude of ABS EMG signal in a period of time, we can obtain abdominal EMG activity. As an important indicator of the evaluation of ABS function, EMG activity is widely used in the existing studies [5]. The inertial sensor is one of the most commonly used devices to monitor the human body actions, and some studies have shown that there is a certain correlation between the inertial signal produced by the human motion and the EMG signal of the muscle [6]. This study uses the inertial measurement module to monitor human abdominal training action, and to replace EMG sign alto calculate EMG activity of ABS value by inertial signals, so as to realize the monitoring of the abdominal muscle training action.

2. Detection of ABS training action based on inertial signals

If it is proved that the same ABS training action will produce the similar EMG activity, then we can monitor the abdominal training action through sense network. We make use of inertial sensors to collect the inertial signals generated by the abdominal muscle training action, establish the relationship between the inertial signal and the EMG signal of the ABS, and calculate the EMG activity of abdominal muscle to achieve the monitoring of the abdominal muscle training.

2.1. Inertial signal acquisition device

This study uses the inertial measurement module (ADIS16405) produced by American Analog Device Inc for the acquisition of inertia signal produced in the abdominal training actions. ADIS16405 consists of three-axis accelerometer with a high precision and a high precision gyroscope. The maximum range of the acceleration sensor is + 18 g, the resolution is 3.33 mg/LSB, the maximum range of gyroscope is + 300 deg/sec, and the resolution is 0.05 deg per second/LSB. In the experiment, ADIS16405 was installed on the data acquisition board (ADISUSBZ) produced by American Analog Device Inc.

2.2. Naive Bayes classifier

Figure 1 shows the processing of inertial signals in this study. First of all, we make use of Naive Bayesian classifier to identify different ABS actions by inertial signals, and establish different RBF neural networks according to the different recognition results. RBF neural network calculates the corresponding EMG signals through the inertial signals, and further calculate the EMG activity of abdominal muscles.

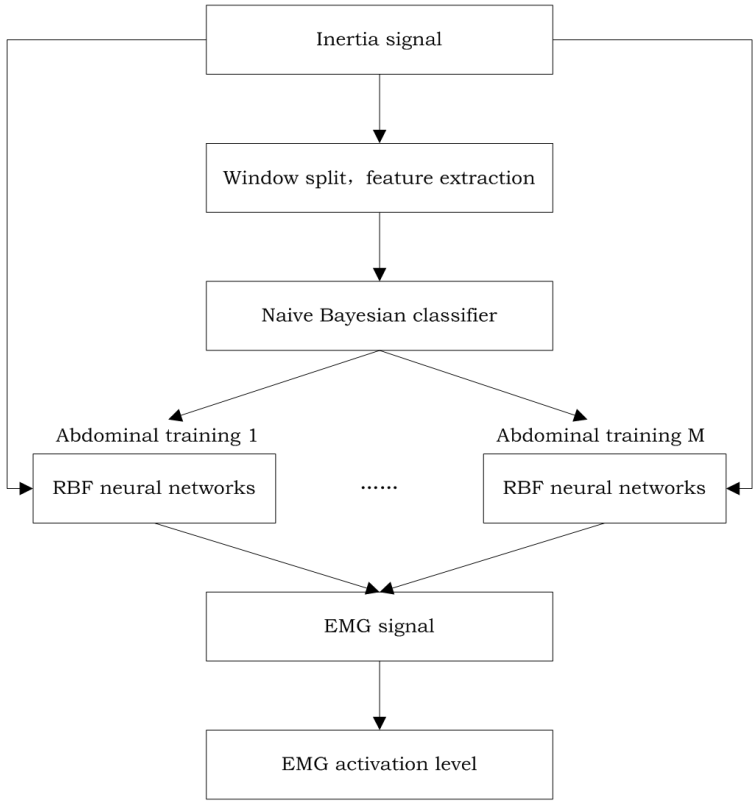

Fig. 1. Diagram of the processing of inertial signals

The Naive Bayes classifier is a classification algorithm based on the theory of the Bayes decision. In the classification process, it is assumed that the different dimensions in the feature space are statistically independent. Assuming that the unknown samples in the L-dimensional feature space are $X = (x_1, \cdots, x_L)$. Based on the independence assumption, X belongs to the probability of m-th category, which can be obtained by equation

$$p\left(X\left|\omega^m\right.\right) = \prod_{l=1}^{L} p\left(x_l\left|\omega^m\right.\right), \quad m = 1, \cdots, M. \tag{1}$$

The Naive Bayes classifier determines the classification category of unknown samples according to relation

$$\omega^* = \arg\max_m \left\{ p\left(\omega^m\right) \prod_{l=1}^{L} p\left(x_l\left|\omega^m\right.\right) \right\}. \tag{2}$$

The advantage of the Naive Bayes classifier is that it only needs to estimate L

one-dimension probability density function $p\left(x_l \left|\omega^m\right.\right)$ in the training data, so that the algorithm training speed is rapid. In this study, the Parzen window method is used to estimate the probability density, and the Gauss function is used as the window function of the Parzen window. Assuming that there are N training samples belonging to the m class and x_l^n represents the lth component of the nth sample, then $p\left(x_l \left|\omega^m\right.\right)$ is estimated by the relation

$$p\left(x_l \left|\omega^m\right.\right) = \frac{1}{N}\sum_{n=2}^{N}\frac{1}{\sqrt{2\pi}\sigma}\left(-\frac{\left(x_l - x_l^n\right)}{2\sigma^2}\right). \tag{3}$$

3. Experimental design and experimental data acquisition

In order to verify the feasibility of the proposed method in the paper, the paper selects the double-bridge movement for the training of abdominal muscles. Double-bridge movement is the common strength training action of abdominal muscles, which can effectively stimulate the rectus abdominis, external oblique, internal oblique and multiple abdominal muscles parts. In the experiment, we simultaneously use EMG signals and inertial signals for monitoring abdominal EMG activity in double-bridge movement, and compare the difference of monitoring results of two kinds of monitoring methods. A total of 10 volunteers (6 males and 4 females) participated in the study, aged between 22–27 years old. None of the volunteers had a history of abdominal muscle, back muscle, and spinal disability. Before the experiment, all the volunteers were informed of the experiment objective, the experiment process and the risks of the experiment. 3 participants participated in the experiment, among them, two participants were responsible for the installation of the experimental equipment and the assistance of volunteers to complete the designated movement, and one participant was responsible for the receiving and sending of control collection system and data storage operation.

3.1. EMG signal acquisition of maximum voluntary contraction movement

In the standardized processing of EMG signal, it is necessary to implement the MVCs action to find the maximum EMG amplitude for each abdominal muscle. In this study, we selected 3 kinds of effective MVCs movements, the upper body forwarding, the upper body turning left and the upper turning right. Volunteers sat on the experimental platform, with his legs flat on the experimental platform; an experimenter tied the two legs, the volunteers back straight on the body of the other experimenter; the upper part of the body was bound by the experimenter. In the experiment, after the volunteers and members were in place, the volunteer back straight and forced forward bending of the body [7]. In this process, the experimenter strived to bound IS and make his body keep static, to help the volunteers stimulate the maximum EMG activity. And then, in this way, volunteers and experimenters completed the upper body turning left and the upper body turning right two MVCs movements. In the experiment, each MVC movement lasted for 3 seconds, and

between the two adjacent MVCs, volunteers had 5 minutes to rest, to relax the abdominal muscles. The sampling frequency of EMG signal in the experiment is 1 kHz.

3.2. Inertia signal and EMG signal acquisition of double-bridge movement

The characteristics of double-bridge movement is that the actions are basically completed by the trunk. The upper limbs, lower limbs and other body parts still keep static. As a result, in the study, we need only an inertial measurement module worn in thoracic central to monitor the double-bridge movement. After completing all 3 groups of MVCs movements, the volunteers were given a 30-minute break. Then, the experimenter helped volunteers to wear the inertial measurement module in the thoracic central position. Volunteers conducted the double movement in 4 different postures, including the supine and prone double-bridge movement, lying on double-bridge movement, the left side lying double-bridge movement, and the right side lying double-bridge movement. In the experiment, each double-bridge movement lasted for 20 seconds, while volunteers needed to complete 6–7 action cycles. Each of the volunteers repeated a double-bridge movement for 5 times, and two adjacent double-bridge movement had the interval of 10 minutes. In the experiment, the sampling frequency of the EMG signal is 1000 Hz, and the sampling frequency of inertial signals is 435 Hz.

4. Analysis of experimental results

The inertial signals acquired in double-bridge are conducted with smooth processing of moving mean window with length of 100 m sec, and then we can get the inertial signals with sampling frequency of 10 Hz.

4.1. Classification accuracy of Naive Bayes classifier

1) Data preprocessing

The duration of each double-bridge movement in the experiment was 20 seconds, including 6–7 operation cycles, so the sliding window segmentation length is 4 seconds, making each observation window contain a complete action cycle. The characteristics of the inertial signals extracted from the observation window are mean and variance, and each feature is 12-dimensional.

2) Validation method

In this paper, the remaining-one method is used to verify the classification accuracy of the Naive Bayes classification. In 10 volunteers, choose the experimental data of a volunteer as the test data, and the experimental data of the other 9 volunteers as the training data. The verification process is repeated 10 times. Take the experimental data of different volunteers selected each time as test data, and the final results of the verification take the average value of the verification process for 10 times.

3) Experimental results

In the experiment, the recognition accuracy of all the 4 kinds of double-bridge movements using the Naive Bayesian classifier all reached 100 %. The reason for the high accuracy is that the body showed different postures in the 4 kinds of double-bridge movements, and it can easily distinguish by the acceleration signals. Figure 2 shows the acceleration signals of two kinds of actions, lying on the left and lying on the right (unit for the gravity accelerating). The body lying on the left double-bridge movement, axis acceleration signal value gets close to 1, while lying on the right double-bridge movement, the axis y acceleration signal is close to –1.

4.2. Calculation of the EMG activity of abdominal muscles by using the Radial basis function neural network (RBF)

1) Data preprocessing

For the EMG signal collected in the experiment, first of all, the RMS smooth processing and standardized processing are carried out.

2) Validation method

In the experiment, we established 4 RBF neural networks, and each network corresponds to a double-bridge movement. In the experiment, each volunteer repeated a double-bridge movement for 5 times. The inertia signal and EMG signal of the former 4 times double-bridge as the training data, and the test data is the inertial signal and EMG signal of fifth time double-bridge movement.

3) Experimental results

As shown in Fig. 4, it is the mean and standard of myoelectric activity, external oblique, EMG activity of internal oblique in four different double-bridge movement. From Fig. 4, we found that myoelectric activity of EMG activity was obtained by calculating the inertial signal and EMG activity obtained by EMG signal is very similar. The average calculation error of the 8 blocks of the abdominal musclesin the 4 kinds of double-bridge movement were 2.56 (MVC %), 2.99 (MVC %), 1.73 (MVC %) and 3.13 (MVC %). The experimental results showed that for the double-bridge movement, we can use inertial sensor to replace EMG acquisition equipment to realize the supervision of ABS training actions.

The mean errors in bridge motion were 2.56 (MVC %), 2.99 MVC %), 1.73 MVC %, and 3.31 MVC %). The experimental results show that inertial sensors can be used instead of EMG acquisition equipment to supervise the training of abdominal muscles.

Experimental results show that different dual bridge motions can be accurately identified by inertial signals. At the same time, the EMG activity of the abdominal muscles computed by inertial signals can be well matched with the level of EMG activation calculated by the EMG signal. It is worth emphasizing that the effectiveness of the approach presented in this study is currently limited to dual bridge exercise. For the feasibility of other abdominal exercises, a large number of experimental verification and calculation methods are needed. For example, abdominal exercises performed in Rutkowska-Kucharsk's study required the upper limbs, lower limbs and trunk to work together. If inertial sensors are used to monitor this train-

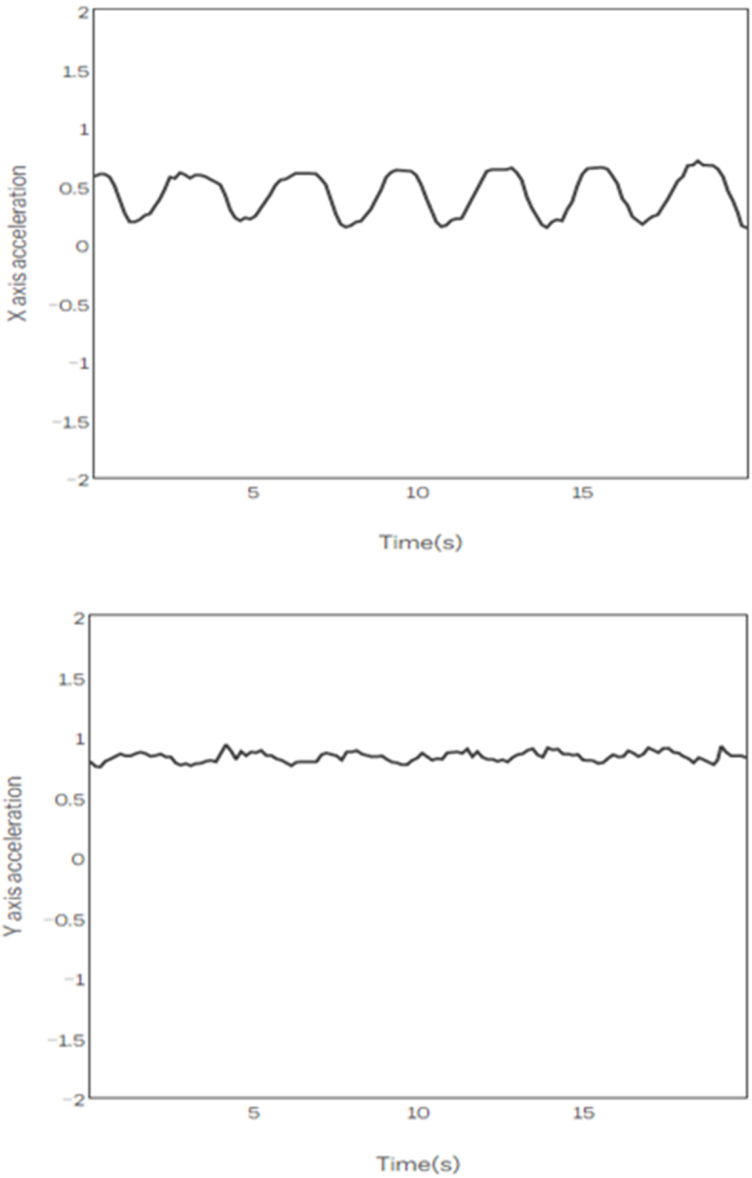

Fig. 2. Acceleration signal of lying on the left double-bridge movement

ing, a number of sensor nodes needs to be worn on the arm, thigh and upper body. Therefore, it is necessary to adjust the corresponding calculation process. In addition, some abdominal training exercises use additional load (such as dumbbells) to enhance the abdominal muscle stimulation intensity. The weight of the load does not have a direct effect on the inertial signal, but it can cause different EMG activity. For one of these abdominal exercises, external factors need to be incorporated into the calculation.

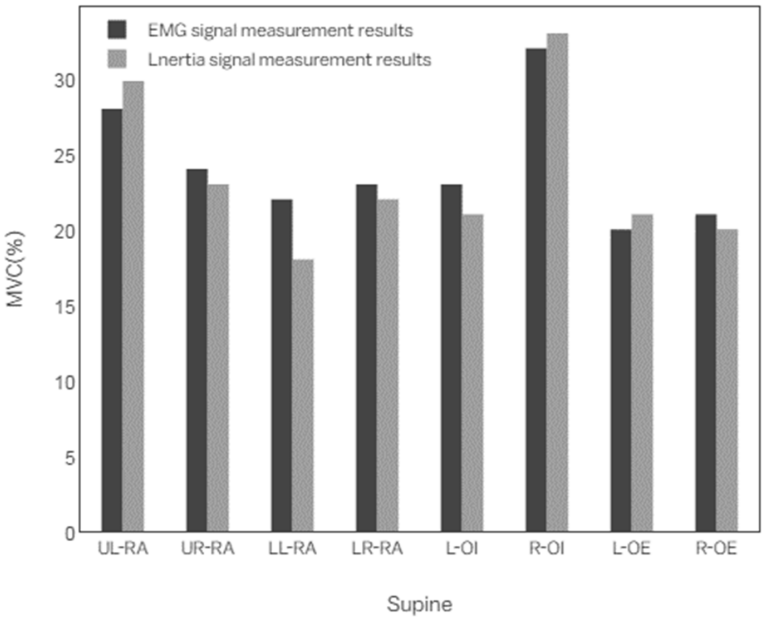

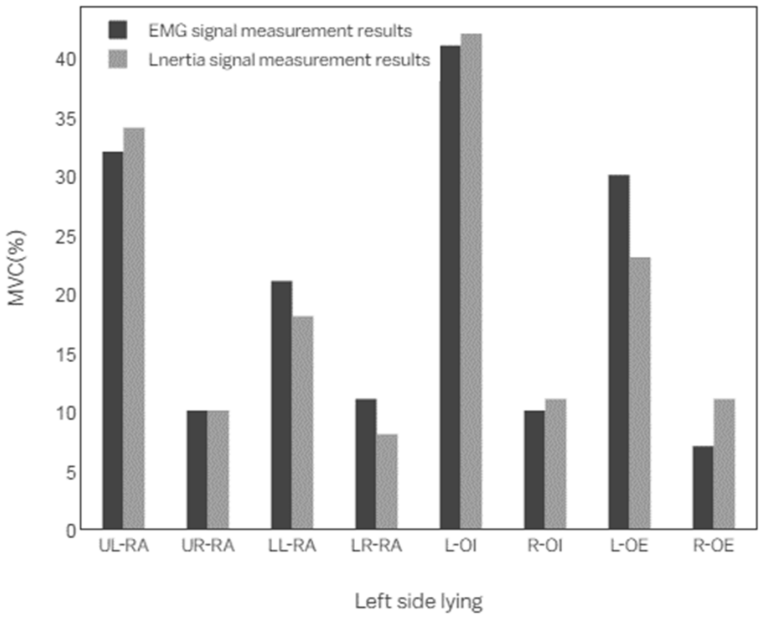

5. Conclusion

In this paper, taking double-bridge movement as a case study, we analyzed the feasibility of using inertial signal for monitoring abdominal training action. We

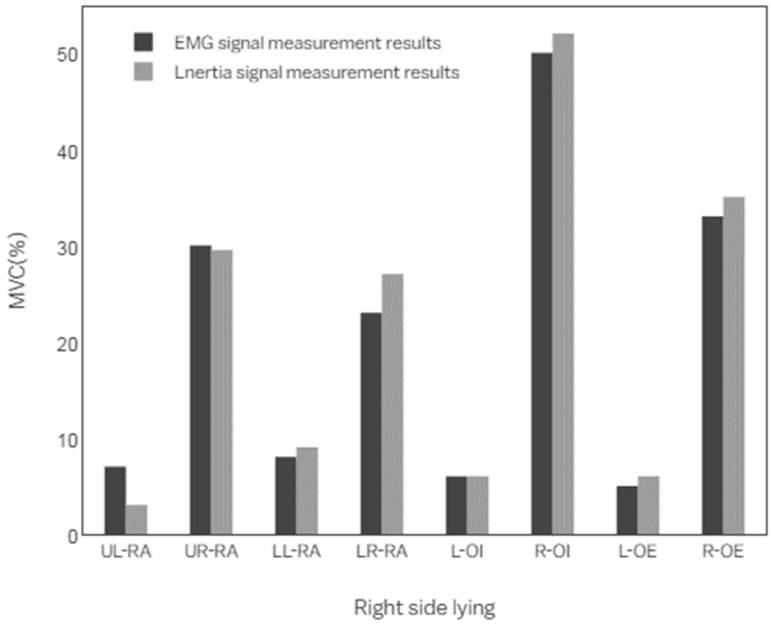

Fig. 3. Mean and standard of rectus abdominis (up), external oblique (middle) and EMG activity of internal oblique (bottom) in 4 kinds of different double-bridge movements

studied and established the Naive Bayes classifier to identify different double-bridge movements by inertial signals. The experimental results showed that the Naive Bayes classifier achieved high recognition accuracy. In addition, the EMG activity obtained through the inertial signal is similar to that obtained through using EMG signal. The experimental results showed that for the double-bridge movement, we can fully use inertial sensors to replace EMG acquisition equipment to realize the supervision of abdominal training action.

References

[1] [P. Kjaer, C. Leboeuf-Yde, L. Korsholm, J. S. Sorensen ,T. Bendix: *Magnetic resonance imaging and low back pain in adults: a diagnostic imaging study of 40-year-old men and women.* Spine *30* (2005), No. 10, 1173-1180.

[2] K. Freburger, G. M. Holmes, R. P. Agans, A. M. Jackman, J. D. Darter, A. S. Wallace, L. D. Castel, W. D. Kalsbeek, T. S. Carey: *The rising prevalence of chronic low back pain.* Archives of Internal Medicine *169* (2009), No. 3, 251–258.

[3] J. A. Hides, W. R. Stanton, M. Freke, S. Wilson, S. McMahon, C. A. Richardson: *MRI study of the size, symmetry and function of the trunk muscles among elite cricketers with and without low back pain.* British Journal of Sports Medicine *42* (2008), No. 10, 809–813.

[4] M. Monfort-Pañego, F. J. Vera-García, D. Sánchez-Zuriaga, M. A. Sarti-

Martínez: *Electromyographic studies in abdominal exercises: A literature synthesis.* Journal of Manipulative & Physiological Therapeutics *32* (2009), No. 3, 232–244.

[5] P. W. Marshall, I. Desai: *Electromyographic analysis of upper body, lower body, and abdominal muscles during advanced Swiss ball exercises.* Journal of Strength & Conditioning Research *24* (2010), No. 6, 1537–1545.

[6] H. D. Cho, J. H. Lee, J. H. Jeong, J. Y. Kim, S. T. Yee, S. K. Park, M. K. Lee, K. I. Seo: *Production of novel vinegar having antioxidant and anti-fatigue activities from Salicornia herbacea L.* Journal of the Science of Food and Agriculture *96* (2016), No. 4, 1085–1092.

[7] B. Yang, Y. Lei, B. Yan: *Distributed multi-human location algorithm using naive Bayes classifier for a binary pyroelectric infrared sensor tracking system.* IEEE Sensors Journal *16* (2016), No. 1, 216–223.

Received May 7, 2017

Acta Technica *62* No. 3A/2017, 235–246

A study on the influence of the change of football artificial turf's particle filling density on sports biomechanics characteristics

Xiangde Mo[1]

Abstract. In order to research the influence of the change of football artificial turf's particle filling density on sports biomechanics characteristics, the density of rubber particle filled in artificial turf is changed and its influences on traction on the interaction surface of football shoes and artificial turf are also explored. Tests on kinesiology of the player's 45 degree side cut and linear start and dynamics are carried out to discover the changes of biomechanical characteristics on the condition of different tractive forces, find out the influence on the sports performance and injury of players when the interaction surface traction of shoes and artificial turf are changed and meanwhile provide theory support and experimental basis for the standard making and instrument developing of artificial turf.

Key words. Artificial turf, sports performance, biomechanics, traction.

1. Introduction

The traction on the interaction surface made by shoes and the field is the key factor affecting action forms and performance of players, which support players the starting, braking and steering. Interaction surface of low traction may lead to "slipping" under the feet of players and feet may be "fixed" on the field if the traction is too high [1]. It turns out that the interaction surface traction is an important feature after shoes comfort through an investigation on football shoes. It is more critical than stability, traction, weight of shoes and the speed and accuracy of football playing. The type, fiber length, density, and type, size, depth and density of fillings as well as different humidity around may give rise to changes of the traction's effect [2]. But at present, when evaluating on changed interaction surfaces caused by different types of shoes, there are more studies about functions of the traction rather than the change of field surface.

[1]Hainan Tropical Ocean University, 572022, Hainan, China; E-mail: xiangdemostudy@126.com

2. Literature review

Playing football is a sport involving body moving. It is found that injuries occurring in football are more common than other sports. Main injures are contusion, sprain and strain, and the main injuring positions are knee and ankle joints and muscle in ligament of the thigh and lower leg [3]. Combining former literature, Inklaar figures out that 60 % to 90 % injuries occur in the lower limbs and discovers that some internal factors such as age, old injuries and external factors including lacking of training, low training or race rate and field environment can contribute to injury decrease [4]. Studies about injuries caused by football playing focus on the low limbs and some on cranial part. The injuries result from direct hit and upward impact force after on the ground. Theobald et al. [5] test on cushioning property of the third generation artificial turf and defined the standard of head impact to evaluate the performance of moving surface and further offer proper suggestions for decreasing the rate of mild head injury.

45 degree cut side movement is chosen in the study. In that direction change is the common basic movement form in football, and meanwhile, the abrupt direction change in rapid movement will give rise to much load to the legs and will injury ligament structure easily.

On the other hand, the acceleration ability to start from static state can reflect the basic quality of football player which is related with the traction in the interaction interface made by shoes and the field.

3. Methods

3.1. Object

26 male football players from Hainan Tropical Ocean University, with the second exercise level or over and the size of 42 (EUR) were chosen as experimental objects. Before the experiment, they have not strenuous exercise 48 hours before the experiment and there has been no obvious injury in the past a half year and dominant foot of them are the right foot. They are 24.3±1.4 years old with the height of 174.9±3.2 cm, the weight of 70±7.1 kg and training period of 10.4±3.5 years.

3.2. Research data

Experimental shoes are from foreign sports brand with the size of 42 (EUR) and the weight of 0.24 kg. Spikes of the shoes are short plastic spikes with the length of 0.5 to 1 cm which is suitable for players to train and race. The experimental artificial turf is manufactured by special manufactures in China, and the turf meets national standard regulated in Artificial Grass for Sports [6]. Fiber height of grass is 50 mm and the area of turf is the same as the ergograph with the length of 60 cm and width of 40 cm. Fillings of the turf are rubber particles with the size of 0.5 to 2 mm.

During the experiment, the weight of rubber filling particles are 0 kg, 0.5 kg and 1.5 kg. These particles are paved evenly and compacted tightly to create artificial

turf with different densities, which are named Field E, Field H and Field F. Density of Field E is 0 kg in that the non-density field is often chosen to make turf experiment in lab in China and the rest of other countries in the world. Even if there is no clear limitation in the density of real artificial turf, the paving of rubber particles is carried out in 5–8 kg/m^2 referring to advice from manufactures. Thus particles of 0.5 kg and 1.5 kg are chosen to simulate two fields which are within and lower than the above density.

3.3. Data collection and processing

3.3.1. Traction test. The field temperature is 23.3 °C and the humidity is 46.7 % on the experiment day. The artificial turf is put in the environment for over three hours before the experiment. In preparing the experiment, a unfilled artificial turf is pasted on the ground son that there is no slipping between ground and the turf. A shoe last with the size of 42 (EUR) is put in a shoe and later it is fixed on the traction tester. The shoe is parallel with the long side. the shoe and other attachment devices like shoe last weigh 4.748 kg. 30 kg weight is added in the vertical direction. Through the electrode, traction tester drags the shoe at uniform speed of 0.3 m/s. Relatively stable traction values in the process of dragging are recorded and indicated through the sensor. The dragging is repeated for 5 times. The shoe is adjusted to be parallel with the short side of the turf, and the above test is repeated for 5 times. After the test on the traction of non-filling artificial turf is completed, rubber particles with the weight of 0.5 kg are paved in the turf. After they have been impacted tightly, the above experiment process is to be repeated 5 times in terms of vertical and horizontal traction and reaction vales are recorded. At last particles of kg are filled in the turf. Traction test are done after they are impacted. As what have been done before, the experiment process is repeated 5 time and the vertical and horizontal traction values are recorded [7]. The average value and standard deviation of 10 traction values with both vertical and horizontal tests are counted on the condition of same filling density so as to define the traction of shoes and the artificial surface on the condition of different densities.

3.3.2. Kinematic and dynamics tests. 45 degree side cut requires that the object should stats approaching 6 to 8 m from the force measuring platform at the speed of 4 ± 0.3 m/s. The experiment players make side cut moving 45 degree inclined to the left on measuring force platform of the artificial turf with the support of right leg. 3 minutes later they can stop running. At the regulated speed, the objects make no other change in steps and at the same tine, only when their right feet step on the measuring force platform fixed with artificial turf can an effective an effective test be finished.

Linear starting requires that people involved in the experiment should step their both feet on two measuring platforms. They make speed-accelerated start in the standing posture they are familiar to. 3 minutes later they can stop running. Only when both feet of them are on two measuring platforms, the measurement is effective and the test can be finished.

In the real test, the objects are required to make 45 degree cut side and linear start in the non-filling artificial turf at first. Later they repeated the moving on two artificial turfs with particles of 0.5 kg. They are required to repeated again the moving on the artificial turfs with particles of 1 kg based on the turf of 0.5 kg. In the process, every object should make 3 times of test in terms of each moving.

3.3.3. Data processing. 3D coordinates of marking points in the experiment are smoothed through Butterworth low passing filter method with the truncation frequency of 10 Hz.

(1) Calculating the low limbs center

The center of knee joint, external knee center, center of ankle joint and external center as well as hip center are calculated though Bell's [8] research.

Local coordinate system of right hip joint (R.Hip.JC) is HR. The origin is the right and right anterior superior iliac spine point (Mid.ASIS), X, Y and Z standing for i_{HR},j_{HR} and k_{HR}:

$$j_{\mathrm{HR}} = \frac{\mathrm{R.ASIS} - \mathrm{Mid.ASIS}}{|\mathrm{R.ASIS} - \mathrm{Mid.ASIS}|},\ k_{\mathrm{HR}} = \frac{(\mathrm{V.Sacral} - \mathrm{Mid.ASIS}) \times j_{\mathrm{HR}}}{|\mathrm{V.Sacral} - \mathrm{Mid.ASIS}| \times j_{\mathrm{HR}}},$$

$$i_{\mathrm{HR}} = j_{\mathrm{HR}} \times k_{\mathrm{HR}}\,. \tag{1}$$

(2) Establishing local coordinate of lower limb

In the coordinate system of right thigh, the origin is right hip joint (R.Hip.JC), and unit vectors of each axis are

$$k_{\mathrm{R.Thigh}} = \frac{\mathrm{R.Knee.JC} - \mathrm{R.Hip.JC}}{|\mathrm{R.Knee.JC} - \mathrm{R.Hip.JC}|},\ j_{\mathrm{R.Thigh}} = \frac{(\mathrm{R.Knee} - \mathrm{R.Hip.JC}) \times k_{\mathrm{R.Thigh}}}{|\mathrm{R.Knee} - \mathrm{R.Hip.JC}| \times \mathrm{k_{R.Thigh}}},$$

$$i_{\mathrm{R.Thigh}} = j_{\mathrm{R.Thigh}} \times k_{\mathrm{R.Thigh}}\,. \tag{2}$$

In the coordinate system of right foot (R.Foot), the origin is right ankle joint (R.Ankle.JC), and unit vectors of each axis are

$$k_{\mathrm{R.Foot}} = \frac{\mathrm{R.Toe.JC} - \mathrm{R.Ankle.JC}}{|\mathrm{R.Toe.JC} - \mathrm{R.Ankle.JC}|},\ j_{\mathrm{R.Foot}} = \frac{(\mathrm{R.Ankle} - \mathrm{R.Ankle.JC}) \times k_{\mathrm{R.Foot}}}{|\mathrm{R.Ankle} - \mathrm{R.Ankle.JC}| \times k_{\mathrm{R.Foot}}},$$

$$i_{\mathrm{R.Foot}} = j_{\mathrm{R.Foot}} \times k_{\mathrm{R.Foot}}\,. \tag{3}$$

In the coordinate system of right foot (R.Foot), the origin is right ankle joint (R.Ankle.JC), and unit vectors of each axis are

$$k_{\mathrm{R.Foot}} = \frac{\mathrm{R.Toe.JC} - \mathrm{R.Ankle.JC}}{|\mathrm{R.Toe.JC} - \mathrm{R.Ankle.JC}|},\ j_{\mathrm{R.Foot}} = \frac{(\mathrm{R.Ankle} - \mathrm{R.Ankle.JC}) \times k_{\mathrm{R.Foot}}}{|\mathrm{R.Ankle} - \mathrm{R.Ankle.JC}| \times k_{\mathrm{R.Foot}}},$$

$$i_{\mathrm{R.Foot}} = j_{\mathrm{R.Foot}} \times k_{\mathrm{R.Foot}}\,. \tag{4}$$

(3) Lower limb joint angle

Joint angle is cardan angle between two neighboring local coordinate systems, which is the movement of distal link relative to proximal link. Namely, R.Foot relative to R.Shank stands for ankle joint movement and R.Shank relative to R.Thigh stands for knee joint angular movement to rotate around X, Y and Z to get the flexion angle, adduction and inclination angle, and medial rotation and lateral rotation angle.

(4) Calculating body barycenter

Revised inertial parameters of human body of DeLeva is adopted to calculate body barycenter by combing striking point scheme of Helen Hayes. Smoothing works are not done in the light of ground reaction. Three-dimensional moment of knee and ankle joint are got through calculation in the use of inverse dynamics, and the ground reaction is standardized to multiples of body weight and moment is standardized to the multiples of height multiplying weight.

3.4. Data processing

Comparison is made through one-way repeated measures ANOVA and the subsequent pairwise comparison is made through LSD method. The first level of deviation probability less than 0.05 means significant level. All data are dealt with by SPSS 17.0 software.

4. Results

4.1. Results of traction test

Interaction surface traction values of the shoe and turf on the condition of three different filling densities are of significant difference (Table 1, $p < 0.01$) and subsequent pairwise comparisons are all of significance ($p < 0.001$). Thus, three interaction surfaces Field e, Field h and Field f are turfs of low, medium and high traction turf.

Table 1. About the turf with three different densities and traction values ($n = 10$)

Turf	Field e	Field h	Field f
Qualitative	Low traction	Medium traction	High traction
Weight of filling particle (kg)	0	0.5	1.5
Traction (N)	233.68±16.71	347.79±5.4	414.03±33.8

a: Compared with Field e, there is of significant difference; b: compared with Field h, there is of significant difference.

4.2. Results of kinematic and dynamic tests

4.2.1. Results of kinematic parameters in the process of 45 degree side cut retardation. Different tractions have no significant effect on the maximum of knee flexion ($p = 0.649$), knee flexion range ($p = 0.508$), maximum of knee adduction ($p = 0.720$), flex angle of ankle joint touching the ground ($p = 0.269$), maximum of ankle joint enstrophe ($p = 0.345$), enstrophe range of ankle joint ($p = 0.81$) and maximum of external rotation ($p = 0.154$). The results are given in Table 2.

Table 2. The influence of different tractions on the lower limbs parameters (unit: °, $n = 13$)

Lower limbs joint angle parameters	Turf with low traction	Turf with medium traction	Turf with high traction
Maximum of knee flexion	53.89±8.11	54.23±7.34	53.16±8.56
Knee flexion range	19.51±7.55	20.12±9.31	20.50±8.11
Maximum of knee adduction	3.01±1.54	3.05±1.42	2.94±1.45
Knee internal rotation range	14.93±7.19	13.99±8.29	13.87±6.62
Flex angle of ankle joint touching the ground	20.31±5.88	20.31±7.15	19.36±7.65
Maximum of ankle joint enstrophe	11.76±2.74	11.68±1.83	11.24±1.65
Enstrophe range of ankle joint	5.58±2.29	5.43±2.02	5.75±1.93
Maximum of external rotation	21.55±6.02	20.31±5.24	21.11±5.23

Different tractions have significant effect on gravity acceleration in the process of braking ($p < 0.001$). The effect of high traction on gravity braking (–7.05 m/±2.56 m/) is higher than that of the low traction (–6.01,m/±1.77 m/, $p = 0.003$) and medium traction (–5.88 m/±1.79 m/, $p = 0.001$) and the difference is significant.

4.2.2. Results of kinetic parameter in the process of 45 degree side cut retardation. (1) Results of peak value of horizontal and component of ground reaction force

By comparing the peak torque of ground reaction force in side cut retardation in turfs with different traction (Fig. 1), it is clear that different traction turfs can significantly affect the horizontal resultant peak ($p = 0.004$). After checking, it can be found that the difference of turf with high traction is obvious that that of turf with medium and low traction ($p = 0.001$); turf with different traction can significantly affect the vertical peak of ground reaction force ($p = 0.05$). And the vertical ground

reaction through side cut movement in turf with high traction is larger than that of turf with medium traction. Compared with turf with low traction, there is no obvious difference of turf with high ($p = 0.269$) and medium ($p = 0.161$) traction in term of peak value of vertical reaction force.

Table 2. The influence of different tractions on the lower limbs parameters (unit: °, $n = 13$)

Kinetic parameters	Turf with low traction	Turf with medium traction	Turf with high traction
Peak value of horizontal component of ground reaction force (BW)	1.11±0.35	1.13±0.34	1.25±0.43
Peak value of vertical component of ground reaction force (BW)	2.62±0.91	2.41±0.95	2.77±1.05
Loading horizontal component of reaction rate of ground force (BW/s)	41.96±20.12	49.13±21.77	53.14±26.49
Loading rate of vertical component of ground reaction force (BW/s)	99.99±71.38	87.75±56.86	119.25±78.51
Peak torque of knee extension (BWBH)	-0.185±0.048	-0.194±0.043	-0.204±0.037
Peak torque of knee adduction (BWBH)	0.067±0.048	0.075±0.048	0.094±0.043
Peak torque of knee external rotation (BWBH)	0.015±0.004	0.016±0.005	0.018±0.002
Peak torque of ankle flexion (BWBH)	0.153±0.020	0.163±0.017	0.165±0.018
Peak torque of ankle ectropion (BWBH)	-0.054±0.021	-0.055±0.023	-0.059±0.021
hline Peak torque of ankle external rotation (BWBH)	0.017±0.012	0.021±0.009	0.023±0.005

(2) Results of loading rate of horizontal and vertical ground reaction force

By comparing the loading rate of horizontal and vertical ground reaction force in side cut retardation in turfs with different traction (Fig. 2), it is clear that dif-

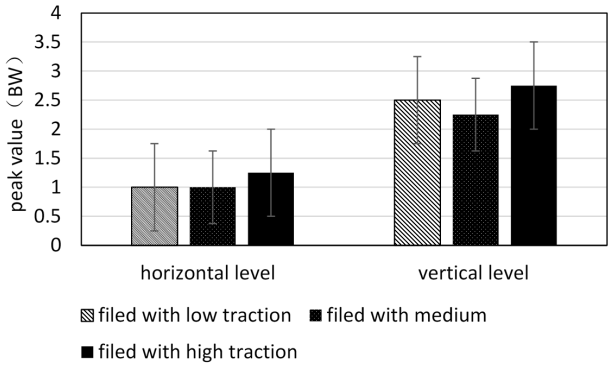

Fig. 1. Comparison of the peak torque of ground reaction force in side cut retardation in turfs with different traction

ferent traction turfs can significantly affect the horizontal resultant loading rate ($p = 0.001$). After checking, it can be found that the difference of turf with low traction is less obvious that that of turf with medium ($p = 0.011$) and high traction ($p = 0.001$); turf with different traction can significantly affect the vertical loading rate of ground reaction force ($p = 0.01$) and the difference of turf with high traction is obvious than that with medium traction ($p = 0.004$).

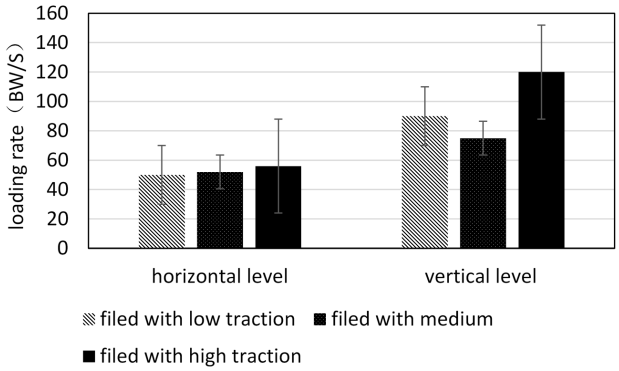

Fig. 2. Comparison of the loading rate of horizontal and vertical ground reaction force in side cut retardation in turfs with different traction

(3) Results of lower limbs three-dimensional peak torque

By comparing peak torque of knee joint in side cut retardation in turfs with different traction (Fig. 3), it can be found that knee extension peak torque in turf with high traction ($p = 0.004$) is obviously higher than that in the low turf ($p = 0.004$). Knee adduction force peak torque in field with high traction is obviously higher than that of field with medium ($p = 0.008$) and low traction ($p = 0.001$). And fields with different fraction have no significant effect on keen external rotation peak torque ($p = 0.624$).

By comparing peak torque of ankle joint in side cut retardation in turfs with

different traction (Fig. 4), it can be found that knee flexion peak torque in turf with low ($p = 0.001$) traction is obviously lower than that in the medium turf ($p = 0.0.001$) and high turf ($p = 0.001$). And fields with different traction have no significant effect on knee ectropion ($p = 0.226$) and external rotation ($p = 0.131$) peak torque ($p = 0.624$).

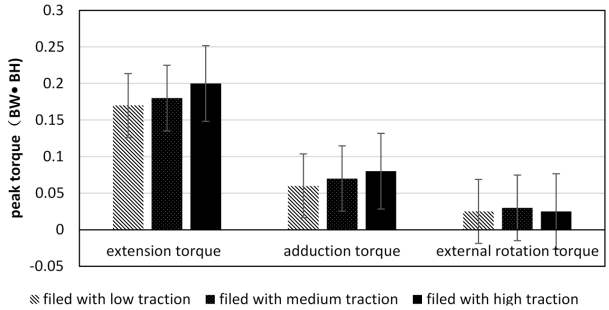

Fig. 3. Comparison of peak torque of knee joint in side cut retardation in turfs with different traction

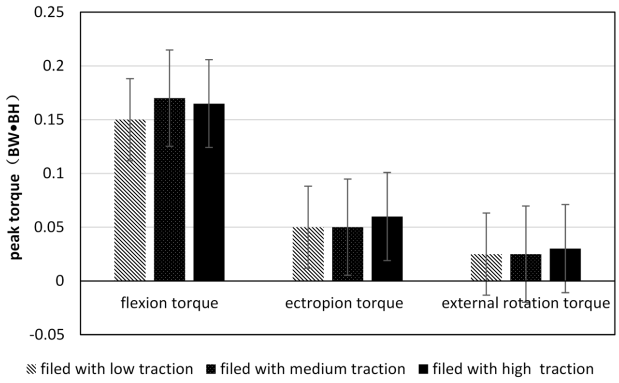

Fig. 4. Comparison of peak torque of ankle joint in side cut retardation in turfs with different traction

4.2.3. Results of biomechanical peak time parameters of ground reaction force in 45 degree side cut retardation. Related kinematics and dynamics parameters of the first peak value of ground reaction in turfs with different densities of shoe-turf interaction surface in 45 degree side cut movement are shown in Fig. 4. In the time, different tractions have significantly effect on vertical ground reaction ($p = 0.013$). After checking, it can be fund that the difference of turf with low traction and high traction is obviously higher than that with medium traction ($p = 0.024$, $p = 0.006$). Different tractions have significantly effect on horizontal background ground reaction ($p = 0.001$). After checking, it can be fund that the difference of turf with low traction is obviously than that with and high and medium traction ($p = 0.004$, $p < 0.001$) and the the difference of turf with medium traction is obviously

lower than that with high traction ($p = 0.002$). Different tractions have significantly effect on knee extension torque ($p = 0.007$). After checking, it can be found that knee extension torque on turf with medium traction and high traction is obviously higher than that with low traction ($p = 0.007,\ p = 0.03$) and there is no significant difference in turf with medium and high tractions ($p = 0.51$). Different tractions have significantly effect on knee adduction torque ($p = 0.02$). After checking, it can be found that the adduction torque on turf with medium traction and high traction is obviously lower than that with low traction ($p = 0.023,\ p = 0.005$) and there is no significant difference in turf with medium and high tractions ($p = 0.51$). Different tractions have a significant effect on knee adduction and abduction angle ($p = 0.004$). After checking, it can be found that the abduction angle of turf with low traction is obviously lager than that with medium and high tractions ($p = 0.005,\ p = 0.001$) and the abduction with medium traction is obviously larger than that with high fraction ($p = 0.015$). In the peak time, it can be found from other related parameters that different traction have no obvious effect on knee internal and external rotations ($p = 0.015$), knee extension angle ($p = 0.675$) and internal and external angles ($p = 0.274$).

Table 4. Biomechanical index of peak time of ground reaction force in turf with different interaction surfaces ($n = 13$)

Parameter	Turf with low traction	Turf with medium traction	Turf with high traction
Vertical ground reaction force (BW)	2.87±1.0	2.54±1.05	2.97±1.1
Horizontal background ground reaction (BW)	0.49±0.28	0.64±0.3	0.77±0.2
Knee extension torque (BWBH)	0.024±0.096	-0.021±0.08	-0.013±0.06
Knee adduction torque (BWBH)	0.074±0.049	0.047±0.04	0.049±0.04
Knee internal and external rotation torques (BWBH)	-0.001±0.006	-0.0002±0.007	-0.0003±0.008
Knee extension angle (§)	37.88±6.06	37.99±5.24	37.13±7.19
Knee adduction and abduction angles (§)	-1.11±3.01	-0.75±2.7	-0.52±2.9
Knee external rotation (§)	11.25±7.94	10.48±8.39	10.03±8.05

4.2.4. Kinetic parameter results of 45 degree thrust phase. By comparing peak values of horizontal resultant and vertical ground reaction on turf with different

traction in thrust phase (Table 5), it can be found that turfs with different tractions have significant effect on the two parameters ($p = 0.015,\ p < 0.001$). After checking, it can be found that the horizontal resultant force of turf with high traction is obviously higher than that with low traction ($p = 0.001$) and vertical force of turf with high and medium tractions is significantly higher than that with low traction ($p = 0.043,\ p < 0.001$).

Table 5. Peak vale horizontal and vertical ground reaction on turf with different traction in thrust phase (unit: BW, $n = 13$)

Parameter	Turf with low traction	Turf with medium traction	Turf with high traction
Horizontal resultant force	1.21±0.19	1.25±0.18	1.27±0.1
Vertical force	2.34±0.28	2.45±0.2	2.47±0.2

a: compared with turf with low traction, it is of significant difference; compared with turf with medium traction, it is of significant difference.

4.2.5. Results of linear start gravity acceleration. Turfs with particles of different densities filled in have no significant effect on gravity acceleration of players. Gravity acceleration indexes of starting process are of no significant difference on turfs with low (12.49 m±1.98 m), medium (12.38 m±2.44 m) and high (12.95 m±2.61 m) tractions ($p = 0.425$).

5. Conclusion

Translational traction tests are carried out in the study in terms of artificial turfs with three different filling densities. And rotational traction tests are undone due to limited experimental conditions. On the other hand, there are studies showing that translational traction is related with the existing of rotational traction, and when translational traction increases, the rotational traction will also increase proportionally. Results of the experiment suggest: the change of filling density has an obvious effect on the interaction surface of shoes and artificial turf. As the density of particles increases, the traction also increases. Different filling densities lead to the change of traction of the interaction surface but the movement form in side cut phase remains unchanged. The increasing of traction of interaction surface will contribute to the increase of ground reaction force, joint torque and other peak values, thus increasing the risk of injury. Traction increase resulting from the changed filling density will provide good braking and thrust force in side cut process, but movement performance of linear start movement is of no significant difference.

References

[1] G. Luo, D. Stefanyshyn: *Identification of critical traction values for maximum athletic performance.* Footwear Science *3* (2011), No. 3, 127–138.

[2] M. Ferrandino, S. Forrester, P. Fleming: *The Player Surface Interaction of Rugby Players with 3G Artificial Turf During Rugby Specific Movements.* Procedia Engineering *112* (2015), 308–313.

[3] U. Lange, U. Müller-Ladner, C. Mülich: *Sport und bewegung bei juveniler idiopathischer Arthritis.* Monatsschrift Kinderheilkunde *160* (2012), No. 8, 764–768.

[4] J. Ekstrand, J. C. Healy, M. Waldén, J. C. Lee, B. English, M. Hägglund: *Hamstring muscle injuries in professional football: the correlation of MRI findings with return to play.* British Journal of Sports Medicine *46* (2012), No. 2, 112–117.

[5] P. Theobald, L. Whitelegg, L. D. Noke, M. D. Jones: *The predicted risk of head injury from fall-related impacts on to third-generation artificial turf and grass soccer surfaces: A comparative biomechanical analysis.* Sports Biomechanics *9* (2010), No. 1, 29–37.

[6] D. M. Twomey, L. Otago, N. Saunders: *Challenges in the development of standards for synthetic turf for Australian football and cricket.* Proceedings of the Institution of Mechanical Engineers, Part P: Journal of Sports Engineering and Technology *225* (2011), No. 2, 93–101.

[7] D. McGhie, G. Ettema: *Biomechanical analysis of traction at the shoe-surface interface on third generation artificial turf.* Sports Engineering *16* (2013), No. 2, 71–80.

[8] J. Sinclair, L. Bottoms: *Gender differences in the kinetics and lower extremity kinematics of the fencing lunge.* International Journal of Performance Analysis in Sport *13* (2013), No. 2, 440–451.

Received May 7, 2017

Acta Technica *62* No. 3A/2017, 247–254

Athlete's gait tactics analysis system based on tactile sensor

Bing Li[1]

Abstract. Deficiencies of tactical information acquisition and analysis of existing methods hinder the correct judgment of coaches, athletes and researchers on the ability of the athletes, which seriously restricts the improvement of the training level and the competition quality. In order to solve this problem, this paper first of all takes tactile sensor as the basis, gives gait analysis model, and then, based on the model, designs and implements the athletes gait tactics analysis system. In addition, the paper tests the accuracy of the system acquisition of plantar pressure data and reflection of footwork technique information. The test results showed that the system can accurately collect the data and reflect the footwork technique information technique, and meet the requirements of coach, scientific research personnel and so on for tactic quantitative analysis, conductive for coach and scientific research personnel making a correct judgment on the athletic ability of athletes. In this way, it can provide effective basis for coaches and athletes making a scheme for daily trains and competitions.

Key words. Tactile sensor, athletes, gait analysis.

1. Introduction

At present, the combination of sports, science and technology has become an irresistible trend of development. The development level of sports to a large extent depends on the level of scientific and modern sports. Deficiencies of the existing tactics information acquisition method hinder the coaches, athletes and researchers to make the correct interpretation and judgment of athletic ability of athletes, which seriously restricts the improvement of the training level and the competition quality [1]. Data acquisition is restricted by environmental change parameters calibration, only obtaining local static information. As a result, in order to fully improve the competitive ability, it is urgent to develop stronger real-time, adaptable, and special tactical ability analysis system.

And the acquisition of gait tactile information in human motion based on tactile sensing technology not only achieves access to relevant kinematic information, also can complete the relevant dynamic information acquisition, so as to realize the real-

[1]Xinxiang University, Xinxiang, 453003, Henan, China; E-mail: alexbinglibl@163.com

time monitoring of sports information feedback. This is an important breakthrough of the modern science and technology in research methods in sports science.

2. Gait analysis model

In order to design the athletes gait tactics analysis system, we should first of all analyze the gait of the athlete in the designed gait analysis model. In this paper, the flexible sensor array based on tactile sensor and its data processing system are used to obtain the pressure distribution of the foot, the curvature and the acceleration of the foot in the movement. Through the original data, it is difficult to complete the tactics ability analysis of athletes within a time window [2]. As a result, we need to preprocess the original data, and extract the parameters of gait characteristics during exercise, so as to facilitate further analysis and processing.

2.1. Multi-characteristics parameters extraction used for gait analysis

Set a rectangle on the insole, inner vertex of the heel set as the origin, set the two adjacent edges of the origin to X axis and Y axis, and set the vertical direction to the rectangle as Z axis, consisting of the coordinates.

In the coordinate system XOY, first of all, measure and obtain the position coordinates of 8 flexible pressure sensors, recorded respectively as $\{(x_1, y_1), (x_2, y_2), \cdots, (x_8, y_8)\}$. Symbols $(x_i,\ y_i)$, $i = 1, 2...8$ refers to the position coordinate of the ith flexible pressure sensors, respectively [3]. We make use of 8 flexible pressure sensors to obtain the pressure value of the 8 pressure sensors at the moment t, recorded as $\{F_1,\ F_2,\ ...,\ F_8\}$. After determining the distribution position of the pressure sensors, we measure the pressure of 8 pressure sensors at the moment t, using pressure center method. We also use the following equations to obtain the center point information $(x_c,\ y_c)$ of the pressure distribution.

$$x_c = \frac{\sum_{i=1}^{8}(x_i \times F_i)}{\sum_{i=1}^{8} F_i}\,, \tag{1}$$

$$y_c = \frac{\sum_{i=1}^{8}(y_i \times F_i)}{\sum_{i=1}^{8} F_i}\,, \tag{2}$$

The bending C_t at the t moment is obtained by the flexible tension sensor.

The accelerations a_x^t, a_y^t, and a_z^t in the X, Y, Z directions at the t moment are obtained by the inertial sensor, and the scalar value S_t of the acceleration at the t moment is obtained by using the formula

$$S_t = \sqrt{(a_x^t)^2 + (a_y^t)^2 + (a_z^t)^2}\,. \tag{3}$$

For gait analysis within a time window, we first of all select the characteristics parameters of gait information within the window. In the previous part, we get 7

kinds of gait sensing information within the window, and calculate four features values of the 7 kinds of sensing information discrete data within the window, including the maximum and minimum value, mean and variance [4]. These 28 parameters are used as the characteristic parameters of gait analysis within the window.

2.2. Gait analysis model

We make use of the neural network toolbox in MATLAB software, and establish the mapping relationship between the 28 kinds of characteristic parameters and gait, so as to determine the gait of athletes.

(1) Selection of neural network algorithm

In this paper, the feed-forward neural network is used to classify and recognize the gait model of athletes. The most commonly seen in feed-forward neural network are BP (Back Propagation) neural network and RBF (radial basis function) neural network. About 80 % to 90 % of the neural network model use BP neural network and its change form.

The BP algorithm is used for network training.The network consists of an input layer, a hidden layer and an output layer. The results showed that the increase of hidden layer number or unit number is not positively related to the precision of the network and the ability to express. A hidden layer can also produce high accuracy, and a number of hidden layers will lead to the increase of the amount of calculation andslowing down the speed. Therefore, only one hidden layer is selected in this paper.

In the case of the n input units X_1, X_2, ..., X_n of the input layer of BP neural network, the input of the hidden layer neural unit is

$$I_j = \sum_{i=1}^{n} W_{ji} X_i = T_j,\ j = 1, 2, ..., n\,. \tag{4}$$

In (4), W_{ji} refers to the connection weights between the hidden layer neural unit J and input layer neural unit I, while T_j represents the threshold value of the hidden layer neural unit J.

The output of the hidden layer neural unit is

$$O_j = f(I_j)\,. \tag{5}$$

In (5), the activation function f always takes continuous and differentiable S-type function. The input calculation of the output layer neural unit is similar to (4).

The output of the output layer neural unit is

$$O_k = f\left(\sum_{i=1}^{m} W_{kj} O_j + T_k\right),\ k = 1, 2, ..., q\,. \tag{6}$$

BP neural network algorithm is a supervised learning algorithm. The main rule

of this supervision method is, for a plurality of input samples $(P_1, P_2, ..., P_q)$ and the corresponding output samples $(T_1, T_2, ..., T_q)$, through training, to make the squared error between the actual output of the network and the target vector achieve the minimum.

(2) BP neural network training

BP neural network can, through artificially prepared input and output sample data with corresponding relationship, analyze the potential rules between the input samples and output samples [5].

In this paper, the author selected the neural network toolbox in MATLAB software to create a three-layer feed-forward BP network as shown in Fig. 1: the first layer is the input layer containing 28 input nodes; the second layer is the hidden layer, and the number of nodes in the hidden layer is determined in the training process; the third layer is the output layer with 2 nodes. The components of two-dimensional output vector $(Y_1, Y_2)^{\mathrm{T}}$ are used for the representation of the gait analysis results.

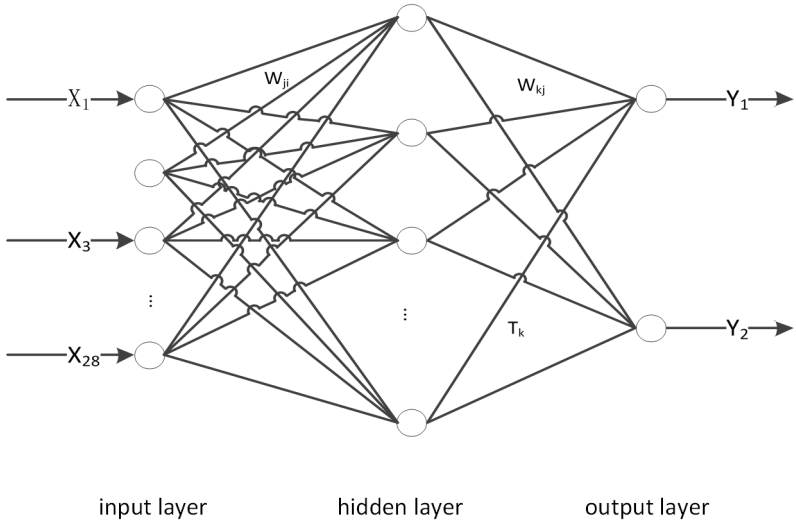

Fig. 1. Three-layer BP network structure for gait analysis

In the BP neural network, we are supposed to select the appropriate number of hidden layer nodes on the premise of ensuring the gait discrimination rate. According to these weight coefficients and thresholds, we can obtain the gait analysis model.

3. Design of athlete's gait tactics analysis system

According to the purpose of the gait tactics analysis system, the system can be divided into three modules, which are system management, data acquisition and management module, and tactical analysis and report module. Its functional structure is shown in Fig. 2.

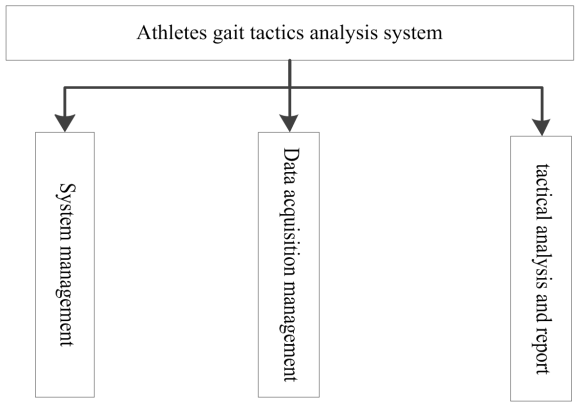

Fig. 2. System functional structure

3.1. System management

The system management mainly includes parameter setting, parameter script code processing and analysis, and system setting function. The script interpreter realizes tactical information statistics and analysis. The delimiter uses "&" to represent the connection of two movements, "#" represents the end of the turn, followed by the tactics used in the turn.

After the system reading into the script code group, the word is divided by the delimiter, and then the word rules and the semantic rules are used to explain the technique and tactics. According to this project, we need to design a special interpreter. The main function of the interpreter is to input the script code group and to explain and output the natural language.

3.2. Data acquisition management

Data acquisition management can be divided into video editing, digital site acquisition, synchronous acquisition and data validation of storage. Video editing mainly realizes video capture and playback, and video analysis. Clicking on the corresponding button can classify and store the corresponding tactics analysis information along with the corresponding video clips; video analysis means that the operator can refer to the competition video clips according to the query conditions of the athletes, the technology, the tactics, the round and so on, and can also classify and store again after editing.

The data confirmation storage module mainly completes the modification of error data and data storage in the data acquisition process.

3.3. Tactics analysis and report

Tactics analysis and report can be divided into analysis function and reporting function. In the tactics analysis and report module, the analysis function serves the

on-site guidance and preparations, and training summary these two aspects; report function mainly relies on the crystal report to realize, which can realize the report presentation and print.

4. System test results

For testing the system acquisition plantar pressure data and reflecting the accuracy and effectiveness of gait technology information, this paper selects 50 badminton players as the test samples, so these athletes play badminton at the same site. In the test samples, 10 athletes defense samples, first of all use first guaranteeing and later defensing tactics; 25 athletes attacking samples, use attack-after-service tactics; 15 athletes normal walking samples, without using any tactics. If the data information collected by the system and the gait technology information reflected by the method are consistent with the test samples classification, the test is normal. The final test results are shown in Table 1.

Table 1. Test results

Test samples	System analysis results			Accuracy
	First defensing and later attacking tactics	Attack-after-service tactics	No tactics	
Sample of players in defense	10	0	0	100 %
Sample of players in attack	0	25	0	0 %
Sample of players in normal walking	0	0	15	0 %

It can be seen from the test results that the system can correctly identify all the test samples, and prove the accuracy and validity of the data collected by the system.

5. Conclusion

The gait analysis system designed in this paper made use of script decoding technology of digital encoding technology with strong operability, and realized data automatic acquisition when the athletes are exercising. This paper designed the actual tests to test the accuracy of the system data acquisition of plantar pressure and reflection of gait technology information. The test results showed that the gait tactical analysis system based on tactile sensor designed in the paper not only can collect the plantar pressure data, but also can accurately reflect the gait technical information and tactical information. At the same time, the system can well meet

the needs of coaches, athletes, and researchers for the tactics quantitative analysis, providing an effective basis for the coaches and athletes to do the daily training and pre-competition strategies.

References

[1] S. Saga, R. Taira, K. Deguchi: *Precise shape reconstruction by active pattern in total-internal-reflection-based tactile sensor.* IEEE Transactions on Haptics *7* (2014), No. 1, 67–77.

[2] Y. Xin, H. Tian, C. Guo, X. Li, H. Sun, P. Wang, C. Wang: *A biomimetic tactile sensing system based on polyvinylidene fluoride film.* Review of Scientific Instruments *87* (2016), No. 2, 025002.

[3] J. A. Sánchez-Durán, F. Vidal-Verdú, Ó. Oballe-Peinado, J. Castellanos-Ramos, J. A. Hidalgo-López: *A new model based on adaptation of the external loop to compensate the hysteresis of tactile sensors.* Sensors *15* (2015), No. 10, 26170–26197.

[4] G. Zhu, W. Q. Yang, T. Zhang, Q. Jing, J. Chen, Y. S. Zhou, P. Bai, Z. L. Wang: *Self-powered, ultrasensitive, flexible tactile sensors based on contact electrification.* Nano Letters *14* (2014), No. 6, 3208–3213.

[5] M. Makihata, M. Muroyama, Y. Nakano, T. Nakayama, U. Yamaguchi, H. Yamada, Y. Nonomura, H. Funabashi, Y. Hata, S. Tanaka, M. Esashi: *Development of a 35Mbps Asynchronous Bus Based Communication System for Tactile Sensors.* IEEJ Transactions on Sensors & Micromachines *134* (2014), No. 9, 300–307.

[6] M. T. Woo, K. Davids, J. Liukkonen, D. Orth, J. Y. Chow, T. Jaakkola: *Effects of different lower-limb sensory stimulation strategies on postural regulation—A systematic review and meta-analysis.* PloS ONE *12* (2017), No. 3, e0174522.

Received May 7, 2017

Acta Technica *62* No. 3A/2017, 255–262

Design and experimental analysis of gesture analysis system of basketball players for human kinematics

Guoqing Wang[1]

Abstract. Body motion is a complex process and the study of body motion has a far-reaching influence on many research fields. In the basketball game, we can use the body movement measurement to scientifically plan the training of basketball players. In the automatic control system of robot, the human kinematics measurement provides a theoretical basis and verification platform for motion control such as bionic robot. In clinical medicine, the human motion measurement provides reliable data for the diagnosis and monitoring of medical staff. Gait is a branch of the human movement. Human gait is a long-term formation of a regular movement, and the gait movement contains a lot of sports information. In this paper, we use low-cost inertial sensors, including accelerometers and gyroscopes, to measure human gait data, and through these data to analyze the gait of human body. It is necessary to establish a gait database by collecting the experimental data of many people, so as to lay the foundations for future gait recognition work.

Key words. Gait movement, inertial sensor, gait database.

1. Introduction

Human kinematics is a popular science. As the human body movement is a highly-automated process, each person will have different movement patterns in different environment, that is, the human body movement has a certain random, so many studies are hoping to find the pattern of motion from human kinematics. In human kinematics, human gait is a relatively regular branch. From the birth of a human being to the learning of bipedal walking, the gait of a human being has formed a basic pattern that can be observed and measured, and further analyzed. There is no doubt that the theory of human gait movement can provide guidance for many scholarships and practices. For example, the gait pattern can be used in biped robot gait control strategy, so that the robot can be closer to people walking habits movement, to achieve a high degree of intelligent bionic movement [1].

[1]Zhejiang Industry Polytechnic College, 312000, Zhejiang, China; E-mail: emailguoqingwang@163.com

In addition, the measurement of human gait can be applied to clinical medicine. Doctors can use the patient's gait data to determine whether the patient needs treatment, or to provide strong data support for treatment [2]. Gait analysis emerged in the European renaissance. In the early days, in order to understand and record the gait information, most people use the method of observation and hand drawing to understand the human gait. A variety of computer equipment are used to collect and deal with human gait information. These methods include video image processing, pressure sensor signal processing and inertial sensor signal fusion processing [3]. These methods provide a theoretical and practical basis for the development of clinical medicine, intelligent robot control and other disciplines.

In this paper, we use low-cost inertial sensors, including accelerometers and gyroscopes, to measure human gait data, and through these data to analyze the gait of human body. It is necessary to establish a gait database by collecting the experimental data of many people, so as to lay the foundations for future gait recognition work [4].

2. 2. Algorithm flow design of gait analysis

After the node's hardware is filtered, the raw data of the inertial sensor is stored in the computer. The host computer program separates the two-node data into left and right node data, and each time the data packets are marked with time, so that the data can be further analyzed to calculate the gait parameters. Figure 1 is a flow chart of data analysis [5].

The data of the two nodes also contain information about the movement of the feet. Through the acceleration and angular velocity data fusion, we can get a single foot of the walking cycle. The original data of the acceleration and angular velocity are the data at the inertial boundary system, so we must project it into the navigation coordinate system and then obtain some spatial parameters such as step size by further integration [6].

In order to automatically identify the number of steps, we use the sliding window method to find the peak, so as to get the number of steps. The specific method is as follows. In the collected N data points, starting from the Mth one, if the ith point to meet the following relationship

$$\theta(k_1) \leq \theta(i) < \theta(k_2) \tag{1}$$

where k_1 and k_2 are the serial numbers of the sampling point, and its range is $k_1 :\ i - N \sim i - 1$, $k_2 :\ i + 1 \sim i + N$, $i :\ M \sim N - M$, M being the size of the sliding window.

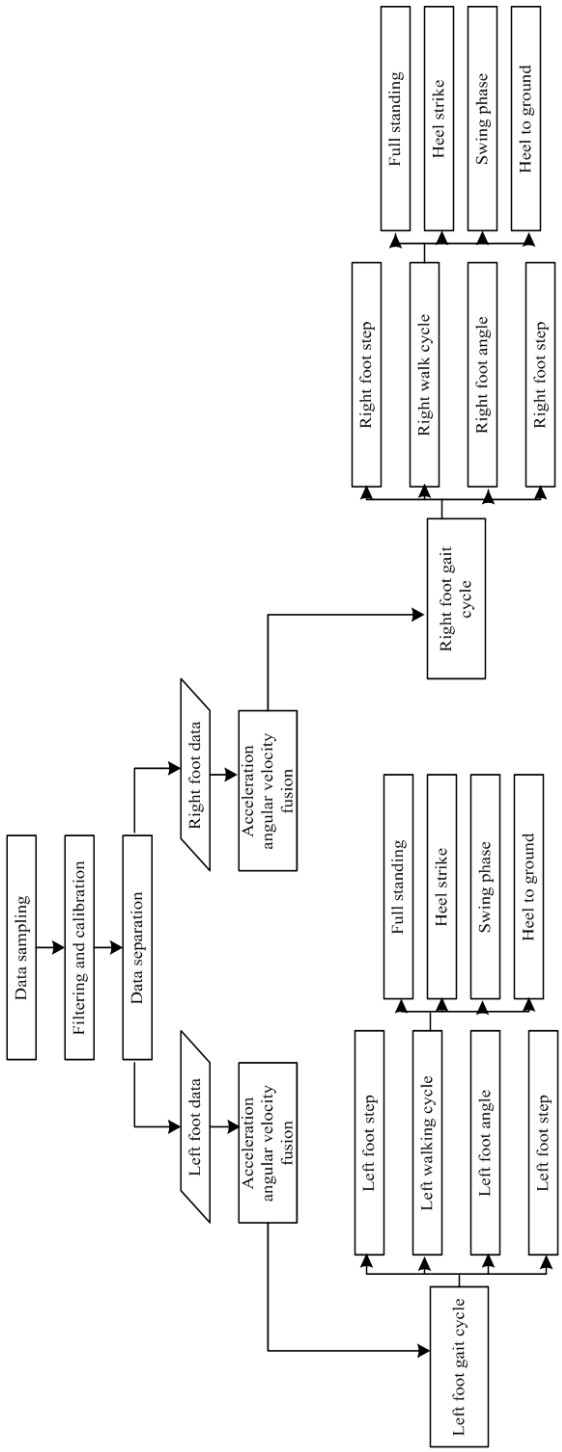

Fig. 1. Flow chart of data analysis

3. Walking cycle

3.1. Introduction of the walk cycle

The human walking process is a regular pattern. For regular movements, it can study its periodicity, and a walking cycle is divided into standing and oscillating phases. The stance phase is the time period when the foot is in contact with the ground. On the contrary, the time period when the foot leaves the ground and moves forward is called the swing phase.

The standing phase and the oscillating phase can be preliminarily divided into gait cycles, which can be done using the pressure sensor to complete the division of these two phases. Because of the use of inertial sensors, the complete process of motion can be captured, so the station can be further divided into heel off, heel strike, and foot flat.

In this way, our walking time can be divided into four stages as shown in Fig. 2, which are full standing, heel to ground, swing phase, and the heel strike. Heel off the ground is the experimental man still, or the heel first left the ground in the next step, but at the same time, the toes are also connected with the ground. The swing phase, as described earlier, is the foot that leaves the ground. Then, followed by the heel hit the ground, when the swing phase is completed, the foot to fall back to the ground, the heel first contact with the ground, and then flat the feet. Finally, when the foot is completely stationary, the other foot will move, and then the foot cycle of a single foot will end.

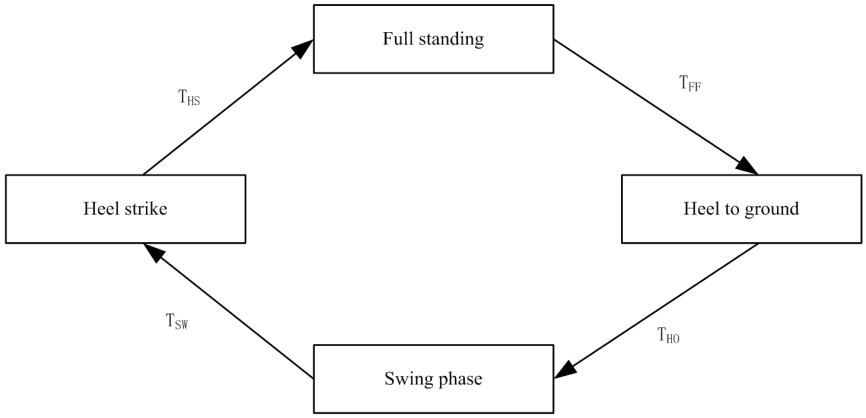

Fig. 2. Single foot walking phase

3.2. Motion decomposition of vector plane

Figure 3 shows the motion process in the vector plane, where $X - O - Y$ is the navigation coordinate system and $x - o - y$ is the inertial sensor coordinate system. Since the gait parameters are mostly in the vector plane, it is necessary to do a specific analysis of the motion within the vector plane.

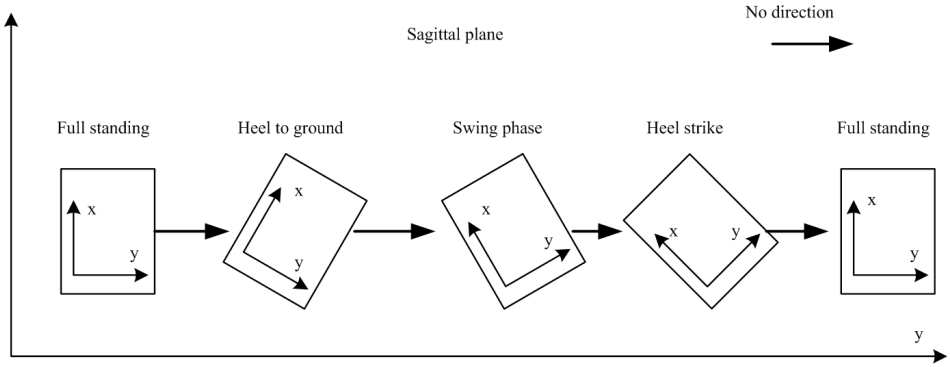

Fig. 3. Motion decomposition of vector plane

When the experimenter stats the experiment, or at the end of the step, it is in the complete standing stage, and this stage of the angle and acceleration are static output; When the gait movement begins, we enter the heel off the ground. With the movement of the experimenter, the sensor that tied to the ankle also rotates and moves. At this time, the gyroscope will produce a negative angular velocity, and when the negative angle reaches the maximum, the heel off the ground stage is end. The gyroscope will measure a positive angular velocity change, and then turn off the negative angle until it reaches the maximum angle, the swing phase is end. In the very short time of the heel to offset the adjustment angle, complete a gait cycle, return to the gait of the initial state, and prepare the beginning of the next cycle.

3.3. Sliding variance algorithm

For a sample value, if we want to know its fluctuation throughout the sample, variance is a good choice. We can use the sliding variance to evaluate the fluctuation of the sampling sequence in the experiment. The specific method of sliding variance is as follows:

First, using formula (2) we calculate the moving average:

$$E_i(j) = \frac{1}{M} \sum_{j=0}^{M} a(j+i)\,. \tag{2}$$

Here, M is the size of the sliding window, $a(j+i)$ is the data size of the $j+i$th sample point and $E_i(j)$ represents the moving average of the jth point in the window M.

4. Discussion of the results

Through the study of the gait mode, we accurately divide the walking cycle into four stance phases, which are heel strike, swing phase, heel off and foot flat. As

shown in the follows, Table 1 is the average of the single-step gait time information of the four experimenters. In the table, we give the form of (mean ± standard deviation). In the table, HO refers to the heel off the ground, SW refers to the swing phase, the HS finger abraded. Their units are seconds (s), and the table gives the data of the left foot and right foot.

Table 1. The average of the single-step gait phase (mean standard deviation

Param.		Experimenter 1	Experimenter 2	Experimenter 3	Experimenter 4
HO(s)	Left	0.296±0.024	0.295±0.058	0.357±0.043	0.278±0.026
	Right	0.284±0.038	0.273±0.026	0.336±0.032	0.273±0.036
SW(s)	Left	0.437±0.024	0.425±0.024	0.387±0.058	0.382±0.059
	Right	0.437±0.026	0.426±0.016	0.406±0.053	0.418±0.043
HS(s)	Left	0.257±0.024	0.218±0.037	0.146±0.017	0.197±0.024
	Right	0.354±0.047	0.203±0.037	0.154±0.017	0.183±0.17

From the above table, we can get that, when normal people walking, the time to complete a walk cycle is about 1.2 seconds. In a walk cycle, the time of the heel off the ground is about 0.3 seconds, the time of the swing phase is about 0.4 seconds, the time of the heel strike is relatively short for about 0.2 seconds, and the time of full standing is about 0.3 seconds. Everyone's walk has a certain difference, and the average of the walking cycle can reflect a general law of the pedestrian.

Figure 4 shows the percentage of the gait cycle of the right footers. For example, the heel to ground of the right foot accounts for 24 % of the entire walking cycle. The swing phase of the right foot accounts for 36 % of the total walking cycle. The heel strike of the right foot accounts for 14 % of the total walking cycle. The full standing of the right foot accounts for 26 % of the whole walking cycle. In this way, we can see that the right feet is balanced in a normal walking process, so the comparison results of the stance phases are also relatively symmetrical.

5. Conclusion

In this paper, we use the inertial measurement device to collect the acceleration and angular velocity signals in the walking process of the human body, and make a detailed analysis of the human gait movement. Through the error model to eliminate the static error, we correct the sensitivity of the sensor, so as to get a more accurate sensor data. We use the two inertial sensor nodes that are tied to the ankle of the experimenter to collect the inertia signals of the human gait movement. Through the study of the gait mode, we accurately divide the walking cycle into four stance phases, which are heel strike, swing phase, heel off and foot flat. The results show that the percentage of the gait cycle of the left and right swing phase is relatively large, and the percentage of the gait cycle of the left and right heel strike is relatively small.

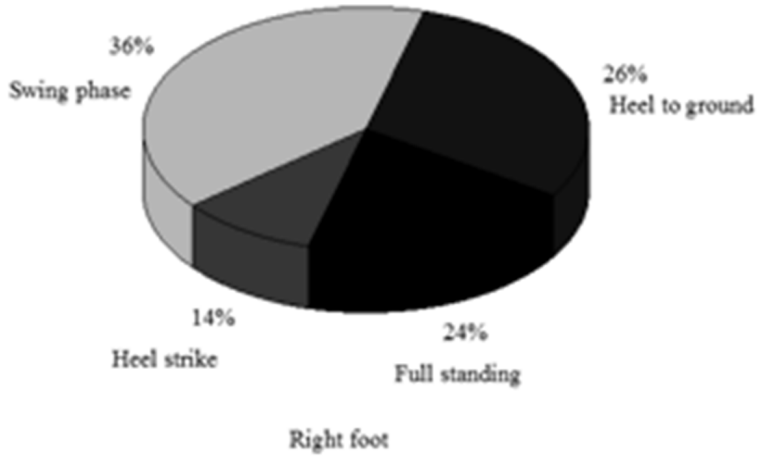

Fig. 4. Pie chart with the percentages of the walking cycle

References

[1] H. van Welbergen, J. Zwiers, Z. M. Ruttkay: *Real-time animation using a mix of physical simulation and kinematics.* Journal of Graphics, GPU, and Game Tools *14* (2009), No. 4, 1–21.

[2] A. Bouënard, M. M. M. Wanderley, S. Gibet: *Gesture control of sound synthesis: Analysis and classification of percussion gestures.* Acta Acustica United with Acustica *96* (2010), No. 4, 668–677.

[3] Z. Mohammed: *Which visual sight skill tested and developed the interaction between central and peripheral vision case duels dribbling soccer skills.* International Journal of Applied Exercise Physiology *5* (2016), No. 3, 31–37.

[4] J. B. Lee, R. B. Mellifont, B. J. Burkett: *The use of a single inertial sensor to identify stride, step, and stance durations of running gait.* Journal of Science and Medicine in Sport *13* (2010), No. 2, 270–273.

[5] A. Mannini, A. M. Sabatini: *Gait phase detection and discrimination between walking–jogging activities using hidden Markov models applied to foot motion data from a gyroscope.* Gait & Posture *36* (2012), No. 4, 657–661.

[6] V. J. Moorman, D. D. Frisbie, C. E. Kawcak, C. W. McIlwraith: *Effects of sensor position on kinematic data obtained with an inertial sensor system during gait analysis of trotting horses.* Journal of the American Veterinary Medical Association *250* (2017), No. 5, 548–553.

Received May 7, 2017

Acta Technica *62* No. 3A/2017, 263–274

The application of characteristic symbol detection and the scene recognition in football match video

Kuan Wang[1]

Abstract. In some football game videos, video data need to be segmented into different scenes to realize the retrieval of video data, thus analyzing the performance of different players in the field. How to effectively segment video data, therefore, becomes a significant application problem in the field of information retrieval. Video data is studied in the paper with camera pictures taken as the appearance of stereoscopic effect. A scene recognition algorithm similar to information pyramid is put forward at first so as to target at the moving scene of the player; the moving player in the camera can be seen as a circle symbol, whose detection algorithm is studied; meanwhile, in order to distinguish symbol pictures better, the algorithm of scene segmentation is researched from the minimum unit of the video. According to the situation when the accuracy and speed cannot be realized by using the current algorithm, a segmentation algorithm, based on the characteristic symbol detection and scene recognition algorithm, is figured out, whose accuracy improves gradually at a certain speed.

Key words. Scene recognition, characteristic symbol, scene segmentation.

1. Introduction

As a form of data, video [1] works better in helping people comprehend the information than text and carries much more information. A football match lasts 90 minutes, and the 90-minute video contains many massages for the coach, players and fans as well. People can see that the scenes and one scene switches to another very fast. The coach may focuses on the defense of midfield player, because the result of defense in midfield affects the pressure of defense line; players hope that they can see the moving ways of their counterparts so as to know about their attack modes; they care more about the wonderful moments of their favorite players.

When videos are uploaded to the Internet, they can be clipped and segmented in various ways and then they can be edited with titles. The way to manually handle with videos is inaccurate and time-consuming. Generally, the search engine defines

[1]Weinan Normal University, Shaanxi, 714099, China; E-mail: peterkuanwang@126.com

video in the way of text, which is limited. If video retrieval [2] is to be realized, the contents of the video itself should be taken into consideration.

2. Literature review

Scene recognition [3] is an important field of computer vision which is applied in many fields. It works in the data vectorization [4] of pictures in the scene, designing correspond data model and classifying different scenes. SIFT feature algorithm [5] has good recognition ability, but it has lower recognition rate in spatial distribution. Some researchers attempt to introduce certain information about spatial distribution to the semantic meaning, thus raising recognition rate. The literature points out that using spatial pyramid mode [6] to divide spatial area to extract SIFT features can greatly improve the scene recognition rate. Census transformation [7] is combined with special pyramid model in the literature, which works better than the former algorithm.

Pictures in video is stereoscopic [8], which is based on stereoscopic vision detection including camera calibration, picture data correction and picture fitting and three-dimensional positioning of objects. Characteristic symbol detection is crucial to three-dimensional positioning of objects.

This paper combines with spatial pyramid model and refers to the concept of similar information. A scene recognition algorithm is proposed and from the perspective of testing logo, players are taken as circular logo, to extract the edge information. And then a new symbol detection algorithm based on least squares fitting method is put forward. Combining scene recognition algorithm with symbol detection algorithm and from the perspective of scene segmentation, referring to the concept of entropy, an improved shot segmentation algorithm is proposed.

3. Research methods

3.1. Scene recognition algorithm similar to information pyramid

The traditional spatial pyramid mode uses the regular grid as the segmentation unit and extracts the features of correspond unit. But this method lacks in the description of semantic information of pictures. Based on spatial pyramid model, segmentation method with the similar information is adopted in the study so that the segmented grid units are of semantics.

The use of similar information can increase the computation of picture recognition, which normalizes small modules with several different colors to one color. This segmentation method combining similar information is based on entropy rate, which transforms the problem into another similar to clustering.

The function of the problem is expressed as

$$E(A) = F(A) + \beta G(A) \tag{1}$$

In the function, $F(A)$ is used to compute the entropy rate. The incoming picture is seen as an undirected graph. Panel points in the picture show the pixels, and edges of the picture indicate the connection of pixels. The function adopts the way of random walking to cover all points in the picture, so there are many pixel paths which can be used to compute the uncertain rate, namely, entropy rate. Clustering is analyzed based on several entropy rates and correspond pixel points. The bigger the entropy, the closer the pixel placer. Thus, the region of picture modules can be judged and divided. Expression $\beta G(A)$ is used to avoid the entropy rate tends to 0.

In using the method of segmenting similar information, information of similar modules of pictures can be clear, which lays a good foundation for the coming feature extraction. As is shown in Figs. 1 and 2, the way of segmenting similar information is applied and the picture is divided into several parts, and here there are 10 parts.

Fig. 1. Input image

Fig. 2. Similar image split

This kind of segmenting method ensures every pictures module has one or less objects when they are segmented in different resolving powers, which reduces the possibility that one picture module has more than one objects. This can improve the semantics of the picture module, which is shown in Fig. 3.

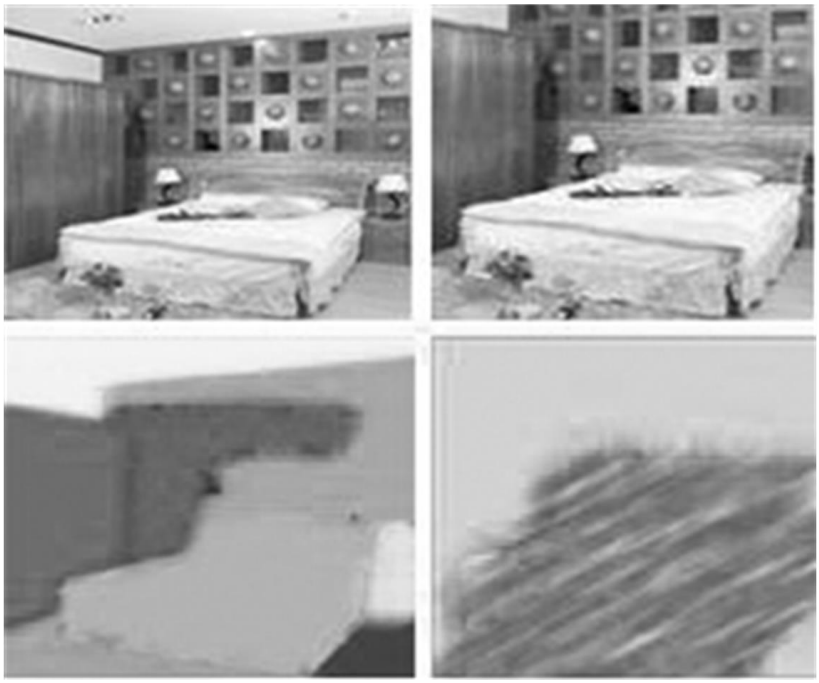

Fig. 3. Similar image split with different pixels

When the picture is segmented, features will be extracted by Census Transformation (CT), which is often used in connecting partial regions. It sets a founder with the size of 3×3. By comparing center point of the founder and the neighbor points, the transformation value can be known.

$$CT(q) = \underset{q' \in WT(q)}{\otimes} \text{MinMax}(U(q), U(q')), \tag{2}$$

$$\text{MinMax}(U(q), U(q')) = \begin{cases} 1, U(q) < U(q'), \\ 0, U(q) \geq U(q'). \end{cases} \tag{3}$$

In formulae (2) and (3), $CT(q)$ is the Census Transformation value corresponding to pixel q, $WT(q)$ is the transformation window corresponded to center point of the founder and $U(q)$ is the gray value of pixel q.

If the founder is $[(32,54,60),(45,54,70),(50,54,80)]^{\mathrm{T}}$, and has been transformed, there are 8 numbers which can be compared. According to (3), it can be transformed to $[(1,1,0),(1,1,0),(1,1,0)]^{\mathrm{T}}$, which corresponds to a binary number, whose range is [0, 255]. This is the CT value of the center point. Every change of pixel point through CT will reflect the transformation effect of the picture, which is shown in Fig. 4.

CT retains all features of the picture, and the picture is describe 256 degrees of vector, among which o and 255 is removed in that they go against the description. From the perspective of matrix theory, the picture structured by this method is of good sparsity and can help analyze main elements.

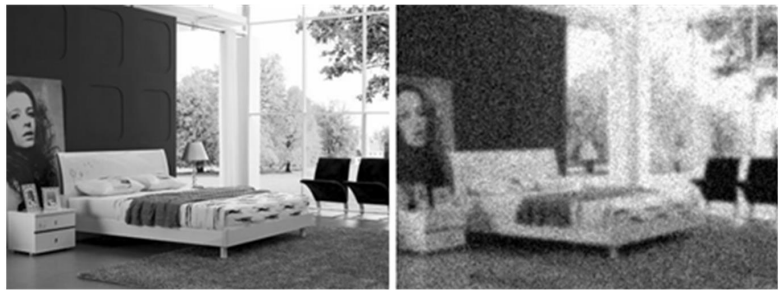

Fig. 4. Image transform with census

3.2. The algorithm of edge-least square fitting detection

In football match video, the characteristic symbols of players should be positioned if the moving track, the position and the defense in midfield of players are to be observed. Circles are common in characteristic symbol, which are easy to deal with and will not change with the pace of the geometry. In stereoscopic vision of the video, circle, the characteristic symbol, will be transformed into oval through affine. As the center of oval pictures does not mean the center of the three-dimensional circle picture, there is certain deviation between centers, and the center of the oval picture should be positioned.

The algorithms of least square oval fitting are:

3.2.1. Algebra fitting method. The method is to put discrete nodes to the equation to know the distances of deviation, and coefficient of the equation can be known in the method of least square. The method is easy to get results. If certain conditions are set, there will be less impossibility that the fitting result is oval. But it tends to be affected by abnormal nodes and isolated nodes, so the stability of it is not sure, which may lead to the difference of the least deviation function after transformation.

3.2.2. Geometry fitting method. This method defines that the deviation distance is the shortest distance from the point to the oval. It is different from algebra fitting method for there is no difference of the least deviation function, but it shows the exponential growth in computing.

3.2.3. Least median square method. The method requires that the median of residual sum of squares is the least. After extracting from the edge every time, 5 characteristic points are used to get corresponding parameters through linear transformation, this method features in excluding some characteristic points with great deviation, but the group numbers of correspondent oval parameters affect the performance of the algorithm.

In order to increase the precision of edge detection and make it the grade of subpixel, Zernike matrix is used here. It is an orthogonal complex which is of orthogonal invariant property.

The correspondent T-order polynomial of Zernike matrix is as the following:

$$W_{TF}(\beta,\,\alpha) = C_{TF}\mathrm{e}^{\mathrm{i}F\alpha}\,. \tag{4}$$

In the formula, T and F are integers and conform to the condition: $T \geq 0$ and $T-|F|$ is an even number. The parameter i refers to the imaginary unit. Polynomial formula CTF is defined as

$$C_{TF}(\beta,\,\alpha) = \sum_{d=0}^{\frac{T-|F|}{2}} \frac{(-1)^d(T-d)!\beta^{T-2d}}{d!(\frac{T+|F|}{2}-d)!(\frac{T-|F|}{2}-d)!}\,. \tag{5}$$

The T-order polynomial of Zernike is orthotropic in unit grid, namely, it conforms to the formula

$$\iint_{a^2+b^2\leq 1} W_{TF}(\beta,\alpha) \times W^*_{RV}(\beta,\,\alpha)\,\mathrm{d}a\,\mathrm{d}b = \frac{\pi}{T+1}\,. \tag{6}$$

Formula (6) is right when $T = R$ and $F = V$ and $W^*_{RV}f(x)$ means the complex conjugate.

Two-dimensional picture corresponding to Zernike matrix is defined by the formula (7):

$$Q_{TF} = \frac{T+1}{\pi}\iint_{a^2+b^2\leq 1} f(a,b) \times W^*_{TF}(\beta,\,\alpha)\,\mathrm{d}a\,\mathrm{d}b\,. \tag{7}$$

Considering that the picture is made up of scattered signals, Zernike matrix of two-dimensional picture $f(a,b)$ is

$$QTF = \sum_a \sum_b f(a,b) \times W^*_{TF}(\beta,\,\alpha),\ a^2+b^2 \leq 1\,. \tag{8}$$

Zernike matrix has less redundancy, strong ability of anti-interference, high precision and other merits. Good effects will appear if it is used in edge detection. The principle of detection is to compute the parameters of every pixel points in use of third-order Zernike matrix. According to the results, the pixel point will be judged whether it is the edge point. Parameters of the pixel point are: p, the gray coefficient of the background, $p+k$, the gray coefficient of foreground picture; om, the distance the foreground projects to the edge; θ, the included angle of project line and X axis. Symbol k is the span from the background gray value to the foreground.

At first, Canny operator is used to extract the correspondent pixel coordinate of the oval, and then Zernike matrix is used to further improve the precision of edge coordinate. According to the edge coordinate of sup-pixel, the parameter of the oval fitting is known and the correct oval center is also clear in the way of the least square fitting.

3.2.4. Scene segmentation algorithm In the algorithm of segmenting the scene, it is easy to mix the moving of camera or objects and the switching of scene. But the former is changing with the step of the position of edge, and the edge position

is relatively stable when pictures are switched. Based on the feature, "interframe information entropy is put forward.

$$E_p = -\sum_{t=0}^{W} |a_t^Y - a_t^W| \log |a_t^u - a_t^v| \,. \tag{9}$$

In the formula (9), u means any frame, v means a frame after u, t means the tth column of the histogram and $t \in [0, 255]$. 5 frames is an interval, which means that the difference of v and u is 5.

When adaptive threshold function is used to segment a group of moving videos with a camera or object, it will be mistaken as the switched candidate scene. Within a particular range, "interframe information entropy" is computed through Gaussian distribution formula. The related range can be changed by using the sliding of windows. Threshold R_s is shown in the following:

$$R_s = \eta + \beta\theta \,. \tag{10}$$

In the formula, η and θ refer to mean value and standard variance, in which β is the judging factor analyzed according to experiments. The parameter can be chosen properly to increase the rate of misjudging.

When the candidate scene is certain, further selection works should be carried out to remove the misjudging caused by the object or camera moving from the switching of scenes. Considering that there is overall change between frames in the moving video, but there change between frames in switching scene is partial. In accordance with the feature, the algorithm of scene edge detection is figured out, and the flow of it is as follows:

(1) Symbol A_i denotes the ith frame, and the interval is T_1, here its value is 2. At first, the pixel difference of two frames DA_i is figured out, shown in subfigure (b) of Fig. 5.

(2) The edge DA_i is detected by using Canny operator, and thus, WA_i (the corresponding moving effect) is shown in subfigure (c) of Fig. 5. The moving edge of switched scene is relatively stable and exhibits only a small change, but the edge change caused by the camera or object moving is greater.

(3) WA_i is simply expanded and segmented the effect picture of moving edge WA_i in the size of 6×6 window. The number of edge pixel in each unit is respectively collected. If one of them is over a pixel, it means the adjacent region of 6×6 is the edge. The edge expansion effect picture is shown in subfigure (d) of Fig. 5.

(4) After the edge picture of expansion is known, the edge information is gathered. Here the edge picture is divided into $Q \times H$ regions, and the resolving power of a single frame picture is $q \times h$. The number of unit region is $Q * H/(q * h)$. In the experiment, the unit region is set as 60×40, and the resolving power of a single frame is 1024×768. The information value of moving edge is figured out in the method of interframe information entropy:

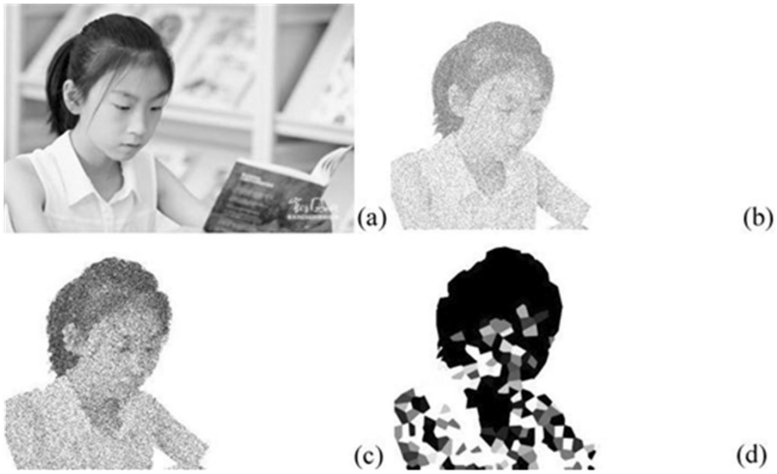

Fig. 5. Process of scene boundary detecting algorithm

$$E_p = -\sum_{v=1}^{Q\times H/(q\times h)} F_v^o/(q\times h)\log(F_v^o/(q\times h))\,. \tag{11}$$

In the above formula, F_v^o means the number of the edge pixel in unit region o, and $o \in [1, Q \times H/(q \times h)]$. Then the same computation is repeated in every frame so as to get the information difference of each frame using the formula

$$DA_v^F = |F_v - F_{v+1}|\,. \tag{12}$$

By doing this, a group number, namely, $DA_1^F, \cdots, DA_n^F$ misjudged in the video sequence is known, in which n means the number of the frame.

The whole process of segmenting scene develops from the group to the fine. The first step is based on interframe information entropy, which is to compute the candidate scene to be judged. As the similar performance of switching scenes and object or camera scene in general algorithms, it is impossible to select further. Therefore, in the second step, the distinguishing algorithm for switching scene and object or camera moving scene is designed based on the feature that the change appearing in switching scenes between frames is partial.

4. Experiment results and analyses

4.1. The experiment and analysis of scene recognition

In order to prove the algorithm put forward in the study is effective, different picture databases are compared and analyzed. Similar segmenting is adopted to segment the picture to two subregions with different grades: 128, 32, 8, 2. Owing to Census transformation, it is just based on the pixel intensity and lacks of multi-

dimensional information of pictures. Thus, some features of picture data are introduced. The feature dimension under the two grades is shown as: (38+5)×(8+2+128 +32)=7310. To extract characteristics, adopt the clustering algorithm to establish word dictionary for the characteristics, then get the word frequency of each scene, and the overall feature of the picture will be known, whose feature vector is expressed by 7310 dimensions.

10 kinds of scene are chosen here, and 300 pictures are used on average. The standard number of pixels of each picture is 1024×768 with the color omitted. In the data, the corresponding test set and training set are obtained based on Mahout, and the rate of them is loosely 1:4. The experiment is repeated 10 times to select the average recognition rate. Here the recognition rate is classified by using Bayes approach and sparse matrix is taken as the judging standard.

Table 1. Film scene labeled with alphabet

Film Scene	Alphabet
The Godfather	a
American Beauty	b
Raiders of the Lost Ark	c
The Silence of the Lambs	d
Paths of Glory	e
Toy Story 2	f
North by Northwest	g
The Sixth Sense	h
Crouching Tiger,Hidden Dragon	i
Homeless to Harvard	j

As what is shown in Table 1, it shows the scene of 10 movies. Symbols $[a, j]$ are used for better marking. For example, the movie American Beauty corresponds the letter b.

Table 2 shows that the scene recognition of each movie is high. From the main diagonal of the table, the average scene recognition can be computed as

$$(0.85 + 0.78 + 0.85 + 0.8 + 0.9 + 0.86 + 0.88 + 0.89 + 0.96 + 0.76)/10 = 0.853\,.$$

It can be seen that the average recognition rate put forward in the study is over 85 %. 8 out of 10 items have the recognition over 80 %, among which recognition rate of the movie Crouching Tiger, Hidden Dragon is up to 96 %, which shows the distinctive scene characteristics.

4.2. Simulation and analysis of characteristic symbol detection

Circle, the characteristic symbol, is studied. The design of detection algorithm is to solve the problem that project enter point of characteristics symbol is uncertain due to the deviation. Circle is adopted in the study, which will be projected to oval.

In the ideal state, the oval center is a point with the circle symbol projected. In practical detection, the oval centers which are fitted on the oval edge are not at one point.

Table 2. Scene recognition based on confusion matrix

	a	b	c	d	e	f	g	h	i	j
a	0.85	0.12						0.10		
b		0.78			0.13		0.02			
c			0.85	0.10		0.05				
d				0.8	0.13				0.07	
e					0.9			0.02		0.08
f						0.86	0.10		0.04	
g		0.12					0.88			
h			0.03		0.12	0.05		0.89	0.04	
i					0.04				0.96	
j				0.05			0.06			0.76

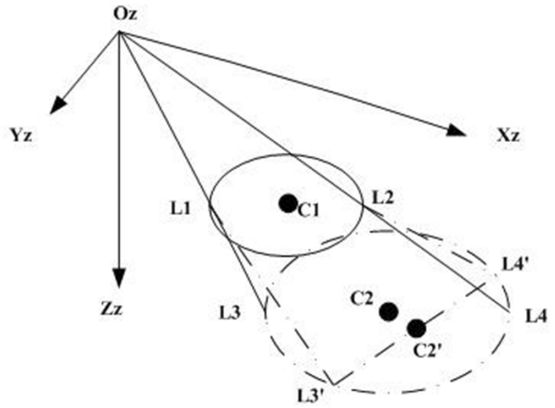

Fig. 6. Projection center deviation

As shown in Fig. 6, Oz-XzYzZz consists of the camera coordinate system. With C1 as the circle center, it establishes the photographed plane. The plane where the camera makes an image is the plane with C2 as the circle center. It is assumed that L1 and L2 are the diameters of an ellipse on a plane. OzL1 and OzL2 are extended to the space object plane, namely, they intersect with the plane whose center is C2 to L3' and L4'. In addition, from the figure, it is easy to find that, between the correspondent points, there holds $L3 \neq L3'$ and $L4 \neq L4'$.

L3' and L4' are connected and the center point C2' is selected. And then it will be clear that C2' and C2 are not the same points. It means that the projection point of the center on the space object plane is not in the circle point after it is transformed in the camera imaging plane. In the pretreatment of video data, it is usually divided into many pictures, so the deviation of the projection circle is common.

In order to reduce this kind of deviation as much as possible and better depict players in the field, it is important to compute the center of the projected oval. The method put forward in the study is to detect the edge and then extract the related edge coordinates of characteristic symbols, and get the edge coordinate of sub-pixel in using Zernike matrix. Hence, the detection precision can be improved. Through comparing the deviation of center of three-dimensional project imaging, the advantage and disadvantages of this method can be found.

Table 3. Coordinates of ellipse center with different algorithms

Algorithm	Center of grey	Ellipse fitting	Zernike fitting	Installed center
Ellipse 1	241.55, 209.58	242.15, 211.45	241.07, 208.70	240.65, 209.01
Ellipse 2	269.80, 271.05	269.96, 270.15	269.11, 269.75	269.00, 269.01
Ellipse 3	284.80, 286.05	284.96, 285.15	284.11, 284.75	284.00, 284.01
Ellipse 4	521.75, 234.30	521.39, 234.15	520.60, 233.75	520.80, 233.55
Ellipse 5	412.86, 270.59	412.34, 270.19	412.41, 269.50	412.13, 269.50

According to what is shown in Table 3, the root mean square of the center deviation, the pixel with maximum pixel, and the time for performance are computed using the following algorithms.

$$\text{Max}\Delta\text{Pix} = \max \sqrt{(X_t - XO_t)^2 + (Y_t - YO_t)^2}\,, \tag{13}$$

$$\text{RMSquare} = \sqrt{\frac{1}{m}\sum_{t=1}^{m}\left[(X_t - XO_t)^2 + (Y_t - YO_t)^2\right]}\,. \tag{14}$$

According to formulae (13) and (14), it can be concluded that the edge detection for the grade of sub-pixel is carried out by using Zernike matrix, and then the error of the ellipse center coordinates by fitting is relatively small, and thus, the precision is higher.

5. Conclusion

Focusing on football match video, a method of scene segmentation is put forward to better know the performance of players in the field. In order to carry out scenes segmentation, some pretreatment works should be done at first. The scenes images are carried out with edge detection and classification from the aspect of characteristic symbols and scene recognition. The algorithm of edge detecting of characteristic symbols solves the center deviation appearing in the circular projection; and the pyramid combined with similar information enhances the accuracy of scene recognition. As for the experiment, the picture pretreated is taken into consideration, and by combining with the scene segmentation algorithm, the segmentation experiments can be made in the condition of different scene pictures, which is the work in the

further study.

References

[1] Y. H. Ng, M. Hausknecht, S. Vijayanarasimhan, O. Vinyals, R. Monga, G. Toderici: *Beyond short snippets: Deep networks for video classification.* IEEE Conference on Computer Vision and Pattern Recognition (CVPR), 7–12 June 2015, Boston, MA, USA, IEEE Conference Publications (2015), 4694–4702.

[2] H. Yang, C. Meinel: *Content based lecture video retrieval using speech and video text information.* IEEE Transactions on Learning Technologies *7* (2014), No. 2, 142–154.

[3] B. Zhou, A. Lapedriza, J. X. Xiao, A. Torralba, A. Oliva: *Learning Deep features for scene recognition using places database.* Advances in Neural Information Processing Systems 27 (NIPS 2014) (2014), 487–495.

[4] V. Severo, H. A. S. Leitão, J. B. Lima, W. T. A. Lopes, F. Madeiro: *Modified firefly algorithm applied to image vector quantisation codebook design.* International Journal of Innovative Computing and Applications *7* (2016), No. 4, 202–213.

[5] B. Liao, H. Wang: *The optimization of SIFT feature matching algorithm on face recognition based on BP neural network.* Applied Mechanics and Materials *743* (2015), No.Chapter 4, 359–364.

[6] X. J. Peng, L. M. Wang, X. X. Wang, Y. Qiao: *Bag of visual words and fusion methods for action recognition: Comprehensive study and good practice.* Computer Vision and Image Understanding *150* (2016), 109–125.

[7] C. Stentoumis, L. Grammatikopoulos, I. Kalisperakis, G. Karras, E. Petsa: *Stereo matching based on census transformation of image gradients.* SPIE Videometrics, Range Imaging, and Applications XIII *9528Q* (2015).

[8] M. T. El-Haddad, Y. K. Tao: *Automated stereo vision instrument tracking for intraoperative OCT guided anterior segment ophthalmic surgical maneuvers.* Biomedical Optics Express *6* (2015), No. 8, 3014–3031.

Received May 7, 2017

Acta Technica *62* No. 3A/2017, 275–282

Application and induction properties of novel piezoelectric thin film material in the Wushu electronic gear

Xuelin Luo[1]

Abstract. With the continuous evolution of Wushu competition and the implementation of the new rules, the Wushu martial arts equipment is no longer the pure armor, but an electronic body protect having the protective function to achieve intelligent identification of hitting, automatic scoring, display of strength value and other functions. By studying the advantages and disadvantages of martial arts electronic gear at present, we designed and produced a kind of E-Touch based piezoelectric thin film used embedded in the gear, without disturbance and anti-interference. We can make it into different kinds of universal sensor used in Wushu competition, and prepare for the following calculation of force size, duration, and force frequency, by taking the voltage follower with fast response and good following feature as the calibration result for the conditioning circuit. After the test, the martial arts electronic gear studied in this paper has rapid response, low power consumption, and low cost, meeting the application requirements, suitable for popularization in China Wushu team.

Key words. Electronic protector, piezoelectric film, martial arts.

1. Introduction

The electronic gear, from the beginning of development by Taishan Daedo and Lajust company, has been concerned and disputed. In recent decades, the Wushu electronic gear has been rapidly developed because the response is sensitive, it can determine the force source, and its disturbance is small, even up on the stage of the competition. But due to the rules of the game, the size and different gear using force sensor, non-contact induction chip and the ID chip of recognizing the action, the Wushu electronic gear sometimes take a long time to contact and sometimes can easily get the score by getting close to each other. As a result, the penalties of competition was sometimes questioned by the athletes, and the training difficulty greatly increased [1].

Similarly as the core components of the electronic gear, the acting force, anti-

[1]Xi'an Physical Education University, 710068, China; E-mail: xuelinluoxll01@163.com

interference, service life and further problems directly affect the usage and development of the gear [2]. Aiming at the above problems and the impact of the electronic gear on the competition events, we designed a new replaceable force sensor E-Touch based on piezoelectric thin film without disturbance and anti-interference. There are many flat hole structures in the E-Touch piezoelectric films, and there are permanent positive and negative charges stored in these holes. When the piezoelectric film is subjected to dynamic stress, the thickness changes and produces the corresponding charge, and these charges accumulate in the electrode film, resulting in a charge [3] corresponding to the size of the force. Combined with the conditioning circuit, through the output waveform, we measure the force and the force time, calculate the force frequency, and determine the position of the force by the different parallel network areas. At the same time, according to the needs of different competition event gears, using requirements of athletes in different genders and levels of corresponding protective events, we produced force sensors that met different sizes and stress ranges of event requirements.

2. Methods

2.1. 2.1 System overall design

Wushu, as a competitive sport, the regulations of venue have been relatively perfect. Wushu competition venues are slightly different with the different projects, generally no-obstacle level with 14 meters in length and 8 meters in width, built on the platform with the height of 50 to 60 centimeters according to the needs [4]. Since that the physical fitness of different athletes is different, the gears will bear tens to hundreds of kilograms of power. At the same time, considering the sweat of athletes, the electronic gears need to be installed safely and reliably, and set some waterproof measures or have the function of working under a certain humidity [5].

According to the application features and function requirements of Wushu electronic gears, the whole system is composed of MSP430F149 microcontroller as the core processing chip, piezoelectric film sensor, charge amplifier circuit and wireless transmission module Bluetooth 4.0. Figure 1 shows the schematic diagram of the system.

In the gear part, we use the lightweight plastic of new piezoelectric thin film, design large-area thin film pressure plate to fully cover the effective part of gears, and then fill in the proper polyurethane high resilience foam to ensure the anti-resistance of piezoelectric film for being stricken. At the same time, we realize the basic functions of gears, and make use of piezoelectric features of piezoelectric sensor to output different amounts of charges for the hitting in different intensities. After suitable amplification of the charge amplifier, the current signal is transformed into a voltage signal convenient for monitoring.

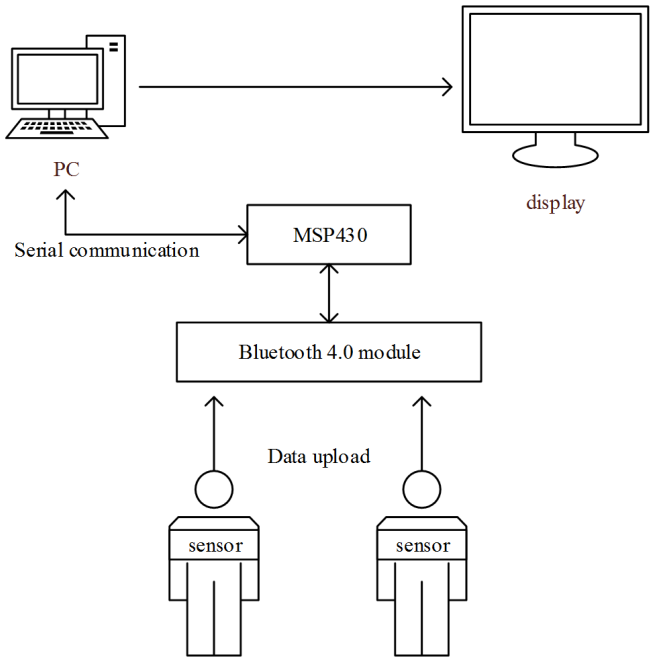

Fig. 1. Schematic diagram of the system

2.2. System hardware design

In sports, there is not much room for choice because it is complex and irregular and it cannot be monitored. In general, there are h kinds of sensors for measuring the force, resistance, capacitance and piezoelectricity. In general, the resistance is in block form, greatly affected by environmental conditions; the capacitive sensor structure has high requirements, not suitable for large area sensors, generally in cylindrical probe shape; and the acquisition of a capacitor and a resistor type sensor belongs to static acquisition, low in working frequency, and not timely in the response. The piezoelectric sensor was characterized by its high bandwidth, high sensitivity, high signal-to-noise ratio, simple structure, and light weight. The early piezoelectric materials were piezoelectric single crystals and common piezoelectric ceramics. In recent years, polyvinylidene fluoride (PVDF), as a new type of polymer piezoelectric material, has been widely used.

E-Touch piezoelectric thin film is a new organic film with patented technology, which was launched in October 2011 by Shanghai Mstar Technology Ltd. The widest application of E-Touch piezoelectric film is the sensor. In the field of sensor applications, it is necessary to package the piezoelectric film so as to protect it. The E-Touch-SS sensor consists of a E-Touch piezoelectric film, an upper and a lower electrode, a protective layer film or a shielding layer. In order to ensure the high sensitivity, it has the characteristics of good flexibility, waterproof, anti-wearing,

resistance and so on.

In the good arrangement of packaged sensors, the output signal is the charge of a small charge or voltage, cannot be directly accessed to the system. As a result, in the sensor and the system processor, it also needs to design a charge amplifier circuit, and to amplify the change of a small charge and voltage to the great voltage output that is easily recognized by the system. The basic principle of the charge amplifier is shown in Fig. 2.

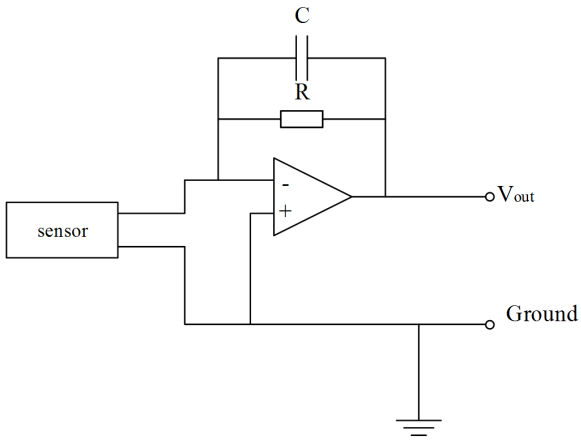

Fig. 2. Basic principle of charge amplification

The output value of the charge amplifier is determined by the piezoelectric charge coefficient and the capacitance of the sensor. The output frequency is determined by the ratio of capacitance and resistance of the RC circuit. When the frequency is greater than $(1/2\pi) \times R \times C$, the amplifier output voltage can be approximated as

$$V_{\mathrm{p}} = \frac{1}{C} \times d \times F_{\mathrm{p}} \tag{1}$$

In (1), F_{p} is the vertical force applied to the sensor surface.

2.3. System software design

The design selects the Bluetooth module BTMO608C2X following the Bluetooth 4 standard launched by Chongqing Jinli Science and Technology Development Co., Ltd. The module uses CSR8760 as the master chip, with built-in Bluetooth 4 driver, and down compatible the Bluetooth protocol of the first few versions.

Not stricken, the sensors that the system read are the stable voltage value with small amplitude clutters. When the strike occurs, the output voltage value began to rise until the hitting energy all transformed into the sensor material deformation. When the voltage value reaches the maximum value, then the combat force with draws, and the elastic material springs back, starting the reverse pull sensor and making the voltage decrease. At the same time, the piezoelectric material began

to conduct reverse electricity effect, and release the excess charge, so the voltage continues to decline, and gradually reduces the amplitude and tends to the initial state. In the process of the electronic gear utilization, the flow charts of PC terminal and gear terminal are shown in Figs. 3 and 4.

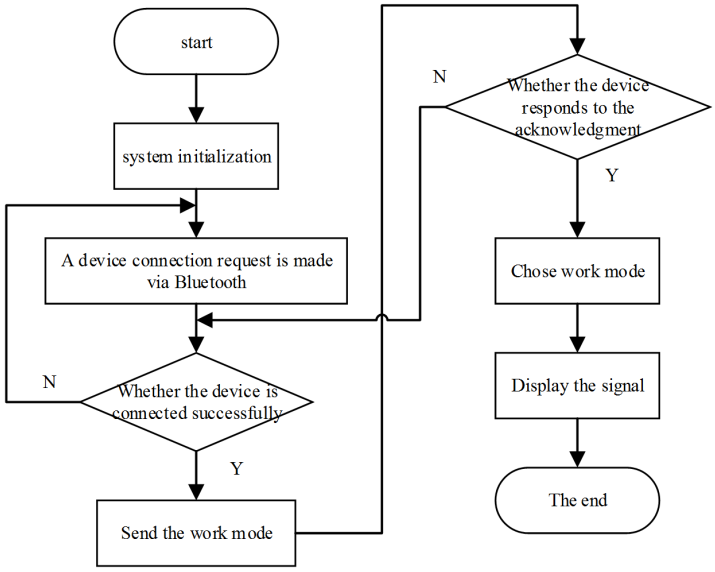

Fig. 3. Flow chart of PC terminal

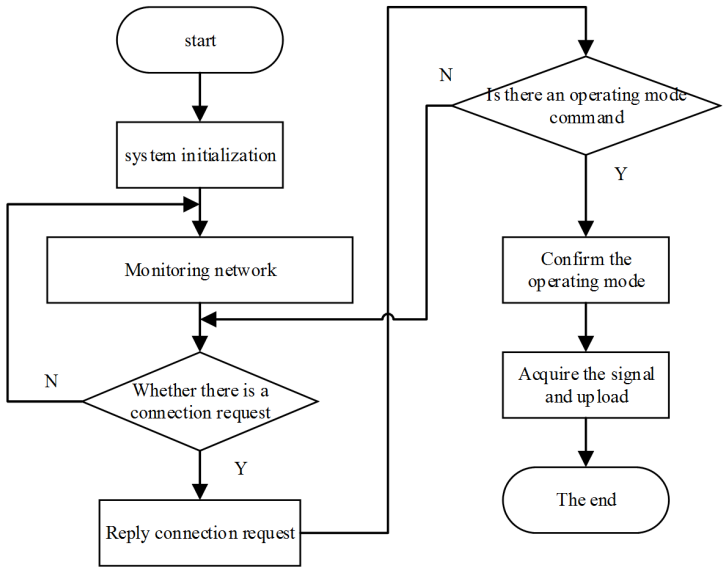

Fig. 4. Flow chart of gear terminal

3. Results and discussion

In the Wushu and other fighting projects the athletes get the score by hitting the effective region of each other. This paper argues that the strike effect should be determined by the change of momentum, that is, impulse. This design adopts the way of "rock fall" for impulse calibration. The specific method is to place a ball with the mass of m at a certain height of h, to allow it to fall freely and hit the packaged sensor placed horizontally on the ground. At the same time, the output voltage curve of the sensor is monitored in real time by oscilloscope, and the maximum voltage value and the strike time t in the strike process are read.

For heavy objects, before the collision, the gravitational potential energy is transformed to the kinetic energy. And then, according to the theorem of momentum, we can calculate the average momentum. The theoretical value of impulse is obtained by calculation, and the experimental data ($g = 10\,\mathrm{m/s^2}$) is obtained by reading the voltage variation through the oscilloscope. The most important data are listed in Table 1.

Table 1. Drop hammer realization data

Weight (g)	Height (cm)	Impulse (Ns)	Crash time (ms)	Maximum voltage (V)
500	10	0.707	38	0.82
500	20	1.000	74	1.20
500	30	1.225	74	1.46
500	40	1.414	67	1.72
500	50	1.581	65	1.88
1000	10	1.414	72	1.79
1000	20	2.000	64	2.16
1000	30	2.449	68	2.23
1000	40	2.828	72	2.34
1000	50	3.162	60	2.58

Compared with the experimental data, it is found that there is a clear relationship between the impulse theory value and the measured maximum voltage value. The relationship between the maximum voltage and impulse is shown in Fig. 5.

The experimental data showed that there is a good linear relationship between the maximum voltage and the impulse, and the ratio is relatively determined, relative to 1.1. In the program design, the voltage can be read directly through the impulse by a certain proportion of the sensor, and it can be used as the general strike effect characterization to effectively distinguish the strength of the strike.

3.1. System power consumption test

Through the tests of experiments for several times, the general strike action from contact to each other to discharge lasted in milliseconds. The power consumption contrast between Group A without adding low power consumption program implementation function and Group B with the design and writing of low power function

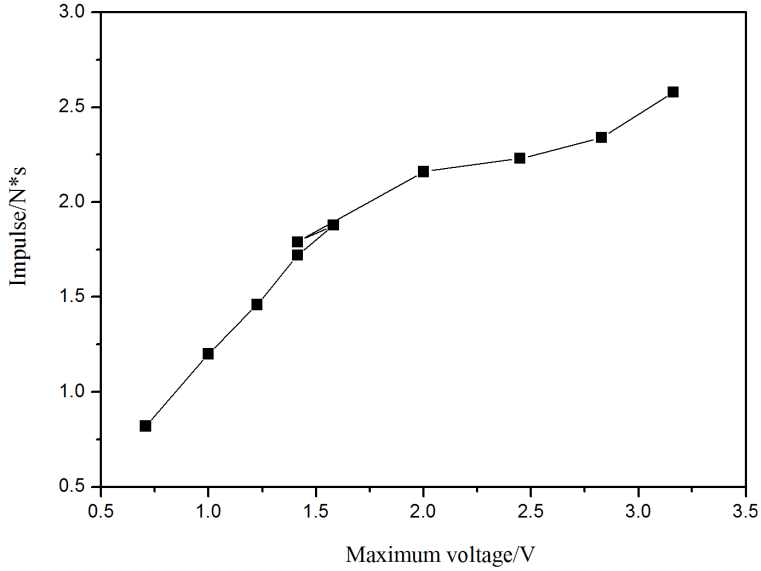

Fig. 5. Relationship between the maximum voltage and impulse

implementation code is shown in Table 2.

Table 2. System power consumption application

	Group A system	Group B system
Test duration	About three hours	More than 18 hours
Test results	Test accuracy without omission	A few omissions
System anomaly	Bluetooth module with serious burning	Good, no obvious abnormality

3.2. Cost calculation

This system only completed a set of functional prototypes, which does not involve the final product appearance and so on design costs. In the materials acquisition process, the main cost comes from the piezoelectric film. This design uses the gears in the middle level. Two sets of gears are purchased, and the price is 600 yuan in total. Electronic components, modules and related supplies are not more than 30 yuan per unit price, but generally needed to be purchased in bulk. For instance, the unit price of the resistance is a few cents, generally sold from 200–300. Currently, in the industry, a single plate with PCB opening below 100 mm×100 mm area is not more than 100 yuan. In the specific design, the system board opening is 60 yuan for 10 sets, and later, 5 yuan for one; charge amplifier circuit opening is 10 yuan for 10 sets, and later, 3 yuan for a piece. Based on the above situations, and compared the price of the electronic gears in the market, it is seen that the material cost of electronic gears in this design is relatively low. The main expenses

incurred during the development phase where different instrumentation is needed for repeatedly debugging, and finally specific equipment is needed for testing and calibration of the system. For example, heavy bond testing machine, the market price of a set of equipment is about fifty thousand. According to the estimation of some Wushu professionals, the demand of national Wushu electronic gear is about 100 sets per year. If the design can at last achieve mass production, after considering the premise investment, production costs and profits, the price is still lower than 70 % of the price of similar foreign products.

4. Conclusion

The research takes the electronic gear product realization as the ultimate goal. We completed the intelligent identification of strike effective value in Wushu movements, realized the scoring function of electronic gears used in the competition, and quantitative monitored Wushu specialized strike ability training. These preparations provide the theoretical basis for independent research and development of electronic gears used in Wushu competition. The purpose is to complete the autonomous design of electronic gear as soon as possible and the replacing of the existing foreign electronic gear products. In this way, unnecessary funds and energy investment for Chinese Wushu team to adapt to foreign products can be reduced, and the popularity of electronic gears can be further promoted.

References

[1] A. Khan, Z. Abas, H. S. Kim, I. K. Oh: *Piezoelectric thin films: An integrated review of transducers and energy harvesting.* Smart Materials and Structures *25* (2016), No. 5, 053002.

[2] J. Kim, H. Jung, M. Kang, K. Chung: *3D Human-gesture interface for fighting games using motion recognition sensor.* Wireless Personal Communications *89* (2016), No. 3, 927–940.

[3] M. A. Fraga, H. Furlan, R. S. Pessoa, M. Massi: *Wide bandgap semiconductor thin films for piezoelectric and piezoresistive MEMS sensors applied at high temperatures: An overview.* Microsystem Technologies *20* (2014), No. 1, 9–21.

[4] B. A. Griffin, M. D. Williams, G. Wang, B. V. Sankar, L. N. Cattafesta, M. Sheplak: *The electromechanical behavior of piezoelectric thin film composite diaphragms possessing in-plane stresses.* Journal of Micromechanics and Microengineering *27* (2017), No. 4, 045017.

[5] V. Ostaševičius, I. Milašauskaité, R. Daukševičius, V. Baltrušaitis, V. Grigaliunas, I. Prosyčevas: *Experimental characterization of material structure of piezoelectric PVDF polymer.* Mechanics *86* (2010), No. 6, 78–82.

[6] K. Shimizu, H. Hojo, Y. Ikuhara, M. Azuma: *Piezoelectric materials: Enhanced piezoelectric response due to polarization rotation in cobalt-substituted BiFeO3 epitaxial thin films.* Advanced Materials *28* (2016), No. 39, 8639–8644.

Received May 7, 2017

Acta Technica *62* No. 3A/2017, 283–294

Design and research on the information collection system of digitized discus throwing

Zhao Chen[1]

Abstract. Information collection system of digitized discus throwing is designed to achieve the diagnosis and analysis of the mechanical information about athletic technical movements. Firstly, upper and lower covers and circle of the digitized discus as well as other parts are drawn according to the general structure of discus measuring system, physical connection among all devices, object appearance and its structural design. And then, hardware and software design are made for information collection system of digitized discus throw. The achievement for hardware circuit system function of digitized discus is depended on the software design. Hardware consists of power source, SCM, sensor, A/D transformation, wireless communication and RS232 serial communication. And anti-interference design is also made to hardware system. Lastly, throwing experiment is carried out. Data collected in practical throwing is compared with data collected in the experiment, combined with discus movement rules, which testifies the feasibility of hardware circuit system design of digitized discus. And with stable equipment job, diagnosis and analysis of mechanical information is made to athletic technical movements.

Key words. Digitized discus, information collection, wireless launch, sensor.

1. Introduction

In the throwing events, athletic discus performance needs to be improved through technical means improvement as athletic break-out force is hard to improve. Before throwing the discus, acting force applied on the discus by hands and discus posture at that time all influence the athletic throwing performance to some extent. Therefore, a research is made from the discus posture in the throwing process and forced direction of discus [1]. At present, interaction force between human beings and ground can be acquired by 3-D force platform. However, the acting force applied on the discus by hands cannot be acquired directly. Yet, there is no ideal equipment for measuring discus throwing events. The present research method for measuring discus is by means of dynamical information [2]. In view of this situation,

[1]Physical Education College of Zhengzhou University, Zhengzhou, Henan 450000, China; E-mail: zc_zhaochen@126.com

a hardware circuit system of digitized discus is designed to acquire the dynamical information when the athlete is throwing the discus, which is fully prepared for the further research of discus posture angle.

2. Literature review

In the throwing events, electric resistance gauge, used to measure the force [3], which hardly achieve the discus without discrimination; with the acceleration of social modernization, the demand for sensor technology in industrial production and in daily life is increasing, and the demand for accuracy becomes higher and higher. And the sensor technology is indispensable in the throwing events and becomes an important part of information technology. Application level of sensor technology directly affects the automation development. Since 1980s, sensor technology has developed rapidly in Japan, USA and other countries, and the sensor technology has been extended to some field, such as defense technology and industrial production control. Since that, China has paid more and more attention to the development of sensor technology and taken it as one of priorities in national high-tech development.

According to the international standard, the discus structure of built-in circuit board is designed by the hardware circuit system of digitized discus, and a discus with 3-D accelerated velocity and 3-D angular velocity in the whole discus throwing process can be developed based on the acceleration sensor and angular sensor. And the acquired data can be sent by wireless transmitter module and received by wireless receiving module. Eventually, the discus motion parameter is dealt with by the computer to fulfill the real-time acquisition of dynamical information [4]. Computer can handle the data and store useful information; this system can be used alone or matched with other instrument and equipment. Researchers working for sports can take advantage of this measuring means to get the data and search for new theories and rules about discus throwing.

3. Methods

3.1. Overall design of digitized discus

Digitized discus mainly consists of upper and lower discus covers, stand column, nut and discus circle that connects with upper and lower covers as well as circuit board with relative function.

It is functional circuit board is small enough in the experiment that it can be put into discus. Functional circuit board is put in the central place of discus by the stand column, which can narrow the error brought by vibration in the throwing process [5].

Overall design for hardware circuit system of digitized discus is shown in Fig. 1.

In the discus throwing, digitized discus system is used to get 3-D acceleration velocity and 3-D acceleration velocity information in the throwing. And the force, posture velocity and other parameters of discus can be worked out through integra-

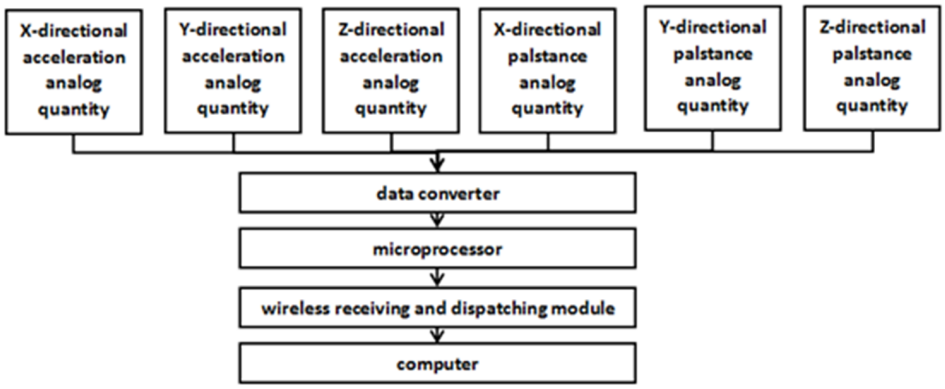

Fig. 1. Overall design for hardware circuit system of digitized discus

tion and INS. After throwing the discus, 3-D information is collected respectively by three-axis acceleration sensor and angular velocity sensor; sensor is driven by analog-digital converter to collect that analog quantity that is turned into 12 figures with digital quantity; digital signals that are turned by microprocessor are sent to launching cache. And then the wireless transmitter module is launched. Finally, digital signals are received and stored by the computer through the receiving module [6].

The circuit board in the discus is integrated by the ADXL78 acceleration sensor, ADXL278 acceleration sensor, Tri-Rate free-velocity sensor, TLC2543 A/D converter, C8051F320 SCM, AT26F004 storage, LTC4602 battery charging IC, MAX 1760 boost IC, lithium battery, PTR6000PA wireless transmitter module and other main devices; PTR6000PA wireless receiving module integrated with C8051F320 SCM as one unit are inserted into computer.

3.2. Hardware structure and function of digitized discus system

3.2.1. Power source. C8051F320 SCM system needs to be supplied power by relatively stable 4 V–5.25 V power source; LTC4062 battery charging is adopted in the circuit design of digitized discus hardware structure. Interface and socket of lithium ion battery is supplied with direct voltage 3.6 V from external power source. Voltage of power source is increased to 5 V by MAX1760, which can provide a stable 5 V voltage for SCM, spinning top, acceleration sensor, A/D and other components and parts to use.

3.2.2. SCM. There are several ports used in SM, such as P0.0 (SCK), P0.1 (MISO), P0.2 (MOSI), P0.6 (IRQ_nRF24L01), P0.7 (IRQ_LTC2543C), P1.0 (CS_nRF24L01), P1.1 (CS_FLASH), P1.2 (CS_LTC2543), P1.7 (CE_nRF24L01) and so on. RST/C2CK and P3.0/C2D are used for restoration and system debugging. When VBUS inputs 5 V voltage and the USB is surly connected, REGIN is voltage

stabilizer input in SCM, VDD is 3.3 V voltage stabilizer output, D– and D+ are the data output and input.

3.2.3. Sensor. (1) ADXL278(AD22285) is a double-axis acceleration sensor whose measurement range is ±50,g. ADXL278 measures the value of accelerated velocity in X, Y direction and its volume is 5 mm×5 mm×2 mm. When the accelerated velocity is 0 g, the frequency is 100 Hz. When VCC is 5 V, the value of VOUT—VCC/2 is between –150 mV and 150 mV, and its sensitivity is 36.1–39.9 mV/g.

(2) ADXL78 (AD22280) is a double-axis acceleration sensor whose measurement range is ±50,g. ADXL78 measures the value of accelerated velocity in Z direction and its volume is 5 mm×5 mm×2 mm. When the accelerated velocity is 0 g, the frequency is 100 Hz. When VCC is 5 V, the value of VOUT—VCC/2 is between –150 mV and 1150 mV,, and its sensitivity is 36.1–39.9 mV/g [7].

(3) TriRate (TR1200S050) is a three-axis angular velocity sensor whose measurement range is ± 12000/s. TriRate measures the values of angular velocity in X, Y, and Z directions and its volume is 0.70 in×0.70 in×0.40 in. When the angular velocity is 0, the voltage output value is 2.5 V, and its sensitivity is 1.25 mV/°/s.

3.2.4. A/D converter. TLC2543 is a 12-figure analog-digital conversion chip. First and foremost, TLC2543 configuration is connected to the two corresponding pins of SCM: pin EOC is corresponded to the SCM P0.7, pin CLK is corresponded to SCM P0.0, pin DIN to the SCM P0.2, and pin CS to the SCM P1.2. Thus, SCM is attached to the TLC2543 through SPI. And SCM data conversion comes to end by interruption (EOC is high level). Because SCM has no specialized SPI port, it uses software to achieve SPI function in order to have a communication with TLC2543. It takes time-delayed method to collect data. Mode configuration register is output through port 0 and P0.0, P0.1 and P0.2 is set up as push-pull output. 8-bit data is serially input from DIN port (00000001), which is called control word. Analog channel (0-8) is controlled by the high-four figure of 8-bit data to use. Output length of 12-bit data is achieved the third and second configurations. The first one stands for high order is first sent out. Number 0 controlling achievement is output with 2 complement form [8].

3.2.5. Wireless communication. Receiving module of wireless launch adopts nRF24L01 as its core component, which can fulfill wireless communication in six channels [9–10]. Major operating modes and pin functions of nRF24L01 are shown in following Tables 1 and 2.

In the Shock Burst mode, SPI port is provided for nRF24L01 to be linked together with bradytelic acceleration sensor and angular sensor. After sending data, the IRQ becomes high level to inform SCM. And SCM can read out the data that received by RXFIFO register. In the data launching and receiving process, nRF24L01 can share with one channel to launch and receive data from six different channels. All the data from channels can be set up as enhancement mode to recover the lost data without increasing SCM workload.

Table 1. Thermophysical properties of regular fluid and nanoparticles

Mode	Receiving mode	Sending mode	Sending mode	Standby mode II	Standby mode I	Power down mode
PWR_UP	1	1	1	1	1	0
PRIM_RX	1	0	0	0		
CE	1	1	10	1	0	
FIFO register state		Data is put into TX FIFO register	Sending mode, until data is sent out	TX FIFO has no data	Data is not transmitted	

Table 2. Pin function of nRF24L01

Pin name	CE	CSN	SCK	MOSI	MISO	IRQ
Direction	Input	Input	Input	Input	Three-state output	Output
Sending mode	High level 10 us	SPI chip selection enabling, low level enabling	SPI clock	SPI serial input	SPI serial output	Interruption, low level enabling
Receiving mode	High level					
Standby mode	Low level					
Power down mode						

When some data in SCM needs to be sent out, MOSI will receive node address (TX_ADDR) and valid data (TX_PLD) written into nRF24L01. And the length of emit data (bytes) are written into TX FIFO from SCM. When CS_nRF24L01 is in low level, chip begins in a work state and nRF24L01 is written into [11]. When CE_nRF24L01 is in high level, launching mode starts and duration time should last for 10 s or more in a high level state. After sending out the data, channel 0 is set up as receiving mode to receive answering signals. Both receiving answering signals and retransmission outnumbers the set value result in interruption. And then TX FIFO is eliminated, which makes preparation for next set of data to be launched.

3.2.6. RS232 Serial communication. RS-232 is a widespread serial interface, using P0.4 and P0.5 of SCM. RS-232 serial communication interface adopts single-ended communication (unbalanced transmission mode); Data signal from receiving and dispatching end of RS-232 serial communication interface has a bigger differ-

ence from ten-signal earth level. When RS-232 serial communication interface sends and receives serial port data, driven positive level of its sending and dispatching end ranges from +5 V to + 15 V and its negative level ranges from –5 V to –15 V. When the data of discus accelerated velocity and angular velocity is transmitted by adopting RS-232 serial communication interface, on-line voltage of systematic signal is converted TTL level by transforming chip to RS-232 level, and then connected to RS-232 communication interface of the computer [12]. Voltage multiplying circuit and special circuit are included in MAX232AESE chip, without control signal. It only needs +5 V power source to make a double-four-directional transmission between RS232 level and TTL level; it should be noted that when used, it needs several external capacitance 0.1 uF. C8051F320 machine is connected with MAX232AESE through TX and RX pins; and then it connected with 9-core RS-232 serial communication interface of computer [13].

There are two purposes for baseplate system expanding serial interface: one is served as serial communication; another is for tool of computer debugging embedded system. As long as there are three pins—RXD, TXD and GND, serial communication can be achieved.

3.2.7. Anti-interference design of hardware system. (1) A large capacitor used to ensure the minimum distance between VDD pin and direct-current main in chip. For instance, 4.7 uF/16 V tantalum capacitor has a parallel connection with a little common capacitor. The power source must have a filtering processing that can supplies power for system. And the simulation is bound to be separated from data.

(2) When wired at PCB board, long power line should be avoided. Crystal oscillator and power line should keep far away from digital signal and control signal line.

(3) Ground electrode and power line of all integrated devices is respectively joined into decoupling capacitor. Because of on the printed-circuit board, all devices have large power consumption and potential difference is generated on the ground electrode; a solution to this problem is narrowing the linear length of switched current; so, PCB power line and the entrance of ground electrode have a parallel connection with decoupling capacitor. And then every ground electrode port and power port of integrated chip on the PCB is all joined into a decoupling capacitor with 0.01–0.1 uF capacitance.

(4) When wired at PCB of hardware structure, power line of circuit board and width of ground electrode are needed to be widened so that larger current can convey the circuit board; in addition, the whole PCB is pavaged and the circuit components and parts have a close ground connection, which avoided a long ground lead.

(5) In the hardware structure design, printed-circuit board is not divided into digital block and model area. Most chips on the printed-circuit board are digital chips. The sensor should keep away from strong interference source as much as possible (e.g. power switch); USB cable and clock line adopt parallel lines, and the distance between centers of tracks is possibly wide; under quartz oscillator and wireless radio frequency module, GND area is possibly large, without through signal line. When software draws printed-circuit board, it is noted that power line of the

whole circuit board and ground electrode direction should keep a same direction with USB as much as possible. The line is possibly short as well as semiconductor device, capacitance and resistance. And they needed to be avoided intersection with other guide lines. In the meanwhile, ground electrode is encrypted possibly, which can reduce impedance from ground electrode.

3.3. Software design of hardware system

Functional achievement of digitized discus hardware circuit system depends on systematical software design. Software writing is based on the deep understanding of systematical hardware.

3.3.1. Launching unit design. Program flow chart of launching unit system is shown in Fig. 2.

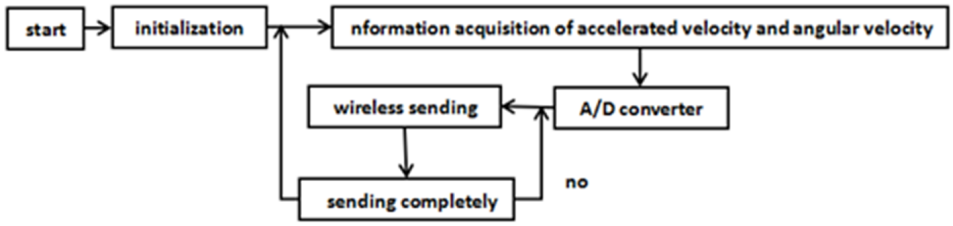

Fig. 2. Program flow chart of launching unit

3.3.2. Receiving unit design. System flow chart of receiving unit is shown in Fig. 3.

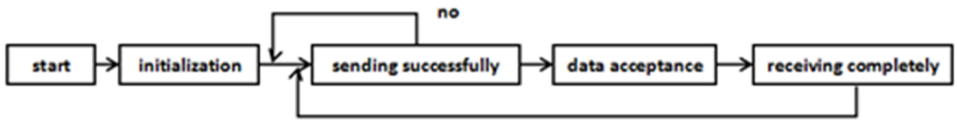

Fig. 3. Program flow chart of receiving unit

3.4. Throwing experiment

In Physical Education College of Zhengzhou University stadium, several throwing experiments are made. Transmitter module is wrapped in discus with foam, sponge, and foam is used to protect the exterior. In the experiment, accelerated velocity and angular velocity and other original parameters are gained.

Data in the Table 3 is a part of original data. In the Table 3, ACC_X, ACC_Y and ACC_Z respectively express the accelerated velocity component with front-and-back direction, up-and-down direction as well as right-and-left direction in coordinate system in the center of discus. And, GYRO_X, GYRO_Y and GYRO_Z

respectively represent angular velocity with front-and-back direction, up-and-down direction as well as right-and-left direction in coordinate system in the center of discus.

Table 3. Original data

Sequence number	1	2	3	4	5	6	7	8	9	10
ACC_X	2032	2032	2030	2033	2032	2031	2037	2038	2031	2032
ACC_Y	2007	2000	2002	2001	1998	2000	1999	2002	1998	1999
ACC_Z	2021	2026	2021	2022	2022	2024	2018	2024	2022	2023
GYRO_X	2055	2055	2059	2065	2081	2094	2104	2115	2120	2128
GYRO_Y	1987	1971	1957	1944	1936	1927	1921	1913	1904	1900
GYRO_Z	2139	2149	2157	2165	2174	2181	2187	2194	2201	2215

According to collected original data, Beijing aerospace inertial navigation is applied to make a calculation to the coordinate transformation and differentiation as well as integral calculation. And then original data is processed, and accelerated velocity value of navigation system can be worked out by other parameters such as integrated pitch and roll compensated by algorithm and accelerated velocity.

Table 4. Navigation system data

Seq. numb.	1	2	3	4	5	6	7	8	9	10
A_x	-0.28	-0.29	-0.40	-0.65	-1.03	-1.48	-1.94	-2.32	-2.58	-2.70
A_y	-0.21	-0.20	-0.17	-0.09	0.02	0.14	0.26	0.35	0.37	0.31
A_z	9.21	9.20	9.31	9.51	9.82	10.20	10.58	10.92	11.21	11.46
V_x	2.12	2.11	2.11	2.10	2.09	2.08	2.06	2.03	2.01	1.99
V_x	-2.32	-2.31	-2.32	-2.32	-2.32	-2.32	-2.32	-2.31	-2.31	-2.31
V_z	-5.02	-5.03	-5.03	-5.03	-5.03	-5.03	-5.02	-5.01	-5.00	-4.98
Pitch.	-6.11	-5.64	-5.10	-4.47	-3.75	-2.98	-2.15	-1.31	-0.45	0.41
Roll.	-79.75	-79.90	-80.01	-80.08	-80.13	-80.15	-80.14	-80.10	-80.01	-79.89

The data in the Table 4 is a part of navigation system. In the table, A_x, A_y and A_z, respectively, express the accelerated velocity component with front-and-back direction, up-and-down direction as well as right-and-left direction in ground coordinate system in the center of discus. Symbols V_x, V_x and V_z respectively represent linear velocity with front-and-back direction, up-and-down direction as well as right-and-left direction in ground coordinate system in the center of discus; pitch angle is a included angle with front-and–back direction between discus surface and ground, roll angle is a included angle with right-and-left direction between discus and ground. As shown in Fig. 4, accelerated velocity is in the X direction. In Fig. 5,

accelerated velocity is in the Y direction. In Fig. 6, accelerated velocity is in the Z direction. Figure 7 is the integrated pitch and Fig. 8 is the integrated roll.

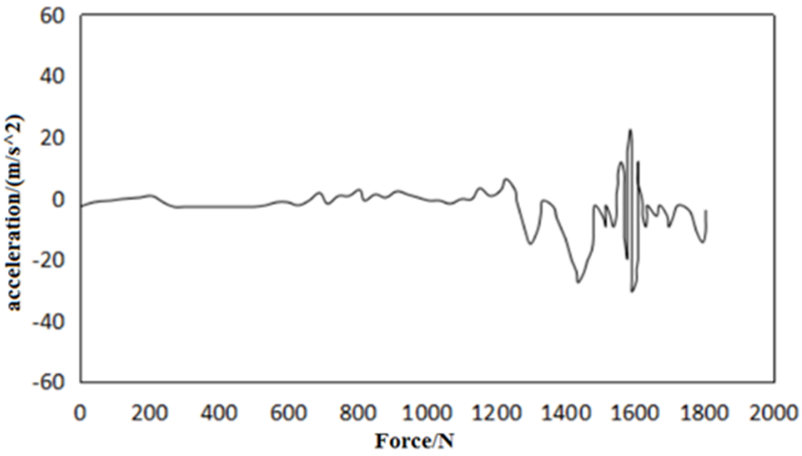

Fig. 4. X-directional accelerated velocity

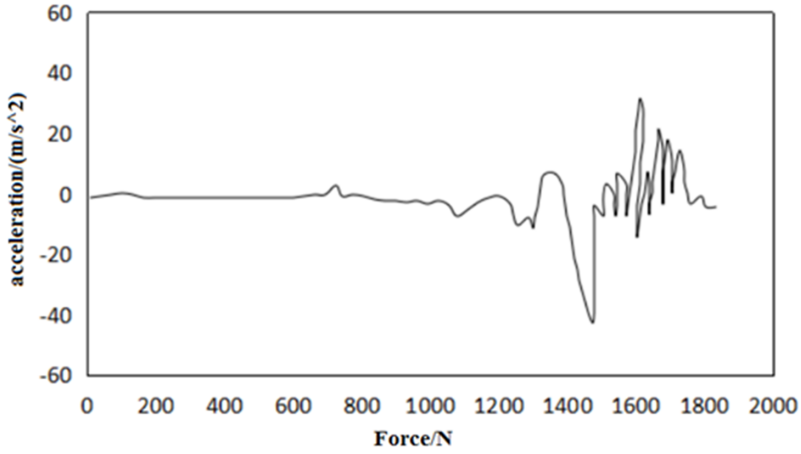

Fig. 5. Y-directional accelerated velocity

4. Conclusion

It is clear that, to some extent, data collected by digitized discus reflects motion law in the discus throwing process in terms of processed data. Therefore, this method is feasible and has a chance to find out new force application law of discus throwing. A large quantity of data is acquired for data mining with plenty of experiments. And combined with throwing experiments of discus athletes, laws are discovered to improve their score.

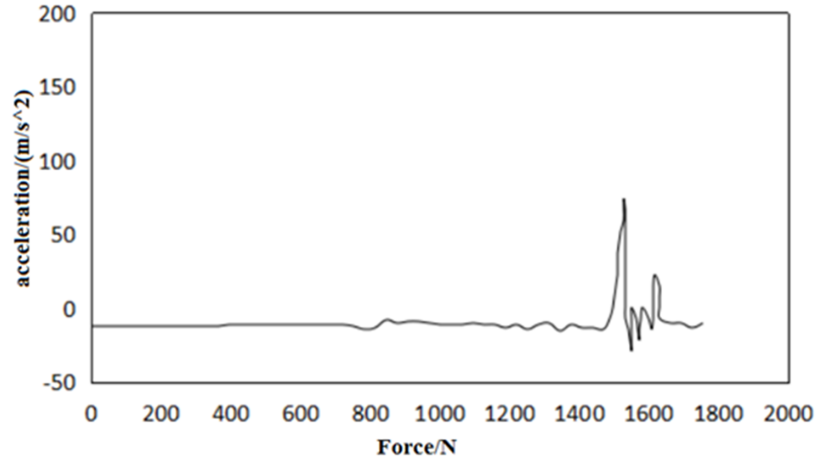

Fig. 6. Z-directional accelerated velocity

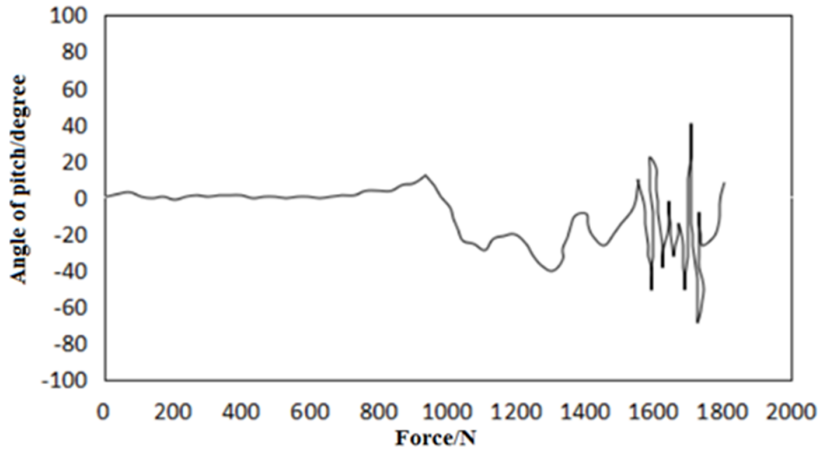

Fig. 7. Integrated pitching

Hardware circuit system of digitized discus achieves the function for acquiring 3-D accelerated velocity and angular velocity information with real time in the discus throwing process, which fulfills the transmission in hectometer. Sufficient experiments are made for real-time data acquisition and wireless transmission in long distance, to acquire sets of data and videos, which receives expectant results of force and postures.

References

[1] W. T. Wang, Q. J. Song, Y. M. Nie, B. Y. Wang, H. Y. Ren, Y. J. Ge: *Development and implementation of a novel digital shot sensor system.* Applied Mechanics and Materials *364* (2013), Chapter 3, 228–232.

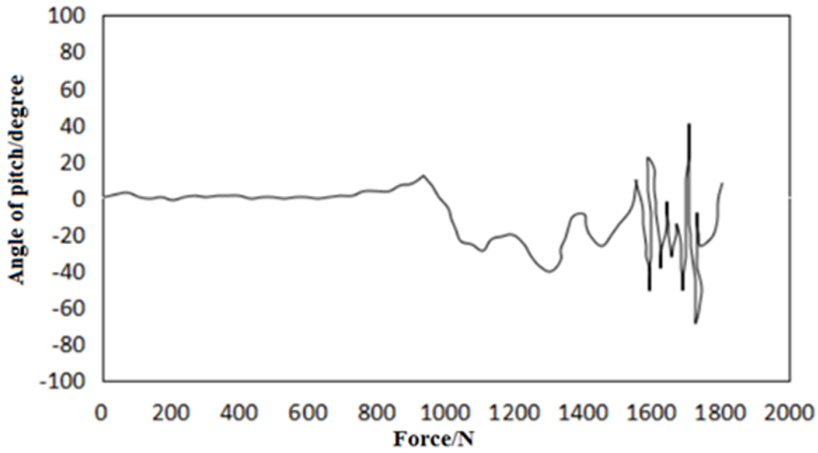

Fig. 8. Integrated rolling

[2] B. Lechner, I. Filzwieser, M. Lieschnegg, P. Sammer: *A climbing hold with an integrated three dimensional force measurement and wireless data acquisition.* International Journal on Smart Sensing and Intelligent Systems *6* (2013), No. 5, 2296–2307.

[3] A. Deckers, B. Serrien, J. P. Baeyens: *A three-dimensional kinematical analysis of the handball jump shot, using the finite helical axis (FHA) approach.* Annals of Research in Sport and Physical Activity (2013), No. 4.

[4] H. Huang, M. Pan, S. Gong: *Estimating and calibrating the response of multiple wideband digital radio frequency memories in a hardware-in-the-loop system using shuffled frog leaping algorithm.* IET Radar, Sonar & Navigation *10* (2016), No. 5, 827–833.

[5] K. Väänänen-Vainio-Mattila, T. Olsson, J. Häkkilä: *Towards deeper understanding of user experience with ubiquitous computing systems: Systematic literature review and design framework.* Proc. International Conference on Human-Computer Interaction INTERACT, 14–18 September 2015, Bamberg, Germany, Springer Verlag (LNCS) *9298* (2015), No. 18, 384–401.

[6] K. Kim, J. Lee, W. Jung: *Method of building a security vulnerability information collection and management system for analyzing the security vulnerabilities of IoT devices.* In: J. Park, S. C. Chen, K. K. Raymond Choo (eds.) Advanced Multimedia and Ubiquitous Engineering. MUE 2017, FutureTech 2017. Lecture Notes in Electrical Engineering, Springer, Singapore *448* (2017).

[7] Z. Wu, W. Wang, X. Liu, L. Zhang: *An efficient and reliable meter registration method for the power information collection system.* Proc. 2nd International Conference on Electromechanical Control Technology and Transportation (ICECTT), 14—15 January 2017, Zhuhai, China, 245–254.

[8] M. Perenzoni, N. Massari, D. Perenzoni, L. Gasparini, D. Stoppa: *A* 160 *times*120 *pixel analog-counting single-photon imager with time-gating and self-referenced column-parallel A/D conversion for fluorescence lifetime imaging.* IEEE Journal of Solid-State Circuits *51* (2016), No. 1, 155–167.

[9] B. Zou: *Electricity information collection system design and information security based on WiMAX over 230 MHz dedicated frequency band.* In: Q. A. Zeng (eds.) Wireless Communications, Networking and Applications. Lecture Notes in Electrical Engineering, Springer, New Delhi *348* (2016).

[10] T. Osaragi, I. Niwa, N. Hirokawa: *Development of Web application for disaster-information collection and its demonstration experiment.* Advances and New Trends in Environmental Informatics. Springer International Publishing (2017), 63–73.

[11] E. Martos, A. E. M. García: *Artefactos culturales y alfabetización en la era digi-*

tal: Discusiones conceptuales y praxis educativa. Revista Interuniversitaria *26* (2014), No. 1, 119–135.

[12] K. Kaiya, A. Koyama: *Design and implementation of meal information collection system using IoT wireless tags.* Proc. 10th International Conference on Complex, Intelligent, and Software Intensive Systems (CISIS), 6–8 July 2016, Fukuoka, Japan, 503–508.

[13] Y. Wang, Y. Ding: *First-principles study of the electronic and magnetic properties of 4–8 line-defect-embedded BN sheets decorated with transition metals.* Annalen der Physik *526* (2014), Nos. 9–10, 415–422.

Received May 7, 2017

Acta Technica *62* No. 3A/2017, 295–302

Design and research of basketball fixed-point shooting automatic test system based on background difference method

Min Zhou[1], Tian Zhou[1,2]

Abstract. In this paper, aiming at the problem of current fixed-point shooting test system of inconvenient installation, missed detection and false detection, we propose to use the method of moving target detection technology to detect the shooting. In this paper, we study and compare the optical flow method, interframe difference method and background difference method. Finally, we choose the background difference method as the shooting detection method. Based on the background difference method of basketball fixed-point shooting automatic test system, we compare the accuracy of the system with the accuracy of the current detection system. The results show that the automatic determination system of basketball based on background difference method still needs to be further strengthened in accuracy, but the stability is significantly better than the current detection system.

Key words. Background difference method, fixed point shooting, test system.

1. Introduction

In the fixed-point shooting test project, it is very important to get the position information of basketball [1]. Because the traditional detection method has many shortcomings, we must adopt a new method to detect the location of the basketball or other features. As we all know, human beings are mainly through visual, auditory and tactile to access external information [2]. However, in these perceptual organs, human eyes are the important sense organ that can gain the outside information by the light stimulation primarily [3].

This paper designs and develops a set of basketball shooting automatic recognition systems based on moving target detection technology. The method is realized by using the camera to capture the scene image, and from the video image sequence

[1]Sichuan University, Sichuan, 610000, China
[2]Corresponding author; E-mail: marktianzhou@163.com

to obtain the current location and characteristics information of the basketball, so as to judge whether the ball drops into the basket. The main advantage of this method is stability, convenience and reliability.

2. The background difference method

At present, the main shooting monitoring methods are the following: light flow method, frame difference method and background difference method. The background difference method and the frame difference method are also suitable for the camera in the case of static installation, and has the characteristics of accurate detection, simple algorithm, easy to implement and so on. If the background model is known, the method can extract the feature data completely and can extract the moving target feature quickly and accurately through the subsequent processing. It is very important to establish a good background reference model in the process of extracting the moving region by using the background difference method [4–5]. As the calculation of the optical flow is relatively large, it takes a lot of time in the calculation process, and the feedback signal of the fast moving target cannot reach the real-time requirement of the subject. However, since the inter-frame difference method is not sensitive to the target of fast or slow motion, it cannot extract the target completely, so the method cannot be used. The main advantage of the background difference method is that the calculation is simple and the detection results are accurate. Therefore, in this system, we use the background difference method to design and develop basketball shooting automatic identification system.

The basic idea of the background difference method is to match the current frame image with the known background model reference image, and calculate the similarity measure of the point of the image and the point in the background model. We can use formula (1) for foreground/background classification.

$$I_{\text{object}}(x,y) = \begin{cases} 1 \, |I_{\text{current}}(x,y) - I_{\text{background}}(x,y)| \geq \text{Threshold}, \\ \\ 0 \, |I_{\text{current}}(x,y) - I_{\text{background}}(x,y)| < \text{Threshold}. \end{cases} \tag{1}$$

In the above formula, point x, y is any pixel in the image, $x = 0, 1 \ldots, M-1$, $y = 0, 1 \ldots, N-1$, where N and M represent the vertical resolution and horizontal resolution of the image, respectively. Symbol $I_{\text{background}}(x,y)$ is the eigenvalue of the pixel x, y in the background reference model, $I_{\text{current}}(x,y)$ is the eigenvalue of the pixel x, y of the currently captured image frame, and Threshold is the set or adaptive segmentation threshold.

$I_{\text{object}}(x,y) = 1$ represents x, y points for pre-exercise points, $I_{\text{object}}(x,y) = 0$ represents x, y points as background points. If the difference between the gray value of the background reference point and the gray value of the point to be measured exceeds a certain range, then the change point can be judged as the image movement front point, otherwise it will be regarded as the image back point.

3. Shooting monitoring algorithm

Through the determination of the position of the camera and the characteristics of the basketball in the shooting process, the algorithm of the basketball position detection in the system is realized by the above research and learning on the background difference method. Figure 1 shows the basic flow of the shooting algorithm in this system.

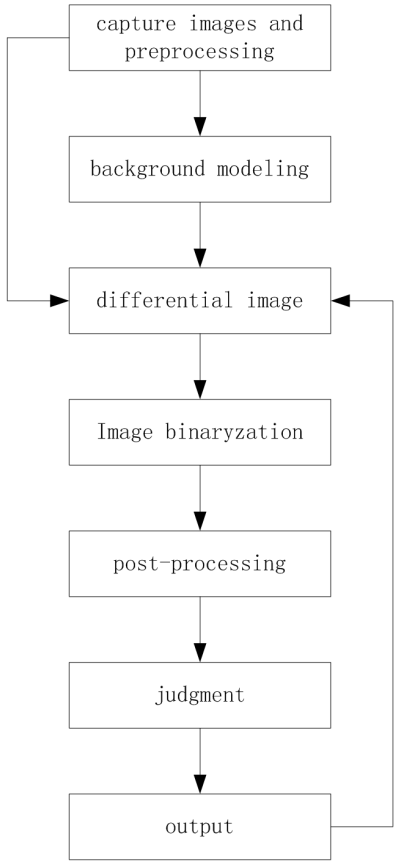

Fig. 1. Algorithm flow chart

3.1. Image capture and preprocessing

In the process of detection, first of all, there is a need for live video, with the use of recorded Test One video detection.

Test One video parameters:

- Resolution: 320×240,
- Frame rate: 18 f/s,

• Format: RGB24.

Because the video format is RGB24 [6], the color space parameters are not required during the detection process, so the RGB image is converted to a grayscale image after the image is acquired. The purpose is not only can reduce the use of system memory, but also can improve the processing speed. The image captured by the camera is susceptible to noise interference and contamination during transmission, conversion and storage, which can lead to the inability to extract useful information in the image, so that the image is denoised by the neighborhood averaging method after capturing and converting the image.

3.2. Background modeling

When using the background difference method to detect the motion area, we must first prepare the background reference model. After the background reference model is determined, the image difference can be performed. In this paper, the background of the scene is relatively simple and other objective factors are less affected. In this subject, we use the mean method for background modeling. Its principle is to use the continuous image of the image, and then the continuous frames of the image are summed to get the background reference model.

3.3. Image difference

With the reference model, we can make the difference in the video image, so as to get the moving area in the image, and separate the background from the image. It is shown in Fig. 2.

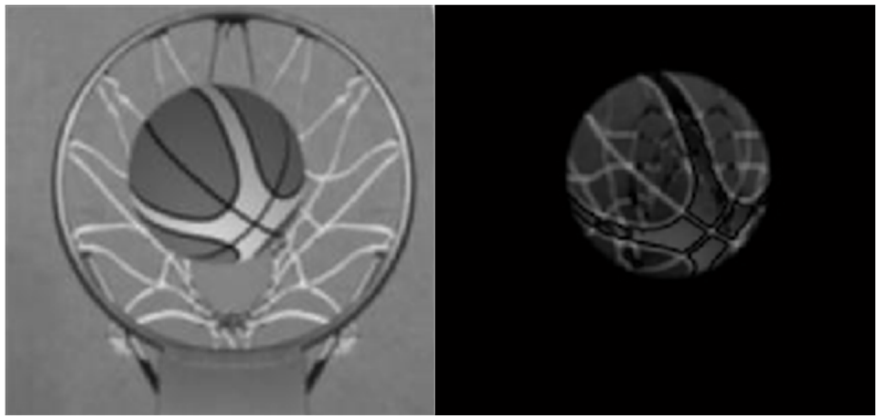

Fig. 2. The capture image (left) and differential image (right)

3.4. Extract features

In the extraction of features, the most critical is the image of the basketball X and Y direction of the coordinates of the detection, all the calculations are based on

the four coordinate points for analysis. Here are some of the above parameters of the calculation method:

$$\begin{cases} \text{BallInfor}x = \max(x) - \min(x), \\ \\ \text{BallInfor}y = \max(y) - \min(y). \end{cases} \tag{2}$$

In the above formula, $\min(x)$, $\min(y)$, $\max(x)$ and $\max(y)$ represent the minimum and maximum pixel coordinate values in the basketball X direction and Y direction, respectively. Symbols BallInfor$x$ and BallInfor$y$ represent the total number of pixels in the X and Y directions.

$$\text{Ball}R = \frac{\text{BallInfor}x + \text{BallInfor}y}{2} \times m\text{CamDis}\,\tan(ce)\,. \tag{3}$$

In the above formula, mCamDis $\tan(ce)$ represents the calibration factor, Ball$R$ is the diameter of the basketball.

$$\text{BallCenter}(x, y) = \left(\frac{\max(x) - \min(x)}{2}\right), \left(\frac{\max(y) - \min(y)}{2}\right). \tag{4}$$

In the above formula, BallCenter(x, y) are the spherical coordinates.

$$K = \frac{\text{BallInfor}x}{\text{BallInfor}y}\,. \tag{5}$$

In the above formula, K is the ratio of the difference between the X direction and the Y direction pixel coordinates. BallInfor$x$ and BallInfor$y$ represent the total number of pixels in the X and Y directions.

$$\begin{cases} \text{Ball}X = \text{BallInfor}x \times m\text{CamDis}\,\tan(ce), \\ \text{Ball}Y = \text{BallInfor}y \times m\text{CamDis}\,\tan(ce). \end{cases} \tag{6}$$

In the above formula, BallInfor$x$ and BallInfor$y$ represent the total number of pixels in the X and Y directions. Ball$Y$ and Ball$X$ are the actual size of the basketball in the Y direction and X direction in the image, respectively.

4. System design

Basketball shooting automatic identification system is divided into four parts: input part, processing, output and graphical interface. The block diagram is shown in Fig. 3.

The main functions consists of the four parts:

• Input section: The input section provides the video frame for the system, including the image preprocessing and capturing the image [7].

• Shooting detection: to capture the image frame for some processing, and then through the differential image and post-processing to extract and calculate the bas-

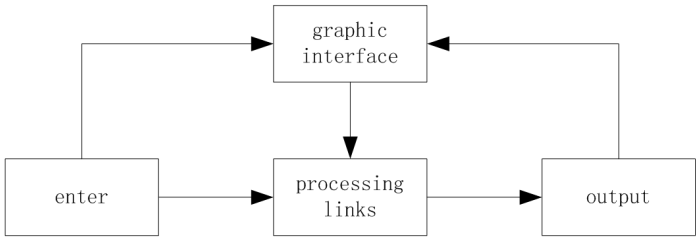

Fig. 3. System frame diagram

ketball feature information and determine whether it is scored.

• Graphical interface: used to display the current system status, the results of the display and the current video stream data [8].

• Output: The output section is the output.

5. Performance testing

The performance of the system is compared with the automatic test system (A system) based on the background difference method and the 30 groups of tests are carried out through the continuous test of the groups. The results are shown in Fig. 4 and Table 1.

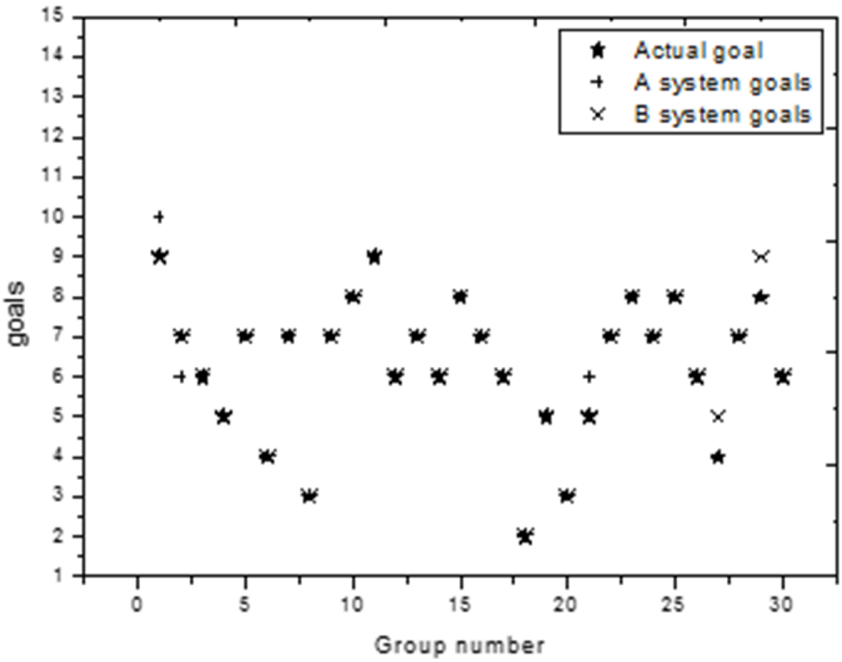

Fig. 4. Accuracy comparison between A system and B system

Table 1. Detection accuracy evaluation

Name	False rate		Missed rate		Accuracy	
	A system	B system	A system	B system	A system	B system
30 sets of data	6.66 %	6.66 %	0 %	3.33 %	93.34 %	90.01 %

As can be seen from Table 1 and Fig. 4, the accuracy of the A system is higher than that of the B system, and the accuracy rate is up to 93.34 %. However, the A system error occurred mainly in the back of the data, that is, in the process of shooting, the number of basketball hit more and more, the accuracy of the A system will decline sharply. The B system error detection and missed seizure is random, and will not be because of the increase in the number of shooting and its accuracy decreased. If the more the system detected, the B system accuracy will be higher than the A system. In terms of accuracy, the B system still needs to be further strengthened, but the stability is significantly better than the current detection system.

6. Conclusion

In this paper, combined with the characteristics of basketball during the shooting process and the background difference method, we determine the shooting detection algorithm and testing process. Through the experiment and analysis, we verify the feasibility and accuracy of the shooting detection algorithm, and use the shooting detection algorithm to achieve the shooting automatic recognition system in MATLAB. Through the analysis and comparison of the 30 sets of test data of the existing test system and the background difference method, we analyze and evaluate the results of the automatic shooting system from the aspects of accuracy.

References

[1] S. Avugos, M. Bar-Eli, I. Ritov, E. Sher: *The elusive reality of efficacy–performance cycles in basketball shooting: An analysis of players' performance under invariant conditions.* International Journal of Sport and Exercise Psychology *11* (2013), No. 2, 184–202.

[2] F. Chen ,C. de Vleeschouwer: *Personalized production of basketball videos from multi-sensored data under limited display resolution.* Computer Vision and Image Understanding *114* (2010), No. 6, 667–680.

[3] D. I. Ellis, H. Muhamadali, S. A. Haughey, C. T. Elliott, R. Goodacre: *Point-and-shoot: rapid quantitative detection methods for on-site food fraud analysis – moving out of the laboratory and into the food supply chain.* Analytical Methods *7* (2015), No. 22, 9401–9414.

[4] J. Han, L. Shao, D. Xu, J. Shotton: *Enhanced computer vision with microsoft kinect sensor: A review.* IEEE Transactions on Cybernetics *43* (2013), No. 5, 1318 to 1334.

[5] K. X. Zhao, D. J. He: *Target detection method for moving cows based on background*

subtraction. International Journal of Agricultural and Biological Engineering *8* (2015), No. 1, 42–49.

[6] P. C. Wen, W. C. Cheng, Y. S. Wang, H. K. Chu, N. C. Tang, H. Y. M. Liao: *Court reconstruction for camera calibration in broadcast basketball videos*. IEEE Transactions on Visualization and Computer Graphics *22* (2016), No. 5, 1517–1526.

[7] N. Rezazadeh, H. Zarrabi: *Using adaptive approach to enhance the accuracy of forward and backward algorithms in solving the evaluation problems of non stationary environments*. International Journal of Computer Science and Information Security *15* (2017), No. 1, 80–89.

[8] R. R. D. Oudejans: *Effects of visual control training on the shooting performance of elite female basketball players*. International Journal of Sports Science & Coaching *7* (2012), No. 3, 469–480.

Received May 7, 2017

Acta Technica *62* No. 3A/2017, 303–312

Hardness measurement and impact test for table tennis ball

Delei Wang[1]

Abstract. A new hardness measurement method for table tennis was put up based on theoretical analysis on hardness measurement mechanism for table tennis ball. First, two hardness measurement methods for table tennis were put forwarded based on traditional measurement methods, with which table tennis ball were classified on its hardness. Tests results showed that the measurement methods were more effective than the original one. Then, impact test device for table tennis ball were designed to study relation of hardness of table tennis ball and its speed when hitting at different positions with the same force. Test results showed that these two measurement methods were practical and reasonable. The maximum rebound speed of table tennis ball was different when the ball was hit at different positions with the same force. Three-star table tennis ball was more suitable for international games because its hardness was distributed more evenly and the speed was almost the same when hit at different positions.

Key words. Table tennis ball, hardness measurement, impact, deformation.

1. Introduction

Table tennis is the national sport of China, thus there is a growing demand for table tennis every year. Complex steps and long period was needed to produce a table tennis ball [1]. With the increasing demand of table tennis ball, original hardness measurement method for table tennis could not meet the requirement of modern industrial manufacturing. Fortunately, hardness measurement for table tennis ball was greatly promoted by the improved modern measurement instrument for table tennis ball, especially high sensitive electronic material tester [2]. Thus, improving hardness measurement efficiency for table tennis ball was of practical significance for improving measurement efficiency of table tennis ball. Based on hardness measurement mechanism for table tennis, a new method was put forward to provide theoretical basis for design hardness measurement instrument with high efficiency and accuracy.

[1]Zhejiang Pharmaceutical College, Zhejiang, 315000, China; E-mail: dl1753@tom.com

2. Literature review

Nowadays, most studies were about metal hardness and devices for measuring it while there were few studies about hardness measurement method for table tennis. Before studying mechanism for measuring hardness of table tennis ball, mechanism of table tennis ball should be studied. Table tennis ball was similar to spherical shell. And studies about spherical shell were mainly focused on quasi-static, large deformation and back-buckling and elastic deformation and bounce back of thin-wall spherical shell after impact [3]. D. P. Updike [4] was the first one to theoretically research spherical shell. Spherical shell deformation in quasi-static compression process was regarded as complete elastic deformation and ideal plastic deformation respectively. When spherical shell was under concentrated load, relation of force and load displacement was inferred theoretically and experimentally. Instability and energy change of spherical shell under dynamic impact was studied by M. Shariati et al. [5], whose theoretically study was essential for the following studies.

It was aimed to find out a new hardness measurement method for table tennis in order to provide a theoretical basis and technical parameters to reasonable classify table tennis according to its hardness. With the new practical hardness measurement method for table tennis, measurement efficiency was improved and the produced table tennis was standardized. This new method played an important role in strengthening companies' competitiveness in domestic and international markets. Thus, study on hardness measurement for table tennis ball and its speed after impact provided the crucial theoretical foundation and technical parameters for increasing efficiency of production line.

3. Research method

Traditionally, hardness of table tennis was measured by its deformation. However, with the increasing demand for table tennis ball, the traditional method was no longer suitable for modern production line. A new platform for hardness measurement method for table tennis ball was provided by modern measurement instrument. Using this method, 15 seconds should be remained before reading. In practical table tennis, table tennis ball was hit instantaneous, thus there was no science basis for waiting 15 seconds before reading. Besides, production efficiency would be lowered with this method. Thus, a new hardness measurement method for table tennis was put forward, with which no remaining time was needed and deformation was measured directly under limit load. Principle for measuring was that measuring hardness of table tennis ball with the bearing load when deformation was the same. It meant that impose load to table tennis ball gradually and stop loading at a certain degree of deformation. Therefore, hardness of table tennis ball was classified on the load value.

Electronic material tester of LRXPLUS 5KN was used to measure hardness of table tennis ball. Double Happiness table tennis ball of the same batch of one-, two- and three-star were chosen to be studied. And for each level, 70 table tennis balls were chosen and numbered. Before experiment, all table tennis balls should be

put under temperature of 20–25 °C and humidity of 50–60 % for 4 days. One of the important parameters for measuring hardness of table tennis ball was bearing capacity [6]. For identify the bearing capacity, there were two methods- experimentation (combining static load experiment with measurement technique) and theoretical calculation (specification-based approach and balance method). The bearing load of table tennis was identified by experiment, which can be used to identify its limit load before deforming. Both the limit load and the ultimate displacement measured by new method can be inferred by the limit load. Ultimate load of those table tennis balls studied (all table tennis ball of one-, two- and three-stars) was 80 N and load-displacement curve before deformation was almost in linear relation. In order to increase hardness measurement efficiency, 50 N, 60 N and 70 N were taken as the limit loads for experiments respectively. Thus, limit load of the new method was identified by comparison. Structure of the hardness measurement device is shown in Fig. 1.

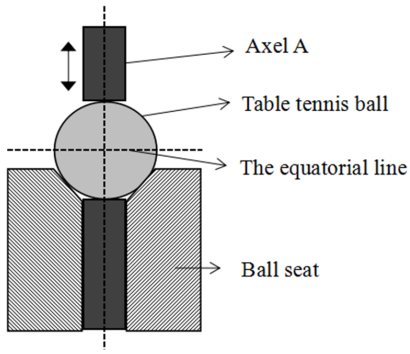

Fig. 1. Hardness measurement device for table tennis ball

Specifically, there are two testing schemes which were shown as follows:

Scheme 1: Measuring deformation of table tennis ball with limit load.

Step 1: First, No. 1 table tennis ball of one-star was put on ball seat and its junction line was kept parallel to horizontal line of ball seat. Load axis A was down moving with speed of 12 mm/min. When the load of table tennis ball reached 50 N, put load axis A back to the initial position and record its load-deformation curve graph. Then, table tennis ball was rotated by 180 degrees and measured with the same method to record its load-deformation curve graph.

Step 2: Table tennis balls of one-star from No. 1 to No. 10 were put on the ball seat and experimented with above method, respectively. Curve graph of deformation and load-deformation was recorded.

Step 3: Change those table tennis balls into one-and two-star respectively to repeat Step 1 and Step 2.

Step 4: Take limit load as 60 N, 70 N and 80 N respectively and repeat Step 1–Step 3.

Scheme 2: Set ultimate deformation to measure corresponding loading value Measurement principle: impose load to table tennis ball gradually and stop it when

the deformation reached a certain degree. Hardness of table tennis ball was classified with the loading value. Measurement steps were as follows:

Step 1: No. 51 table tennis ball of one-star was put on ball seat and its junction was kept parallel to horizontal line of ball seat. Down move axle A with constant speed of 12 mm/min and stop it when table tennis ball was caved into 0.8 mm. And record load-deformation curve graph and the relevant data.

Step 2: Ten other table tennis balls of one-star were changed into repeat step 1 and then, record relevant data.

Step 3: Repeat above steps on table tennis ball of two- and three-star and record relevant data.

Step 4: Set limit-deformation as 1.0 mm and 1.2 mm and repeat above steps.

3.1. Impact test

For explaining hit by luck, it was necessary to study speed of table tennis ball when it was hit at different positions, which study was also important for further table tennis manufacturing and performance measurement. Experiment for hardness measurement and speed of table tennis ball after hit was studied.

Structure of hardness measurement was shown in Fig. 1 that it was made up of electronic material tester and self-made ball seat. Nine Double Happiness table tennis ball of one, two- and three-star of the same batch were chosen and numbered. Mark 9 points on those table tennis balls in the direction of longitude, including 0 degree, 25 degrees, 45 degrees, 70 degrees, 90 degrees, 115 degrees, 135 degrees, 160 degrees and 180 degrees. First, No. 1 table tennis ball of one-star was put on ball seat and mark of 0 degree was put right below axis A. Down move axis A with speed of 12 mm/min and stop it and remain 15 seconds when table tennis ball was loaded 50 N. Then, move axis A back to the original position. All those 9 marked points have to be studied with the above method and all experimental data was recorded.

Impact tester device was mainly made up of impact test device for table tennis (built with 30×30 proximate matter), HG-100K high-speed camera and signal analysis system. Table tennis ball was put on the horizontal ball seat of impact test device and self-made scale mark caliper was stick on the appropriate position of proximate matter. Impact tests for one-, two- and three-star table tennis balls were made on marked points of 0 degree, 45 degrees, 90 degrees, 135 degrees and 180 degrees and each experiment was repeated for 3 times. In the same time, process of table tennis ball ascending to the highest point was recorded by medium-high speed camera with which signal was transmitted to DASP intelligent data acquisition and analysis system.

4. Results and analysis

4.1. Hardness measurement result and analysis

Curve graph of elongation-loading value was outputted by electronic material tester. However, when elongation started changing, load value was not 0. In order

to reflect relation of deformation and loading, Matlab software was used to fitting data outputted by tester again.

- Scheme 1:

  When limit load was 50 N, the curve graph of deformation and load is shown in Fig. 2. Curves 1–5 are the experimental values randomly selected and curve 6 is the mean value of those 5 curves. It can be seen from Fig. 2 that there wi a linear relation between deformation and load when the limit load is 50 N. In this situation, deformation of table tennis ball represents an elastic deformation, under which table tennis ball could resume its original shape, thus table tennis ball can be used normally.

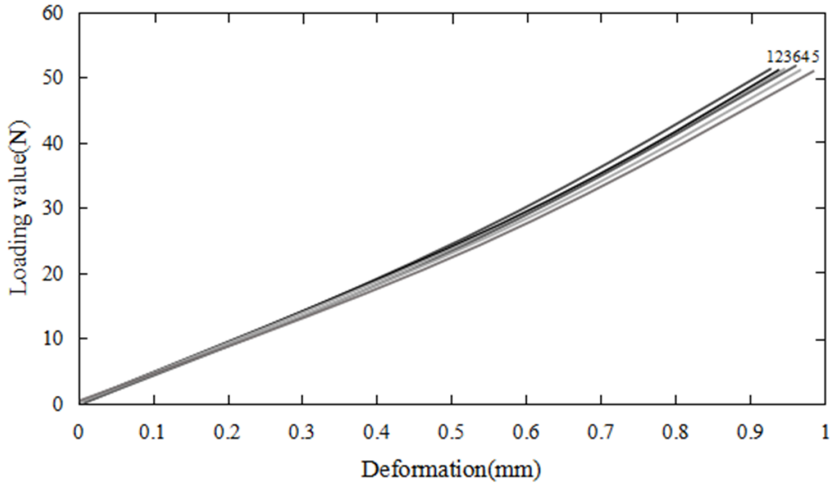

Fig. 2. Curve graph of elongation-loading value when limit load was 50 N (one-star table tennis ball, loading speed 12 mm/min, temperature 24 °C)

The maximum deformations of table tennis balls of one-, two- and three-star under limit load of 50 N are depicted in Fig. 3. And it can be seen from this figure that under the conditions of same loading speed and temperature and no remaining time during the process, different deformation is shown by table tennis balls of different stars. Besides, deformation of table tennis ball of different levels satisfy the relation that three-star deformation is smaller than two-star deformation and this is smaller than one-star deformation, which basically conforms to classification of table tennis ball of different number of stars.

Experiments on those table tennis balls of one-, two- and three-star were made on 4 different limit loads, respectively. When limit load was 80 N, there was squash deformation for all table tennis ball, thus those measurement data was not included in Table 1. The other data are shown in Table 1.

It can be seen from Table 1 that under the same loading, there was relation of three-star deformation $<$ two-star deformation $<$ one-star deformation. It

can be known form standard deviation that hardness value of three-star table tennis was more concentrated than that of two-and one-star table tennis ball, which meant that three-star table tennis ball was more suitable for major match because of more stable quality.

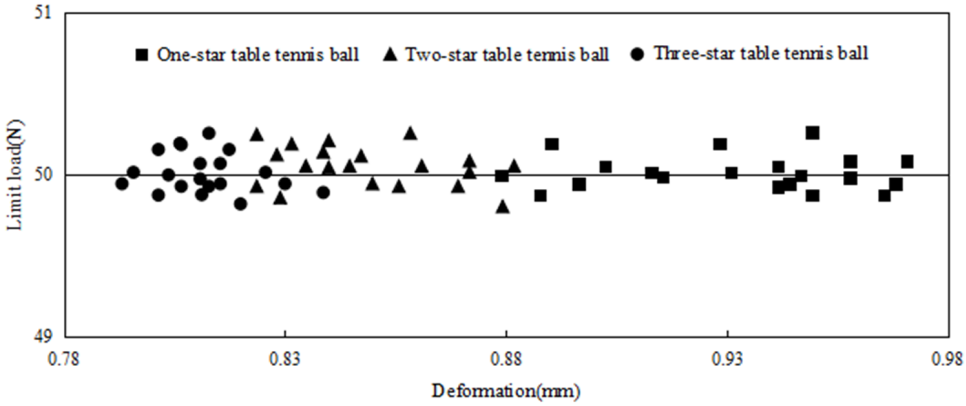

Fig. 3. Distribution of the maximum deformation of table tennis ball of different level under loading of 50 N

Table 1. Detection accuracy evaluation

Limit load	50 N			60 N			70 N		
	Times	Mean value (mm)	Standard deviation	Times	Mean value (mm)	Standard deviation	Times	Mean value (mm)	Standard deviation
One star ball	20	0.922	0.0262	20	1.169	0.0378	20	1.231	0.0282
Two star ball	20	0.843	0.0238	20	0.992	0.0367	20	1.122	0.0265
Three star ball	20	0.828	0.0157	20	0.978	0.0117	20	1.085	0.0379

- Scheme 2:

  When deformation was 1.2 mm, curve graph of deformation and loading of table tennis ball of one-, two- and three-star is shown in Fig. 4 and the corresponding loading is shown in Table 2.

  It can be seen from Fig. 4 and Table 2 that when deformation was less than 1.2 mm, loading value of table tennis ball was increasing with the increasing deformation and there was a linear relation for fitting curve of loading-deformation. Under the same ultimate deformation, there was a relation of

three-star deformation > two-star deformation > one-star deformation, which means that quality of three-star table tennis ball is more stable.

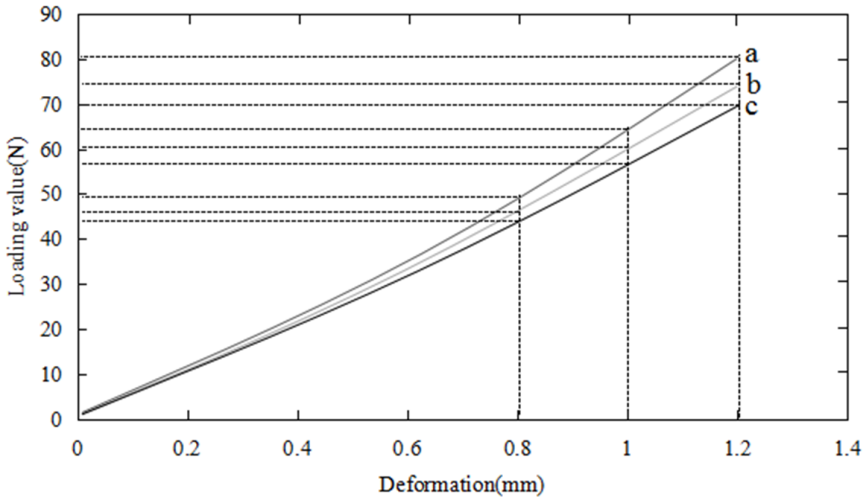

Fig. 4. Curve graph of deformation and loading when limit deformation of table tennis ball was 1.2 mm (a: one-star table tennis ball, b: two-star table tennis ball, c: three-star table tennis ball)

Table 2. Maximum load of table tennis ball of all three stars under the same deformation

Limit load	0.8 mm			1.0 mm			1.2 mm		
	Times	Mean value (mm)	Standard deviation	Times	Mean value (mm)	Standard deviation	Times	Mean value (mm)	Standard deviation
One star ball	20	43.68	2.754	20	55.15	4.586	20	48.72	5.712
Two star ball	20	46.05	3.562	20	60.18	3.068	20	64.09	6.927
Three star ball	20	49.13	0.931	20	74.62	1.788	20	79.11	4.138

To sum up, table tennis ball can be classified with these two measurement methods put forward.

4.2. Result and analysis of impact test

Data of those 9 tests for table tennis ball of one-, two- and three-star was outputted. Deformation of table tennis ball under load was calculated. Then, the mean values of those 9 points were calculated. Matlab software was used to fit tests results of table tennis balls for 4 times. Curve graph of deformation and position angle of half of the table tennis balls was obtained and is shown in Fig. 5.

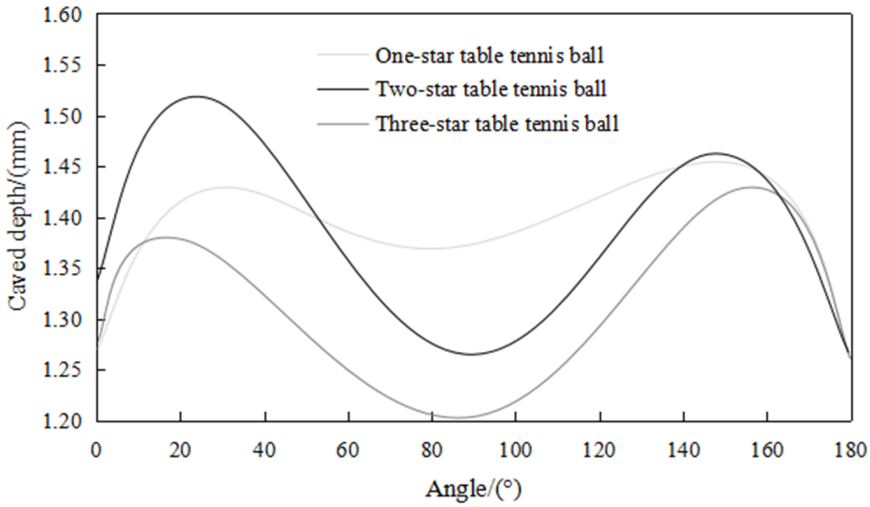

Fig. 5. Curve graph of deformation changing with position of table tennis ball

It can be seen from Fig. 5 that hardness of table tennis ball at the junction was larger than that of other monolayer around it. Junction line was a ring-like strengthening rib of table tennis ball. In the thin-shell structure, ring-like strengthening rib was able to stabilize the structure, improve loading bearing capacity of axial stress and lower the rate of squash.

High-speed camera was used to record process of table tennis ball moving up to the highest point. Image that contained complete picture of table tennis ball was selected. Gaussian Mixture Model [7] was used to identify position of table tennis, thus binary image was obtained. In this situation, dash area in image was remained, which was removed according to differences of color of table tennis ball and the dash area. A circular area in image was extracted by Hough Transform whose center was identified by function provided by OpenCV, thus center of table tennis ball was calculated. After image processing, the highest point of each experiment result was selected. Mean value of those highest points was computed. Curve graph of the highest point changing with angle was obtained by data fitting, which was shown as Fig. 6.

It can be seen from Fig. 6 that the given table tennis ball was hit by the same force in the same direction, table tennis ball rose to its peak when hit at 90 degree mark and rose to its lowest point when hit at the junction. The closer to 90 degree position, the higher position of table tennis ball rose to.

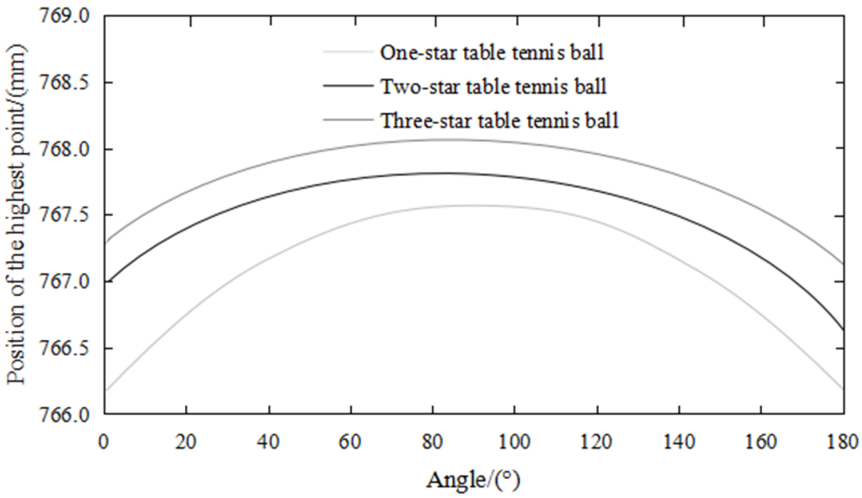

Fig. 6. Curve graph of the highest point changing with angle

In conclusion, speed of table tennis ball was changing regularly to a certain degree when it was hit by the same force because hardness of table tennis ball was changing with angle. However, changing rule of speed and its hardness was not completely the same. Hardness at junction line was relatively larger than that of other areas. However, when table tennis was hit at junction line, the speed after hit was the slowest. It can be inferred from the results that the larger hitting force, the more energy lost and the larger difference between initial speeds of table tennis balls because of uneven hardness of table tennis ball. Besides, one of the important reasons for hitting by luck was that contact area of table tennis ball and racket was increased because table tennis ball rotation was influenced by the uneven hardness.

5. Conclusion

First, two hardness measurement methods for table tennis ball was put forwarded, which was verified effective by a serial of experimentations and analysis of Matlab software. Then, impact test was designed to study relation of hardness of table tennis ball and the speed after hitting when table tennis ball was hit at different place with the same force. With the methods put forwarded, it can not only classify table tennis but also provide an explanation for hit by luck during match, which provided a reference standard for future table tennis production.

References

[1] J. Q. Liu, B. Wang, X. Zhao, Y. Dou: *The application of rubber materials on table tennis racket.* Applied Mechanics and Materials *473* (2013), No.Chapter 2, 116–120.

[2] R. H. Bao, T. X. Yu: *Impact crushing and rebound of thin-walled hollow spheres.* Key Engineering Materials *535–536* (2013), 40–43.

[3] X. W. Zhang, Z. Tao, Q. M. Zhang: *Dynamic behaviors of visco-elastic thin-walled spherical shells impact onto a rigid plate.* Latin American Journal of Solids and Structures *11* (2014), No. 14, 2607–2623.

[4] D. P. Updike: *On the large deformation of a rigid-plastic spherical shell compressed by a rigid plate.* Journal of Manufacturing Science & Engineering *94* (1972), No. 3, 949–955.

[5] M. Shariati, H. R. Allahbakhsh: *Numerical and experimental investigations on the buckling of steel semi-spherical shells under various loadings.* Thin-Walled Structures *48* (2010), No. 8, 620–628.

[6] H. Dong, N. Figueroa, A. E. Saddik: *"Load balance" control for a humanoid musculoskeletal arm in table tennis movement.* International Journal of Control, Automation and Systems *13* (2015), No. 4, 887–896.

[7] T. Celik: *Image change detection using Gaussian mixture model and genetic algorithm.* Journal of Visual Communication and Image Representation *21* (2010), No. 8, 965–974.

Received May 7, 2017

Acta Technica *62* No. 3A/2017, 313–320

Research on the design of wireless control system for basketball stands elevator

Min Zhou[1], Xiaodong Yi[1,2]

Abstract. To realize the lifting of basketball stands elevator scientifically and reliably. Through a portable control terminal equipped with a touch screen, we use the ZigBee wireless network to control each elevator node. The hand-held remote control terminal based on STM32F103 as the core processor, realizes data transmission by using CC2530 wireless communication chip, and the elevator control terminal, through ZigBee receiving nodes with the same CC2530 as the core, receives the command sent from the remote terminal. After testing, this system has friendly man-machine interface, low power consumption, low cost, high reliability, good expansibility and so on advantages. The system not only can be used in lifting system of basketball stands, but also can be easily transplanted into other specific applications with the broad application prospect and market value.

Key words. Basketball stands elevator, ZigBee wireless communication, control system.

1. Introduction

With the development of social material civilization, people's keen degree of sports activities also grows with each passing day. In addition, leisure fitness becomes the most effective way for people to relax the heart and alleviate the pressure of work, and the stadium has become the first choice of people in sports activities. On the other hand, with the rapid development of Chinese sports, more and more sports items have been widely promoted, except for basketball, badminton, table tennis and so on traditional items, billiards, yoga, aerobics and other emerging sports project has obtained more and more people's love and participation. In order to enrich the function of stadium, large stadiums are installed with basketball stands that can be moved up or down. Driving the winch by the motor, it drives the mechanical mechanism, and lifts the basketball stands to the ceiling, which makes the basketball stands do not interfere with the running of other sports activities [1]. How to realize

[1]Sichuan University, Sichuan, 610000, China
[2]Corresponding author; E-mail: xiaodongyixdy@163.com

the lifting and lowering of the basketball stands elevator quickly and scientifically has become an urgent problem to be solved. In the field of short distance communication, there is very fierce competition. However, ZigBee technology, with its low cost, low power consumption, high safety, large network capacity and many other advantages, showed itself in many short distance communication technologies [2].

ARM core design is more advanced, with higher frequency and more powerful processing capabilities; FPGA integration is greatly improved, having entered the era of 28 nm [3]. A single chip can integrate with hundreds of thousands or even millions of gates. In addition, through a portable control terminal equipped with a touch screen, we make use of the ZigBee wireless network, to control each elevator node. We can also record the elevator using information in the PC terminal database, easy to use, safe and reliable, low in cost, high in performance, and easy to modern management of the stadium.

2. Overview

ZigBee network is a short distance wireless network composed of up to 65536 wireless communication modules, and any of the two devices in the network can communicate with each other directly or indirectly. In the protocol stack, the theoretical communication distance between ZigBee network nodes is 75 meters. Through increasing the extra power amplifying circuit (such as low noise amplifier), it can greatly extend the communication distance. For instance, after making use of CC2591 power amplifier, the communication distance is up to several kilometers [4]. In addition, the ZigBee device can be connected to the mobile communication network or Ethernet, which is convenient for the remote monitoring of the equipment and greatly expands the application range. ZigBee technology has many advantages, such as low rate, low power consumption, low cost, large network capacity, short time delay, high safety, high reliability and so on [5], ZigBee technology applications field is very extensive, including industrial automation, building automation, lighting control, environmental control, medical monitoring system, smart card, remote control, wireless data acquisition system and so on. ZigBee technology in 2004 was named one of the ten latest technologies in the world's fastest-growing and most extensive market prospects.

The stadium elevator controller is mainly designed for lifting basketball stands in the stadium. The basketball stand is more common in foreign countries. In the 1960s, it was designed and produced by a professional company of lifting equipment, mostly installed in large gymnasium. The basketball stand is lifted up to the roof, avoiding the trouble for making room space to remove the basketball stand from the original place to the off-site, so the lifting basketball stand has been rapidly promoted. The traditional stadium lift control is wired, roughly divided into separate control mode for each lift and all lift networked control [6]. In our country, since that the stadium equipped with the lifting basketball stand is relatively small, the stadium elevator controller is blank. However, with the modernization grading of stadium construction and the development of control technology, the convenient and reliable lifting system is bound to have a broad market prospect.

3. Methods

3.1. Overall scheme design

The system is mainly composed of three parts: a hand-held remote controller, several lift control units and a plurality of ZigBee network modules. The hand-held remote controller provides man-machine interface, convenient for users to operate; elevator control units directly control the winch motor reversing and realize the lifting action of elevator; ZigBee network module is responsible for data transmission between the hand-held remote controller and the elevator control unit; in addition, the PC machine realizes the data record of the elevator operation case in the database, but also uploads the database to the network, so as to achieve the management of a number of stadium. The system structure is shown in Fig. 1.

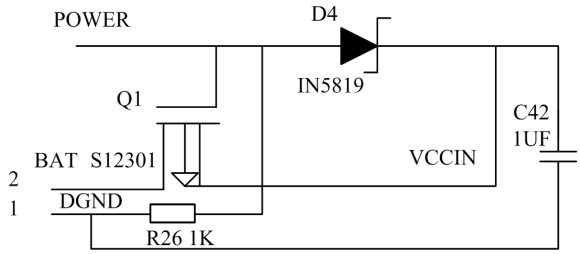

Fig. 1. Input power schematic circuit

3.2. System hardware design

The stadium elevator wireless control system is the complex system composed of hand-held remote controller, elevator control system units and ZigBee network modules. The hardware design contains a lot of contents, relating to the embedded ARM system hardware, CPLD programmable logic device system hardware, ZigBee RF module hardware, power management circuit, expansion interface circuit and so on hardware's design [7]. It is supposed to follow the modular, standardized, and generalized ideas, to make the hardware design simple and reliable, and to ensure the stability and good expansibility of each module circuit.

In the hand-held remote controller hardware system, power supply related circuit includes input power arbitration circuit, charging circuit, TFT-LCD backlight LED power supply and so on. The design of this part is more complex, which is one of the most important parts in the hand-held remote controller hardware design. The input power arbiter determines which power is used to provide power supply for the hardware system. The schematic diagram is shown in Fig. 1.

Hand-held remote controller uses the TFT-LCD screen. Because the system has not high requirements on the touch screen accuracy, for cost considerations, we select four-wire resistive touch screen. Figure 2 is the equivalent model of the resistive touch screen. The value of the output voltage Vmeas is determined by the

ratio of the two series resistors. Among them, the equivalent resistance R1 and the reference voltage Vref are connected, the other end of the resistance R2 grounding, and the Vmeas terminal can be connected to the ADC, for the voltage measurement.

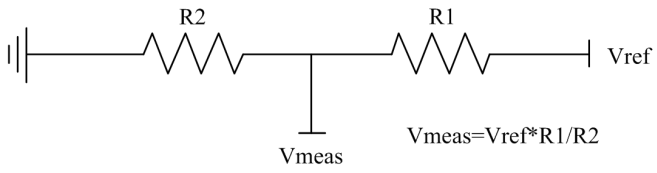

Fig. 2. Schematic diagram of resistive touch screen

In the hardware design of ZigBee network module, taking into account the design cost and the requirements of product technology, the elevator control unit and ZigBee module PC machine terminal use the similar minimum system hardware design. And hand-held controller end ZigBee module, except for the minimum system hardware design, in order to meet the need of communication distance, also adds the power amplification circuit and SMA omnidirectional antenna.

Power amplifier relevant circuit diagram is mainly the link part between the CC2530 and the CC2591, and the connection circuit is shown in Fig. 3.

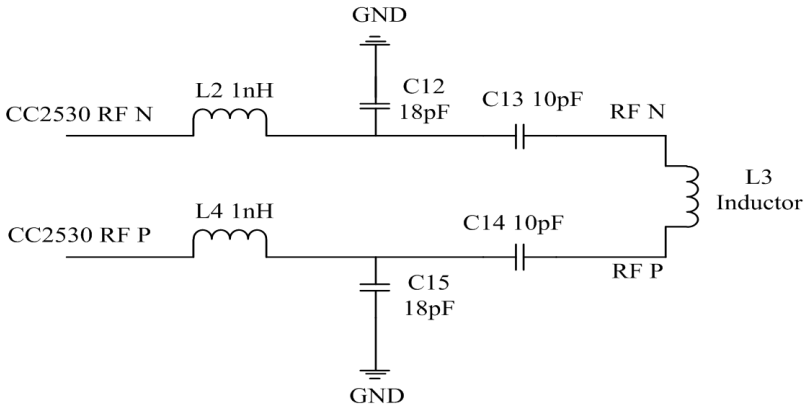

Fig. 3. Connection circuit diagram of CC2530 and CC2591

3.3. System software design

The software design is the core work of the elevator wireless control system design. The hardware of the system is equivalent to the human body. And the system software is equivalent to the brain of human, controlling the entire system for normal working. With the development of embedded technology and integrated circuit technology, the hardware circuit design more uses the integrated circuit and the design difficulty continuously decreases. The performance of the system mainly depends on

the quality of the software design, and it puts forward higher requirements to the software design.

The hand-held remote control is the most complex part in the whole system, and the corresponding software design is also the most difficult. The microcontroller uses STM32F103VC and uses the standard C language for programming it. It is worth mentioning that the ST company, in order to facilitate the user to develop software, provides a set of open source peripheral firmware library. Users only need to call the interface functions inside can it operate on all peripheral sources on the microprocessor, which greatly reduces the difficulty of software design. Figure 4 is the flow chart of main function of the hand-held remote controller.

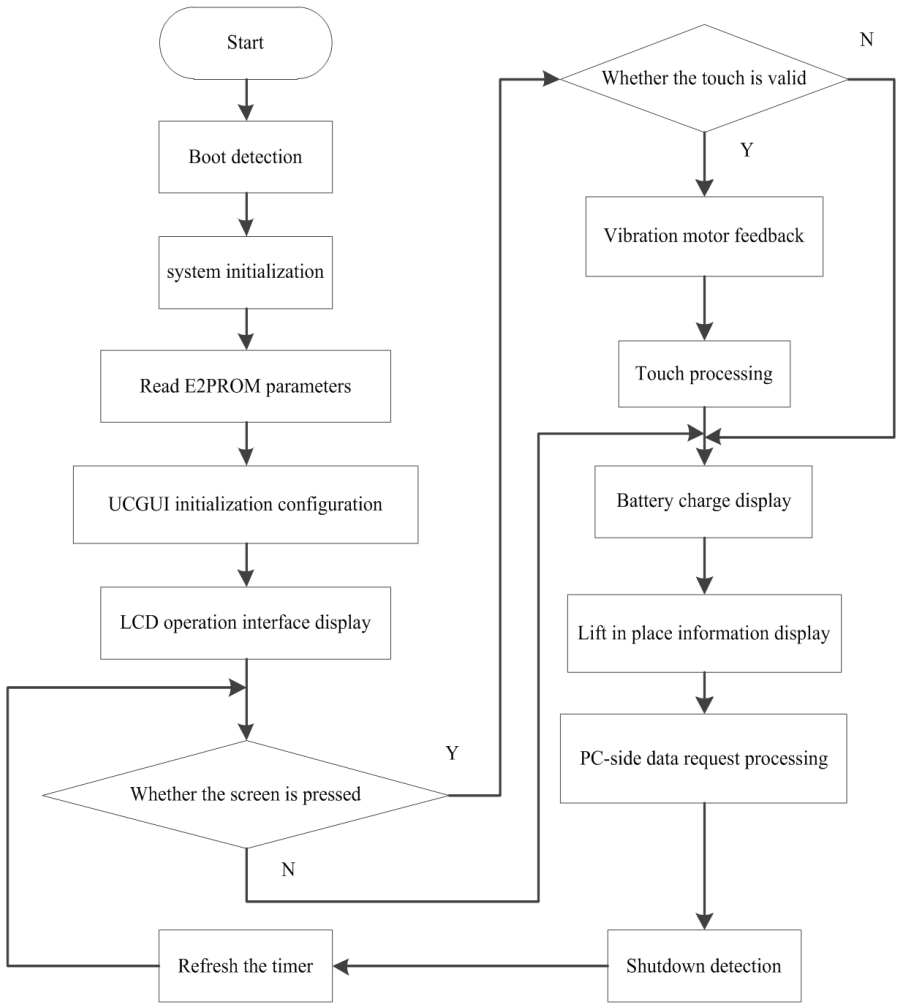

Fig. 4. Flow chart of main function of the hand-held remote controller

Lift control unit function is relatively simple, including the receiving of lifting

command data packets, sending a response packet and in place report data packets, and relay operation.

4. Results and discussion

After the design of hardware and software, whether the system can realize the design function accurately and reliably according to the design requirements needs comprehensive and systematical test. The test of the basketball stand lifting system mainly includes two parts: function test and performance test. The function test of the system is to mainly test the correctness of the system, including the function of the touch screen, the transmission function of the ZigBee network, the lifting function of the elevator and so on. The specific test cases and test results are shown in Table 1.

Table 1. System test cases

Number of cases	Test items	Expected results	Practical results
1	Click the function keys of touch screen to test whether each function key can send the correct instructions.	Each function key is normal in functions.	Each function key can be morally used.
2	The elevator motion command is sent by the touch screen, to test whether the wireless network communication is normal.	The elevator can successfully receive instructions.	Elevator can successfully receive instructions.
3	After the elevator receives the instructions, test whether the elevator is in accordance with the normal operation of the command.	The elevator can follow the instructions.	The elevator can follow the instructions.

Table 1 shows that the system function is normal.

The performance test of this system mainly tests the anti-interference of the system, because it is very important that the system can run stably and reliably. ZigBee network works in the 2.4 GHz band. In the laboratory, we use the Bluetooth signal of the mobile phone and the wireless routing signal as the interference source, respectively, to verify the anti-interference ability of the communication module. The specific results are shown in Table 2.

As can be seen from Table 2 that, there is no obstacle in the network communication in the interference of same frequency signal.

There is a high power relay in the elevator control unit, which is installed near the winch motor. If the number received currently minus the last number and the result equals to 1, it suggests that the control unit has high reliability; otherwise, it represents that the internal program of microcontroller is not normally operated under

electromagnetic interference. And it needs to take measures to further improve the anti-interference ability. The experimental results showed that the internal program of the microcontroller operates normally under the electromagnetic interference and it has high reliability.

Table 2. Anti-interference test of system communication function

Sources of interference	Communication situation of system ZigBee wireless network
Bluetooth signal	System wireless communication function is completely normal.
Wireless routing Wi-Fi signal	System wireless communication function is completely normal.
Radiotelephone signal	System wireless communication function is completely normal.

5. Conclusion

At present, the large-scale stadium often sets a number of basketball stands equipped with the elevator. In order to meet the sustainable development route in line with the green environmental protection and energy conservation, and to further realize the modernization management of stadium elevator control, based on the analysis of the shortcomings of the traditional control method, we put forward the stadium elevator wireless control system based on ZigBee short distance wireless RF technology, embedded technology and database technology.

The system designed in this paper has the advantages of friendly human-machine interface, low power consumption, low cost, high reliability, good expansibility and so on. At the same time, the system can be easily transplanted to other specific applications, with broad application prospects and market value.

References

[1] M. Ciman, M. Donini, O. Gaggi, F. Aiolli: *Stairstep recognition and counting in a serious Game for increasing users' physical activity.* Personal and Ubiquitous Computing *20* (2016), No. 6, 1015–1033.

[2] J. Fernandez, P. Cortés, J. Muñuzuri , J. Guadix: *Dynamic fuzzy logic elevator group control system with relative waiting time consideration.* IEEE Transactions on Industrial Electronics *61* (2014), No. 9, 4912–4919.

[3] J. R. Fernandez, P. Cortes: *A Survey of elevator group control systems for vertical transportation: A look at recent literature.* IEEE Control Systems *35* (2015), No. 4, 38–55.

[4] H. Zhang, P. Cheng, L. Shi, J. Chen: *Optimal DoS attack scheduling in wireless networked control system.* IEEE Transactions on Control Systems Technology *24* (2016), No. 3, 843–852.

[5] J. M. Jang, S. Y. Shin, Y. J. Ji, S. Chae: *Wireless control system using spherical*

camera. Journal of Korean Institute of Communications and Information Sciences *41* (2016), No. 4, 461–466.

[6] A. Tsiftsis, I. G. Georgoudas, G. C. Sirakoulis: *Real data evaluation of a crowd supervising system for stadium evacuation and its hardware implementation.* IEEE Systems Journal *10* (2016), No. 24, 649–660.

[7] B. N. K. Pryor: *Hope's elevator young black women and the performance of identity.* Qualitative Inquiry *22* (2016), No. 5, 406–416.

Received May 7, 2017

Acta Technica *62* No. 3A/2017, 321–334

Modeling and kinematics simulation of freestyle skiing robot

Xiaohua Wu[1,3], Jian Yi[2]

Abstract. Freestyle skiing robot model and gait planning are used for the robot model moving in the snow. First, data of human body is collected by 3-D laser scanning technique. Sports biomechanics and computer simulation methods are used to structural design and analyze freestyle skiing robot. Then, 3-D modeling software Pro/E is used to build entity model then gait planning based on bionics is studied. Finally, virtual prototype technology is used to modeling the robot at the slipping stage to verify the feasibility of gait planning. Results show that slipping stage can be dynamically simulated by the freestyle skiing robot. Displacement and velocity change of joints of theoretical movement are very close to that of simulation movement. Moreover, theoretical angular acceleration curve is relatively close to simulation results. In conclusion, gait planning of bionics is suitable for motion planning of freestyle skiing robot and robots' all movements at slipping stage can be achieved.

Key words. Freestyle skiing robot, ADAMS, Pro/E, gait planning, kinematics.

1. Introduction

Robotics is widely used in modern production, national economy and people's livelihood with the development of modern science and technology. Among all kinds of robot, system structure of humanoid robot is the most complex one and its integration level is high, which represents the cutting-edge technology of robot and is essential for study robot [1].

2. Literature review

Nowadays, humanoid robot has entered an essential stage where intended functions can be realized. Humanoid robot is on the cutting edge of robot research,

[1]Jilin Sport University, Jilin, 130022, China
[2]College of Humanities & Information, Changchun University of Technology, Changchun, 130122, China
[3]Corresponding author; E-mail: xiaohuawuxh@126.com

which is important for research on humanoid robot [2]. Problems occurred during research and development of humanoid robot product of long development cycle and expensive cost cannot be solved by traditional design flow of physical prototype. Virtual prototype technology is used to assist study, such as kinematic modeling and simulation, dynamics simulation and analysis and optimization design of structure of humanoid robot [3]. Virtual prototype technology advances the development of humanoid robot greatly. With their development and combination, more and more kinds of humanoid robots are produced, for example soccer robot, basketball robot and running robot.

Ontological mechanical structure of freestyle skiing robot is designed based on characteristics of physical structure of freestyle skiing athlete and motion mechanism analysis of human skeleton and muscle. Design thought and implementation method for lower limbs, trunk, upper limbs and head are put forwarded according to different functions of joints and body parts [4]. Bionic gait planning method is adopted for freestyle skiing robot on the basis of existing experimental data of freestyle skiing robot and feature of mechanical structure. Cubic spine interpolation algorithm is used to planning joints track of hip, knee, shoulder and elbow. Virtual prototype model of freestyle skiing robot is built in ADAMS then track planning parameters of joints are used to generate STEP function which is added to corresponding joints of freestyle skiing robot in virtual prototype. Thus, simulation experiment for freestyle robot is conducted and the simulation results show that bionic gait planning is feasible and all movements of robot at slipping stage can be achieved.

3. Methods

3.1. Structural design and analysis of freestyle skiing robot

3.1.1. Body frame and structure design. Below aspects should be taken into consideration when designing body frame of freestyle skiing robot- First, size (height and weight) of body frame should be identified according to human body proportion. Second, main control computer, data acquisition card (DAQ Card), motor driver, and power management module were installed and carried on body frame, for which rational distribution and load bearing strength and stiffness of body frame should be considered. Third, heat dissipation of motor drive and main control computer should be taken into account when designing body frame [5].

3.1.2. Joint structure design and analysis for lower limbs. Limbs structure of freestyle skiing robot was symmetrical, which meant structure of left and right legs was the same. Thus, structural design of left leg was taken as an example. There were six rotary joints in the left leg of the robot.

1) Structural design and analysis of hip joint

For inverse kinematics solution of leg, axes of hip joints in three directions should meet in one point, thus there was closed-form solution. It meant that DOF (degree of freedom) of joint rotation, roll and pitching should meet in one point. Mechanical

structural of DOF of hip joint pitching and roll was made up of servo motor, synchronous belt and harmonic reducer. Servo motor and reducer were near joint and power was output to joint through synchronous belt. There was small moment of inertia while large driving torque because synchronous belt was directly connected to joint which is not suitable to precision positioning.

2) Structural design and analysis of knee joint

Drive capability of knee joint was important for robot movement because it supported upper body and carried outfast start and stop functions. Dual motor drive and V-belt pulley were used to knee joint, with which there were two advantages. First, due to dual motor drive, there was superposition of output torque of electric machine. Thus, capability of joint to output torque was improved and heat caused by long-working time was avoided. Second, the small-adjustment eccentric tensioning wheel was adopted by driving mechanism of knee joint. Thus, distances between input axis of knee joints can be adjusted by changing installation angle of the small-adjustment eccentric tensioning wheel. Counting-rate-difference feedback signal of dual motor can be acquired by two encoders in real time, which was convenient for master-slave control of dual-motor, joint angle information acquisition, mechanical transmission error correction and control accuracy improvement.

3) Structural design and analysis of ankle joint

According to bionics principle, ankle joint was of two degrees of freedom - pitching and roll. Besides, those two axes were met in one point, which was similar to structure of hip joint. Also, modular design method was used to design degree of freedom of pitching and roll of ankle joint and it was made up of servo motor, harmonic reducer and synchronous belt. There was a criss-cross construction at its pitching and roll joints, because of which there were a compact structure of ankle joint and a downsized ankle joint. Potentiometers were put on degree of freedoms of pitching and roll of criss-cross construction joint to detect practical output angle of joint.

3.1.3. Structural design and analysis of the upper arm joint. This structural design was similar to that of hip joint. According to document literature, as long as axis of shoulder joint in three directions was met in one point, there was closed-form solution of the upper arm when conducting inverse kinematics solution. It meant that when designing, DOF (degree of freedom) of rotation, roll and pitching of shoulder joint should met in one point.

3.1.4. Design and analysis of waist joint and neck joint. Two structural designs have to be considered.

1) Structural design and analysis of waist joint

In this design method, there were two degree of freedoms for waist – pitching and roll. Electric machine 1 was used to control pitching degree of freedom of waist joint by transmitting power to harmonic reducer. Then, waist support frame was controlled by reducer to support its pitching movement. Besides, the other end of

waist support frame was connected to bearing. Electrical machine 2 was used to control the waist rotation by transmitting power to harmonic reducer. Then, waist rotation support frame was controlled by reducer to support its rotation movement through sleeve.

2) Structural design and analysis of head joint

There were two degree of freedom for head – pitching and rotation. Electrical machine 1 was used to control pitching degree of freedom by transmitting power to harmonic reducer. Then, head support frame was controlled by reducer to support head pitching movement. Besides, the other end of head pitching support frame was connected to bearing. Electrical machine 2 was used to control rotation joint of head by transmitting power to harmonic reducer. Support frame of head pitching was controlled by reducer to rotate head joint.

3.2. Motor process analysis of freestyle skiing robot

Competition field of freestyle skiing aerials was made up of start area, speed-up skiing slope, transition area 1, ski jump, transition area 2, landing slope and terminal area [6]. Movement of speed-up skiing phase of freestyle skiing was studied. It can be known after the study on material of freestyle skier in speed-up skiing phase that skiers' postures can be divided into start sliding skiing, squat skiing, standing skiing and body extension preparation. In Changchun University of Technology, H-dimensional laser scanning technique was used to acquire data of skiers in national freestyle skiing aerial team and data of several specific skills were collected. Rotation angles of those four movements of joints are shown in Table 1. Ski-shank angle was included angle of ski and shank. Knee joint angle was included angle of shank and thigh. Hip joint angle was included angle of thigh and trunk in the same side. Shoulder joint angle was included angle of trunk and the upper arm in the same side. Elbow joint angle was included angle of the upper arm and forearm in the same side. Trunk dip angle was included angle of trunk and the snow surface. Neck dip angle was included angle of neck and the snow surface. Head dip angle was included angle of head and the snow surface. Thigh dip angle was included angle of thigh and the snow surface. Ski dip angle was included angle of ski and the snow surface in speed-up skiing phase when slope gradient was changed.

3.3. Gait planning of freestyle skiing robot

3.3.1. Motion curve of freestyle skiing robot in speed-up skiing phase. First, quartic polynomial was used to plan motion curve of 0–3 meters. Then, three cubic polynomials were used to plan motion curve of 3–8 meters, 8–24 meters and 24–52 meters, respectively. Then, quartic polynomial was used to plan motion curve of 52–65 meters. Thus, the whole motion curve was matching with 4–3–3–3–4. Standard global time variable of the whole motion was set as t and local time variable of the jth motion phase was indicated as τ_j. The initial time of each motion phase was $\tau_{j\mathrm{i}}$ and terminal local time of each motion phase was $\tau_{j\mathrm{f}}$. Thus, all motion phases were start from local time of $\tau_{j\mathrm{i}} = 0$ and finish up with the given local time $\tau_{j\mathrm{f}}$. The

equations of those five motion phases are

Table 1. Data acquisition of different phases

Joint angles	Angles in the phase of starting and sliding skiing (°)	Angles of the squat skiing phase (°)	Angles of the body extension preparation phase (°)	Angles of raising arm (°)
Ski-shank	82.25	91.08	79.97	84.17
Knee joint	152.34	123.68	178.05	179.41
Hip joint	153.34	99.40	175.92	176.85
Shoulder joint	13.22	18.77	27.14	160.52
Elbow joint	143.60	138.16	170.02	13.34
Trunk dip angle	82.65	66.80	93.75	100.28
Neck dip angle	75.47	65.44	81.50	86.46
Head dip angle	75.90	73.57	76.38	86.09
Thigh dip angle	109.3	147.41	89.66	97.13

$$\begin{cases} z(t)_1 = a_0 + a_1 t + a_2 t^2 + a_3 t^3 + a_4 t^4, \\ z(t)_2 = b_0 + b_1 t + b_2 t^2 + b_3 t^3, \\ z(t)_3 = c_0 + c_1 t + c_2 t^2 + c_3 t^3, \\ z(t)_4 = d_0 + d_1 t + d_2 t^2 + d_3 t^3, \\ z(t)_5 = e_0 + e_1 t + e_2 t^2 + e_3 t^3 + e_4 t^4. \end{cases} \tag{1}$$

Replacing higher-degree polynomial with multistage low order polynomial, the below equations were obtained:

$$\begin{cases} z_1 = a_0, \\ \dot{z}_1 = a_1, \\ \ddot{z}_1 = 2a_2, \end{cases} \tag{2}$$

$$\begin{cases} z_2 = a_0 + a_1\tau_{1\mathrm{f}} + a_2\left(\tau_{1\mathrm{f}}\right)^2 + a_3\left(\tau_{1\mathrm{f}}\right)^3 + a_4\left(\tau_{1\mathrm{f}}\right)^2, \\ z_2 = b_0, \\ a_1 + 2a_2\tau_{1\mathrm{f}} + 3a_3\left(\tau_{1\mathrm{f}}\right)^2 + 4a_4\left(\tau_{1\mathrm{f}}\right)^3 = b_1, \\ 2a_2 + 6a_3\left(\tau_{1\mathrm{f}}\right) + 12a_4\left(\tau_{1\mathrm{f}}\right)^2 = 2b_2, \end{cases} \tag{3}$$

$$\begin{cases} z_3 = b_0 + b_1\tau_{2\mathrm{f}} + b_2\left(\tau_{2\mathrm{f}}\right)^2 + b_3\left(\tau_{2\mathrm{f}}\right)^3, \\ z_3 = c_0, \\ b_1 + 2b_2\tau_{2\mathrm{f}} + 3b_3\left(\tau_{2\mathrm{f}}\right)^2 = c_1, \\ 2b_2 + 6b_3\left(\tau_{2\mathrm{f}}\right) = 2c_2, \end{cases} \tag{4}$$

$$\begin{cases} z_4 = c_0 + c_1\tau_{3\mathrm{f}} + c_2\left(\tau_{3\mathrm{f}}\right)^2 + c_3\left(\tau_{3\mathrm{f}}\right)^3, \\ z_4 = d_0, \\ c_1 + 2c_2\tau_{3\mathrm{f}} + 3c_3\left(\tau_{3\mathrm{f}}\right)^2 = d_1, \\ 2c_2 + 6c_3\left(\tau_{3\mathrm{f}}\right) = 2d_2, \end{cases} \tag{5}$$

$$\begin{cases} z_5 = d_0 + d_1\tau_{4\mathrm{f}} + d_2\left(\tau_{4\mathrm{f}}\right)^2 + d_3\left(\tau_{4\mathrm{f}}\right)^3, \\ z_5 = e_0, \\ d_1 + 2d_2\tau_{4\mathrm{f}} + 3d_3\left(\tau_{4\mathrm{f}}\right)^2 = e_1, \\ 2d_2 + 6d_3\left(\tau_{4\mathrm{f}}\right) = 2e_2, \end{cases} \tag{6}$$

$$\begin{cases} z_6 = \mathrm{e}_0 + e_1\tau_{5\mathrm{f}} + e_2\left(\tau_{5\mathrm{f}}\right)^2 + e_3\left(\tau_{5\mathrm{f}}\right)^3 + e_4\left(\tau_{5\mathrm{f}}\right)^2, \\ \dot{z}_6 = \mathrm{e}_1 + 2e_2\left(\tau_{5\mathrm{f}}\right) + 3e_3\left(\tau_{5\mathrm{f}}\right)^2 + 4e_4\left(\tau_{5\mathrm{f}}\right)^3, \\ \ddot{z}_6 = 2e_2 + 6e_3\left(\tau_{5\mathrm{f}}\right) + 12e_4\left(\tau_{5\mathrm{f}}\right)^2. \end{cases} \tag{7}$$

Substituting those known data –$z_1 = 0$, $\dot{z}_1 = 1$, $\ddot{z}_1 = 0$, $\tau_{1f} = 1$, $z_2 = 3$, $\tau_{2f} = 1$, $z_3 = 8$, $\tau_{3f} = 2$, $z_4 = 24$, $\tau_{4f} = 2$, $z_5 = 52$, $\tau_{5f} = 1$, $\dot{z}_6 = 16$ and $\ddot{z}_6 = 2$ to above equations, motion equation of freestyle skiing robot in speed-up skiing phase can obtained and shown in equation (8).

$$\begin{cases} z_1 = t + 0.5t^2 + 3.17t^3 - 1.67t^4, \\ z_2 = 3 + 4.83t - 0.0036t^2 + 0.17t^3, \\ z_3 = 8 + 5.34t + 0.51t^2 + 0.41t^3, \\ z_4 = 24 + 12.3t + 3t^2 - 1.06t^3, \\ z_5 = 52 + 11.46t - 3.39t^2 + 8.39t^3 - 3.46t^4, \end{cases} \tag{8}$$

3.3.2. Motion curve planning of hip joint. Given motion curve equation of hip joint. In the second motion phase it can be written as

$$\theta_{\mathrm{h}2}(t) = f_{20} + f_{21}t + f_{22}t^2 + f_{23}t^3 + f_{24}t^4 + f_{25}t^5. \tag{9}$$

Substitute boundary conditions to equation (9), the below equation can be obtained:

$$\begin{cases} 153 = f_{20}, \\ 100 = f_{20} + f_{21} + f_{22} + f_{23} + f_{24} + f_{25}, \\ 0 = f_{21}, \\ 0 = f_{21} + 2f_{22} + 3f_{23} + 4f_{24} + 5f_{25}, \\ 0 = 2f_{22}, \\ 0 = 2f_{22} + 6f_{23} + 12f_{24} + 20f_{25}, \end{cases} \tag{10}$$

Thus, the polynomial equation of location is obtained in the form

$$\theta_{\mathrm{h}2}(t) = 153 - 530t^3 + 795t^4 - 318t^5. \tag{11}$$

The motion curve equation of hip joint in the fourth motion phase is

$$\theta_{\mathrm{h}4}(t) = f_{40} + f_{41}t + f_{42}t^2 + f_{43}t^3 + f_{44}t^4 + f_{45}t^5. \tag{12}$$

Substituting boundary conditions to equation (12), the below equation is obtained:

$$\begin{cases} 100 = f_{40}, \\ 176 = f_{40} + 2f_{41} + 4f_{42} + 8f_{43} + 16f_{44} + 32f_{45}, \\ 0 = f_{41}, \\ 0 = f_{41} + 4f_{42} + 12f_{43} + 32f_{44} + 80f_{45}, \\ 0 = 2f_{42}, \\ 0 = 2f_{42} + 12f_{43} + 48f_{44} + 160f_{45}. \end{cases} \tag{13}$$

Thus, polynomial equation of location was:

$$\theta_{\mathrm{h4}}(t) = 100 + 95t^3 - 71.25t^4 + 14.25t^5 . \tag{14}$$

Equations of five motion phases of hip joint were obtained as follows

$$\begin{cases} \theta_{\mathrm{h1}}(t) = 153, & 0 < t \le 1, \\ \theta_{\mathrm{h2}}(t) = 153 - 530t^3 + 795t^4 - 318t^5, & 0 < t \le 1, \\ \theta_{\mathrm{h3}}(t) = 100, & 0 < t \le 2, \\ \theta_{\mathrm{h4}}(t) = 100 + 95t^3 - 71.25t^4 + 14.25t^5, & 0 < t \le 2, \\ \theta_{\mathrm{h5}}(t) = 176, & 0, < t \le 1. \end{cases} \tag{15}$$

3.3.3. Motion curve planning of knee joint. Given motion curve of knee joint. In the second motion phase it has the form

$$\theta_{k2}(t) = g_{20} + g_{21}t + g_{22}t^2 + g_{23}t^3 + g_{24}t^4 + g_{25}t^5 . \tag{16}$$

Substitute boundary conditions in (16), the below equation can be obtained

$$\begin{cases} 153 = g_{20}, \\ 124 = g_{20} + g_{21} + g_{22} + g_{23} + g_{24} + g_{25}, \\ 0 = g_{21}, \\ 0 = g_{21} + 2g_{22} + 3g_{23} + 4g_{24} + 5g_{25}, \\ 0 = 2g_{22}, \\ 0 = 2g_{22} + 6g_{23} + 12g_{24} + 20g_{25}. \end{cases} \tag{17}$$

Thus, polynomial equation of location has the form

$$\theta_{\mathrm{k2}}(t) = 153 - 290t^3 + 435t^4 - 174t^5 . \tag{18}$$

Given motion curve equation of knee joint in the fourth motion phase as

$$\theta_{\mathrm{k4}}(t) = g_{40} + g_{41}t + g_{42}t^2 + g_{43}t^3 + g_{44}t^4 + g_{45}t^5 . \tag{19}$$

Substituting boundary conditions to equation (19) provides

$$\begin{cases} 100 = g_{40}, \\ 176 = g_{40} + 2g_{41} + 4g_{42} + 8g_{43} + 16g_{44} + 32g_{45}, \\ 0 = g_{41}, \\ 0 = g_{41} + 4g_{42} + 12g_{43} + 32g_{44} + 80g_{45}, \\ 0 = 2g_{42}, \\ 0 = 2g_{42} + 12g_{43} + 48g_{44} + 160g_{45}. \end{cases} \tag{20}$$

Thus, the polynomial equation of location can be obtained in the form

$$\theta_{\mathrm{k4}}(t) = 124 + 67.5t^3 - 50.63t^4 + 10.13t^5 \tag{21}$$

Thus, equations of five motion phases of knee joint reads

$$\begin{cases} \theta_{\mathrm{k1}}(t) = 153, & 0 < t \le 1, \\ \theta_{\mathrm{k2}}(t) = 153 - 290t^3 + 435t^4 - 174t^5, & 0 < t \le 1, \\ \theta_{\mathrm{k3}}(t) = 124, & 0 < t \le 2, \\ \theta_{\mathrm{k4}}(t) = 124 + 67.5t^3 - 50.63t^4 + 10.13t^5, & 0 < t \le 2, \\ \theta_{\mathrm{k5}}(t) = 178, & 0 < t \le 1. \end{cases} \tag{22}$$

3.3.4. Motion curve planning of shoulder joint. The motion curve equation of shoulder joint in the second motion phase is

$$\theta_{\mathrm{s2}}(t) = h_{20} + h_{21}t + h_{22}t^2 + h_{23}t^3 + h_{24}t^4 + h_{25}t^5 . \tag{23}$$

After substituting the boundary conditions into equation (23) we get

$$\begin{cases} 10 = h_{20}, \\ 80 = h_{20} + h_{21} + h_{22} + h_{23} + h_{24} + h_{25}, \\ 0 = h_{21}, \\ 0 = h_{21} + 2h_{22} + 3h_{23} + 4h_{24} + 5h_{25}, \\ 0 = 2h_{22}, \\ 0 = 2h_{22} + 6h_{23} + 12h_{24} + 20h_{25}. \end{cases} \tag{24}$$

Thus, the polynomial equation of location is

$$\theta_{\mathrm{s2}}(t) = 10 + 700t^3 - 1050t^4 + 420t^5 . \tag{25}$$

The motion curve equation of shoulder joint in the fourth motion phase is

$$\theta_{\mathrm{s4}}(t) = h_{40} + h_{41}t + h_{42}t^2 + h_{43}t^3 + h_{44}t^4 + h_{45}t^5 . \tag{26}$$

After substituting the boundary conditions to equation (26), we obtain

$$\begin{cases} 120 = h_{40}, \\ 10 = h_{40} + 2h_{41} + 4h_{42} + 8h_{43} + 16h_{44} + 32h_{45}, \\ 0 = h_{41}, \\ 0 = h_{41} + 4h_{42} + 12h_{43} + 32h_{44} + 80h_{45}, \\ 0 = 2h_{42}, \\ 0 = 2h_{42} + 12h_{43} + 48h_{44} + 160h_{45}\,. \end{cases} \tag{27}$$

Thus, the polynomial equation of location has the following form

$$\theta_{\mathrm{s}4}(t) = 120 - 137.5t^3 + 103.13t^4 - 20.63t^5\,. \tag{28}$$

Thus, equations of five motion phases of shoulder joint are

$$\begin{cases} \theta_{\mathrm{s}1}(t) = 10, & 0 < t \le 1, \\ \theta_{\mathrm{s}2}(t) = 10 + 700t^3 - 1050t^4 + 420t^5, & 0 < t \le 1, \\ \theta_{\mathrm{s}3}(t) = 120, & 0 < t \le 2, \\ \theta_{\mathrm{s}4}(t) = 120 - 137.5t^3 + 103.13t^4 - 20.63t^5, & 0 < t \le 2, \\ \theta_{\mathrm{s}5}(t) = 10, & 0 < t \le 1. \end{cases} \tag{29}$$

3.3.5. Motion curve planning of elbow joint The motion curve equation of elbow joint in the second motion phase is

$$\theta_{e2}(t) = k_{20} + k_{21}t + k_{22}t^2 + k_{23}t^3 + k_{24}t^4 + k_{25}t^5\,. \tag{30}$$

After substituting the boundary conditions to equation (30)we obtain

$$\begin{cases} 144 = k_{20}, \\ 138 = k_{20} + k_{21} + k_{22} + k_{23} + k_{24} + k_{25}, \\ 0 = k_{21} \\ 0 = k_{21} + 2k_{22} + 3k_{23} + 4k_{24} + 5k_{25}, \\ 0 = 2k_{22}, \\ 0 = 2k_{22} + 6k_{23} + 12k_{24} + 20k_{25}, \end{cases} \tag{31}$$

The polynomial equation of location has the form

$$\theta_{\mathrm{e}2}(t) = 144 - 60t^3 + 90t^4 - 36t^5\,. \tag{32}$$

The motion curve location of elbow joint in the fourth motion phase is

$$\theta_{\mathrm{e}4}(t) = k_{40} + k_{41}t + k_{42}t^2 + k_{43}t^3 + k_{44}t^4 + k_{45}t^5\,. \tag{33}$$

After substituting the boundary conditions to equation (33), we obtain

$$\begin{cases} 138 = k_{40}, \\ 170 = k_{40} + 2k_{41} + 4k_{42} + 8k_{43} + 16k_{44} + 32k_{45}, \\ 0 = k_{41}, \\ 0 = k_{41} + 4k_{42} + 12k_{43} + 32k_{44} + 80k_{45}, \\ 0 = 2k_{42}, \\ 0 = 2k_{42} + 12k_{43} + 48k_{44} + 160k_{45}. \end{cases} \tag{34}$$

Now, the polynomial equation of location has the form

$$\theta_{c4}(t) = 138 + 40t^3 - 30t^4 + 6t^5 . \tag{35}$$

Finally, the equations of five motion phases of elbow joint may be written as

$$\begin{cases} \theta_{e1}(t) = 144, & 0 < t \le 1, \\ \theta_{e2}(t) = 144 - 60t^3 + 90t^4 - 36t^5, & 0 < t \le 1, \\ \theta_{e3}(t) = 138, & 0 < t \le 2, \\ \theta_{e4}(t) = 138 + 40t^3 - 30t^4 + 6t^5, & 0 < t \le 2, \\ \theta_{e5}(t) = 170, & 0 < t \le 1. \end{cases} \tag{36}$$

4. Motion simulation of freestyle skiing robot

4.1. Virtual prototype modeling of freestyle skiing robot

The simplified model of freestyle skiing robot built in Pro/E was saved as file type "Parasolid". Import it into software ADAMS then its rigid body component attribute was modified and constraint and motion drive was added. Motion curve of all joints of freestyle skiing robot was used as control basis, which was input in ADAMS to generate STEP function. Simulation analysis of motion of freestyle skiing robot was conducted.

4.2. Motion simulation and its results analysis of freestyle skiing robot

Motion curves of all joints of freestyle skiing robot obtained through gait planning was used as control basis and those motion curves was parameterized to generate STEP functions. Driving function of all joints obtained through gaiting planning is shown in Table 2. Then, the STEP functions were added to the corresponding joints of freestyle skiing robot of virtual prototype. Before simulation analysis, check prototype model again. Interactive kinematics simulation of freestyle skiing robot was conducted.

Table 2. STEP driving function of all joints

Joints name	STEP FUNCTION
Ankle joint	0d×time
Knee joint	STEP(time,1,0d,2,29d) + STEP(time,4,0d,6,-54d)
Hip joint	STEP(time,1,0d,2,-53d) + STEP(time,4,0d,6,76d)
Shoulder joint (Roll)	STEP(time,6,0d,7,-180d)
Shoulder joint (Pitching)	STEP(time,1,0d,2,70d) + STEP(time,4,0d,6,-70d)
Waist joint	0d×time
Sliding movement	STEP(time,0,0,1,3000) + STEP(time,1,0,2,5000) + STEP(time,2,0,4,16000) + STEP(time,4,0,6,28000) + STEP(time,6,0,7,13000)

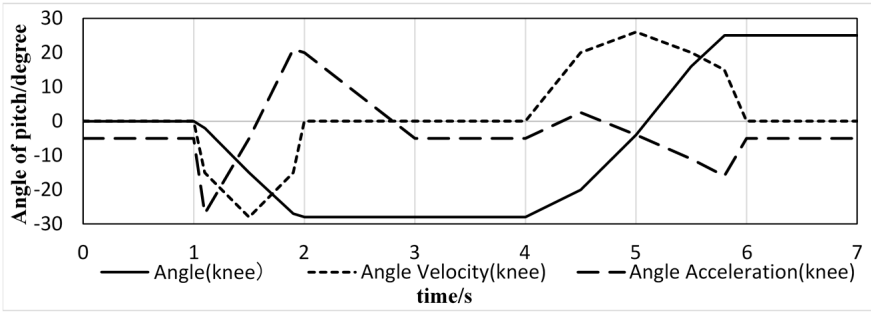

Fig. 1. Pitching of right knee joint

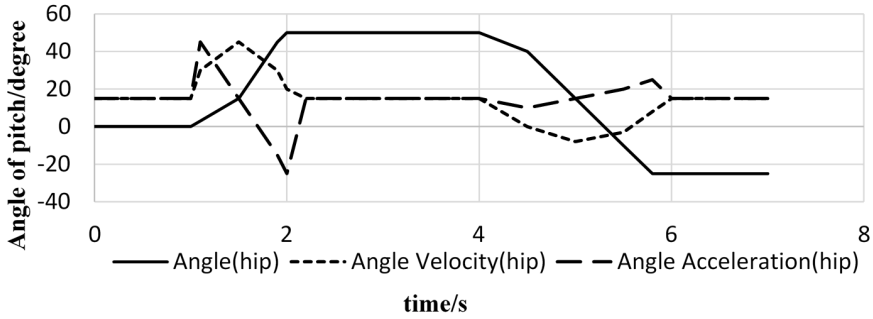

Fig. 2. Pitching of right hip joint

Experimental simulations show that freestyle skiing robot can dynamically simulate speed-up skiing phase well, including starting and sliding skiing, squat skiing, body extension preparation and raising arm. Then, post-processing module ADAMS/Post-Processor was used for post-process simulation analysis of results of

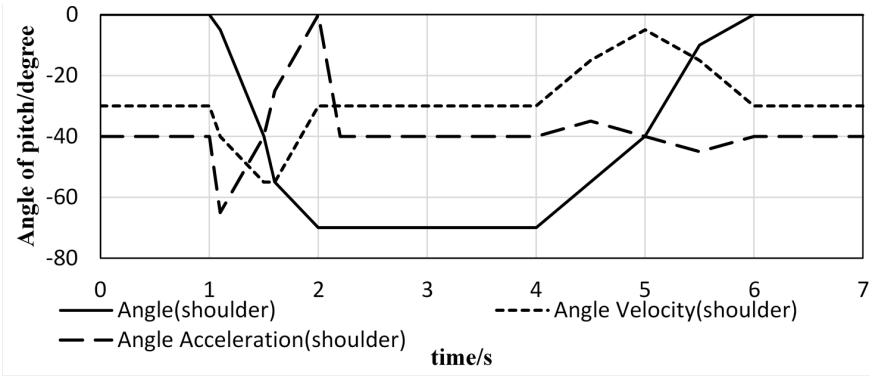

Fig. 3. Pitching of right shoulder joint

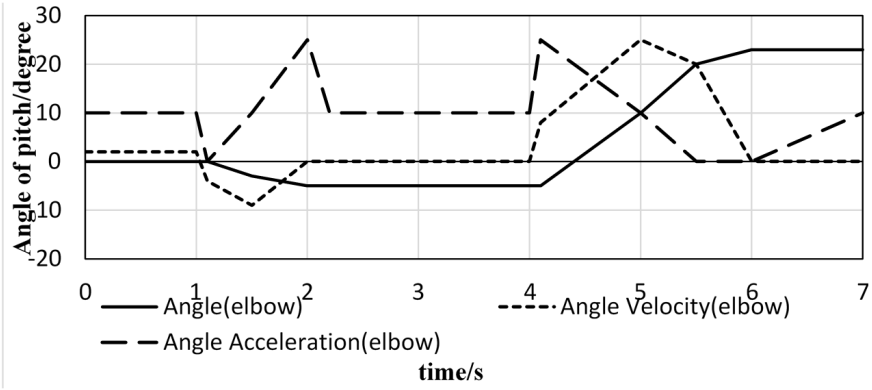

Fig. 4. Pitching of right elbow joint

ADAMS software. With this function, results of simulation calculation and analysis research of ADAMS can be displayed, thus model characteristics was reflected more accurately. Simulation curves of angular displacement, speed, and accelerated speed of joints rotation of freestyle skiing robot during movement are shown in Figs. 1–4. Because freestyle skiing robot was a symmetrical structure, simulation curve of the right arm joint and right leg joint was chosen.

5. Conclusion

Pro/E with powerful modeling function is used to build the simplified mechanical model of freestyle skiing robot. Virtual prototype of freestyle skiing robot is built in ADAMS for motion simulation. The simulation results show that bionic gait planning is suitable for motion planning of freestyle skiing robot, with which all movements of freestyle skiing robot in speed-up skiing phase are achieved.

References

[1] Z. Liu, C. Chen, Y. Zhang: *Decentralized robust fuzzy adaptive control of humanoid robot manipulation with unknown actuator backlash.* IEEE Transactions on Fuzzy Systems *23* (2015), No. 3, 605–616.

[2] H. Gritli, S. Belghith, N. Khraief: *OGY-based control of chaos in semi-passive dynamic walking of a torso-driven biped robot.* Nonlinear Dynamics *79* (2015), No. 2, 1363–1384.

[3] L. Žlajpah: *Simulation in robotics.* Mathematics and Computers in Simulation *79* (2008), No. 4, 879–897.

[4] Q. Nguyen, K. Sreenath: *L1 adaptive control for bipedal robots with control Lyapunov function based quadratic programs.* Proc. IEEE American Control Conference (ACC), 1–3 July 2015, Chicago, IL, USA, IEEE Conference Publications (2015), 862–867.

[5] D. Rollinson, A. Buchan, H. Choset: *Virtual chassis for snake robots: Definition and applications.* Advanced Robotics *26* (2012), No. 17, 2043–2064.

[6] X. Wang, Y. Ma, Q. W. Hao: *Kinematic analysis on Chinese female athletes' bFdF action in freestyle skiing aerialse.* International Journal of Advancements in Computing Technology *4* (2012), No. 16, 175–182.

Received May 7, 2017

Acta Technica *62* No. 3A/2017, 335–346

Analysis on modeling and numerical simulation for badminton racket of braiding composite material based on ANSYS

Liyan Zhang[1]

Abstract. Braiding composite material featured good mechanical property such as high strength and high modulus is widely used in badminton racket manufacturing. Parameterized finite element models for badminton racket of braiding composite material is built by ANSYS software based on Domain Superposition Technique of finite element, such as filament reinforcement phase model and matrix phrase model. Then, statics analysis, elastic properties prediction, invalidation discrimination and modal kinetic analysis are made for badminton racket model, which provides theory for design racket. Finally, elastic property of racket shaft is predicted and its result proves that Domain Superposition Technique of finite element is feasible.

Key words. Braiding composite material, badminton racket, ANSYS, Domain Superposition Technique of finite element, parameterized modeling.

1. Introduction

Composite material, a new material with excellence performance, is made up of no less than two materials of different properties by chemical or physical treatment, such as organic polymer, inorganic nonmetal and metal. Braiding composite material with well mechanical property is made up of pre-form and matrix phase material [1]. And pre-form with overall structure is woven by different methods. Nowadays, studies on braiding composited material are generally focused on unit cell model. Then, proper periodic boundary condition and load was used for mechanical analysis. However, few studies were focused on building overall model with braiding composite material. Badminton racket made up of braiding composite material was taken as object of study and its material model was built to study the overall mechanical property was studied.

[1]Shenyang Normal University, Liaoning, 110034, China; E-mail: liyanzhang00@aliyun.com

2. Literature review

In the early 1980, Ko [2] identified "fibrage" in his thesis and elaborated cubic unit cell model with rectangle surface for the first time. A finite element model with multi-scale was built by Wang et al. [3] using fiber, unit cell and laminate in three dimensions. Multi-scale progressive damage analysis was made on composite material of 2×2 braiding structure. However, finite element analysis can only focus on a certain parameters of the structure because of diverse model parameter. Theory and experiment was combined by Masters [4] to analyze mechanical properties of braiding composite material. Among those four methods, laminate model was the easiest one to be achieved. For even laminated board, direction of fiber bundle was the same and a bending correction factor was introduced to represent bending property of the fiber.

Thee badminton racket designed here is manufactured by resin transfer moulding (RTM), a technology developed from wet molding process and shooting technique and the most widely used and mature liquid modeling technology. Products of RTM molding is featuring smooth surface, stable quality, high fiber volume content, minor pollution, low cost and high efficiency. Finite element method can be used to simulate lay-up of fiber material and resin impregnation-reinforced fiber material and to study technological parameter, temperature and pressure those influence molding. Based on previous study, modeling and numerical simulation for badminton racket of braiding composite material was analyzed using ANSYS.

3. Research method

3.1. Domain Superposition Technique of finite element

At present, study on braiding composite material modeling was almost all focused on unit cell model, a representative elementary volume. Unit cell model built by traditional braiding composite material was aimed to reflect fiber reinforced phase model and matrix phase model as well as the overall construction of component as true as possible. True braiding composited material model was obtained after fiber reinforcement phase model was subtracted from matrix phase model with Boolean operation based on ANSYS. Thus, two phases finite element model with no crossover and overlap in space were obtained. Besides, special unit should be added at the junction of the two phases, thus related mechanical relation between them was produced. Within the final model, periodic boundary condition was used to finish pretreatment.

Braiding composite material was generally identified as an interconnection of a large number of representative periodic unit cells. Thus, variation of boundary surface of neighboring unit cell should be the same when under load. Variation of any point on surface and its corresponding node should be the same. Displacement field of any pair of parallel surface can be described as follows [5]

$$\mu_i^{j+} = \varepsilon_{ik} X_k^{j+} + \mu_i^*, \ (i,j,k = x,y,z)\,, \tag{1}$$

$$\mu_i^{j-} = \varepsilon_{ik} X_k^{j-} + \mu_i^* \,. \tag{2}$$

In above equation, μ denotes denoted displacement of any point during a unit, $j+$ denotes in the positive direction, $j-$ denotes in the negative direction, ε_{ik} is the average full-field strain and X_k^{j+} denotes the coordinates of corresponding node of two interfaces of X_{j^+} direction in k direction. The below equation can be obtained by combining equation (1) and (2):

$$\mu_i^{j+} - \mu_i^{j-} = \varepsilon_{ik} \left(X_k^{j+} - X_k^{j-} \right) = \varepsilon_{ik} \Delta X_k^j \,. \tag{3}$$

APDL program was used to matching coupling and node. Corresponding coupling and node relationship was identified through equation (3), thus periodic boundary condition was identified.

Topological structure with internal complex, high fiber volume fraction and interlaced fiber bundle are hard to be solved by traditional modeling method. Thus, Domain Superposition Technique (DST) of finite element [6] is put forward based on finite element. Finite element model for matrix phase and fiber reinforcement phase should be built for implement Domain Superposition Technique (DST) of finite element. And entity unit is adopted by those two phases model. There is an overlap of junction of the built matrix phase and fiber reinforcement phase. Two problems can be tackled by Domain Superposition Technique (DST) of finite element; the first one is stiffness matching of the two phases and the second is coupling the two phase modes properly. Therefore, displacement of the same point in overlapping region is the same when under stress. Model built by DST can simulate the structure of composite material only when stiffness matching and coupling are properly tackled.

A "negative" matrix is needed to match material stiffness by Domain Superposition Technique. Under the same stress state, stress state of "negative" matrix material is opposite to that of matrix material. For linear elastic material, "negative" nature of matrix material is the negative value of its stress-strain stiffness matrix. For isotropic linear elastic matrix material, its stress-strain stiffness matrix may be written in the form

$$D_{\text{host}} = \frac{E(1-v)}{(1+v)(1-2v)} \cdot \begin{bmatrix} 1 & \frac{v}{1-v} & \frac{v}{1-v} & 0 & 0 & 0 \\ \frac{v}{1-v} & 1 & \frac{v}{1-v} & 0 & 0 & 0 \\ \frac{v}{1-v} & \frac{v}{1-v} & 1 & 0 & 0 & 0 \\ 0 & 0 & 0 & \frac{1-2v}{2(1-v)} & 0 & 0 \\ 0 & 0 & 0 & 0 & \frac{1-2v}{2(1-v)} & 0 \\ 0 & 0 & 0 & 0 & 0 & \frac{1-2v}{2(1-v)} \end{bmatrix} . \tag{4}$$

In the above equation, E denotes the elasticity modulus of material and v denotes Poisson's ratio of matrix material. "Negative" stress-strain matrix is given as

$$D_{\text{Negative material}} = D_{\text{Actual matrix}} \,. \tag{5}$$

Here, $D_{\text{Negative material}}$ is the stress-strain matrix of negative material and $D_{\text{Actual matrix}}$

is the stress-strain matrix of actual matrix.

When implementing the Domain Superposition Technique (DST), it should match material nature to fiber reinforcement phase. The final filamentary phase material after matching equals the subtract matrix material nature from filament phase material nature, which can be obtained by subtracting the actual matrix phase stress-strain stiffness matrix from actual fiber reinforcement phase tress-strain stiffness matrix:

$$D_{\text{cor}} = D_{\text{en}} + D_{\text{ho}} \,. \tag{6}$$

In the above equation, D_{cor} denotes the matrix of modified reinforced stress-strain matrix, D_{en} denotes the matrix of actual reinforced stress-strain matrix and D_{ho} denotes the matrix of actual stress-strain matrix (substrate). In a word, the nature of matrix material was identified by grid cell of overall model and modified material constitutive model was identified by unit of fiber bundle region. Thus, material characteristics of overall superposition domain and true fiber bundle material was the same. For any designated node in any unit, its coordinate of the coupling of model fiber phase and matrix phase node is identified as

$$x = \sum_{i=1}^{m} N_i x_i, \quad y = \sum_{i=1}^{m} N_i y_i, \quad z = \sum_{i=1}^{m} N_i z_i \,. \tag{7}$$

In the above equation, x, y and z denote the coordinates of the overall coordinate system for a node in the unit. This is an interpolation function of the unit which is identified under natural system of coordinates. Symbol N denotes the shape function that is given as $N = \mu/\delta^e$, μ being the distance of any point during the unit and δ^e the displacement of the element node. Also, the displacement of the designated node is identified as

$$u = \sum_{i=1}^{m} N_i u_i, \quad v = \sum_{i=1}^{m} N_i v_i, \quad w = \sum_{i=1}^{m} N_i w_i \,. \tag{8}$$

Here, u, v and w denote the displacement components of a node in the unit.

The principle of Domain Superposition Technique is coupling of the designated node and freedom degree of the node on the same unit with the designated node. Thus, node coupling method is used to couple node of the fiber reinforcement phase model to the matrix model.

3.2. Parametric modeling and mechanical analysis

For the designed racket handle, its diameter was 7.3 mm, thickness was 1.5 mm and length was 450 mm. Given racket frame was an oval, whose major semi-axis was 140 mm, minor semi-axis was 110 mm, thickness was 14 mm and its diameter was set as 0.7 mm. Composite material of carbon fiber-epoxy resin was used, whose fiber reinforcement phase material was M40 carbon fiber and matrix phase and bracing wire was bisphenol A (BPA) epoxy resin. Parameters of material used for fiber and resin are shown in Table 1.

Table 1. Thermophysical properties of regular fluid and nanoparticles

Material property	E_1 (GPa)	E_2 (GPa)	G_{12} (GPa)	G_{23} (GPa)	v_{12}	v_{23}
Carbon fiber	393	25.53	25.53	11.94	0.20	0.25
Resin	3.62	3.62	-	-	0.35	0.35

(1) Analysis on finite element model

Solid64 entity unit was used to build fiber reinforcement phase and matrix phase of racket of two-dimension and three-direction braiding. There were three axial yarn and four braiding yarn included in the unit cell model of braiding composite material [7]. Fiber bundle material with filament dip-dyed part of resin and elastic constant of fiber bundle material was calculated by weighted average method. Through calculation below we obtained: $E_1 = 141.90\,\text{GPa}$, $E_2 = E_3 = 7.13\,\text{GPa}$, $G_{12} = G_{13} = 4.65\,\text{GPa}$, $G_{23} = 3.93\,\text{GPa}$, $v_{12} = v_{13} = 0.23$, $v_{23} = 0.36$. For simulating pre-stress of positions that bracing line connected with racket frame, PSMESH command was used to build pre-load stretching section of each positions. Then, SLOAD command was used to exert preload and poundage of bracing wire can be parameterized. Two-dimension and two-direction braiding and two-dimension and three-direction braiding were adopted by fiber reinforcement phase and both of their knitting angles are 45 degree. Fiber volume fraction of racket of two-dimension and three-direction braiding was 21.56 %. Finite element model of fiber phase and matrix phase for badminton racket handle of two-dimension and three-direction braiding are shown in Figs. 1 and 2. Other specified model are not listed one by one here.

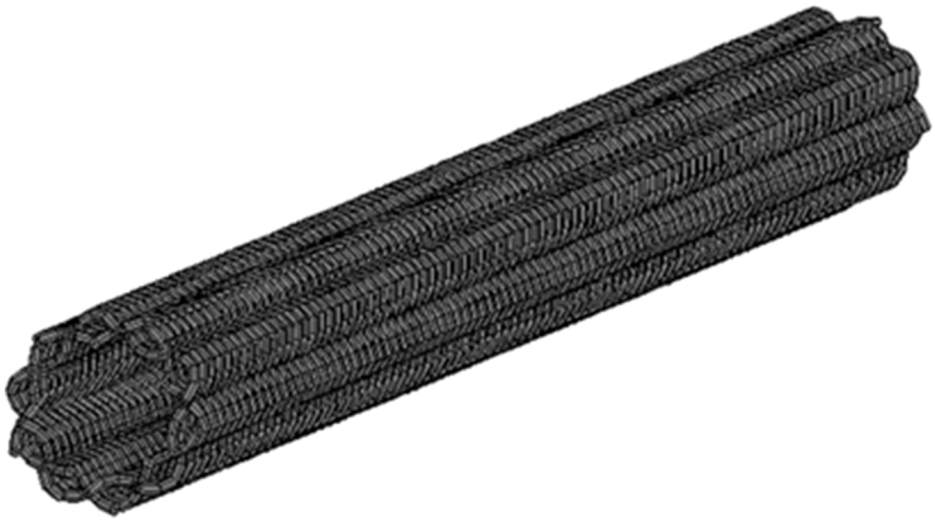

Fig. 1. Finite element model for fiber phase of racket handle of two-dimension and three-direction braiding

According to the practical situation of badminton racket under stress, two different forces were put on the two end faces of ANSYS model of racket handle using

Fig. 2. Finite element model for matrix of racket handle of two-dimension and three-direction braiding

DST- a full constraint and a vertical force. Diameter of badminton cork was 20 mm–25 mm, thus a round area was defined to be hit by vertical force (300 N). For the round area, midpoint of bracing wire was identified as a center of a circle and 25 mm was set as the diameter. Domain Superposition Technique was used to process the built finite element parameterized model, thus the final model was identified as shown in Fig. 3.

Fig. 3. Finite element model of badminton racket modified by Domain Superposition Technique

Under above constraint and stress, it can be calculated by ANSYS that the maximum equivalent stress of the whole racket was 154.28 MPa and the maximum equivalent displacement was 1.25 mm, which was positioned around the top of racket frame. The maximum equivalent stress of racket frame was 72.86 MPa at cross point of fiber and matrix phase. The maximum equivalent stress of racket handle was 154.82 MPa around the contact position of racket handle and racket frame. Position around the connection point of racket frame and racket handle can be easily broken off because figure of the contact position was changed. Thus, it can be inferred that distribution of whole equivalent stress of braiding composite material was uneven and whole equivalent stress of fiber bundle was obviously higher than whole equivalent stress of the matrix. Therefore, it can be known that fiber bundle of braided composite material was bearing the main force. Besides, apart from the stress concentration at top, whole fiber bundle was under even distributed force and whole equivalent displacement of racket was linear distributed. Thus, whole

performance of braiding composite material under stress was proved basically the same.

For finite element model for racket of two-dimension and two-direction braiding, its fiber volume fraction was 13.75 %. Above parametric modeling and mechanical analysis was made for racket of two-dimension and two-direction braiding, thus it can be found that under the same constraint and loading, the maximum equivalent stress of model of two-dimension and two-direction braiding and model of two-dimension and three-direction braiding was 154.28 MPa and 198.18 MPa, respectively. The whole equivalent stress of two-dimension and three-direction was much less than that of two-dimension and two-direction. Besides, their whole equivalent displacement was different. The reason that the whole bearing capacity of braided racket of two-dimension and three-direction braiding was much better than that of braided racket of two-dimension and two-direction braiding was that part of the loading was born by the added axial fiber of racket of two-dimension and three-direction braiding. The whole equivalent stress of fiber bundle of racket of two-dimension and two-direction braiding was obviously higher than that of the matrix. The whole force of fiber bundle was even distributed except that there was stress concentration at the end of constraint.

(2) Failure identification

With the wider application scope of braiding composite, it was of more and more practical importance to have a failure criterion. Nowadays, strength criterion of modified traditional material was applied by many researchers to braiding composite material, including the maximum stress criterion, Tsai-Hill criterion and Tsai-Wu multinomial criterion. Among all these mature criterion to explain fracture of composite material, Tsai-Wu multinomial criterion was the most comprehensive one and it would not be described in detailed as the limited to layout. According to failure identification criterion of Tsai-Wu, when failure factor was no less that 1, component was identified as failure. When intensity factor was less than 1, component was identified as safe. For racket handle of two-dimension and two-direction braiding, the maximum overall intensity factor of Tsai-Wu failure criterion was 0.51. For racket handle of two-dimension and three-direction braiding, the maximum overall intensity factor of Tsai-Wu failure criterion was 0.36. Because intensity factor of those two braiding method was less than 1, the overall component was identified as safe and would not fail. Security coefficient of racket handle of two-dimension and three-direction braiding was higher than that of the racket handle of two-dimension and two-direction braiding. The racket design was identified as reasonable and safe because it was measured within security coefficient under above extreme case.

(3) Elastic performance prediction for racket handle

Nowadays, mechanical performance analysis on composite material was mainly focused on elastic performance, specifically numerical modeling on elastic modulus, Poison's ration and shear modulus based on unit cell. Thus, elastic performance of the overall racket handle of composite material was analyzed as bellow based on Domain Superposition Technique (DST) of finite element.

Two different forces were put on the end faces of finite element model of racket handle using DST—a full constraint and a displacement loading. Let $\delta = 0.05 \times L$, which means that the overall strain is 0.5 %. The mean strain ε and mean stress δ_x on the plane $X = L$ was calculated by ANSYS software. Then, elasticity modulus E_y, Poisson's ratio μ_{xy} and shear modulus G_{xy} of the composite can be obtained according to this formation and definition formula. Besides, $E_y = E_z$, $\mu_{xz} = \mu_{yz}$ and G_{xy}, G_{yz} can be obtained using the common approach.

ANSYS finite element analysis model for predicting elastic performance is shown in Fig. 4.

Fig. 4. Model for predicting elastic performance of racket handle with full constraint and displacement loading

It can be concluded that with Domain Superposition Technique (DST) of finite element, it is effective to analyze overall component of racket handle, which effectiveness is also proved by accurate result of sparse finite element mesh. Elastic performance of racket handle predicted by DST is shown in Table 2.

Table 2. Predicting result of elastic performance

	E_x (GPa)	E_y (GPa)	E_z (GPa)	μ_{xy}	μ_{xz}	μ_{yz}	G_{xy} (GPa)	G_{xz} (GPa)	G_{yz} (GPa)
Two-dimension and two-directions	40.33	6.35	6.33	0.31	0.31	0.93	13.6	13.6	3.2
Two-dimension and three-directions	61.75	9.31	9.31	0.31	0.35	0.97	15.4	15.1	4.7

In conclusion, because part of the loading was born by the added axial fiber, racket of two-dimension and three-direction braiding was better that racket of two-dimension and two-direction braiding. Weight of those two rackets was almost the same. Besides, hand feeling and overall anti-bending and anti-torsion of racket of two-dimension and three-direction braiding was better than that of racket of two-dimension and two-direction braiding. Thus, racket of two-dimension and three-direction braiding was more and more popular among designers and amateur of badminton.

3.3. Analysis of modality dynamics

Modality is the inherent vibration of object. There are corresponding inherent frequency, damping ratio and modal shape for each order of mode. Those parameters can be used to design and optimize badminton racket to avoid unnecessary loss caused by resonance during hitting through modal analysis on finite element and finite element analysis result. Finite element model for modal analysis is the same model for static analysis and material property used in statics. Fixed constraint was put on one of the end of racket handle. Modal calculation of finite element for racket was calculated by ANSYS software with partitioning Lanczos method when there was not loading on finite element model, which calculation was based on parameterized calculation procedure developed according to static calculation method. For modality of high order, its contribution value to response was low and its rate of decay was relative fast. Generally, only modality of low order was included in modality analysis, thus, inherent frequency of the first-four-order was selected. For racket of two-dimension and three-direction braiding, conclusion of inherent frequency and mode of vibration of the first-four-order are shown in Table 3.

Table 3. Inherent frequency and mode of vibration of the first-four-order of racket of two-dimensional and three-directional braiding

Order	Inherent frequency (Hz)	Mode of vibration
1	34.25	Vibration in $X--Z$ plane
2	56.83	Vibration in $X--Y$ plane
3	75.92	Vibration in $X--Z$ plane
4	120.60	Compound vibration in plane $X--Y$ and $X--Z$

4. Design result and analysis

Overall size of badminton racket and the automatic analysis software were designed based on visual programming software Microsoft Visual Basic6.0 and finite element analysis software ANSYS. The analysis result can be extracted by the pre-programmed procedure and automatic generated a report saved as WORD format.

The software designed has to be logged in with user name and code for security. At the top of operation interface, there were menu item, tool bar and diagram figure of ANSYS finite element for badminton racket. In function menu, there were system, parametric modeling of finite element, analytical calculation and analysis report. There were options for specific function in pull-down menu, such as initial installation path of software, material property setting for matrix phase and fiber phase, boundary conditions and loading, ANSYS solving and exit. Statics analysis, failure identification and modal analysis were included in this software. Click statics

analysis, load and boundary constrain interface would popup. User can load badminton racket according to specific requirement. Thus, the earlier stage of designing size of badminton frame and handle, constraint and load were accomplished. After loading, a box of "save data" would popup. Click "confirm", the software would start analysis and solving with background program. When background program finished reading, dialog box would return to operational status and popup "ANSYS calculation finished". Then, information bar would remind user the succeed solving. The final solving result can be checked by clicking "result query". At the left side of interface, result of overall badminton racket, racket frame, racket handle can be checked according to the need. Corresponding equivalent stress and displacement fringe can also be checked. Partial enlarged details of fiber phase equivalent stress at racket handle of two-dimensional and three-directional braiding are shown in Fig. 5.

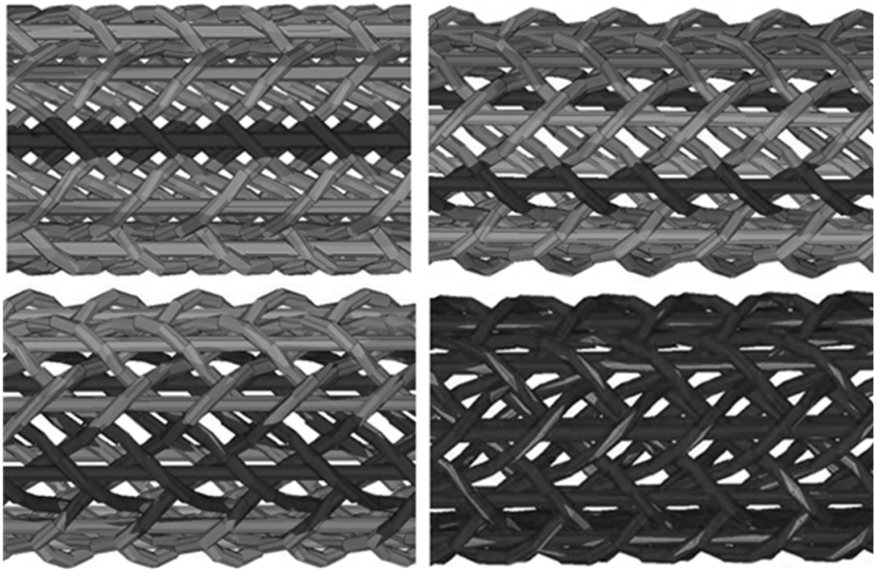

Fig. 5. Partial enlarged detail of fiber phase equivalent stress at racket handle of two-dimension and three-direction braiding

With this software, overall parameterization design of badminton racket and computation requirement of automatic finite element analysis can be satisfied, which is of practical significance because a more convenient guideline for badminton racket design is provided.

5. Conclusion

Main research result:

(1) Finite element model for badminton racket of two-dimension and two-direction braiding and two-dimension and three-direction braiding was built based on Domain Superposition Technique (DST) of finite element. Equivalent stress and equivalent

displacement fringe of racket when hitting can be calculated with ANSYS analytical software. Besides, statics analysis, elastic performance prediction, failure identification and modal mechanical analysis for racket were complete.

(2) Calculation and optimization software for badminton racket structure was developed based on visual programming software VB 6.0 and software of finite element analysis ANSYS, which can be used to design structure of badminton racket and analyze and calculate it with finite element.

References

[1] Z. X. Tang, R. Postle: *Mechanics of three-dimensional braided structures for composite materials – part I: fabric structure and fibre volume fraction.* Composite Structures *49* (2000), No. 4, 451–459.

[2] F. K. Ko: *Three-dimensional fabrics for composites. An introduction to the weave structure.* Proc. International Conference on Composite Materials, ICCM IV, 25–28 October 1982, Tokyo, Japan, Progress in Science and Engineering of Composites, Japan Society for Composite Materials *2* (1982), 1609–1619.

[3] Y. Q. Wang, A. S. D. Wang: *On the topological yarn structure in 3-D rectangular and tubular braided preforms.* Journal Composites Science & Technology *51* (1994), 575–586.

[4] J. E. Masters, R. L. Foye, C. M. Pastore, Y. Gowayed: *Mechanical properties of triaxially braided composites: Experimental and analytical results.* Journal of Composites, Technology and Research *15* (1993), No. 2, 112–122.

[5] Z. Xia, Y. Zhang, F. Ellyin: *A unified periodical boundary conditions for representative volume elements of composites and applications.* International Journal of Solids and Structures *40* (2003), No. 8, 1907–1921.

[6] W. G. Jiang: *Implementation of domain superposition technique for the nonlinear analysis of composite materials.* Journal of Composite Materials *47* (2013), No. 2, 243–249.

[7] C. Zhang, X. Xu, X. Yan: *Three unit-cell structure models of 3-D five-directional and full five-directional braided composites.* Journal of Nanjing University of Aeronautics & Astronautics *45* (2013), No. 02, 170–178.

Received May 7, 2017

Acta Technica *62* No. 3A/2017, 347–354

Research on athletes' mental state monitoring of spot athletics based on facial expression analysis

Li Zhu[1]

Abstract. Facing the furious competition of the athletics field at the present times, athletes' physical and psychological qualities have been greatly tested. Meanwhile, athletic mental state has been taken seriously. Athletic mental state is the mental state of the game. It is not only the psychological reaction to the current game environment, but also is the background factors of their game behavior. And it plays an important role in the athletes' performances. This study is supported by the theory of "embodied emotion", and it takes the national team diving team athletes as experimental and intervention objects. It intervenes in the athletes with "embodied" form to influence and change the negative emotions of athletes. In this study, the athlete's emotion can be changed to the acceptable and appropriate situation. Meanwhile, this method can promote athletes to obtain an ideal attitude and mood in the competition thereby achieving an ideal achievement. We analyze the psychological significance behind the facial expression based on sports and athletes own characteristics, and reveal the psychological state of high level athletes on site. Meanwhile, we can better grasp the mental state of athletes, and help coaches and sports psychologists to carry out targeted psychological training of athletes. Moreover, we provide real-time monitoring and guidance for coaches to better guide the game and athletes to achieve the desired athletic performance, so as to promote their competitive level.

Key words. Facial expression, athlete, spot athletics, mental state monitoring.

1. Introduction

Recently, with the rise of embodied cognitive ideas, the subjects' mood based on emotion/posture has aroused the interest of psychology researchers. The view of emotion induced by expression and physical posture can be traced back to Darwin, James and Lange. After years of silence, the researchers put forward the idea of "embodied emotion" based on a series of early studies. They argue that the input of peripheral systems of muscle and visceral (like the facial muscles of happy expression) causes a modal response to the mood-related system (like somatic sensory and motor

[1]Institute of Physical Education, Chu Zhou University, An Hui, 239000, China; E-mail: luhuangwork@yeah.net

cortex, hypothetical "mirror neuron" system, margin system, orbital frontal cortex). Therefore the individual feels the mood, produces an action that is consistent with the mood, and exhibits activation of the nervous system associated with the mood. The study finds that expression feedback can have a stronger or diminishing effect on individual original emotions. When the individual had no emotion, the expression feedback can directly induce the corresponding emotion. Therefore, we induce the emotion by expression or body feedback and study its impact on cognition and behavior, and this pattern is another hot spot in the research of the emotion.

This study is supported by the theory of "embodied emotion", and it takes the national team diving team athletes as experimental and intervention objects. It intervenes in the athletes with "embodied" form to influence and change the negative emotions of athletes. In this study, the athlete's emotion can be changed to the acceptable and appropriate situation. Meanwhile, this method can promote athletes to have an ideal attitude and mood to participate in the competition thereby achieving an ideal achievement.

2. Introduction

Mental state has the relatively stable level and features of psychological activity, which appeared in a certain situation. Soviet Psychologist H. D. Levitov divides people's mental activity into three forms, including mental process, mental state and personality mental characteristic [1–2]. The mental process is constantly changing and temporary, and the personality mental characteristic is solid. The mental state is temporary and stable, which is situated between the two above. It is a unified performance of mental process and personality mental characteristic. Therefore, athletic mental state has a relatively stable mental activity level and characteristics when athlete participates in the competition.

2.1. Facial expression overview

Expression is the external presentation of emotions and it is the explicit form of the movements of the various parts of the body when the emotions and emotions happen. The expression includes body and gesture expression. In different emotional state, the person's physical posture will change. Gestures can express emotions with language, and it can also express emotions alone. The tone is expressed through the voice, rhythm and speed. Facial expression is a combination of changes in the eye, face and mouth muscles. People have more than 20 pairs of muscles on the face, and the combination of these muscles can constitute a different expression mode [3–4].

Facing the furious competition of the athletics field at the present times, athletes' physical and psychological qualities have been greatly tested. Therefore athletic mental state has been taken seriously. Multi-disciplinary multi-field monitoring modes play a role in the field of competitive sports, and it gets a good results. However, the current means of monitoring has a certain hysteresis, because it is completed through pre-match and post-match surveys and interviews, so as to collect the mental state of athletes [5–6]. Moreover, athletic mental state has certain situa-

tion, so the information collected through pre-match and post-match will inevitably has been affected by some other factors, thereby resulting imperfect and inaccurate information.

3. Research methods

3.1. Research objects

HXX, one of the divers on the ten-meter platform of the Chinese national diving team, she is 16 years old, and the gender is female. She has won the top three in the national competitions. The psychological quality of this athlete is ordinary, anxiety and tension motions always appeared on her.

3.2. Research methods

Facial expression adjustment method: the theoretical guidance of this method is "embodied emotion". We use smile imitation and curious facial expressions to intervene in athletes. Mathematical statistics method: we use Excel 2013 and SPSS 21 to analyze the evaluation data of facial expression, so as to provide data support for the study.

3.3. Research process

This research chooses single-case experimental design, and completes the facial expression adjustment intervention in the usual training for five rounds and two months. Meanwhile, we use the facial expression adjustment as the theme to finish the psychological counseling and interview, so that the athletes' spot mood has changed. So we can reduce negative anxiety and tension, so that to facilitate the completion of technical action.

4. Research results and analysis

In this study, we select the facial expressions of the five rounds of intervention to research the emotions and mentality of the athletes' training.

4.1. Research on facial expression adjustment of five rounds intervention

Table 1 is the evaluation results on facial expression adjustment of five rounds intervention. In Table 1, we can see that the athlete's facial expressions are not disgusted and angry in the initial evaluation or five rounds intervention. Although the athlete has made the top three in the national race, there is no sign of facial expression of superiority before diving. The athlete is not very confident, and it may be caused by anxiety and tension. In the facial expression of this athlete, sad mood ratio in the initial evaluation and the first three rounds of the evaluation has

been relatively high. Happiness can be seen in the third round, so the athlete begins to boldly try the facial expression adjustment of the smiling pattern from the third round. There is no fear expression in the fourth round, and there is no pleasure and surprise expression in the initial facial expression.

Table 1. Evaluation results on facial expression adjustment of five rounds intervention

Facial expression	Initial evaluation	First round	Second round	Third round	Fourth round	Fifth round
Delightful expression	0	0	0	5.17±2.01	0	0
Surprised expression	0	8.02±2.34	10.38±2.13	14.34±3.16	16.31±2.71	20.96±4.24
Sad expression	45.36±3.49	37.31±3.41	35.18±2.18	29.31±3.09	24.51±2.61	18.51±4.06
Fear expression	13.13±3.13	9.81±1.74	8.31±2.18	2.24±3.01	0	1.06±2.31
Unaffected expression	39.82±4.31	40.84±3.98	37.31±5.91	46.10±2.98	55.10±2.39	57.01±3.32
Other	16.4±1.09	2.78±0.81	3.34±1.63	2.60±1.08	3.61±0.78	2.44±0.68
N	5	5	5	5	5	5

4.2. Variance analysis of evaluation results on facial expression adjustment of five rounds intervention

Table 2 contains the variance analysis of evaluation results on facial expression adjustment of five rounds intervention. From Table 2, we can see that surprised, sad, fear and unaffected expressions have a very significant difference ($P < 0.001$). In order to facilitate the visual analysis, we draw the curve graphs of mood changes of five rounds intervention of facial expressions. In the horizontal axis, 1 is initial evaluation, and 2–6 are the number of interventions of five rounds. The vertical coordinates presents the proportion of emotions. The results are also depicted in Figs. 1–5 showing the dependence of means of particular expression on the proportion variations.

Table 2. Variance analysis of evaluation results on facial expression adjustment of five rounds intervention

Facial expression	Sum of squares	df	Mean square	F	Sigma
Surprised expression	1345.193	5	269.040	31.376	0.000
Sad expression	2366.331	5	473.266	47.931	0.000
Fear expression	756.423	5	151.309	25.128	0.000
Unaffected expression	1503.381	5	300.817	16.308	0.000
Other	11.291	5	2.259	1.931	0.124

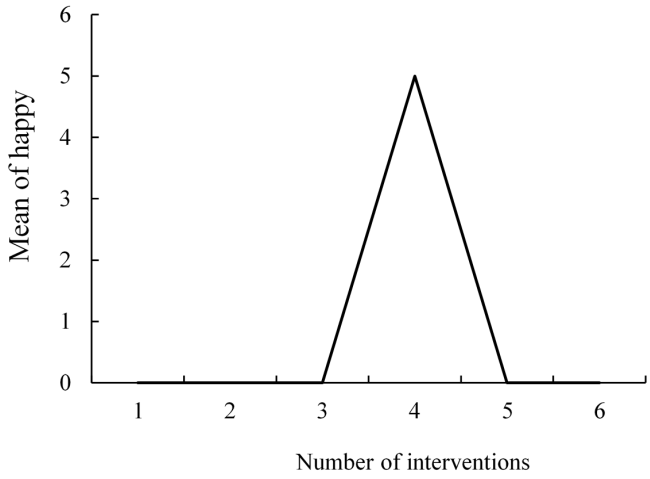

Fig. 1. Proportion variation of delightful emotion of five rounds intervention

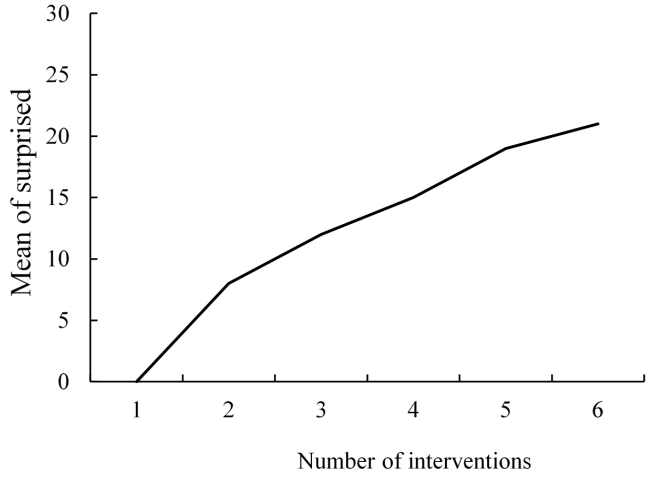

Fig. 2. Proportion variation of surprised emotion of five rounds intervention

5. Conclusion

From Table 2 and Figs. 1–5 we can see that the delightful expression only appeared in the fourth-round and the proportion of the surprised and unaffected expression is increasing with the increases of intervention. In the meantime, the proportion of the sad and fear expression is decreasing with the increases of intervention. The improvement of unaffected expression shows that the mood and mentality of athletes in the spot are more stable. The improvement of surprised expression shows that the attention is more focused. The decrease of sad and fear expression shows that the anxiety and tension mood are decreasing with the increases of intervention.

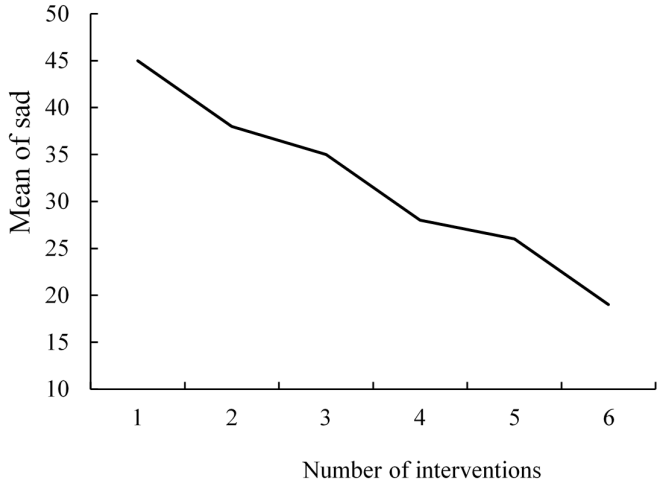

Fig. 3. Proportion variation of sad emotion of five rounds intervention

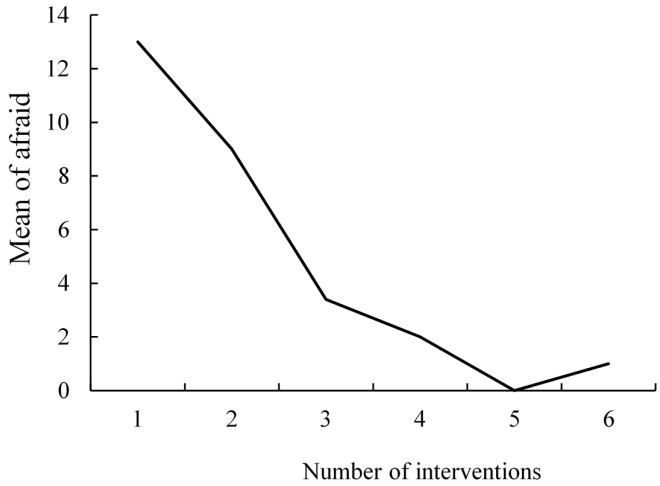

Fig. 4. Proportion variation of fear emotion of five rounds intervention

Coaches are getting more satisfied with the results of the action and scoring based on the interview. Athletes are increasingly interested in facial expression adjustment and they prefer to choose this adjustment method. So, this procedure has become a fixed behavior procedure for the athlete to complete each dive action. Through the above analysis we can know that the facial expression adjustment has the significant effectiveness on the high level diving athletes during the diving training psychological state and real-time emotion. In the next step, we will use the method in the regular game to adjust the facial expression of athletes, so as to improve the anxiety and tension motion during the game. Therefore, we can improve the stability of the

mentality and attention, so as to make it more suitable for sports competitions. Therefore, the athlete can play the normal technical action, thereby achieving the desired results.

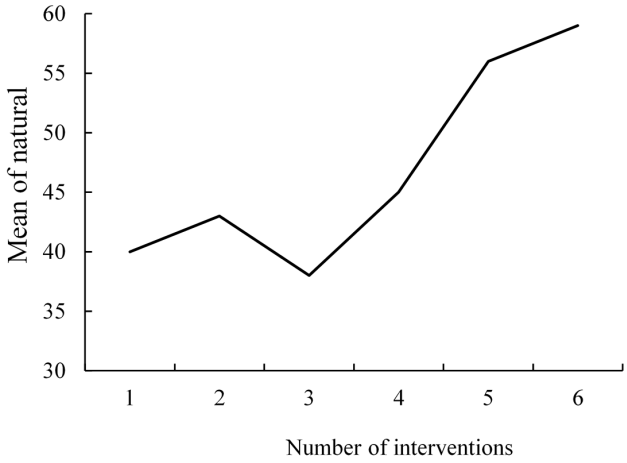

Fig. 5. Proportion variation of unaffected emotion of five rounds intervention

References

[1] S. M. Leite, J. Freitas, M. Campelo, M. J. Maciel: *Electrocardiographic evaluation in athletes: "Normal" changes in the athlete's heart and benefits and disadvantages of screening.* Revista Portuguesa de Cardiologia *35* (2016), No. 3, 169–177.

[2] M. A. Hemmatinezhad, R. Ramazaninezhad, H. Ghezelsefloo, M. Hemmatinezhad: *Relationship between emotional intelligence and athlete's mood with team-efficiency and performance in elite-handball players.* International Journal of Sport Studies *2* (2012), No. 3, 155–162.

[3] V. C. Wang, F. Ottawa, F. Mayer, P. M. Wippert: *Test-retest reliability of an elite athlete-questionnaire for the evaluation of training-related injury risk factors.* British Journal of Sports Medicine *48* (2014), No. 7, 670–671.

[4] D. Matsumoto, B. Willingham: *Spontaneous facial expressions of emotion of congenitally and noncongenitally blind individuals.* Journal of Personality and Social Psychology *96* (2009), No. 1, 1–10.

[5] J. M. Fernández-Dols, C. Crivelli: *Emotion and expression: Naturalistic studies.* Emotion Review *5* (2013), No. 1, 24–29.

[6] K. Kim, M. Sagas, N. A. Walker: *Replacing athleticism with sexuality: Athlete models in sports illustrated swimsuit issues.* International Journal of Sport Communication *4* (2011), No. 2, 148–162.

Received May 7, 2017